REMOTE SENSING OF EVAPOTRANSPIRATION USING AUTOMATED

CALIBRATION: DEVELOPMENT AND TESTING IN THE STATE OF FLORIDA

by

Aaron H. Evans

A Dissertation Submitted to the Faculty of

The Charles E. Schmidt College of Science

in Partial Fulfillment of the Requirements for the Degree of

Doctor of Philosophy

Florida Atlantic University

Boca Raton, FL

August 2014

UMI Number: 3647569

UMI

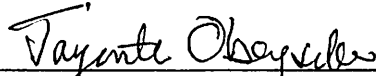Dissertation Publishing

UMI 3647569

ProQuest

REMOTE SENSING OF EVAPOTRANSPIRATION USING AUTOMATED

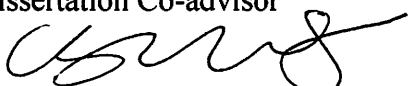CALIBRATION: DEVELOPMENT AND TESTING IN THE STATE OF FLORIDA

by

Aaron H. Evans

This dissertation was prepared under the direction of the candidate's dissertation co-advisors, Dr. Jayantha Obeysekera and Dr. Caiyun Zhang, Department of Geosciences, and has been approved by the members of his supervisory committee. It was submitted to the faculty of the Charles E. Schmidt College of Science and was accepted in partial fulfillment of the requirements for the degree of Doctor of Philosophy.
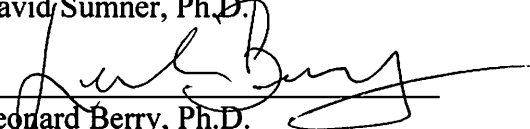
SUPERVISORY COMMITTEE:

Jayantha Obeysekera, Ph.D.
Dissertation Co-advisor

Caiyun Zhang, Ph.D.
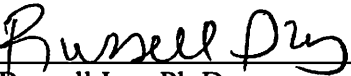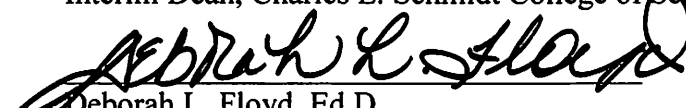Dissertation Co-advisor

David Sumner, Ph.D.

Leonard Berry, Ph.D.

Charles Roberts, Ph.D.
Chair, Department of Geosciences

Russell Ivy, Ph.D.
Interim Dean, Charles E. Schmidt College of Science

Deborah L. Floyd, Ed.D.
Interim Dean, Graduate College

07/09/2014
Date

ii

ACKNOWLEDGEMENTS

I would like to thank my committee members for all the time they contributed towards this dissertation. Specifically I would like to thank Dr. Jayantha Obeysekera for taking on the responsibility of advisor which allowed this dissertation to continue. I very much appreciate everything you have done. I would also like to thank Dr. Caiyun Zhang for the support you have offered. Thank you Dr David Sumner for all of the insight and connections you made available. I would also like to thank Dr. Leonard Berry for the work you put into this dissertation early on as faculty co-advisor. I would also like to thank Dr. Russell Ivy for the advice you provided me during my time at FAU. I would also like to thank Dr. Charles Roberts for all the talks and good times while supporting myself as instructor of the remote sensing courses you created. I also need to express my gratitude to Dr Jorge Restrepo for guiding me down the road towards this dissertation when I found myself at the crossroads. Thank you Barclay Shoemaker for helping me grapple with the eddy covariance data. I would also like to thank Hilton Cordoba for being a mucho loco office mate. Thanks to Dean Monette for not distracting me so much so that I was able to actual finish! It was good brainstorming with you. Thank you Manny McIlroy for putting up with all the arguing with my computer. I would also like to thank all of the other students I forgot to mention.

Thanks Rory and Lester for helping us with the stilt house as this dissertation was carried out. I would also like to thank my sister Kim for looking out for me over the years. Thank you, Jaybo for being a Radcliff and taking such good care of your cousin

while I slaved away at this dissertation. I would especially like to thank my Mother and Father for creating me. Without you this dissertation would not be possible (hah hah). Thank you, Dad for teaching me to think differently. Thank you, Mom for raising me in a loving, peaceful way which allowed me to realize how wonderful this world can be. I also need to thank my son Aaron Junior for bearing with me while I burned the midnight oil. You are more amazing than I could have ever imagined and your perspective of this world consistently intrigues me. This dissertation would not have been possible without the support of my wife Tara. Thank you for all of the hard work you have put into taking care of the house and our son while I was pulling my hair out at school. The sacrifices you have made for this dissertation will not be forgotten. I am so thankful that the universe brought us together. You're beautiful!

ABSTRACT

Author:	Aaron Evans
Title:	Remote Sensing of Evapotranspiration Using Automated Calibration: Development and Testing in the State Of Florida
Institution:	Florida Atlantic University
Dissertation Advisors:	Dr. Jayantha Obeysekera and Dr. Caiyun Zhang
Degree:	Doctor of Philosophy
Year:	2014

Thermal remote sensing is a powerful tool for measuring the spatial variability of evapotranspiration due to the cooling effect of vaporization. The residual method is a popular technique which calculates evapotranspiration by subtracting sensible heat from available energy. Estimating sensible heat requires aerodynamic surface temperature which is difficult to retrieve accurately. Methods such as SEBAL/METRIC correct for this problem by calibrating the relationship between sensible heat and retrieved surface temperature. Disadvantage of these calibrations are 1) user must manually identify extremely dry and wet pixels in image 2) each calibration is only applicable over limited spatial extent. Producing larger maps is operationally limited due to time required to manually calibrate multiple spatial extents over multiple days. This dissertation develops techniques which automatically detect dry and wet pixels. LANDSAT imagery is used because it resolves dry pixels. Calibrations using 1) only dry pixels and 2) including wet pixels are developed. Snapshots of retrieved evaporative fraction and actual

evapotranspiration are compared to eddy covariance measurements for five study areas in Florida: 1) Big Cypress 2) Disney Wilderness 3) Everglades 4) near Gainesville, FL. 5) Kennedy Space Center. The sensitivity of evaporative fraction to temperature, available energy, roughness length and wind speed is tested. A technique for temporally interpolating evapotranspiration by fusing LANDSAT and MODIS is developed and tested.

The automated algorithm is successful at detecting wet and dry pixels (if they exist). Including wet pixels in calibration and assuming constant atmospheric conductance significantly improved results for all but Big Cypress and Gainesville. Evaporative fraction is not very sensitive to instantaneous available energy but it is sensitive to temperature when wet pixels are included because temperature is required for estimating wet pixel evapotranspiration. Data fusion techniques only slightly outperformed linear interpolation. Eddy covariance comparison and temporal interpolation produced acceptable bias error for most cases suggesting automated calibration and interpolation could be used to predict monthly or annual ET. Maps demonstrating spatial patterns of evapotranspiration at field scale were successfully produced, but only for limited spatial extents. A framework has been established for producing larger maps by creating a mosaic of smaller individual maps.

DEDICATION

This dissertation is dedicated to my better thirds, AJ and Tag.

I love you.

∞

REMOTE SENSING OF EVAPOTRANSPIRATION USING AUTOMATED

CALIBRATION: DEVELOMENT AND TESTING IN THE STATE OF FLORIDA

LIST OF TABLES

LIST OF FIGURES

xviii

1. Introduction

Precipitation reaching the surface of the earth can be divided into what can be called green water and blue water. Blue water is that which is leaked into the ground or runs off the surface. Green water is evapotranspiration (*ET*), or the combination of evaporation and transpiration of water vapor from plant leaves. The quantity of precipitation allocated between green and blue water has important implications for the well being of both the natural world and mankind (Fallenmark and Rockstrom, 2006). In terms of mass balance, evapotranspiration is very important to the hydrologic cycle. The amount of water evaporated and transpired over the US land surface accounts for approximately 2/3 of the rainfall (Spellman, 2009). In Florida, the ratio of 30 year averaged evapotranspiration to precipitation ranges from approximately 0.4 to 0.8 (Sanford and Selnick, 2013). The cooling effect associated with evapotranspiration is also important to climatology. The global (ocean and land) latent heat of vaporization accounts for approximately half of the solar radiation absorbed by the surface (Kiehl and Trenberth, 1997). In addition, water vapor is an important greenhouse gas which could lead to a positive feedback to global warming. An increase in surface temperature would lead to an increase in evapotranspiration adding more water vapor to the atmosphere which would absorb more radiation (Held and Soden, 2000). Understanding the contribution of vegetation to evapotranspiration is an important part of understanding the earth system. On smaller scales evapotranspiration is a critical process for water resource management and agricultural/irrigation applications (Sinclair et al, 1984).

The transport of water vapor from the earth surface is accomplished via turbulence. The wind creates eddies at the surface which transports moist surface air up and dry upper air down (Stull, 1988). The rate of this flux depends on the intensity of the vertical gradient of water vapor in the surface boundary layer along with the magnitude of the wind and the buoyancy of the air. The available energy, in the form of solar and thermal radiation, is vital as a fuel for maintaining the water vapor gradient because it heats the surface which increases the density of water vapor that is in equilibrium with liquid surface water. The top end of this gradient is located on the order of 100 meters above the surface. During the day, this top end is typically drier and colder than the surface which is the source of moisture and heat for the boundary layer (Foken, 2008). Availability of water is also a driving factor behind evapotranspiration. This can either be in the form of surface water that is directly evaporating, or deeper water that plants are consuming via their roots and releasing via the stomata on their leaves. Therefore, the availability of vegetation is an obvious requirement for transpiration (Rodriquez and Porporato, 2004). The availability of water and quantity of vegetation typically vary more abruptly in space compared to atmospheric variables such as mean wind, humidity and temperature (at the top of the surface boundary layer). The variation of solar radiation only occurs over large scales unless there is the presence of clouds which produces heterogeneity of solar radiation reaching the surface. In addition, heterogeneity of surface albedo will result in the small scale variation solar radiation absorbed by the surface. In the end, the spatial extent and resolution of interest will determine which factors contribute to the spatial variability of evapotranspiration for the area of interest.

2

Remote sensing of evapotranspiration has a lot of potential for creating maps of evapotranspiration (Courault et al, 2005; Gowda et al, 2008; Li and Lyons, 1999). Eddy covariance towers or weather station profile methods can measure evapotranspiration over a small footprint (on the order of 1 km), but it is difficult to use them to measure spatial variation in the landscape (Baldocci et al, 1988). It is impossible to perform a spatial interpolation between towers due to sudden changes in land cover. This heterogeneity is especially common in human dominated landscapes. In addition, the availability of evapotranspiration measurements is very limited. Remote sensing has a large potential for solving this problem because it is available over large spatial extents. One problem with remote sensing of evapotranspiration is that the atmospheric boundary layer is too thin to be directly measured using remote sensing. Fortunately, surface information (in conjunction with atmospheric forcing) can be used to determine the *ET* flux. Atmospheric forcing can be incorporated into the remote sensing via surface weather stations (Laymon and Quattrochi, 2004).

Many remote sensing of evapotranspiration approaches use a surface energy balance approach. Figure 1.1 shows the important terms in the surface energy balance. *A* is the available energy of radiation which is equal to the net radiation absorbed by the surface (R_{net}) minus the energy used to heat the surface (*G*). R_{net} is equal to combination of the short-wave radiation from the sun (R_{solar}) and the long-wave radiation from the atmosphere (R_{atm}) absorbed by the surface minus the long wave radiation lost from the earth (R_{earth}). The available energy *A* is divided between sensible heat (*H*) and latent heat fluxes (*LE*) as shown in Figure 1.1. Sensible heat (*H*) is the vertical convection of heat while latent heat (*LE*) is the cooling due to evapotranspiration. The remote sensing

3

problem is divided into two parts. The first part consists of determining the available energy from radiation that is available to sensible and latent heat fluxes. The second part consists of determining the fraction of that energy which is allocated to evapotranspiration. This fraction is commonly called the evaporative fraction (*EF*). Since remote sensing directly measures radiation, the first part is usually more straightforward in nature. For the second part, thermal remote sensing is used in order to leverage the cooling effect due to the phase change from liquid to vapor. Specifically, cool areas use a larger fraction of the energy for evapotranspiration compared to hot areas. At times this might be confusing since higher temperatures would seem to produce larger evaporation. While it is true that a warm body of water evaporates more than a cool body of water, only the potential for evaporation increases with temperature for surfaces other than open water. For land surfaces evapotranspiration is limited by the amount of water in the soil so that what really matters is the effect that evapotranspiration has on temperature. For a completely dry surface all of the energy goes to sensible heat. If this surface becomes wet, then some of the energy will go to evapotranspiration resulting in a net loss in energy at the surface resulting in cooling. Sensible heat will decrease with reducing surface temperature until surface energy budget is once again balanced. In the end, the relative temperature of dry areas versus wet areas is more predictive of the evaporative fraction compared to the absolute temperature. A higher absolute temperature means there is more potential for evapotranspiration, but the relative temperature reveals how much of that is realized. This relative temperature is more representative of the variability of available water and quantity of vegetation.
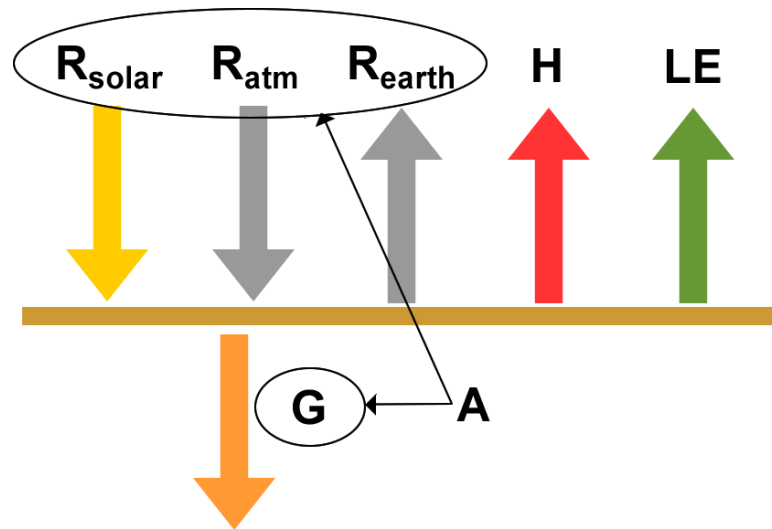
Figure 1.1: Components of the Energy Balance

A large problem in remote sensing of evapotranspiration is low temporal resolution (Junchang and Roy, 2008). Although geosynchronous satellite platforms such as GOES provide high temporal resolution, the spatial resolution is coarse (5-10km). Also, clear sky imagery is necessary for remotely sensing the earth's surface but the high frequency of clouds in Florida (Choi, 2008) produces challenges for remote sensing of *ET* in terms of the temporal resolution of *ET* maps. In addition, these are just snapshots of *ET* and do not have the potential of measuring the daily variability of evapotranspiration. In order to determine daily *ET*, it is typically assumed that the evaporative fraction (*EF*) is constant throughout the day. Although this is a common practice, the evaporative fraction does not necessarily stay constant in the presence of clouds (Loehide and Gorelick, 2005). Assuming *EF* is constant over the day, the daily evapotranspiration can be found by multiplying *EF* by estimates of daily available energy. When estimating the daily available energy, it is important account for the diurnal variability due to clouds . Atmospheric and cloud modeling applied to GOES satellite data has been used to determine radiation that reaches surface in the presence of clouds in south Florida

5

producing estimates of daily available energy (Mecikalski et al, 2011; Paech et al, 2009). One goal of this dissertation is to determine maps of *EF* to accompany these maps of available energy.

1.1 Review of Various Techniques for Remote Sensing of Evapotranspiration

In this section, techniques used for remote sensing of evapotranspiration are divided into various types. The first division is between empirical based algorithms and physically based algorithms. Physically based algorithms use physics for the core of the model with model parameters derived from empirical equations. Purely empirical algorithms are less common. One example uses machine learning techniques to relate surface fluxes measured from eddy covariance towers to surface temperature, vegetation index, and solar radiation obtained from MODIS. A technique known as support vector machine (SVM) is used to perform the regression of this non-linear relationship. This relationship is then used to create *ET* maps for the continental United States (Yang et al, 2006). Another approach is to find empirical relationship between *ET* or *EF* and vegetation indices (Yebra et al, 2013). In the same study *ET* was modeled using the Penman-Monteith (PM) equation where stomatal conductivity was determined by relating it to vegetation indices. The PM variation was only slightly better than *EF* regression but noticeably better than *ET* regression.

Physically based methods can be divided between "direct" methods which directly model *ET* and "residual" methods which find *ET* by modeling sensible heat and subtracting it from the available energy. One example of these "direct" methods is the PT-JPL algorithm (Fisher et al, 2008). This method calculates *ET* using a modified Priestly Taylor (PT) equation to determine soil evaporation, canopy transpiration, and

interception evaporation terms. The coefficients for the PT equation are adjusted due to greenness, temperature, plant moisture, and soil moisture constraints. These constraints are determined using spectral vegetation indices, air temperature and vapor pressure. Vegetation indices are calculated using optical remote sensing while temperature and vapor pressure is calculated using the meteorological reanalysis data set ISLSCP-II which provides monthly values at 1 degree spatial resolution. This algorithm was used to calculate global estimates of monthly *ET* values.

Another physically based "direct" method is the MODIS *ET* product (Mu et al, 2011). This method uses the Penman-Monteith equation to directly calculate soil evaporation, canopy transpiration and interception evaporation. In addition to air temperature and vapor pressure, surface and atmospheric resistances need to be estimated. Each pixel is classified as one of eleven biomes which has a set of parameters assigned to it which can be used to compute surface resistance. The resistances are then calculated from a combination of biome parameters, vegetation indices, temperature and vapor pressure. Temperature and vapor pressure come from global meteorological reanalysis data set GMAO. GMAO is daily data at 1 degree resolution but it is spatially interpolated down to 1 km MODIS resolution. The algorithm is applied for estimating the 8-day average 1 km resolution MODIS *ET* product.

The physically based "residual" method is a popular technique for remote sensing of *ET* in which the sensible heat is subtracted from available energy to find *ET*. For the "residual" method it is critical to remotely sense surface temperature because it is directed related to sensible heat:

$$H = g_{ab} (T_s - T_a) \qquad\qquad 1.1.1)$$

where g_{ab} is the conductance of the combination of the atmospheric and molecular boundary, T_s is the surface temperature, and T_a is the temperature of the atmosphere. The most sophisticated variation of the "residual" method uses a two-source model. Two-source models explicitly account for bare soil and vegetation as individual sources of flux. A very advanced algorithm which uses the two-source model is the ALEXI-DISALEXI algorithm (Anderson et al, 1997; Anderson et al, 2004). The canopy and soil temperature averaged by weighting with their fractional coverage is set equal to the retrieved surface temperature. From this one equation the canopy and soil temperature cannot be found, therefore it is necessary for ALEXI to estimate the transpiration of the canopy using the Priestly Taylor equation. From this, the sensible heat of the canopy is found as the "reverse" residual of the energy balance. From canopy sensible heat, the canopy temperature can be found and used to find soil temperature. The sensible heat of soil can then be found allowing the evaporation of soil to be computed as the residual. The assumption in the model is that when the soil is evaporating, the transpiration of the canopy will be equal to the potential *ET* as calculated using the Priestly Taylor equation. This assumes the canopy will not be stressed unless the soil evaporation is equal to zero. If the model is run as described above and soil evaporation is less than zero, it means that canopy transpiration was overestimated and soil evaporation is really zero. In this case the stressed canopy transpiration can be found using the residual method. The sensible heat of soil is set equal to energy supplied to soil. Sensible heat of soil is used to find the temperature of soil which is used to find sensible heat of canopy. The transpiration of canopy is equal to the residual. It should also be noted that the temperature of the atmosphere at blending height is required for this algorithm. In the ALEXI model this is

done by modeling the temporal dynamics of the atmospheric boundary layer. This requires using the GOES satellite because it has the temporal resolution necessary to model this behavior. The DisALEXI model then uses the blending height temperature found with this process and supplies it to the ALEXI two-source model applied to LANDSAT or MODIS resolution imagery. A schematic of ALEXI/DisALEXI is shown in Figure 1.1.1.
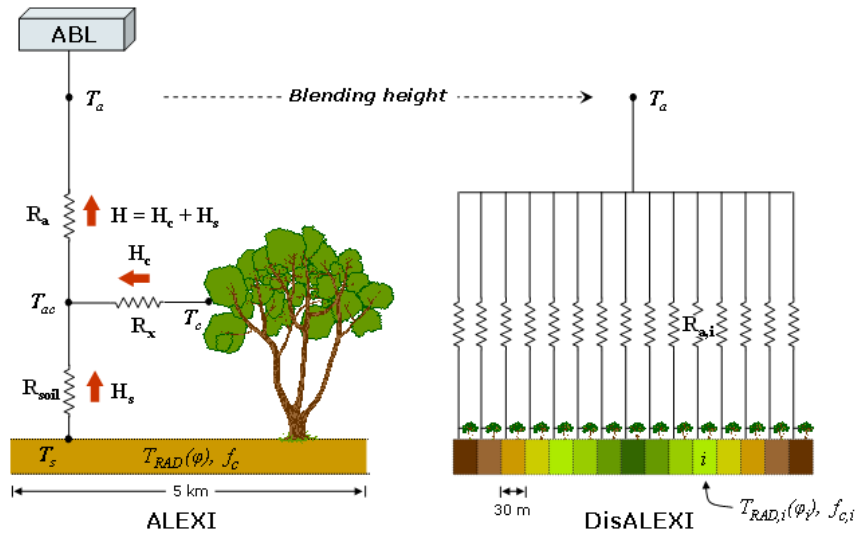
Figure 1.1.1: Schematic of ALEXI/DisALEXI Model

Often the "residual" method uses a one source model for the surface. An example of the one source model is SEBS (Su, 2002). In SEBS, equation 1.1.1 is used to find sensible heat. It requires knowledge of the temperature of the atmosphere and the conductance of the atmosphere. Determining the conductance of the atmosphere as it relates to satellite retrieved surface temperature can be problematic. Typically conductance is calculated with respect to aerodynamic temperature which is the temperature at the roughness length z_o. Figure 1.1.2 shows the difference between the aerodynamic temperature and the radiometric surface temperature. In order to find g_{ab} from equation 1.1.1, it is necessary to model the molecular boundary layer interfacing

with the surface. SEBS accounts for this by using the inverse Stanton number to find the extra resistance due to the molecular boundary layer. A problem with this approach is that the remote sensing of surface temperature is not very reliable in the absolute sense. Due to atmospheric and emissivity effects, it is difficult to accurately retrieve surface temperature (Guzinkski et al, 2013; Zhengming and Dozier, 1989) and therefore it will not be consistent with the atmospheric temperature measured in-situ. ALEXI accounted for this by modeling the atmospheric temperature relative to retrieved temperatures.
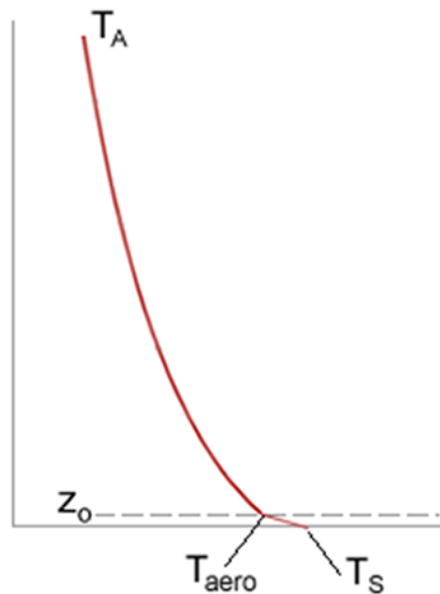
Figure 1.1.2: Difference between Aerodynamic and Radiometric Temperature

Although retrieved surface temperatures can be inaccurate in the absolute sense, they can still be useful in the relative sense. In this manner the temperature is used as an "index" where each scene is calibrated or trained using known values. A very simple example of this type of calibration is the triangle method (Carlson, 2007; Jiang and Islam, 2001; Owen et al, 1998). Jiang et al (2009) used the triangle method to find *ET* in South Florida by multiplying available energy by evaporative fraction. In order to find *EF* they assumed:

$$EF = a + b\, T_s \qquad\qquad\qquad\qquad\qquad\qquad 1.1.2)$$

The calibration procedure consists of finding cold (wet) and hot (dry) end members that

which are used to find coefficients *a* and *b* using equation 1.1.2.The triangle method

consists of plotting temperature vs. a vegetation index which results in a triangle shape.

Figure 1.1.3 is an example of the triangle plot where T0 is the retrieved radiant surface

temperature and *NDVI* is the retrieved normalized difference vegetation index. This

figure reveals the hot and cold temperatures that are used in fitting equation 1.1.2. It is

then necessary to determine the *EF* at these hot and cold limits. At the hot (dry) limit it is

assumed that the *EF*=0. At the cold (wet) limit *EF* is found using the Priestly-Taylor

equation.
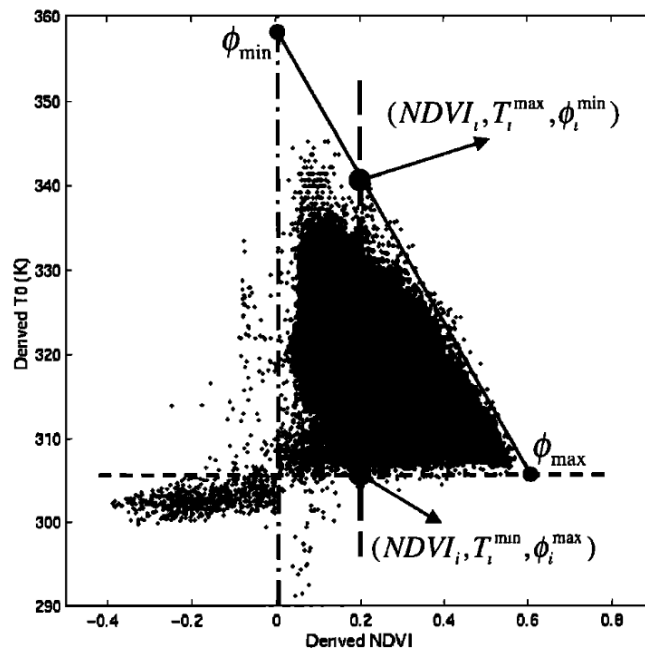
Figure 1.1.3: Example of Triangle Method (Reprinted from: Water Resources
Research, Vol. 37(2), Jiang, L. and Islam, S., *Estimation of Surface Evaporation Map
Over Southern Great Plains Using Remote Sensing Data*, 329-340, (2001), with
permission from Wiley)

11

Evans (2013a) applied the triangle method to LANDSAT imagery near

Gainesville, FL on April 22, 2008. Equation 1.1.2 was also fit using eddy covariance

tower measurements for the wet end members and hot (dry) spots visually detected by

user. Figure 1.1.4 shows a comparison of these two lines with the triangle method in blue

and tower data calibration in red. The triangle method seems to over estimates the *EF*

severely if one assumes the tower data is more reliable. An extension of the triangle

method is the "trapezoid" method which accounts for the variation in temperature for

high vegetation cover due to water stress (Long and Singh, 2012; Moran et al, 1994).

Long and Singh (2012) developed a two-source patch model within the trapezoid method

(TTME) which separates soil evaporation from vegetation transpiration. This model is a

patch model in which soil and vegetation transmit fluxes independently in contrast to the

previously described ALEXI two-source model in which soil and vegetation is coupled.

TTME couples the vegetation and soil so that they dry at a similar rate. ALEXI decouples

the surface and root zone moisture so that either the root zone is well watered or the

surface is completely dry and vegetation is stressed. The surface soil moisture responsible

for evaporation and the root zone soil moisture responsible for transpiration have been

observed to dry at different rates which results in a decoupling between the two layers

(Carlson et al, 2004). Therefore the ALEXI decoupling, although somewhat simplified,

should be more likely than the TTME coupling.
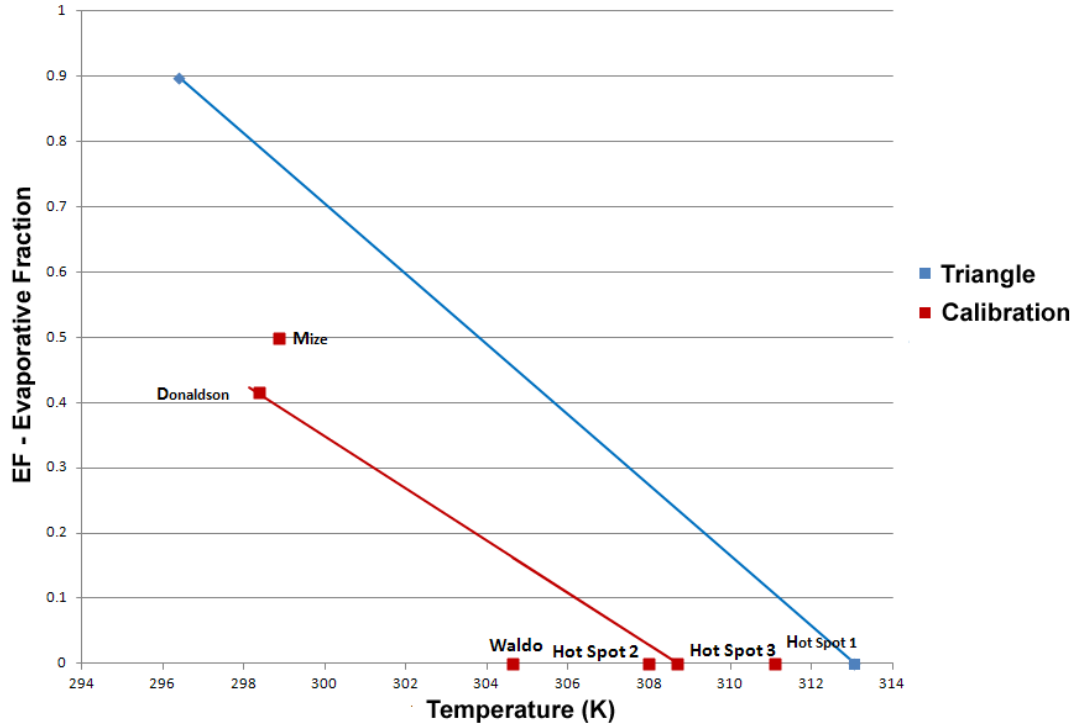
Figure 1.1.4: Comparison of Triangle Method to Eddy Covariance Calibration

Very popular calibration based "residual" methods are SEBAL (Bastiaanssen et al,1998) and SEBAL-METRIC (Allen et al, 2011). In SEBAL, the problem demonstrated in Figure 1.1.3 is avoided by allowing the sensible heat to be proportional to the vertical temperature gradient of an arbitrary slice of the boundary layer (ΔT). Using similarity theory it is further assumed that ΔT is linearly related to the retrieved surface temperature:

$$H = g_a \, \Delta T \qquad\qquad 1.1.3)$$

$$\Delta T = a + b \, T_s \qquad\qquad 1.1.4)$$

Figure 1.1.5 shows the variation of ΔT with surface temperature for a local area where the blending height temperature T_a is approximately spatially uniform. It should be noted that an important assumption in using equation 1.1.4 is that the temperature at blending height is constant over the extent of the image. If this is not true then the

13

coefficient a is not constant. Timmermans et al (2008) demonstrated the variability of air temperature near blending height to be more affected by large scale temperature variations at the surface. This supports the assumption that the atmosphere will vary smoothly even though the surface may be varying abruptly.
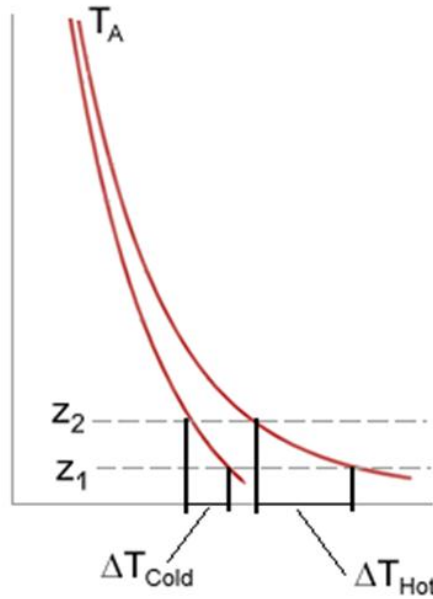
Figure 1.1.5: Variation of ΔT with T_s

Implementing equations 1.1.3 and 1.1.4 means it is no longer necessary to model the resistance due to the molecular boundary layer because the conductance of the atmosphere does not extend to the surface with regards to temperature. In addition, the problem of using a possibly inaccurate surface temperature is accounted for because the calibration process only requires temperature to be accurate in a relative sense. One criticism of this type of approach is that a and b are not constant in space and varies with surface resistance (Norman et al, 2006). From similarity theory the temperature gradients over different slices in the atmosphere are proportional to each other:

$$\frac{T_s - T_a}{\ln\frac{z_a}{z_s} - \psi_h(z_a) + \psi_h(z_s)} = \frac{T_1 - T_2}{\ln\frac{z_2}{z_1} - \psi_h(z_2) + \psi_h(z_1)}$$

1.1.5)

14

where T_a is the temperature of the atmosphere at the mixing height z_a, z_s is the roughness length accounting for the excess resistance of the molecular boundary layer to radiant temperature, ψ_h is a correction accounting for instability of atmosphere, and T_1 and T_2 are the temperatures of atmosphere at the arbitrary heights z_1 and z_2 . $T_1 - T_2$ in equation 1.1.5 is equal to ΔT from equation 1.1.4. Other than T_s and ΔT, the only parameter that cannot be assumed to be constant in space is z_s which would result in the coefficients a and b varying in space. Unfortunately z_s is very difficult to estimate. It is likely that the uncertainty in guessing z_s could be greater than the reduction in error produced by allowing z_s to vary. It is common to assume z_s is constant and therefore a and b are constant in space.

The SEBAL and METRIC algorithms requires the user to visually identify hot and cold pixels on the image. It is also possible to incorporate in-situ measurements of sensible heat into the calibration. Since flux towers are typically installed over vegetated surfaces, in-situ measurements usually only available for cold pixel information. In many cases ground measurements are not available and therefore it is necessary to identify both hot and cold pixels and estimate their sensible heat. For cold pixels, one approach is to use pixels over water and assume sensible heat equals zero which is not necessarily true. Figure 1.1.6 shows modeled EF vs. available energy (A) using Penman equation. In this model EF does not approach unity until A is low. It also demonstrates a variability of EF with temperature. The METRIC algorithm is an extension of SEBAL which uses a vegetation surface which is close to a reference crop as the cold pixel. The sensible heat is then estimated using the reference ET (RET) calculated from weather station information. RET is the ET of a hypothetical reference crop calculated using the Penman

Monteith equation. This is a practical solution since the weather station information does not require expensive instruments for measuring eddy flux, but only temperature, humidity, and wind. The method requires that the area of interest has a surface that behaves similar to the reference crop which typically means the area includes irrigated agriculture. METRIC has been used successfully in agricultural settings in the western United States (Allen et al, 2007). Instead of using the concept of evaporative fraction of available energy (*EF*), it uses evaporative fraction of reference *ET* (*ETrF*). It has been found that the *ETrF* works better in settings in which the advection of dry air into irrigated land from surrounding arid environment is a concern (Allen et al, 2007). For SEBAL and METRIC it is also necessary to find hot or dry pixels on the image. This can be a somewhat difficult practice at times. There are often many hot pixels on the image and choosing which to keep can be a somewhat subjective practice. For hot pixels it is typically assumed that they are totally dry and *EF*=0 which is not always the case. This assumption can be tested using a soil water balance model if soil texture and precipitation is known (Tasumi, 2003).

Calibration makes it possible for less complex one source models to be useful, but it requires user intervention for the identification of calibration pixels. Inconsistencies can arise due to the variation in the manner in which different operators choose calibration pixels. Long and Singh (2013) performed a simple test of the variability of results due to differences in calibration pixels. In this study they found 3 hot and 3 cold pixels and used 1 of each to create 9 sets of calibration coefficients. The resulting root mean squared (RMS) error of evaporative fraction between METRIC prediction and 12 flux tower observations ranged from 0.08 to 0.13. In practice the safest bet would be to use all 9 of

the pixels in one calibration. In Nevada, Morton et al (2013) compared results from METRIC calibration performed by 5 different trained users. This study found a variation in the distribution of retrieved ET_rF values.
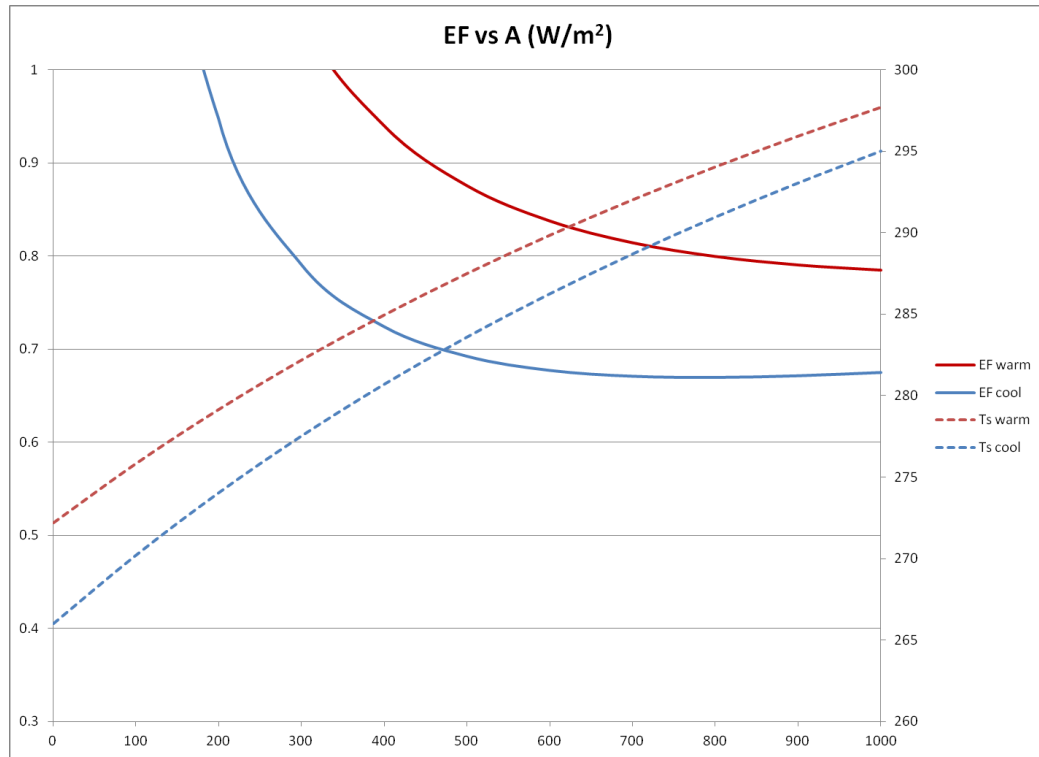
Figure 1.1.6: Modeled *EF* over Open Water

The development of methods which automatically identifies calibration pixels would be valuable in terms of making the algorithm more operational. Allen et al (2013) developed a methodology for detecting hot and cold pixels using thresholds of *NDVI*, temperature and proximity. This is based on a complex set of rules and corrections that worked well in agricultural areas in Idaho. The threshold and correction values would probably need to be modified for different environments. Morton et al (2013) developed an automated algorithm that attempts to reproduce manual calibration by adjusting the automated calibration until it matches with statistics produced from manual calibrations. It first estimates ET_rF with METRIC using the Allen et al (2013) method described above

17

for detecting calibration pixels. This is used to initialize a Monte Carlo simulation based on matching the size of tails of automatically produced ET_rF distribution to the manually produced ET_rF distribution. The Monte Carlo simulation works by randomly choosing target hot and cold tail sizes based on ET_rF distribution generated from the manual calibrations. Next, an iterative process is performed which produces an $ETrF$ retrieval which matches this target. This begins by finding the hot and cold thresholds for the initially retrieved $ETrF$ distribution which produces the target tail sizes. The new hot and cold pixels are those which are closest to these $ETrF$ thresholds. These new hot and cold pixels are then used to calibrate the model and a new $ETrF$ retrieval is produced. The tail sizes from this distribution are compared to the target. If they do not match then the process is repeated by finding the new hot and cold threshold using the new retrieved ET_rF distribution. This produces a different set of hot and cold pixels for each Monte-Carlo simulation. The method seemed to work well when compared to ground measurements in Nevada. A key assumption of this method is that the tail sizes of ET_rF are constant across image dates and study areas. This might be true for similar landscapes, but it would seem that different landscapes should have different distributions of ET_rF.

1.2 Dry Pixel Only Calibration

For this dissertation, the SEBAL-METRIC calibration based approach was chosen. This method was chosen because it was a compromise between simple and complex. The more complex models which directly calculate ET are useful at global and continental scales, but require an estimation of many parameters. Two-source models such as ALEXI-DisALEXI not only require estimation of more parameters than SEBAL-

METRIC, but it also requires the execution of a model describing the diurnal evolution of the boundary layer. Subsequently, the SEBAL-METRIC approach is chosen because it is within reach of the average user.

In this dissertation an automated method for detecting dry pixels in SEBAL-METRIC calibration is proposed. The basis of this method can be demonstrated by plotting available energy vs. temperature as shown in Figure 1.2.1. In Florida, dry pixels are typically brighter than wet pixels and therefore have less energy. These dry pixels form the lower boundary of the plot. As the dry pixels become darker, they absorb more energy and therefore the temperature increases. There comes a point that the surface becomes darker because either the vegetation is absorbing solar radiation for photosynthesis or the surface is wet. In these areas the temperature begins to decrease because the latent cooling of transpiring vegetation or evaporating water offsets the increase in available energy. Figure 1.2.1 clearly shows this transition point as a "peak" temperature in the scatter plot. The final result is a lower boundary extreme to the scatter plot which is made up of dry pixels where temperature increases with energy.

Although this method was originally intended for finding dry pixels in a scene, the range of temperatures in the dry pixels is wide enough to allow them to be used to calibrate equation 1.1.4 without the need of separate wet pixels. This is an advantage in natural areas that do not have surfaces that are similar to reference *ET* surfaces required by METRIC. Eddy covariance measurements at the surface could be used as wet pixels, but the availability of this type of data is limited.
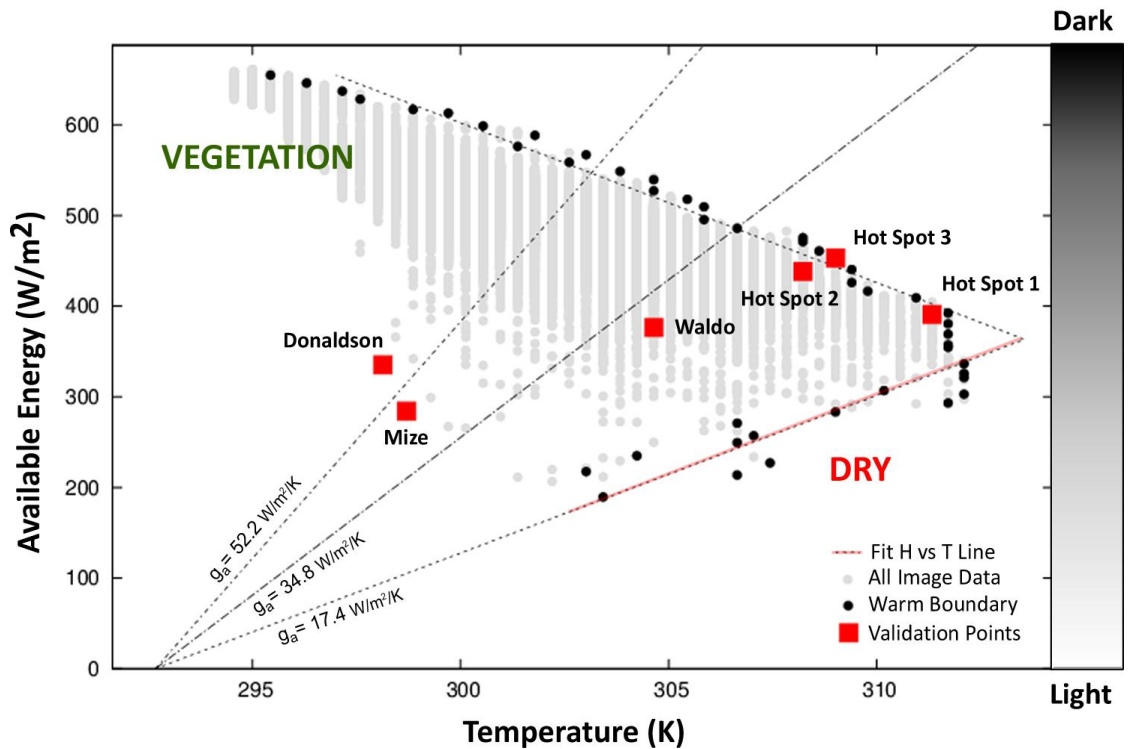
Figure 1.2.1: Scatter Plot Used to Detect Dry Pixels

Previously, S-SEBI (Roerink et al., 2000) used variations in available energy

(actually albedo) in order to calibrate relationship between *EF* and *T*, but this method

does not use only dry pixels in the calibration. S-SEBI plots *T* vs. albedo and finds a

warm and cold boundary to the scatter plot (Figure 1.2.2). For each albedo, *EF* is

assumed to vary linearly from 0 to 1 between the hot and cold limits for that particular

albedo. The problem is that the cold boundary which supposedly represents vegetation is

not clearly defined. The thick red line to the left is much more defined and representative

of various quantity and quality of vegetation. Also, S-SEBI assumes *EF* = 1 at the cold

boundary which is not necessarily true. In theory *EF*=1 where the temperature of the

surface is equal to the temperature of atmosphere which should not increases with the

reflectance of the surface but stay relatively constant over local extents.

20
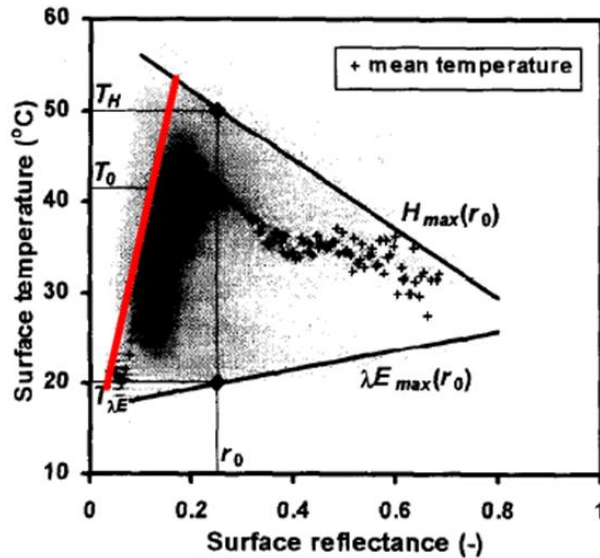
Figure 1.2.2: T$_s$ vs. α S-SEBI Method (Reprinted from: Physics and Chemistry of the Earth, Part B: Hydrology, Oceans and Atmosphere, Vol. 25(2), Roerink, G.J., Su, Z., and Menenti, M., *S-SEBI: a Simple Remote Sensing Algorithm to Estimate the Surface Energy Balance*, 147-157, (2000), with permission from Elsevier)

1.3 Using Data Fusion to Account for Low Temporal Resolution of LANDSAT Imagery

A large problem in remote sensing of evapotranspiration is the trade-off between spatial and temporal resolution. While LANDSAT has 120 m spatial resolution for thermal IR, it has a relatively long return period of 16 days. MODIS has a daily return period, but it has a coarser 1 km spatial resolution for thermal IR. A high frequency of cloud cover in Florida further limits the availability of LANDSAT imagery where the surface is visible. This means that MODIS imagery would probably be required for resolving *ET* at the monthly or seasonal time scale. For applications such as management of water use in agriculture where field scale resolution is required, it would be necessary to use LANDSAT imagery. In the arid Western U.S. where cloud cover is not as much of a problem, interpolation between scenes is possible (Allen et al, 2011). In Florida where cloud cover can result in large gaps between available images, simple interpolation of *ET*

will most likely not account for variability of *ET*. A solution to this problem is to "fuse"

LANDSAT and MODIS data together in order to estimate *ET* maps which have

LANDSAT spatial resolution and MODIS temporal resolution (Figure 1.3.1). For many

hydrological applications the 1 km thermal resolution of MODIS would be adequate. But,

the dry pixel calibration proposed in this dissertation will not work with MODIS spatial

resolution because it is very rare to find 1 km square purely dry areas. It would be even

rarer to find a set of them which has the wide range of albedo required for the calibration.

Figure 1.3.1 demonstrates the inability of MODIS resolution to identify the dry pixels

required by the calibration. The blue pixels were generated from LANDSAT pixels

aggregated to 1 km thermal resolution and 250 m optical resolution. This figure is

generated from a scene over Disney Wildlife preserve on May 5, 2004. Due to the loss of

dry pixels during aggregation, it will be necessary to fuse MODIS and LANDSAT data

together in order to estimate 120 m thermal imagery from which dry pixels can be

identified and used in the calibration.
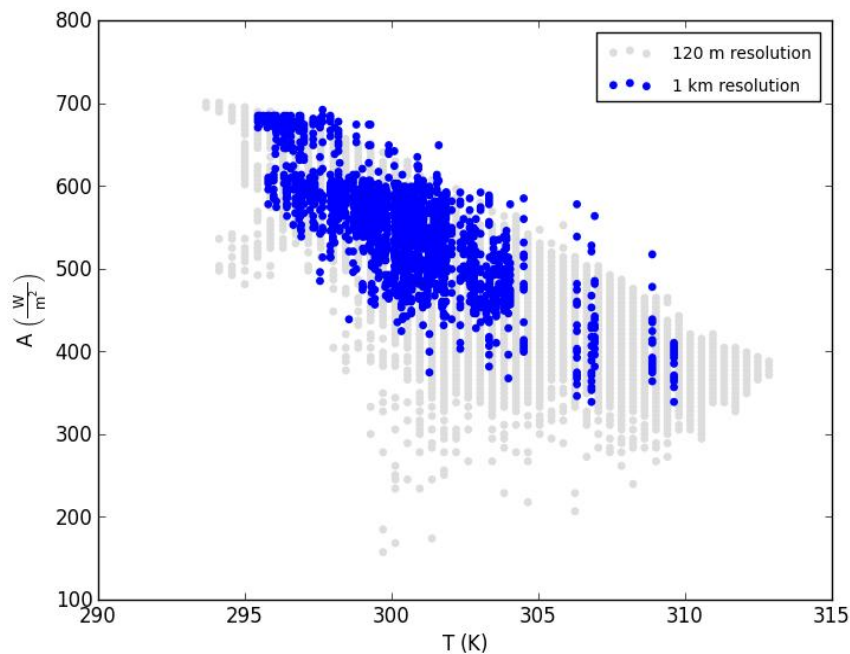
Figure 1.3.1: Energy vs. T$_s$ for LANDSAT vs. MODIS resolution

1.4 Objectives

The objective of this dissertation is to propose a variation to the calibration used in the SEBAL/METRIC algorithm. This new calibration will produce maps independently of eddy covariance data. Eddy covariance data will be used to test the calibration method in Florida. The list of objectives follows:

Develop dry pixel only calibration and compare to calibration that includes wet pixels. The dry pixel calibration algorithm described in section 1.2 will be developed and tested in Florida over five study areas described in the next chapter. A very simple method of determining wet pixels in Florida is also proposed so that the dry pixel only calibration can be compared to a method which includes wet pixels. First, these methods will be tested based on evaporative fraction. Secondly, the methods will be tested based on instantaneous actual evapotranspiration. Different methods of determining boundary in Figure 1.2.1 are proposed and tested. Also different assumptions regarding atmospheric conductance in equation 1.1.3 are tested. Different methods for finding wet pixels are explored and tested. The spatial extents of some of the study areas are altered and the results compared.

Determine the sensitivity of the algorithm to various model inputs. Inputs for the retrieval are temperature, available energy, roughness length, and blending height wind speed. These parameters are varied and the corresponding change to resulting maps is analyzed. The wind speed at blending height is determined using eddy covariance towers. This is contrary to the objective of producing maps independent of eddy covariance data. Therefore wind speed is fixed at an annual average in retrievals and compared to results which use eddy covariance wind speeds. Roughness length is

also varied in the model and the resulting change analyzed. In another test, roughness length is assumed spatially constant while atmospheric stability is still allowed to influence atmospheric conductance. Finally temperature and available energy is altered to analyze their effect on evaporative fraction. It is obvious that available energy will have the largest effect on actual evapotranspiration, but it is useful to determine the effect available energy has on evaporative fraction.

Determine the feasibility of applying data fusion to calibration algorithm

Using the sequence of available images, estimates for each image in the series are produced based on neighboring information. This is performed using 6 different variations of data fusion with varying complexity and compared to 4 methods of simple interpolation. Actual retrieved imagery is compared to fused imagery at the image and pixel scale. This produces errors at the daily times scale as well as the time scale of the entire series. The spatial distribution of the errors is analyzed along with the temporal variability of errors. The final goal is to determine if there is a benefit to using data fusion over simple interpolation methods.

2. Study Areas and Data

2.1 Study Areas

The five study areas in Florida used in this dissertation are 1) Gainesville, 2) Kennedy Space Center 3) Disney Preserve 4) Big Cypress and 5) Everglades (Figure 2.1.1). These study areas were chosen because they contain eddy covariance towers necessary for testing. They also represent a good slice of the different types of environments found in Florida. The next paragraph describes the individual study areas in more detail.
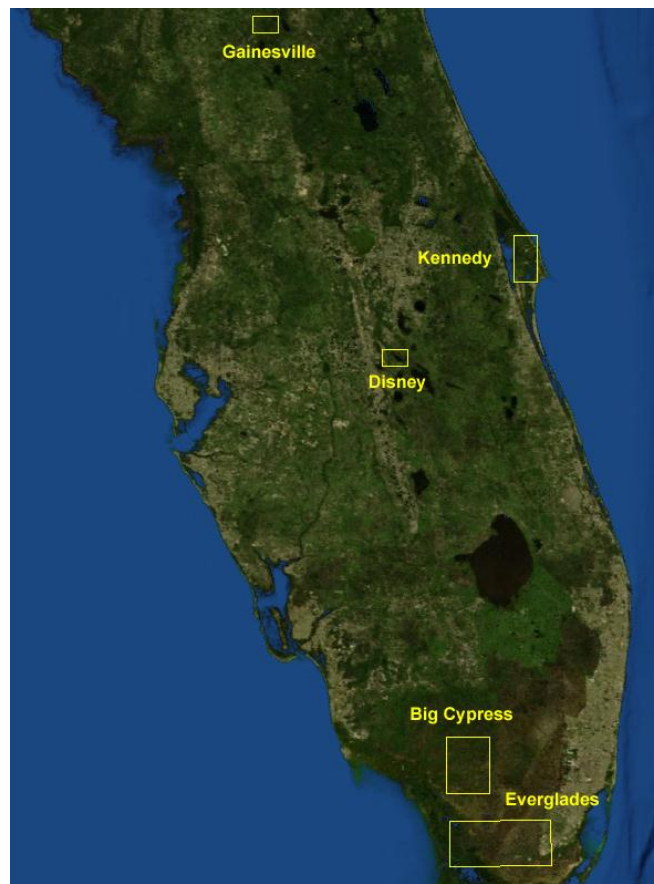
Figure 2.1.1: All Study Areas

2.1.1 Gainesville

This study area is actually located outside Gainesville, FL near the town of Waldo, FL. Three eddy flux towers are located over slash pine plantations experiencing different levels of regeneration. The flux stations are called Austin Cary, Donaldson, and Mize. The study area and tower locations are shown in Figure 2.1.2. This study area is important because 1) the close proximity of flux towers 2) the heterogeneous nature of the landscape in terms of cleared vs. vegetated surfaces will be a good testing ground for the dry pixel calibration 3) slash pine trees are rough surfaces and testing here should help determine the importance of roughness in the retrieval algorithm. The size of the study area is 14.2 km by 9.4 km.
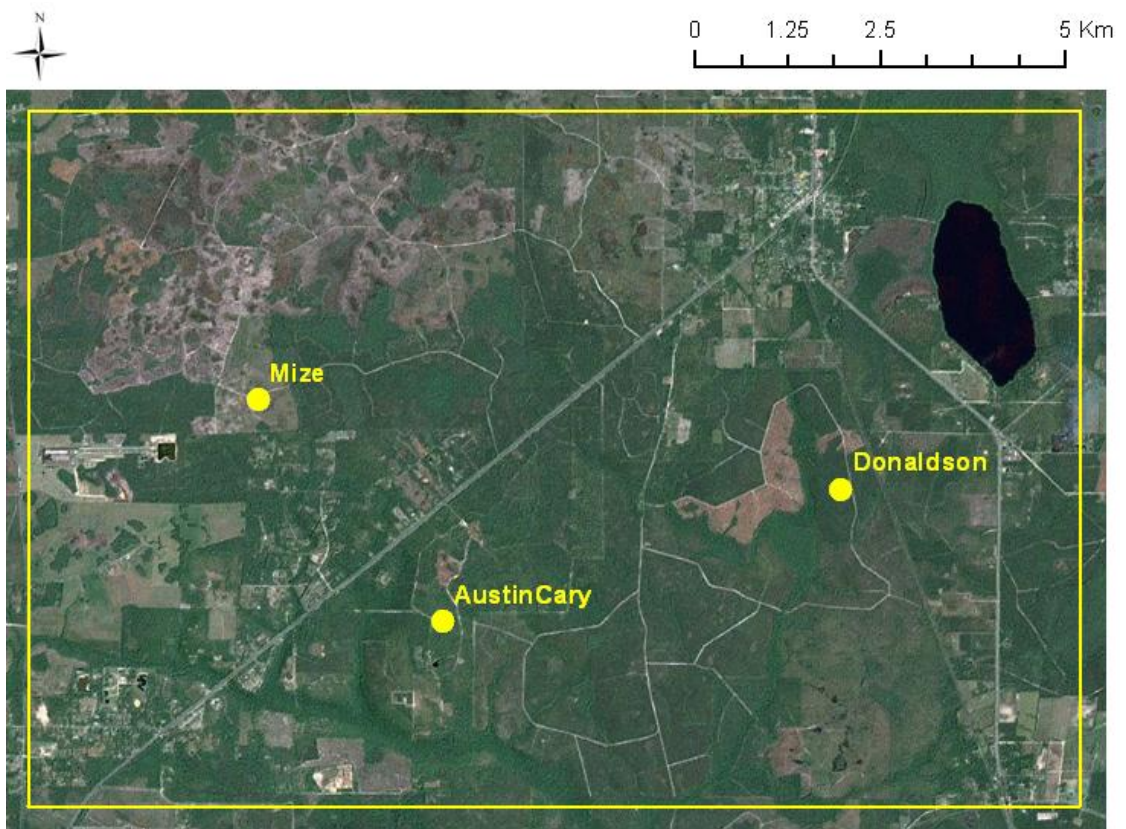
Figure 2.1.2: Gainesville Study Area

2.1.2 Kennedy Space Center

This study area is located near Kennedy Space Center. This study area is interesting because of the coastal environment. Also, the boundary layer over the ocean and land should be very different so this study area should represent a transition between the two. Two eddy flux towers are located in this study area. One tower is located over scrub oak while the other is located over slash pine. Kennedy Space Center study area was broken up into two spatial extents as shown in Figure 2.1.3 which will be called Kennedy Large and Kennedy. Kennedy Large is the full extent that includes both flux towers. Kennedy Large was reduced to a smaller extent because 1) It was necessary to test the effects of spatial extent on algorithm and 2) Slash pine flux tower data was only in service from 2002-2003 and therefore will not provide many test points. The size of Kennedy Large is 13.5 km × 27 km and Kennedy is 6.9 km × 6.3 km.
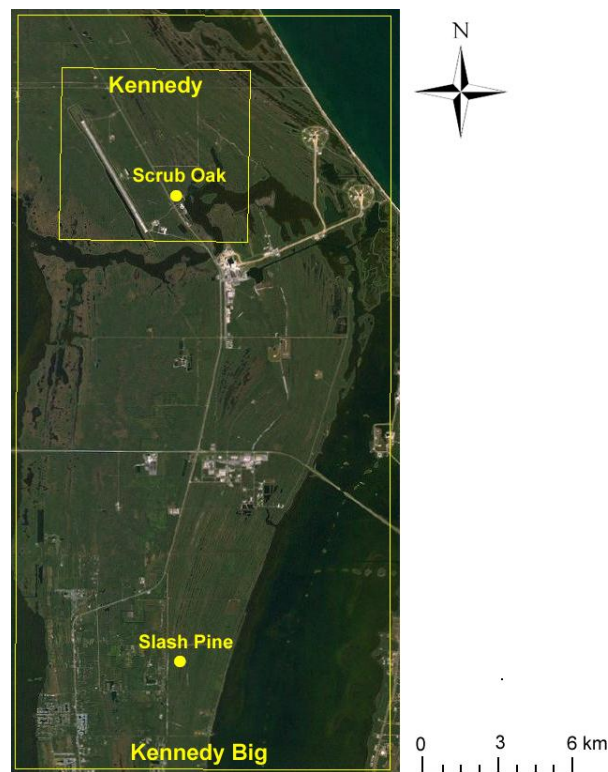
Figure 2.1.3: Kennedy Space Center Study Area

2.1.3 Disney Wilderness Preserve

Disney Wilderness Preserve study area is about 30 miles south of Orlando, FL in Polk County. A single flux tower is located here which is over an area that is mainly grassland. Testing over grassland will be a good compliment to other test sites with trees and scrub. Disney is broken up into two extents called Disney and Disney Small as shown in Figure 2.1.4. The larger extent called Disney contains manmade surfaces to the west. The size of Disney is 14.8 km × 10.1 km and the size of Disney Small is 7.9 km × 7.9 km.
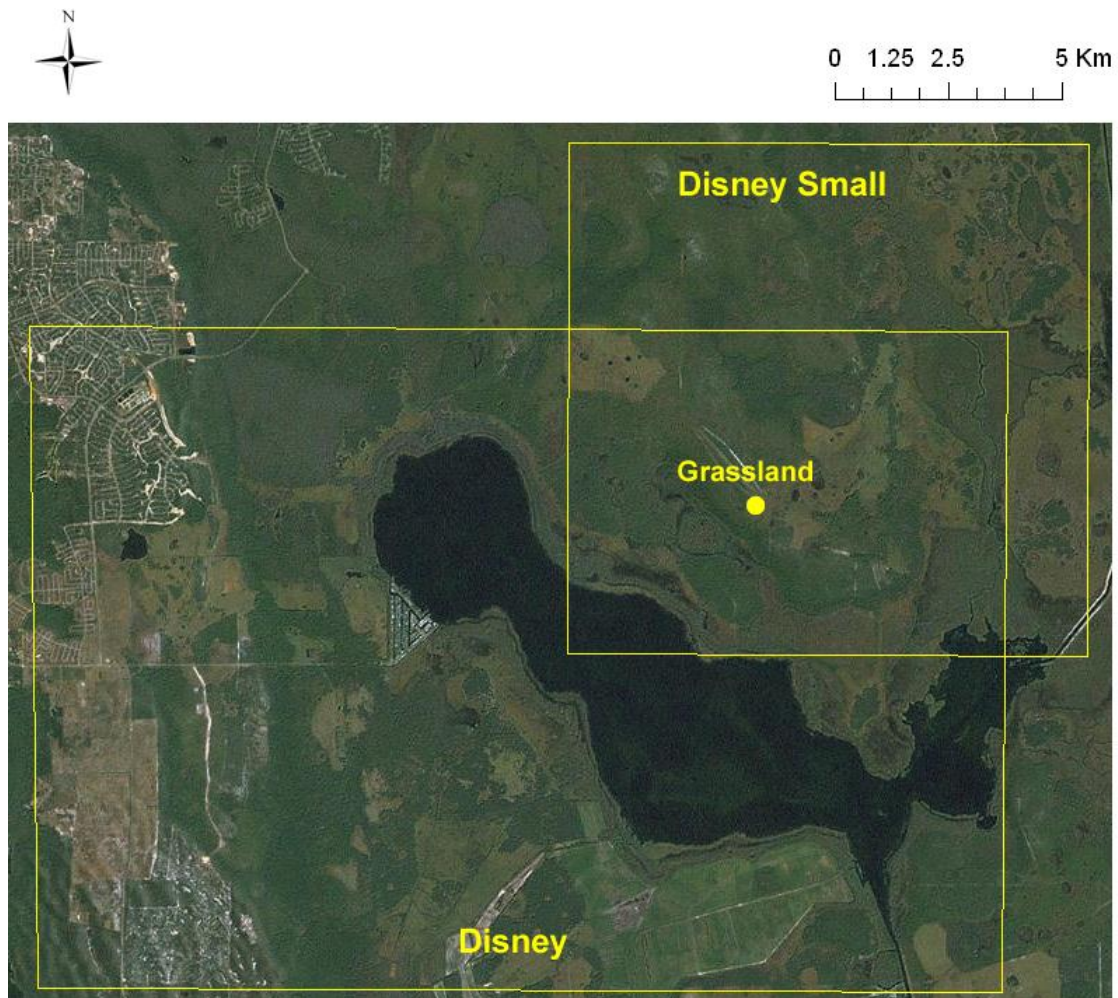
Figure 2.1.4: Disney Wilderness Preserve Study Area

2.1.4 Big Cypress

The Big Cypress study area has 5 towers over a wide variety of plant communities which are Cypress Swamp, Dwarf Cypress Swamp, Pine Uplands, Wet Prairie, and Marsh (Figure 2.1.5). The Marsh site is far to the North, therefore only the first four sites named are used. The Big Cypress study area is 25.8 km × 33.4 km. It is an interesting study area because it will test the algorithm in a very warm, humid environment consisting of tall trees. It would seem there would be a lack of dry pixels available but the airport to the east should provide them.
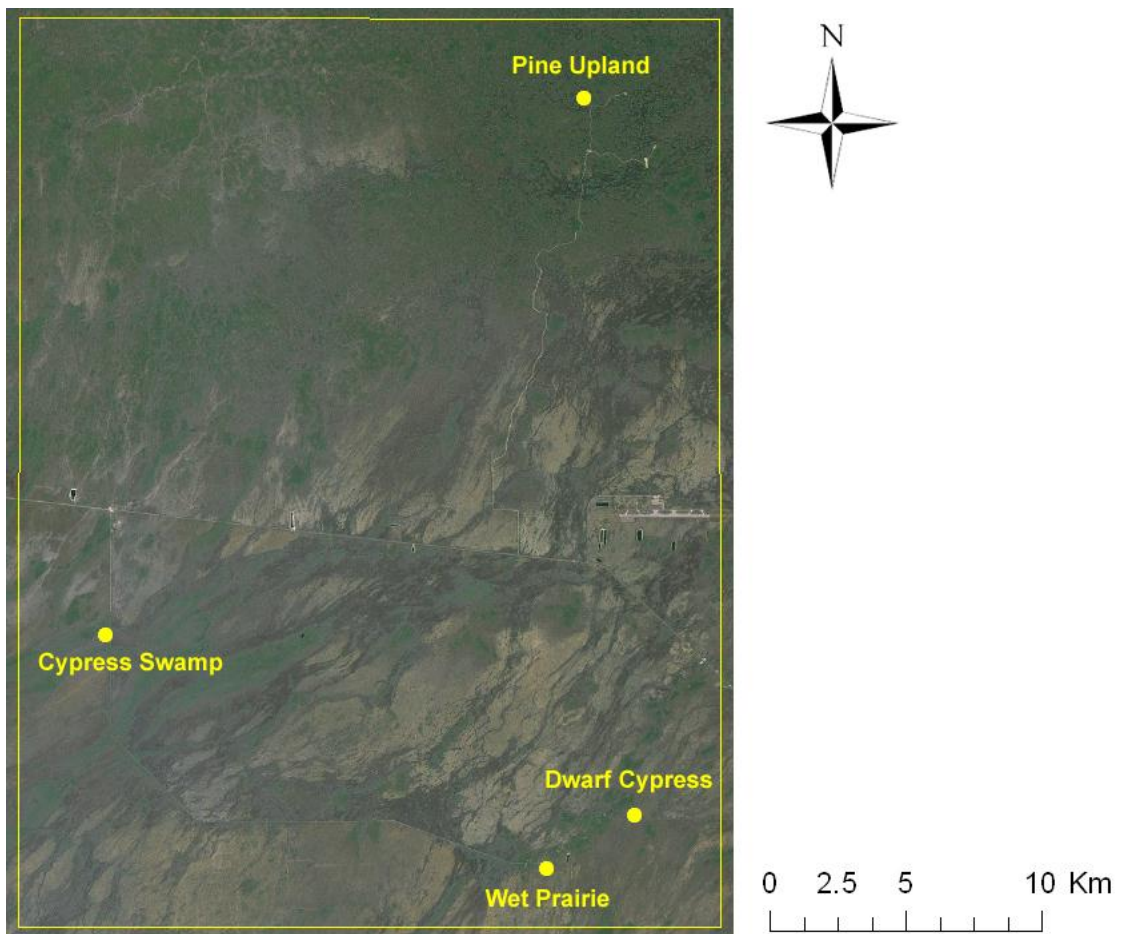
Figure 2.1.5: Big Cypress Study Area

2.1.5 Everglades

The Everglades study area contains three flux tower stations located over Mangroves, Long Hydro-period Marsh and Short Hydro-period Marsh. The Everglades study area is broken up into 3 extents called Everglades, Mangroves and Homestead shown in Figure 2.1.6. The Everglades extent basically contains both of the smaller extents. The Mangroves extent is the western portion with the Mangrove flux towers and Homestead is the eastern portion near Homestead. These were broken up because the full extent is very large at 60.7 km × 27.6 km. Mangroves is 25.5 km × 27.2 km and Homestead is 30.2 km × 27.3 km. Homestead extent will be interesting due to the agricultural areas to the east because calibration methods have been commonly used to map *ET* in agricultural settings.
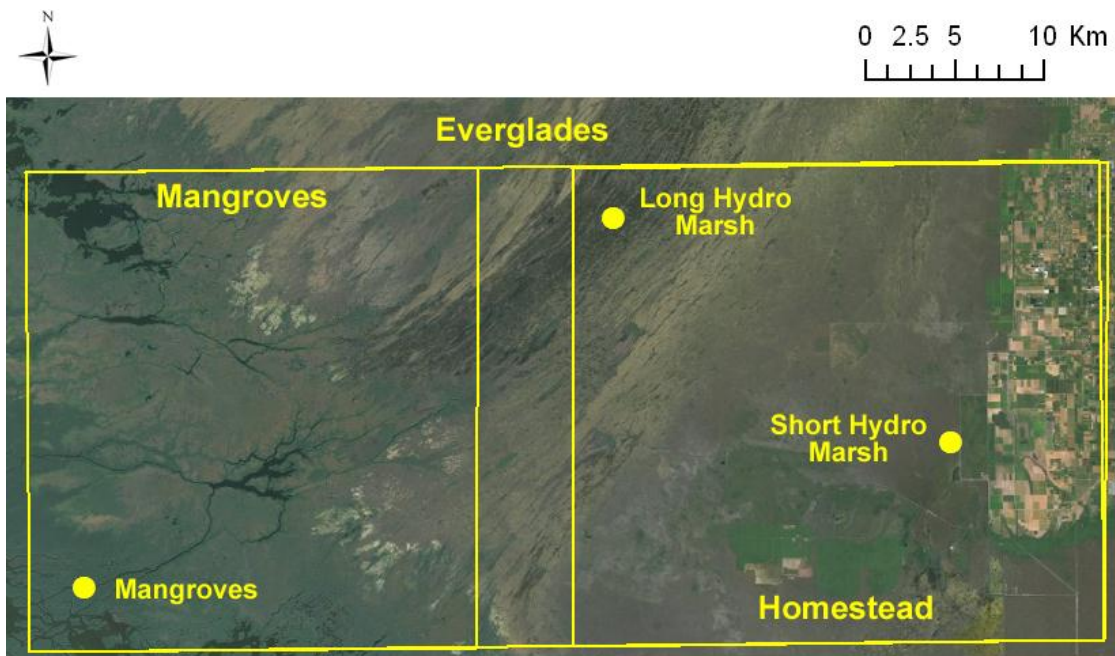
Figure 2.1.6: Everglades Study Area

2.2 Data

2.2.1 Eddy Covariance Data

The flux data used for testing the calibration algorithm proposed in this dissertation come from various towers with sensors which measure latent and sensible heat using the eddy covariance method. The eddy covariance method is performed by using sensors which are able to measure wind speed and other scalars such as temperature and humidity at very high frequencies. It finds the flux of some scalar by using Reynolds averaging which consists of taking the mean of the produce of vertical wind perturbations and perturbations of the scalar quantity of interest (Foken, 2008). The scalars of interest in this study are horizontal wind, temperature and humidity resulting in the fluxes called friction velocity, sensible heat, and latent heat.

The primary source of flux data comes from the Ameriflux network. Ameriflux is a network of flux towers being maintained by different operators in which the operators freely share data over the internet via the Ameriflux website at *http://ameriflux.ornl.gov/*. Ameriflux downloads provide horizontal wind speed, temperature, humidity, net radiation, ground heat flux, friction velocity, sensible heat, and latent heat every 30 minutes. For Big Cypress and Disney Wilderness Preserve study areas the same type of data is provided by the United States Geological Survey.

2.2.2 Satellite Imagery

The source of satellite imagery used in this dissertation is LANDSAT TM 5 which can be downloaded from USGS earth explorer website at *http://earthexplorer.usgs.gov/*. LANDSAT TM 5 contains 7 bands including Blue, Green, Red, Near Infrared, Shortwave Infrared 1, Thermal Infrared, and Shortwave Infrared 2

wavelengths. Each of these bands has 30 m spatial resolution except for the thermal band which has 120 m resolution. The return period for TM 5 is 16 days. The overpass time for LANDSAT is around 10:30 AM Eastern Standard Time. Eastern Standard Time is calculated by subtracting 5 hours from Greenwich Mean Time. The path, row and approximate overpass time for each study area is shown in Table 2.2.1.

Table 2.2.1: LANDSAT Path, Row and Approximate Overpass Time for Study Areas

Study Area	Path	Row	Overpass Time
Big Cypress	15	42	10:35 AM
Disney	16	41	10:40 AM
Everglades	15	42	10:35 AM
Gainesville	17	39	10:40 AM
Kennedy	16	40	10:35 AM
Kennedy	15	40	10:35 AM

2.2.3 Usable Clear Sky Days

For the purposes of remote sensing of surface properties, clear sky imagery is required. Due to the high frequency of clouds in Florida, the length of time between images will be much more than the 16 day LANDSAT return period. In addition, eddy covariance data is not available for every LANDSAT scene due to technical problems which result in gaps in the eddy flux data. Therefore a data set was created which contained clear sky LANDSAT image where flux measurements are also available. In this dissertation, these scenes will be called "usable" clear sky scenes. Table 2.2.2 lists the usable clear sky scenes. The total number of validation points from stations available for each year is shown in parenthesis. For Disney the number of validation points will be equal to the number of usable clear sky scenes because there is only one station. For Big

Cypress, since there are 4 stations, in 2009 there are 8 validation points for the 2 usable scenes because all stations were valid. Big Cypress and Everglades have the lowest average frequency of usable scenes because it is very cloudy. Even though it is cloudy, Kennedy has the highest frequency on average because LANDSAT returns twice over one 16 day return period as shown in Table 2.2.1. Gainesville has the most scenes in total because of the longer duration of eddy covariance data. It is also important to note that for study areas with multiple flux towers, only one flux towers needs to be operational to make the corresponding clear sky image considered "usable". There are some instances where all the flux points in a study area were simultaneously available. For Gainesville study this occurred on 1/28/2001, 4/2/2001, 8/8/2001, 8/24/2001, 2/19/2003, 12/20/2003, 1/23/2005 and 10/25/2006. For Everglades and Big Cypress this occurred on 10/3/2009 and 10/19/2009. For Kennedy only 1/20/2003 had both. A full listing of dates and number of available stations for useable clear sky scenes of all study areas is included in Appendix A. The flux tower data for each station is also included in Appendix A.

It is useful to display the total number of scenes and the total number of validation points from stations available during each season. Because there is more than one eddy covariance station for some study areas, the total number of validation points will be greater than the total number of scenes. This is shown for each of the study areas in Figures 2.2.1 and 2.2.2. Figure 2.2.1 clearly shows that there are a small number of scenes available during the summer when clouds are more likely. Also it shows the small number of scenes available for Big Cypress and Everglades due to a high frequency of clouds. Figure 2.2.2 reveals the large number of validation points available in Gainesville due to 3 stations to pick from and a long period of record.

Table 2.2.2: Summary of Usable Clear Sky Scenes. (Total Number of Validation
Points from Stations for Each Year is in Parenthesis)

Year	BigCypress	Disney	Everglades	Gainesville	Kennedy
1999	0 (0)	0 (0)	0 (0)	1 (1)	0 (0)
2000	0 (0)	0 (0)	0 (0)	2 (3)	3 (3)
2001	0 (0)	0 (0)	0 (0)	5 (14)	4 (4)
2002	0 (0)	0 (0)	0 (0)	0 (0)	2 (2)
2003	0 (0)	0 (0)	0 (0)	2 (6)	4 (5)
2004	0 (0)	3 (3)	0 (0)	2 (4)	4 (4)
2005	0 (0)	2 (2)	0 (0)	3 (6)	6 (6)
2006	0 (0)	4 (4)	0 (0)	8 (14)	2 (2)
2007	0 (0)	3 (3)	0 (0)	2 (3)	0 (0)
2008	1 (3)	3 (3)	1 (2)	4 (7)	0 (0)
2009	2 (8)	2 (2)	2 (5)	2 (3)	0 (0)
2010	1 (3)	4 (4)	1 (2)	1 (1)	0 (0)
2011	0 (0)	0 (0)	1 (1)	4 (4)	0 (0)
Total	4 (14)	21 (21)	5 (10)	36 (66)	25 (26)
Average	1.3 (4.7)	3.0 (3.0)	1.2 (2.5)	3.0 (5.5)	3.6 (3.7)
# Years	3	7	4	12	7
Span	2008-2010	2004-2010	2008-2011	1999-2011	2000-2006

The *EF* data for each station collected between 1999 and 2011 (as reported in

Appendix A) is plotted in Figure 2.2.3 in order to show the seasonal variation of the data

for each study area. The lines are a Gaussian smoothing of the point data with a monthly

bandwidth. The evaporative fraction is highest in the late summer/early fall and lowest in

the winter. This would seem to reflect an increase in *EF* during the growing season when

water is plentiful and leaf area index is peaking.
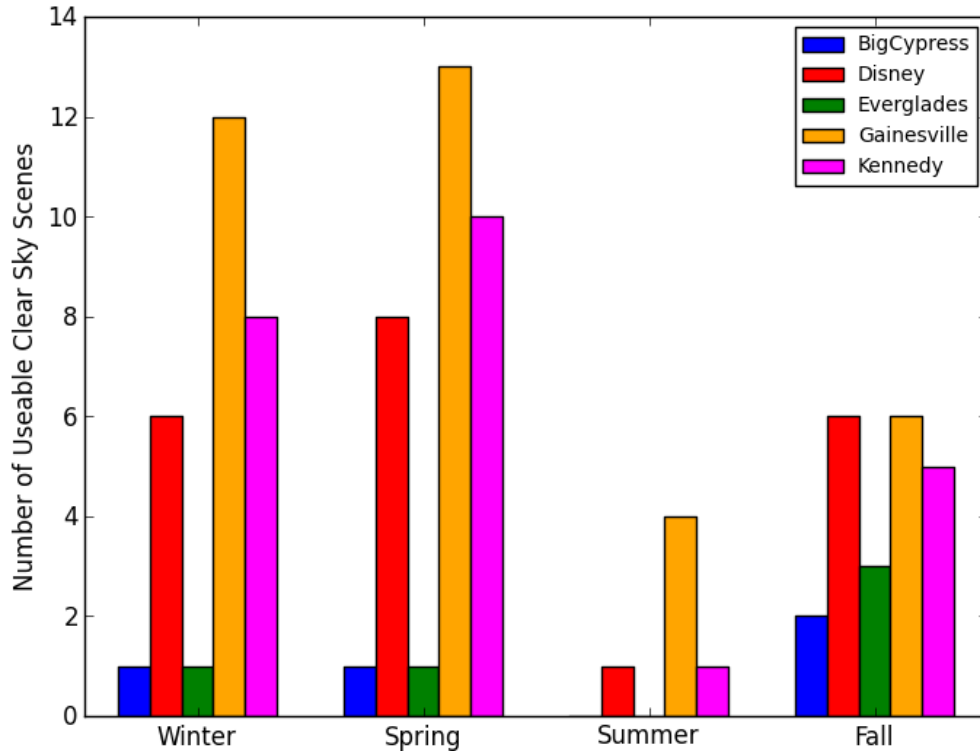
Figure 2.2.1: Number of Scenes Available During Each Season for Each Study Area
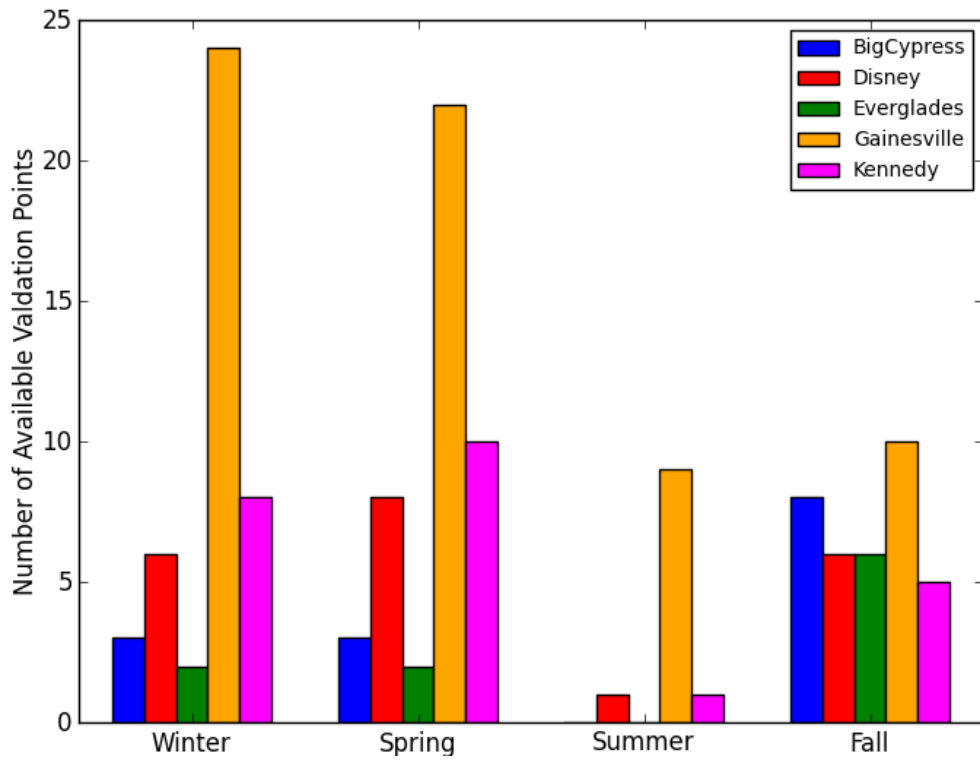
Figure 2.2.2: Number of Available Validation Points During Each Season for Each Study Area
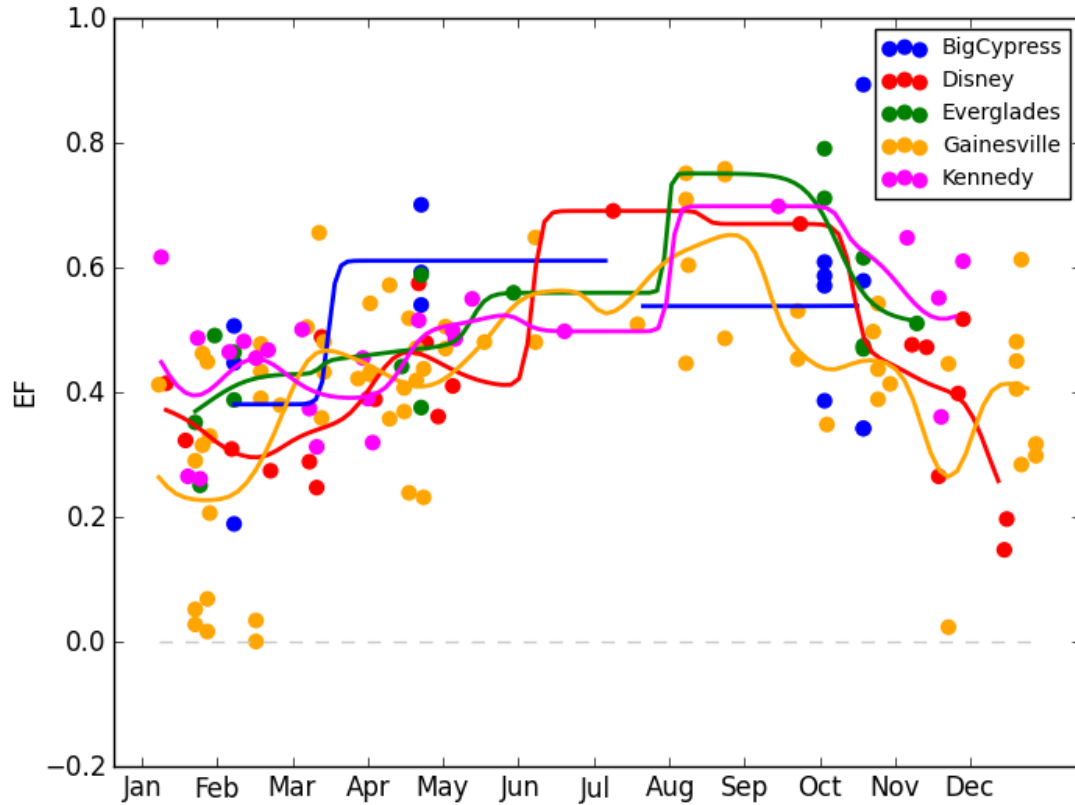
Figure 2.2.3: Monthly Variability of Evaporative Fraction for each Study Area

In order to calculate the wind speed at blending height it was necessary to estimate the tower and vegetation heights. Tower height should be relatively accurate but vegetation height will vary. Estimates were made from information in metadata and references. Vegetation and tower heights for the Ameriflux sites are estimated using the metadata. For Big Cypress the vegetation and tower heights reported in Shoemaker et al (2011) are used. For Disney Preserve an estimate for typical vegetation height and tower height is included in supporting documents. Vegetation height for Everglades was estimated from Schedlbauer et al (2012). Table 2.2.3 shows tower and estimated vegetation height for all stations.

Table 2.2.3: Tower and Vegetation Height

Study Area	Station	Tower Height (m)	Vegetation Height (m)
Big Cypress	DwarfCypress	16.5	7.0
Big Cypress	CypressSwamp	38.0	21.0
Big Cypress	WetPrairie	3.6	1.0
Big Cypress	Marsh	3.6	1.5
Big Cypress	PineUpland	38.0	21.0
Disney	Grassland	3.5	0.5
Everglades	LongMarsh	2.8	1.0
Everglades	Mangroves	30.0	20.0
Everglades	ShortMarsh	3.0	0.75
Gainesville	AustinCary	32.0	24.2
Gainesville	Donaldson	24.3	14.0
Gainesville	Mize	18.5	10.1
Kennedy	ScrubOak	3.8	1.8
Kennedy	SlashPine	18.0	15.0

3. Methodology

3.1 Data Preprocessing

The eddy covariance and LANDSAT data must be processed before it can be used for creating and testing maps of evapotranspiration. This was not a trivial task because of the large quantity of data being used. The process was made easier by using the Python scripting language and the numpy and arcpy modules. The numpy module is a set of functions useful for processing multi-dimensional arrays. The arcpy module provides a programmatic interface between python and ARC GIS procedures.

3.1.1 Eddy Covariance Flux Data Preprocessing

Using the eddy covariance (EC) method, Ameriflux and USGS data contributors produced 30 minute average fluxes on the hour using EST time. In order to compare the satellite retrieved *EF* map to ground measurements, it is necessary to compute *EF* from the flux data. The eddy covariance method often produces sensible and latent head fluxes which do not match measurement of available energy (Lloyd, 1995). It is common for the EC method to underestimate instantaneous fluxes because the correlation is typically measured over small time intervals (30 minutes) where low frequency turbulence is not detected. Averaging over larger time intervals could allow the effect of low frequencies to be measured, but a "snap shot" of flux coinciding with satellite overpass is needed for validation (Foken, 2008). Typically it is assumed that although the absolute fluxes are underestimated, the Bowen ratio (β), where $\beta = H/LE$, will be constant. The validity of

this assumption is currently unresolved, but will be adopted in this dissertation as the best

current solution. Therefore evaporative fraction at the tower will be calculated as:

$$EF_{tower} = LE \: / \: (H+LE) \hspace{5cm} 3.1.1)$$

where LE is the latent heat flux and H is the sensible heat flux measured using eddy

covariance method.

The EF maps created by the algorithm will be compared to the flux measurement

at the time which is nearest to the satellite overpass time shown in Table 2.2.1. When

data for the nearest time is unavailable, the next closest time is used. Only times which

are within an hour of the overpass times are candidates. If all the data is missing within

this window, then this LANDSAT scene will not be used. Another option would be to

validate with the daily averaged evaporative fraction calculated using daily LE and H in

equation 3.1.1.

It is a common procedure to multiply EF retrieved from satellite by daily

available energy to find daily ET because evaporative fraction is typically fairly constant

during the day when the available energy is large. Figure 3.1.1 demonstrates the manner

in which EF is mostly constant during the day. The problem with validating against daily

EF is that there are so many gaps in the flux data which results in erroneous calculations

for daily EF. It could be possible to fill the gaps with standard interpolation techniques,

but the quantity and position of gaps in the data prohibit this in many cases. If only the

useable clear sky scenes that were accompanied by gap free data were used, the already

limited amount of useable clear sky scenes would be extremely reduced. Also, in order to

test actual ET retrievals it is necessary to use EF at overpass time because information on

daily available energy is not available from satellite.
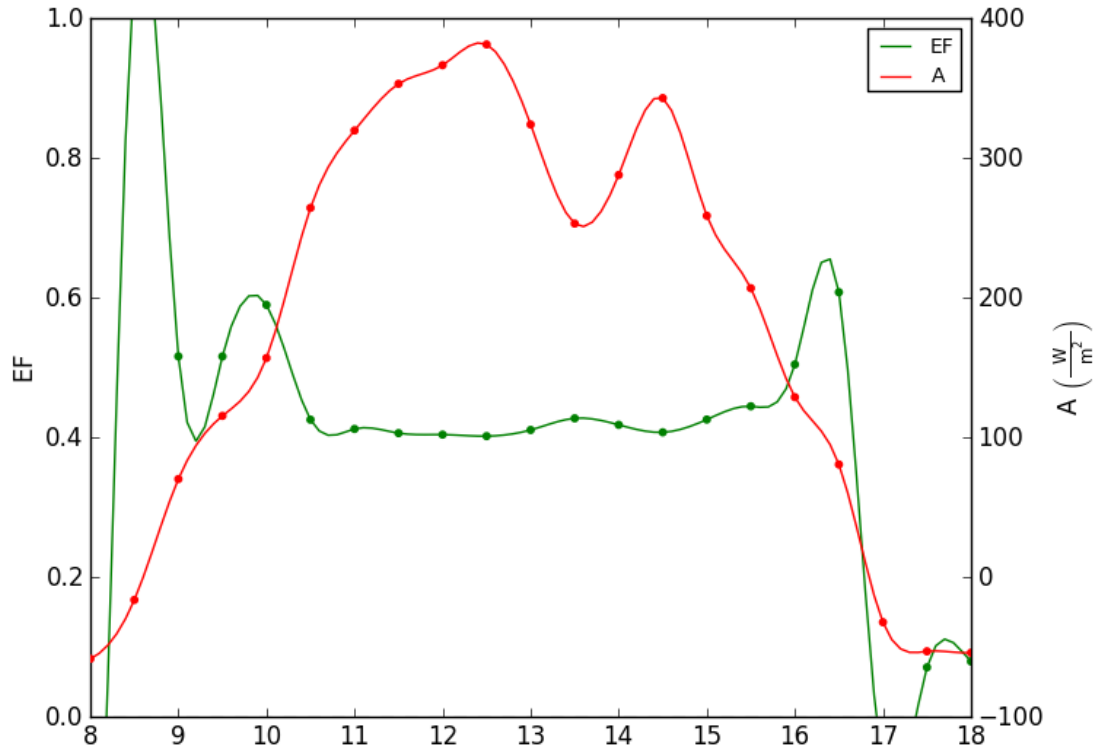
Figure 3.1.1: Diurnal Variability of *EF* and Available Energy (Donaldson 12/01/2002)

An analysis was performed to study the effect of gaps on daily *EF*. This analysis consists of first determining scenes in which no gaps exist to use for testing. Next, the simple probability of gap occurrence was computed for each time interval in the flux data by simply dividing the number of gaps by the total number of measurements. This was used to choose the stations to use for investigating the effect of gaps. Based on the above, Gainesville-Donaldson station and Everglades-Short Hydro-Period Marsh stations were chosen for analysis. Simulations were conducted for estimating the effect of gaps on daily *EF* due to an increase in number of gaps. For one case the gaps were arranged in time completely randomly. For the second case the gaps were clustered so that they were all adjacent to each other. The clustered case has 48 different combinations of gaps due to the single cluster shifting the starting point. The random case has an enormous amount of

combinations which depends on the number of gaps being simulated. The maximum

combinations occur when the number of gaps is equal to 24 resulting in a number of

combinations equal to $48! / 24!^2 = 32.25 \times 10^{12}$. This prohibits the simulation of all

random combinations due to computer memory issues and therefore 10,000 combinations

of gaps were created randomly. The number of gaps was varied from 1 to 47 and used to

simulate daily *EF* when gaps are present for both cases. Next, the *Bias* and *MAE* with

respect to gap free daily *EF* was calculated over all combinations of gaps. This was

repeated for each of the gap free scenes to get a total *Bias* and *MAE*. Actual gaps will not

necessarily follow either one of the above models, therefore the locations in time of

actual gaps from the station flux data was used. These actual combinations of gaps were

then applied to each of the gap free scenes to produce simulated daily *EF* for each

combination of gaps. As described above, this was repeated for all gap free scenes to

calculate a total bias and *MAE* with respect to gap free daily *EF*. For this simulation there

is no need to alter the number of gaps since they are inherent in the data. The use of

interpolation for reducing the effects of gaps on daily *EF* was also tested. This was done

by linearly interpolating fluxes between the actual gaps described above and then

calculating daily *EF* values which include the interpolated fluxes. From this the total *Bias*

and *MAE* with respect to gap free daily *EF* was calculated which could be compared to

results in which interpolation was not used.

The average number of gaps and number of gap free days for each station using

just the days with useable clear sky scenes was determined. This can be used with the

results of the above simulation to get an idea about the effect that number of gaps has on

daily *EF* calculations. Using the gap free useable clear sky scenes, the similarity of daily

EF and satellite overpass *EF* were compared using scatter plots and calculation of *Bias* and *MAE*. The above analysis was also completed using the *EF* averaged over a window between 10 AM to 11:30 AM compared to daily *EF*.

There is a tendency for daily *EF* to be larger than satellite overpass *EF*. This can be explained by representing daily *EF* with the following equation:

$$EF_{\text{daily}} = (EF_+ A_+ + EF_- A_-) / A_{\text{daily}} \qquad\qquad 3.1.2)$$

where *A* is available energy,+ denotes times when $A > 0$ and − denotes times when $A <$ 0. During the day when $A > 0$ EF_+ is fairly constant and can be approximated by overpass *EF*. During the night when $A < 0$ it can typically be assumed that EF_- is close to zero. Substituting this information into equation 3.1.2 produces:

$$EF_{\text{daily}} = EF_{\text{overpass}} A_+ / A_{\text{daily}} \qquad\qquad 3.1.3)$$

A_+ is greater than A_{daily} because of loss of available energy at night and therefore daily *EF* is typically greater than satellite overpass *EF*. The ratio of A_+ to A_{daily} was applied to overpass *EF* as a correction factor to produce a corrected *EF* which was compared to daily *EF*.

Another problem that can lead to differences in daily *EF* and overpass *EF* is that the energy balance closure problem is not necessarily consistent across every time step measured. Before now daily *EF* has been calculated by summing sensible heat and latent heat over the day and using these sums in equation 3.1.1. It would seem this approach works best because averaging over daily cycle should allow low frequency turbulence to be represented. But, energy balance closure can still be significant after daily averaging. Therefore it is possible that correcting the flux at each time step and then summing corrected fluxes before entering them in equation 3.1.1 could provide another estimate of

daily *EF*. The two types of flux corrections used are 1) ratio and 2) residual corrections. The ratio correction consists of applying equation 3.1.1 to find *EF* for each time step and then multiplying it by available energy of corresponding time step to get corrected latent heat. Subtracting this latent heat from available energy produces corrected sensible heat. The residual correction assumes that the difference between measured and true fluxes is the same for both latent heat and sensible heats. Based on this assumption it is possible to determine the residual or difference using:

$$\Delta = (\,A - LE - H\,)\,/\,2 \hspace{6cm} 3.1.4)$$

where Δ is the correction amount which is simply added to *LE* and *H* in order to get the new corrected fluxes. The residual correction is being introduced because it might be more applicable to instances at night when *LE* and *H* are different signs. At these times using the ratio correction can lead to the directions of the flux changing. Therefore, an alternate estimate of daily *EF* is proposed in which the residual method will be used when fluxes are different signs, and the ratio method will be used for all other instances. This new alternate estimate of daily *EF* was then compared to corrected overpass *EF*.

The disadvantage of using clear sky scenes for comparison is that the quantity of available days is limited. Using all the gap free data will produce more data, but it will also include cloudy days which should not produce as strong of a relationship between overpass *EF* and daily *EF* (Loheide and Gorelick, 2005). Therefore, all of Donaldson gap free data were also used to test the similarity of daily *EF* to satellite overpass *EF* and window *EF*. The *Bias* and *MAE* was calculated seasonally to observed seasonal relationships. This was compared to seasonal groupings of results for only useable clear sky scenes to investigate effect of clouds on daily vs. overpass *EF* relationship. It should

43

be noted that this analysis is limited because the size of useable clear sky scenes is much less than all gap free days.

Eddy covariance method measures fluxes over a bell shaped footprint upwind of the tower as shown in Figure 3.1.2. This footprint depends on the direction of wind, height of measurement, and instability of the atmosphere. In order to compare tower flux data with remote sensing it is necessary to perform a weighted average of the remote sensing results over this footprint. If the flux tower is placed in an area with small variations in surface conditions over the footprint, variations in the footprint function should have less influence on the results. Testing in this dissertation assumes this and adopts a uniform footprint function centered on the tower. Table 3.1.1 shows the size of the uniform foot prints that are being used. The size of the footprints were determined from the same metadata and references used to find tower and vegetation heights along with the results of a simple footprint model which can determine the fetch distance at which a certain percentage of the flux is accounted for (Schuepp, 1990):

$$fetch = -2\ \theta_m\ x_{max}\ /\ \ln(\%_{flux}) \tag{3.1.5a}$$

$$x_{max} = z'\ (\ln(z'/z_o) - 1 + z_o/z')\ /\ (2\ k^2\ (1 - z_o/\ z')) \tag{3.1.5b}$$

$$\theta_m = [1 - 16\ (z'/L)]^{\,0.25} \tag{3.1.5c}$$

where z' is height of tower minus the displacement height, $\%_{flux}$ is the percentage of flux measured for distances less than fetch distance, x_{max} is the location where footprint source is maximum, z_o is the roughness length, k is the von karman constant, θ_m is a factor due to instability and L is Monin-Obukhov length. The problem with using a uniform footprint is that it does not account for the changing wind direction and stability of the atmosphere.

A uniform footprint was adopted because it is difficult to obtain data required to model

two dimensional footprint models whereas the Schuepp model is only one dimensional.
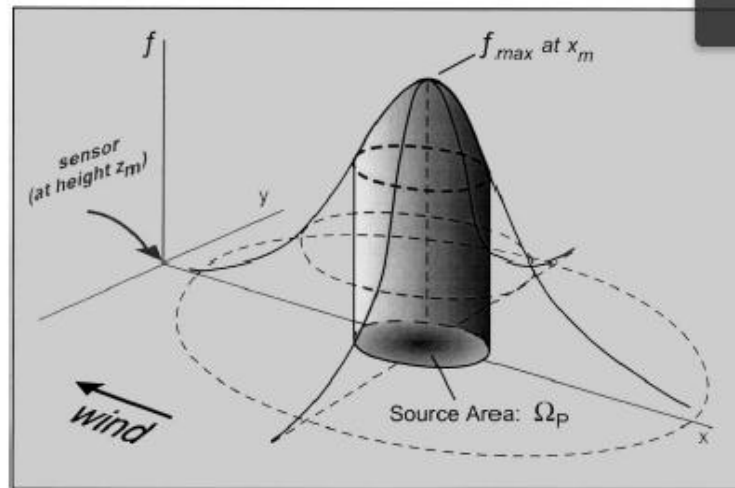
Figure 3.1.2: Eddy Flux Source Function Footprint (Reprinted from: Agricultural and Forest Meteorology, Vol. 93(3), Schmid, H.P. and Lloyd, C.R., *Spatial representativeness and the location bias of flux footprints over inhomogeneous areas*, 195-209, (1999), with permission from Elsevier)

Table 3.1.1: Size of Uniform Footprints for Each Station

Study Area	Station	Footprint Size (m)
Big Cypress	DwarfCypress	650
Big Cypress	CypressSwamp	1000
Big Cypress	WetPrairie	400
Big Cypress	PineUpland	1000
Disney	Grassland	300
Everglades	LongMarsh	200
Everglades	Mangroves	600
Everglades	ShortMarsh	200
Gainesville	AustinCary	1000
Gainesville	Donaldson	1000
Gainesville	Mize	1000
Kennedy	ScrubOak	200
Kennedy	SlashPine	500

In addition to evaporative fraction, wind speed at blending height is derived from the data. It is assumed that the wind speed at blending height is constant over the spatial extent of the *EF* map. Therefore, the average wind speed at blending height for all of the stations in the study area will be used. Sometimes the data necessary for calculating the evaporative fraction is available, but the necessary data for calculating wind speed at blending height is not available. Since average wind speed is being used, the scene will still be useable as long as wind speed at blending height was available for at least one of the stations.

The wind speed at blending height is approximated by extrapolating the wind speed measured at the tower using Monin-Obukhov similarity theory. Assuming the blending height is 200 m, the wind speed at blending height is calculated using:

$$u_{\text{blend}} = u_{200} = [u^* [\ln (200/z') - \psi_{\text{m}}(200/L) + \psi_{\text{m}}(z'/L)] \ / \ k \ ] + z \qquad 3.1.6)$$

where u^* is the friction velocity measured by the flux tower, u is the wind speed, $z' = z - d$, z is the height of the tower, d is the displacement height, L is the Monin-Obukhov length, and ψ_{m} is the stability correction function for momentum. The Monin-Obukhov length is calculated with:

$$L = (-\rho \, C_{\text{p}} \, u^{*3} \, T) / (k \, g \, H) \qquad 3.1.7)$$

where ρ is density of air, C_{p} is specific heat capacity of air, u^* is the friction velocity measured using eddy covariance method, T is temperature measured by flux tower, $k = 0.41$ is the Von Karman constant, g is acceleration due to gravity, and H is the sensible heat flux measured using eddy covariance method. For stable boundary layers L is greater than zero while for unstable boundary layers L is less than zero. For neutral

46

conditions, *L* approaches positive or negative infinity. The form of the stability functions for momentum and heat changes depending on the sign of *L*:

$$\zeta = z/L \qquad\qquad\qquad 3.1.8a)$$

For *L* < 0

$$\Psi_M(\zeta) = 2\,\ln[(1+x(\zeta))/2] + \ln[(1+x^2(\zeta))/2] - 2\,\text{atan}[x(\zeta)] + \pi/2 \qquad 3.1.8b)$$

$$\Psi_H(\zeta) = 2\,\ln[(1+x^2(\zeta))/2] \qquad\qquad 3.1.8c)$$

$$x(\zeta) = [1 - 16\,(\zeta)]^{0.25} \qquad\qquad 3.1.8d)$$

For L > 0

$$\Psi_{M,H}(\zeta) = -5\,\zeta \qquad\qquad 3.1.8e)$$

For L = +/- ∞

$$\Psi_{M,H}(\zeta) = 0 \qquad\qquad 3.1.8f)$$

The displacement height d is estimated using (Allen et al, 1998):

$$d = 2/3\ h \qquad\qquad 3.1.9)$$

where *h* is the average height of obstacles (see Table 2.2.3).

3.1.2 Processing Satellite Imagery

For this dissertation it was necessary to collect clear sky LANDSAT images. This was performed using the USGS earth explorer website. This web site allows the user to search for LANDSAT scenes with less than 10% cloud cover. Although this filtering process produced a good start, it is still necessary for the user to look through resulting images and remove cloudy scenes that made it through cloud filtering algorithm. These clear sky scene dates were then intersected with dates in which eddy covariance flux near overpass time was available in order to determine "useable" clear sky scenes as described

47

in above sections. These "useable" clear sky scenes were then downloaded from the USGS website.

The next step in processing the satellite imagery was to determine the spatial extent to be used for testing the *ET* mapping algorithm. For Gainesville, Big Cypress and Everglades study areas the limits of the spatial extents were mostly determined by the location of eddy covariance stations. Disney and Kennedy only have 1 station each. For these study areas small and large extents was chosen in order to test the effect of the size of the extent on *ET* mapping algorithm. The extent boundaries were then used to clip the full LANDSAT scenes into smaller study area subsets as well as stack the multiple band files into one ERDAS Imagine file for convenience. For a listing of all useable clear sky scenes see Appendix A.

3.2 Evapotranspiration Mapping

3.2.1 Overview of Residual Method Used in *ET* Mapping

The *ET* mapping algorithm uses LANDSAT thermal band 6 for finding temperature and reflectance bands 1-5 and 7 for finding albedo and *NDVI*. A surface energy balance residual method approach based on SEBAL is used. In the residual method the latent heat flux (*LE*) is found by subtracting the sensible heat flux (*H*) from the available energy from radiation (*A*):

$$LE = A - H \tag{3.2.1}$$

$$A = R_{net,SW} + R_{net,LW} - G \tag{3.2.2}$$

where *A* is the sum of the net longwave radiation ($R_{net,LW}$), net shortwave radiation ($R_{net,SW}$), and fluxes into the surface (G). The net longwave radiation is the difference between the radiation emitted from the atmosphere ($R_{Down,LW}$), and the radiation emitted

from the earth ($R_{Up,LW}$). The net shortwave radiation is the difference between the solar

radiation incident on the surface ($R_{Down,SW}$) and the solar radiation reflected from the

surface:

$$R_{net,SW} = (1-\alpha)\, R_{Down,SW} \qquad\qquad 3.2.3)$$

where α is the albedo of the surface. These radiation fluxes are ultimately derived from

radiation measured at the satellite sensor. The satellite sensor cannot detect the sensible

heat flux because it occurs over a relatively thin surface boundary layer on the order of

100 m. In order to determine H, the relationship between aerodynamic surface

temperature (T_{AERO}) and H is utilized:

$$H = g_A\, \Delta T = g_A\, (T_A - T_{AERO}) \qquad\qquad 3.2.4)$$

where g_A is the atmospheric conductance describing how turbulence in atmosphere

transfers sensible heat and T_A is the temperature of the atmosphere. H cannot be directly

computed using this equation since 1) the surface boundary layer is too thin to determine

the temperature in the boundary layer and 2) g_A depends on the roughness of the surface,

wind speed, and the stability of the boundary layer. In addition, surface temperature used

in equation 3.2.4 is the aerodynamic temperature (that of air directly above the surface),

but the satellite detects the radiant temperature (that of emitting surface). The SEBAL

algorithm handles this and problem 1) above by assuming that the vertical temperature

gradient (ΔT) over some arbitrary layer is linearly related to radiant surface temperature

(T_S):

$$\Delta T = a + b\, T_s \qquad\qquad 3.2.5)$$

In SEBAL g_A is calculated using Monin-Obukhov Similarity Theory (MOST) which is based on logarithmic wind and temperature profiles and assumes a constant flux in surface boundary layer:

$$g_a = \rho \, C_p \, u^* / \, [\ln (z_2/z_1) - \psi_h(z_2/L) + \psi_h(z_1/L)] \hspace{4cm} 3.2.6)$$

$$u^* = u_{blend} \, k \, / \, [\ln (z_{blend}/z_o) - \psi_m(z_{blend}/L) + \psi_m(z_o/L)] \hspace{3cm} 3.2.7)$$

where ρ is density of air, C_p is specific heat capacity of air, u^* is the friction velocity, u_{blend} is the wind speed at blending height, k is the von karman constant $= 0.41$, L is the Monin-Obukhov length, ψ_m is a correction related to stability of boundary layer with respect to momentum and ψ_h is a correction related to stability of boundary layer with respect to heat at height z_i. It is important to note that the choice of heights making up the gradient ΔT is somewhat arbitrary in theory. It does not necessarily have to be between the top of the boundary layer and the surface due to scalability in MOST. In SEBAL z_2 is typically set to 2 m and z_1 is set to 0.1 m which is also followed in this methodology. z_{blend} is the height at which it is assumed that the effects on the wind due to irregularities in the surface have blended so that the wind at this height is due to larger scale atmospheric processes. As with SEBAL, a value of $z_{blend} = 200$ m is used. z_o is the roughness length which depends on the roughness of the surface. Because z_o can vary abruptly in space, determining the spatial variation of z_o is important in the residual method.

In order to find H it is necessary to 1) determine wind speed u_{blend} 2) determine the roughness length z_o for pixels in the image to be mapped and 3) determine the coefficients a and b used by equation 3.2.5. Once H is calculated it must be subtracted from available energy A to get LE. Detailed methodology for using LANDSAT imagery

50

to estimate A is in the next section. The determination of the wind speed $u_{blend}=u_{200}$ is discussed in section 3.1.1. Tasks 2 and 3 from above are in upcoming sections.

3.2.2 Estimating Temperature and Available Energy from Satellite Imagery

Satellites cannot directly measure the temperature of the earth's surface, but they can measure the radiation that is being emitted from the surface. The peak wavelength of energy emitted from an object decreases with temperature. Therefore hot bodies like the sun emit short wavelengths of radiation while relatively cool bodies such as the earth emit long wavelengths of radiation. Satellite measurements of these long wavelengths of energy being emitted can be inverted to find the radiating temperature of the source. For LANDSAT this can be performed by inverting the Planck function in the following from (Kosa, 2011):

$$T_s = 1282.71 \,/\, \ln(1 + 666.09/L_6 \,) \,/\, \epsilon^{0.25} \qquad\qquad 3.2.8)$$

where T_s is the radiant surface temperature (K), L_6 is the radiance detected by LANDSAT sensor for band 6 (W/m^2/ster), and ϵ is the broadband emissivity of the surface. Realistically the spectral emissivity of band 6 should be divided by L$_6$ to produce (Schmugge et al, 1998):

$$T_s = 1282.71 \,/\, \ln(1 + 666.09 \; \epsilon_6 \,/\, L_6 \,) \qquad\qquad 3.2.9)$$

where ϵ_6 is the spectral emissivity for band 6. Even if the spectral emissivity is constant equation 3.2.8 is not valid for smaller emissivity values. Figure 3.2.1 demonstrates the difference between T_s retrieved using 3.2.8 and 3.2.9 assuming constant spectral emissivity and various actual T_s. This is because equation 3.2.8 assumes that broad band black body temperature would be the same as spectral black body temperature. In reality, spectral black body temperature varies with wavelength even for constant spectral

emissivity. Figure 3.2.2 shows how the spectral black body temperature increases with decreasing wavelength and emissivity. Therefore, it is not necessarily equal to broad band blackbody temperature (dashed line).

Unfortunately, it is very difficult to estimate broadband emissivity of the surface let alone spectral emissivity. In fact, the remote sensing of surface temperature is an "ill-posed" problem because there is a lack of information (Li et al, 2013). If only a single band is available, there is only one equation but two unknowns (temperature and spectral emissivity). If an additional band is added then there are now two equations but three unknowns because of the introduction of the spectral emissivity of the new band. Complex techniques exist to work around this problem, but typically users use empirical relationships between satellite reflectance values and emissivity while assuming that the spectral emissivity of the surface over LANDSAT band 6 is equal to the broadband emissivity of the surface. Attempts to use relationships between *NDVI* and ϵ in this dissertation produced erratic results in some areas. In light of this, emissivity was assumed to be a constant value of $\epsilon = 0.97$ (Mecikalski et al, 2010). This is an emissivity typical for vegetation and similar to water which should work for study areas being used. If all temperatures are off by the same amount, the calibration should account for it. However, the spatial variation of emissivity could possibly alter retrieved temperature in a relative sense which would introduce errors into *EF* retrieval.
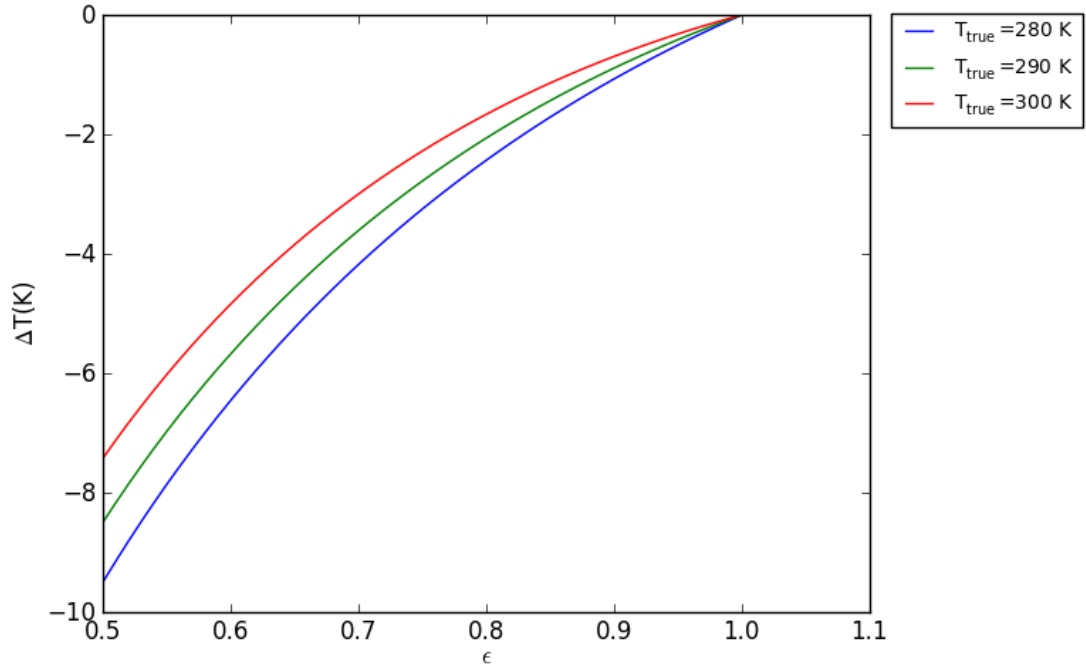
Figure 3.2.1: Difference between _T_ retrieved using eqn. 3.2.8 vs. 3.2.9
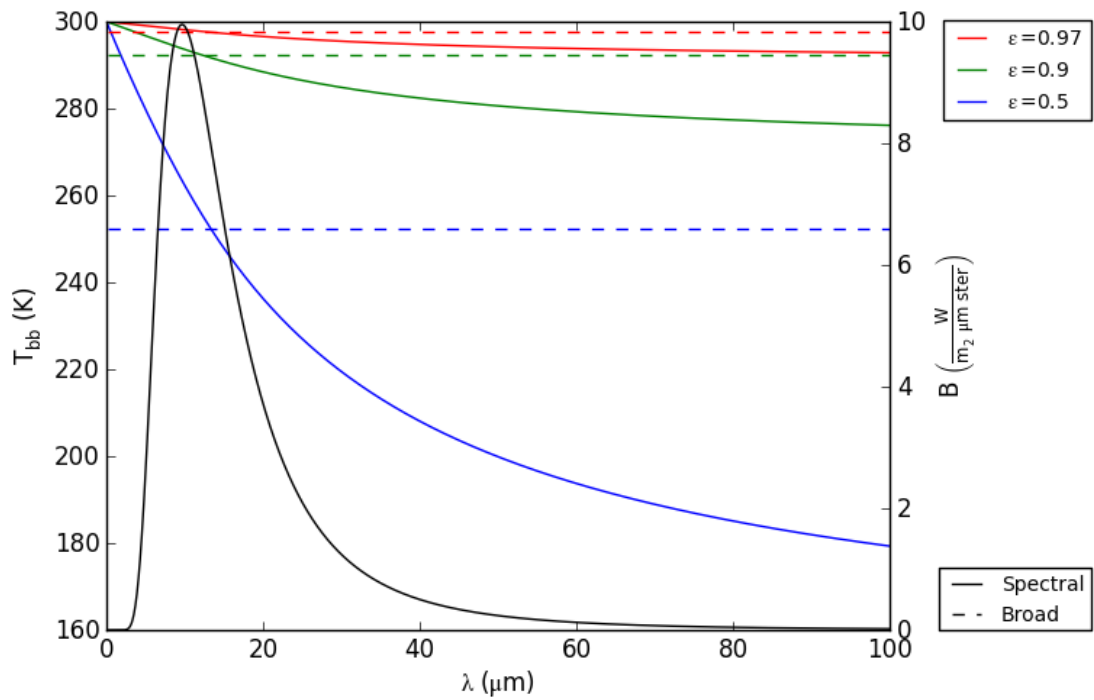
Figure 3.2.2: Difference between Spectral vs. Broadband blackbody T

In order to calculate available energy the following equations were used (Kosa, 2011):

$$A = R_n \, (1 - G/R_n) \tag{3.2.10}$$

$$R_n = (1\text{-}\alpha) \, R_{\text{Down,SW}} + \epsilon \, R_{\text{Down,LW}} + \epsilon \, \sigma \, T_S^{\,4} \tag{3.2.11}$$

$$G/R_n = (T_S - 273.15) \, /1000 \, (3.8 - 7.4 \; \alpha) \, (1 - 0.98 \; NDVI^4 \,) \tag{3.2.12}$$

$$NDVI = (\rho_4\text{-}\rho_3)/(\rho_4\text{+}\rho_3) \tag{3.2.13}$$

$$\rho_i = \pi L_i \, / \, (\, ESUN_i \, \cos \theta \, d_r \,) \tag{3.2.14}$$

$$d_r = 1 \, / \, [1 + 0.033 \, \cos(DOY \, 2\pi \, / \, 365) \,]^{0.5} \tag{3.2.15}$$

where R_n is the net radiation, σ is the Stefan-Boltzman constant, ϵ is broad band emissivity of the surface, $NDVI$ is the normalized difference vegetation index, ρ_i is the planetary reflectance for band i, L_i is the top of atmosphere radiance measured by LANDSAT for band i, $ESUN_i$ is the mean exoatmospheric irradiance for band i, θ is the solar zenith angle, d_r is the earth sun distance, and DOY is the day of year. It is better to use surface reflectance instead of planetary reflectance in order to calculated $NDVI$, but only broadband surface reflectance or albedo was determined in this algorithm. The effect of this on G using equation 3.2.12 should not be large. A bigger problem is that equation 3.2.12 should be fit to local conditions. In addition it is meant to be used over land, therefore in wetland environments it could break down due to large amounts of energy going into the water column at the surface. In that case it would be necessary to model the effect the depth of the water column has on R_n/G. In the absence of this information inaccuracies due to this will have to be accepted.

Downwelling solar radiation is calculated using the following equation:

$$R_{\text{Down SW}} = G_{sc} \, \cos \theta \, d_r \, \tau_{sw} \tag{3.2.16}$$

where G_{sc} is solar constant = 1367 W/m^2 and τ_{sw} is the transmissivity of the atmosphere

to solar radiation. The broadband albedo of the surface is determined by using the

broadband albedo at the top of the atmosphere:

$$\alpha = (\alpha_{TOA} - \alpha_{PATH}) / \tau_{sw}^2 \qquad 3.2.17)$$

where α_{TOA} is the top of the atmosphere albedo and α_{PATH} is representative the albedo of

the atmosphere alone in a simple first order scattering model. The top of atmosphere

albedo is calculated using the planetary reflectance (calculated using equation 3.2.14) of

all LANDSAT bands except for bands 6:

$$\alpha_{TOA} = \Sigma \; \omega_i \, \rho_i \qquad 3.2.18)$$

$$\omega_i = ESUN_i / \Sigma \; ESUN_i \qquad 3.2.19)$$

where ω_i is weighting coefficient for band i.

In the absence of clouds, down welling long wave radiation should depend on the

temperature of the atmosphere above the surface boundary layer which should be fairly

constant for the extents of study areas used. Down welling long wave radiation measured

at weather stations could therefore be applied to the entire study area, but unfortunately

these measurements are not very common. Down welling long wave radiation for each

study area will be estimated using (Kosa et al, 2011):

$$R_{LW\;DOWN} = \epsilon_A \; \sigma \, T_A^4 \qquad 3.2.20)$$

$$\epsilon_A = 0.85 \; (\text{-ln} \; \tau_{sw})^{0.09} \qquad 3.2.21)$$

where ϵ_A is the effective emissivity of the atmosphere and T_A is the effective temperature

of the atmosphere. Realistically the manner in which the atmosphere emits radiance is

highly dependent on atmospheric water vapor, but this value is difficult to estimate from

LANDSAT only. Weather station data could be used along with an empirical relationship between ϵ_A and vapor pressure, but it is the intention to determine available energy independent of ground data. Determining T_A is problematic. Assuming that the coldest temperatures in the scene are reflective of the atmospheric temperature at blending height, T_A is found using:

$$T_A = \overline{T}_s - 2\ \sigma_{Ts} \qquad\qquad 3.2.22)$$

where $\overline{T}_s$ is the mean temperature in the image and σ_{Ts} is the standard deviation of temperatures in the image. Although this might be a crude estimate of the radiating temperature of the atmosphere, it is used due to the absence of other information.

Both net long wave and short wave radiation can be calculated in order to compute available energy. There are many assumptions that went into calculating available energy, and therefore it will be necessary to estimate the sensitivity of resulting *EF* maps to available energy. In addition it will be necessary to compare available energy calculated by satellite to available energy measured at flux towers.

3.2.3 Estimating Roughness Length

Determining the roughness length of the surface is a very difficult process. A simple way to estimate roughness length is to assume (Allen et al, 1998):

$$z_o = h/8 \qquad\qquad 3.2.23)$$

In reality, the representative roughness length of an area also depends on the variability of the height of the obstacles. For example, a heterogeneous environment such as savannah would be rougher than a close canopy forest of uniform height. Also factors such as canopy shape and Leaf Area Index (LAI) will affect roughness. Quantifying these

relationships can be difficult while measuring the parameters needed to describe the relationships can be even more difficult (Schaudt and Dickinson, 2000).

SEBAL and METRIC typically find z_o by 1) using a land cover map and associating z_o to particular land use, and 2) developing a local relationship between z_o and $NDVI / \alpha$ by finding pixels of known z_o. Finding pixels of known roughness length can be difficult if the state of the vegetation is unknown or the scene is urbanized. Another approach would be to use LIDAR remote sensing in order to estimate average height of obstacles (h) that could be used in equation 3.2.8 to find z_o. Unfortunately, LIDAR data are not freely available for most of the study areas and could not be obtained. The methodology used in this dissertation to calculate z_o consists of using the relationship between z_o and α which was fit using data collected worldwide. The following empirical equation relating roughness length to LANDSAT derived surface albedo is adopted (Cho et al, 2012):

$$\log(z_o) = -16.8 \, \alpha + 1.87 \tag{3.2.24}$$

Although this simple relationship may be inaccurate in some locations, it is a necessary compromise when considering the limited availability of data. A possible advantage of this method is that albedo is related to both vegetation height and leaf area index (*LAI*) and therefore the z_o calculated using equation 3.2.24 would seem to be related to *LAI* as well as height. Incorporating the structure and heterogeneity of environment in addition to height using LIDAR would require additional ground data.

It is important to state that the z_o vs. α relationship will not be valid in urban settings or over open water. In urban settings, the z_o of buildings with bright surfaces will typically be underestimated. The study areas typically do not contain many urbanized

areas. On the other hand, the z_o of open water will be overestimated because it is a very dark surface. In order to account for this z_o was set equal to 0.0001 for open water. This was accomplished by performing an unsupervised ISODATA classification using all 7 LANDSAT bands based on 10-15 classes. Typically the first class returned was water. In some cases the second or third class was water and in other cases more than 1 class was determined to be water by visual inspection. Looking at the albedo and *NDVI* of each class helped in determining if the first class was water because it should have the lowest albedo and *NDVI*. In order to make the algorithm more operational, an automated method for masking water would be highly desirable. Existing land cover maps could be used but these might not reflect changes in the location of open water.

3.2.4 Description of Sensible Heat Models Tested

Three different variation of the model described in section 3.2.1 will be used. The difference in the models is the different assumptions used for calculating g_a in equation 3.2.4. The most complex method to be used assumes that g_a varies in space and is a function of atmospheric instability. In this method g_a is calculated using equations 3.2.6 and 3.2.7. This requires calculation of ψ_m and ψ_h which depends on the Monin-Obukhov length (L), but calculating L using equation 3.1.7 requires the friction velocity and sensible heat. The solution of this set of equations depends on whether the model is being used during the calibration of equation 3.2.5 or during the application of equation 3.2.5 for producing an *ET* map. In the calibration case sensible heat is known and ΔT is unknown. Therefore the calculation of L (equation 3.1.7) only requires u^* while the calculation of u^* (equation 3.2.7) only requires L. u^* is initially calculated for neutral conditions which can then be used to find initial L. This L is then used to find a new u^*

after which the process is iterated until the solution converges. Once L and $u*$ are determined they are used to calculated g_a. ΔT required for calibration can be determined by simply dividing the known sensible heat by the g_a just calculated. When the calibrated equation 3.2.5 is being used to make an *ET* map, the sensible heat is unknown but ΔT is known because it only depends on surface temperature. g_a from equation 3.2.6 and ΔT from 3.2.5 can be substituted into equation 3.2.4 to find *H*. This produces a system of three equations (3.2.4, 3.2.7 and 3.1.7) and three unknowns (*H*, $u*$ and *L*). Now both $u*$ and *H* are initially calculated using neutral conditions. These initial $u*$ and *H* can then be used to find initial *L*. This *L* is then used to find $u*$ and *H* after which the process is iterated until solution converges.

A simplification of this first model will be to assume neutral conditions when calculating g_a. g_a will be calculated using equations 3.2.6 and 3.27 where ψ_m and $\psi_h = 0$ which means the complicated iteration procedure described above is not necessary. All that is required is roughness length and wind speed at blending height which has been calculated as described above.

The simplest method used assumes that g_a is constant in space. Therefore g_a can simply be multiplied by both sides of equation 3.2.5 to produce sensible heat (*H*) as a function of T_s:

$$H = a_h + b_h\, T_s \qquad\qquad\qquad 3.2.25)$$

where a_h and b_h are coefficients that are fit using only *H* and T_s which does not require g_a to be calculated. This method requires the least amount of information because wind speed and roughness length are not required. All that is required is sensible heat for calibration and available energy and temperature.

59

These models will be referred to as 1) ΔT vs. T 2) ΔT vs. T neutral, and 3) H vs. T

3.2.5 Dry Pixel Calibration

In order to determine the coefficients in equations 3.2.5 and 3.2.25, a calibration

must be performed. Typically this consists of finding hot and cold pixels on the image

where H is known and T_s is determined from the thermal image. If one of the ΔT vs. T

models is going to be used, then ΔT is calculated as described in section 3.2.4. As

discussed in section 1.2, this dissertation is proposing a calibration in which only dry

pixels are used. This is possible because of a variation in albedo of dry pixels resulting in

a variation in temperature. By plotting available energy (or ΔT) vs. T_s, one can detect the

dry pixels as shown in Figure 1.2.1. In order to calculate ΔT during calibration as

described in section 3.2.4 requires sensible heat. Because the calibration is only

concerned with dry pixels, the ΔT used for calibration is set to that which would be

achieved for a dry pixel where all of the available energy is being used by sensible heat:

$$\Delta T_{dry} = A \, / \, g_a \qquad\qquad 3.2.26)$$

where ΔT_{dry} is the ΔT that would be achieved if the pixel actually was entirely dry. For

those pixels that actually are dry, $\Delta T = \Delta T_{dry}$ and therefore equation 3.2.5 can be fit. For

pixels which are not dry their true ΔT will be less than ΔT_{dry} because the $H<A$. This is

good because it ensures that ΔT_{dry} for wet pixels will not be mistakenly pulled down into

the lower dry boundary. Instead the wet pixels will be pulled up away from the dry

boundary when plotted on ΔT_{dry} vs. T graph. Another issue is the effect that roughness

length has on ΔT_{dry}. As discussed in section 3.2.3., buildings with bright surfaces will be

mistaken as something with a lower than actual roughness length. Fortunately this means

that the predicted g_a will be less than actual which will result in a larger than actual ΔT_{dry}.

60

Therefore this dry pixel will be removed from the lower dry boundary, but it should not disturb the results other than the loss of a calibration point. On the other hand, a low dark smooth surface could be mistaken as rough vegetation. This would bring ΔT_{dry} below the dry boundary line corrupting the results. Because of uncertainties in estimating roughness length, a method is proposed which uses a constant z_o for use in calculating ΔT_{dry}. In a previous study, using fixed z_o was compared to using variable z_o. Using fixed z_o produced results which were at least as good, if not better, than using variable z_o (Evans, 2013b). Fixed $z_o = 0.001$ m was chosen because it is close to reference values for bare soil. Figure 3.2.3 shows little difference in ΔT_{dry} near the dry boundary between z_o Bare = 0.001 m and z_o Bare = 0.01 m because g_a is more sensitive to stability/buoyancy than z_o for smooth/low z_o surfaces. By using a fixed z_o, the problem of smooth dark dry surfaces being mistaken as rougher vegetation is eliminated. For dry rough surfaces such as buildings, the fixed z_o approach will just move these points up away from the dry boundary. Open water pixels will only move below the dry boundary if $g_{a,water}/g_{a,bare}$ is less than $1 - EF_{water}$ which is very unlikely. Detected open water pixels can be excluded from dry pixel consideration. In this dissertation a fixed $z_o = 0.001$ m will be used for dry pixel calibration. The constant z_o approach will work as long as dry surfaces with z_o close to 0.0001 m exist in the image. It is important to note that the fixed z_o is only used in calibration, but the actual spatially variable z_o will be used when the calibration is applied to make ET maps.

In order to automate the algorithm, it is necessary to automate the manner in which the lower boundary of Figure 1.2.1 is produced. It does not matter whether the dependant variable is energy or ΔT. The technique will be described using ΔT, but it is

basically the same for both. The method used for this will be to separate pixels into bins of ΔT and then find the pixel with the maximum temperature in each bin. This will produce the points which make up the upper and lower boundary of the scatter plot. The pixels will be divided into bins using 3 different methods which will be called 1) Even Bins 2) Min-Max Bins and 3) Hybrid. The Even Bins method is the simplest. It simply sets the ΔT bins at a fixed size. The bin sizes used in this study were determined visually as described in Appendix B. The bin size used for ΔT vs. T model is 0.1 K, for ΔT vs. T neutral model it is 1.0 K and for H vs. T model it is 10 W/m^2. Having to supply the bin size parameter is one disadvantage of this method.
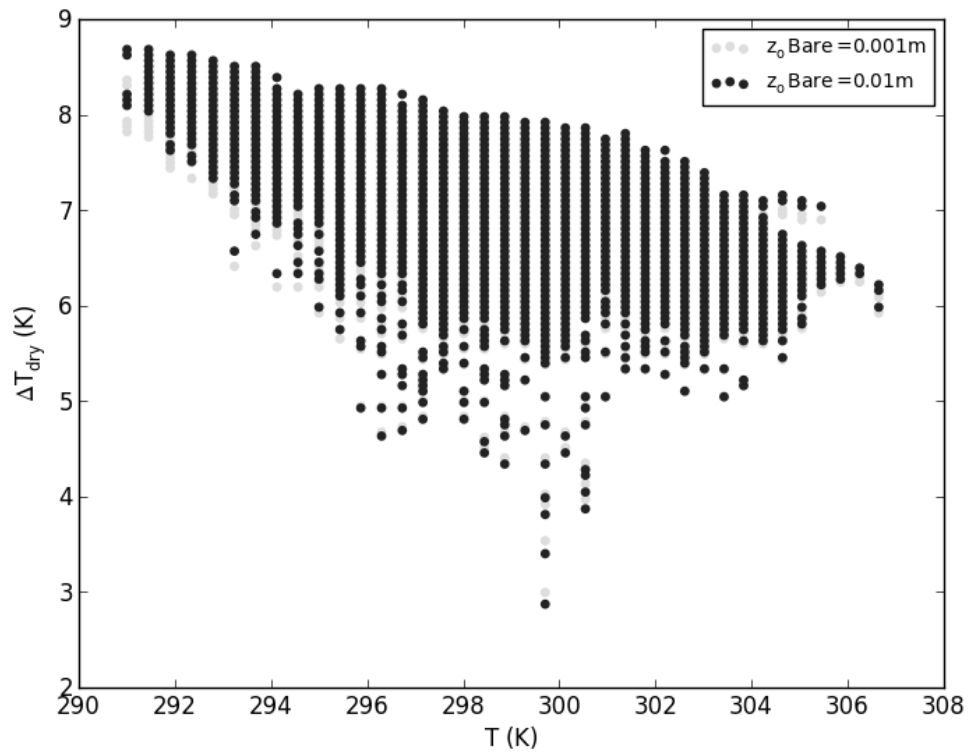
Figure 3.2.3: Variation of ΔT_{dry} Due to Change in z_o Bare

The Min-Max Bins method finds the boundary points by keeping only the points with maximum and minimum energy in each temperature bin. Because LANDSAT data stores radiance with a maximum bit depth of 8 bits (256 integers), the temperature values

retrieved from LANDSAT are inherently already divided into temperature bins. The problem with this method is that it keeps points on the left side of the scatter plot which do not make up the upper or lower boundary. It is necessary to filter these points out. This is done by using ΔT bins and comparing the Min Max points to the original full data set. If the Min Max point does not have the maximum energy in the ΔT bin, then it is assumed to be to the left and filtered out. Originally these ΔT bins were of uneven size and created automatically by making each Min Max point delineate the edge of the bin. Since the Min Max point was on the cusp of two bins, it was defined to only be a member of the bin below it. This method has the advantage of not requiring the selection of bin size, but it is not very successful at removing necessary points. The Hybrid method uses the Min Max method but performs this final filtering using Even Bins described above instead of the automatic bins.

Once the points that make up the boundary are located, it is necessary to use them to find the coefficients in the ΔT vs. T equation. This was performed using two methods which will be called 1) Extreme and 2) Threshold Fit. The Extreme method positions the line so that all of the boundary points are above the line. It then alters the slope and intercept of the line until the *MAE* between the points and the line is minimized (Note: *MAE* and *Bias* are same since all points are on one side of line). RMS is not used because it is too sensitive to outliers. Threshold Fit divides the data between the upper and lower boundary points based on whether they are greater than or less than some threshold ΔT. Least squares regression is then performed on both sets of points to produce a line for the upper boundary and a lower boundary. The total RMS score of all of the points with respect to their associated lines is used as a criterion for determining the optimal

threshold ΔT. The threshold ΔT is varied until the point with the minimum RMS score is determined.

　　To summarize, there are two procedures for performing the calibration. The first is to identify the boundary pixels, and the second is to fit the boundary pixels to a line. These procedures were combined to form 3 different variations of the calibration called the Boundary Variations. These variations are called 1) Extreme 2) Min-Max Threshold Fit, and 3) Even Bins Threshold Fit. The Extreme variation uses the Automatic Min-Max Bins method to find the boundary points and the Extreme method to fit the line. The Min-Max Threshold Fit uses the Hybrid Min-Max Bins method to find the boundary points and the Threshold Fit method to fit the line. The Even Bins Threshold Fit uses the Even Bins method to find the boundary points and the Threshold Fit Method to fit the line. Sample executions of the three Boundary Variations are shown in Figure 3.2.4-3.2.6.
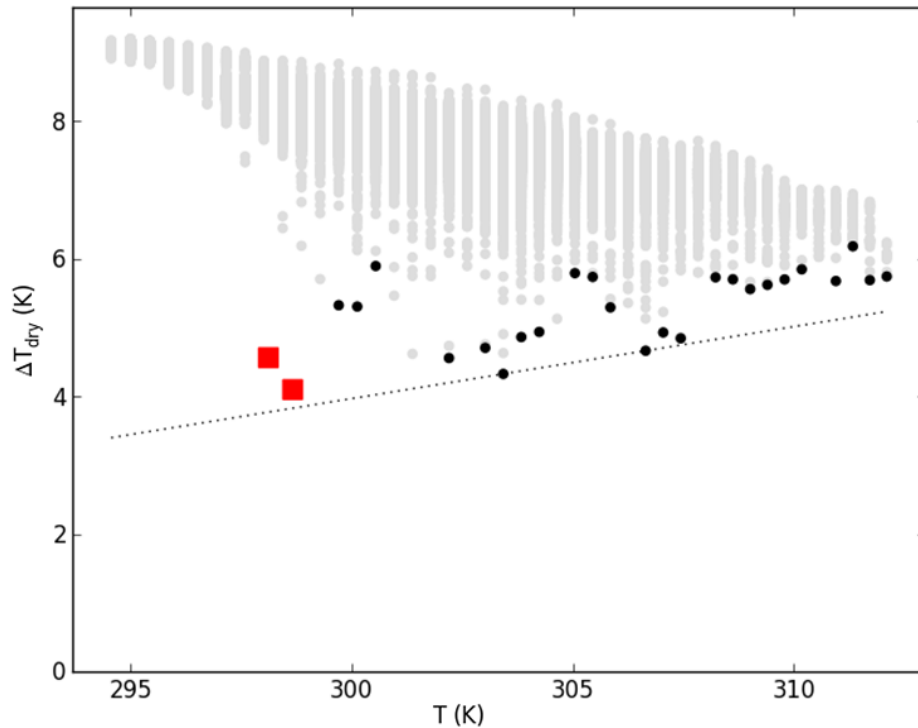
Figure 3.2.4: Example Plot for Extreme Boundary Variation
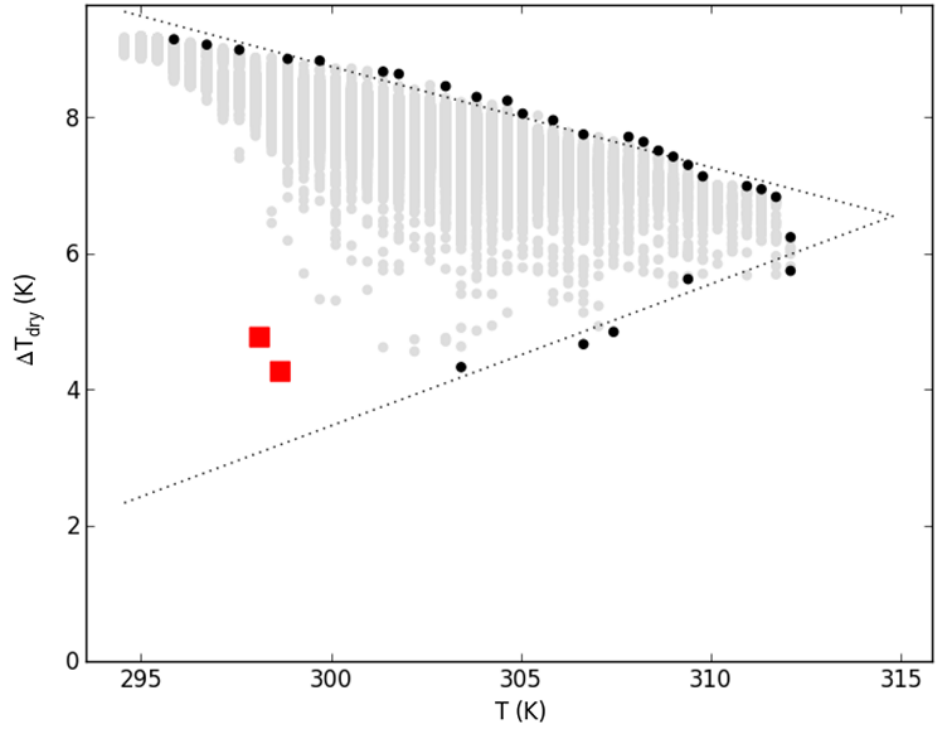
Figure 3.2.5: Example Plot for Min-Max Bins Threshold Fit Boundary Variation
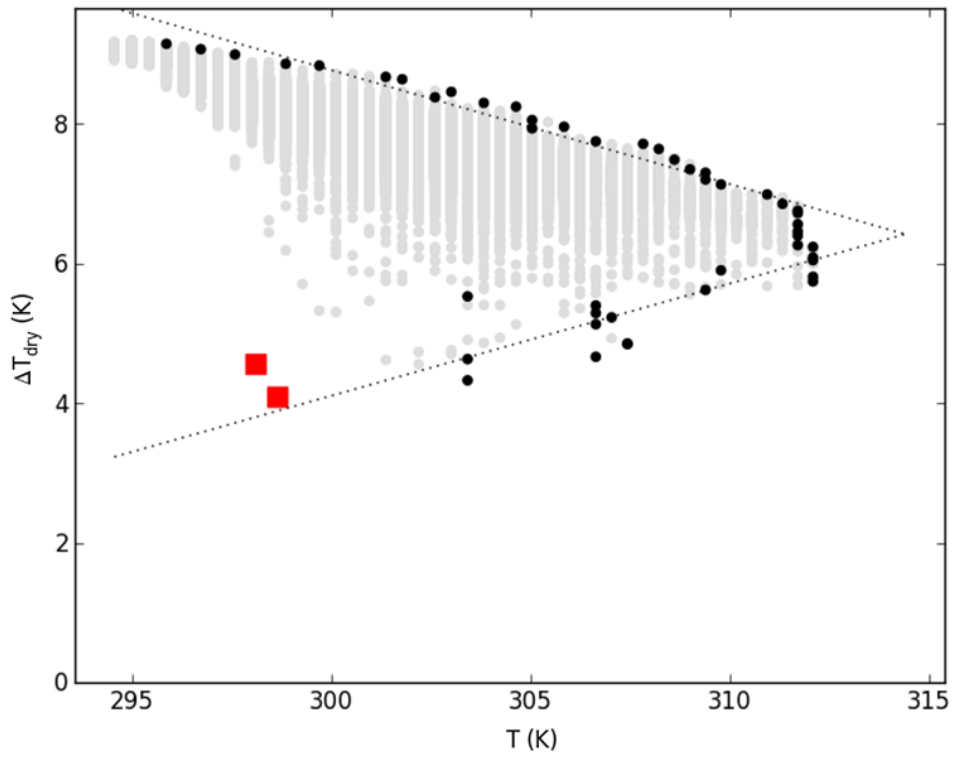
Figure 3.2.6: Example Plot for Even Bins Threshold Fit Boundary Variation

Another modification to the process of determining boundary pixels is to filter out certain pixels before identifying the boundary. The two types of filtering applied are 1) Cloud Filtering and 2) Albedo Filtering. Although care was taken to find clear sky scenes, often a small amount of cloud cover exists on an image. In order to removes these pixels from the calibration data, pixels were filtered by removing pixels which are cooler than a threshold temperature. The threshold temperature is equal to the study area's mean temperature minus two times the study area's standard deviation. For some study areas, very bright surfaces resulted in values in which the energy was very low, but the temperature was larger than expected for such a low energy. This could possibly be due to advection of heat from surrounding areas. This is probably not because of errors due to lower emissivity of manmade surfaces. That would mean actual temperature would be greater than the retrieved temperature. This problem typically only occurred for a small number of pixels in the image, but it could have serious consequence on the resulting coefficients produced for equations 3.2.5 and/or 3.2.10. In order to account for this, all pixels were filtered by removing those which were brighter than a threshold albedo of 0.5.

3.2.6 Validation of Evaporative Fraction Produced by Algorithm

This section describes the manner in which the *EF* produced by the algorithm is validated against the eddy covariance data described in section 2. A future section will describe the extension of this to comparing actual evapotranspiration. The eddy covariance tower measures latent and sensible heat over a footprint as described in section 3.1.1 In order to calculate a retrieved *EF* that can be compared with the *EF* measured by flux tower, the retrieved fluxes must be averaged over a flux tower footprint

such as that shown earlier in Figure 3.1.2. The following equation can be used to calculate the footprint averaged value of some flux F measured on a grid:

$$\overline{F} = \Sigma \, \Sigma \, w_{ij} \, F_{ij} \qquad\qquad 3.2.27)$$

where $\overline{F}$ is the flux averaged over the footprint, w_{ij} is the weight of the source function at grid cell i,j and F_{ij} is the flux value at cell i,j. As described in section 3.1.1, a uniform footprint is assumed for this dissertation and therefore inside the footprint w_{ij} = constant = $1/N$ and outside the footprint w_{ij} =0. N is the total number of cells in the uniform footprint.

The energy balance equation 3.2.1 can be averaged over the footprint and divided by the averaged available energy to produce the footprint averaged EF for comparison with tower:

$$EF_{\text{retrieved}} = 1 - \overline{H}_{\text{retrieved}} / \overline{A}_{\text{retrieved}} \qquad\qquad 3.2.28)$$

where $EF_{\text{retrieved}}$ is the estimate for EF which can be compared to tower estimated EF, $\overline{H}_{\text{retrieved}}$ is the sensible heat produced by ET mapping algorithm, and $\overline{A}_{\text{retrieved}}$ is the available energy produced by ET mapping algorithm.

It is beneficial to be able to visualize the validation points on scatter plot of available energy (or ΔT_{dry}) vs T_{s}. For available energy vs. T_{s} plots the validation sensible heat will be plotted against the retrieved temperature. The validation sensible heat H will be calculated using:

$$H_{\text{tower}} = (1\text{-}EF_{\text{tower}}) \, \overline{A}_{\text{retrieved}} \qquad\qquad 3.2.29)$$

where H_{tower} represents the validation sensible heat measured by the tower and EF_{tower} is the evaporative fraction calculated for the tower as described in section 3.1.1. It should be

noted that the difference between actual and retrieved available energy is not accounted for in this equation. In essence this equation is only representing the effect of differences in *EF* on *H* but not the differences in actual and retrieved available energy. Description of the analysis between the differences between actual and retrieved available energy and its effect on retrieved fluxes is included in a future section. In closing, the use of retrieved energy is adopted in order to visualize the ability of the calibration to predict *EF*.

It is also necessary to average the retrieved temperature over the footprint when plotting the validation point. This is because the averaged retrieved sensible heat is equal to:

$$\overline{H}_{\text{retrieved}} = a + b\,\overline{T}_{\text{retrieved}} \qquad\qquad 3.2.30)$$

where *a* and *b* are the calibration coefficients and $\overline{T}_{\text{retrieved}}$ is the footprint averaged retrieved surface temperature. Therefore the line produced by equation 3.2.15 can be compared to the point created using H_{tower} and $\overline{T}_{\text{retrieved}}$. In order to visualize validation points on *ΔT* vs. T_{s} plot it is necessary to also average over g_{a}. The following equation is produced by multiplying g_{a} by the retrieved *ΔT* and averaging over footprint:

$$\overline{H}_{\text{retrieved}} = a\,\overline{g_{\text{a}}} + b\,\overline{T\,g_{\text{a}}} \qquad\qquad 3.2.31)$$

where $\overline{g_{\text{a}}}$ is g_{a} averaged over footprint, and $\overline{T\,g_{\text{a}}}$ is the product of retrieved surface temperature and g_{a} averaged over the footprint. Then $\overline{H}_{\text{retrieved}}$ and $\overline{H}_{\text{tower}}$ can be divided by $\overline{g_{\text{a}}}$ to produce a *ΔT* values which can be compared on plot:

$$\overline{\Delta T}_{\text{tower}} = \overline{H}_{\text{tower}} / \overline{ga} \qquad\qquad 3.2.32)$$

$$\overline{\Delta T}_{\text{retrieved}} = a + b\ \overline{T\ ga} / \overline{ga} \qquad\qquad 3.2.33)$$

Therefore *ΔT* for the validation point will equal validation sensible heat calculated using equation 3.2.29 divided by the footprint averaged g_a and the temperature used for the validation point will equal the footprint averaged temperature weighted by g_a.

The above method is just for visualization. To quantitatively analyze the model, EF_{tower} and $EF_{\text{retrieved}}$ is compared. The *Bias* and *MAE* error will be computed using:

$$BIAS_{\text{EF}} = 1/ N_{\text{obs}}\ \Sigma\ (EF_{\text{tower}} - EF_{\text{retrieved}}) \qquad\qquad 3.2.34)$$

$$MAE_{\text{EF}} = 1/ N_{\text{obs}}\ \Sigma\ |\ EF_{\text{tower}} - EF_{\text{retrieved}}\ | \qquad\qquad 3.2.35)$$

where the summation is over all available observations from stations among all "useable" scenes for particular study area and N_{obs} is the total number of observations. *MAE* is used instead of *RMS* to reduce the effect of outliers. *RMS* is often used in regression situations in which maximum likelihood between observed and predicted is sought after. It can also be used to estimate percentiles of the residuals. In this study, *MAE* is used because the aim is to determine the error that is produced. Determining percentiles of the absolute residuals is done easily using a non parametric cumulative distribution function.

3.2.7 Using Wet Pixels in Calibration

In order to test the performance of the dry pixel calibration, it will be beneficial to compare it to a calibration that also includes wet pixels. A simple method for incorporating wet pixels into the calibration is proposed here. The method consists of finding wet pixels via an automated process, and then averaging the *ΔT* (or *A*) and T_s of these wet pixels to produce a wet "end member" value. A dry "end member" value is produced by using the results of the dry pixel only calibration. This consists of finding

the point where the upper and lower boundary intersect after the boundary lines are produced using the Threshold Fit method. The straight line that connects these end members represent the calibrated relationship between ΔT (or A) and T_s. Figure 3.2.7 shows an example of the wet pixel calibration for Disney. In this example using only dry pixels severely overestimated ΔT and adding wet pixels (in blue) improved the results. Worthy of mention is that the validation ΔT for the dry pixel calibration (in red) is different than that for the wet pixel calibration (in orange) because g_a changed due to instability. The predicted ΔT is used to calculate the g_a used to calculate the validation ΔT. The wet pixel calibration shown in Figure 3.2.7 decreased the predicted ΔT which decreased the buoyancy/instability which in turn decreased g_a leading to increase in the validation ΔT.
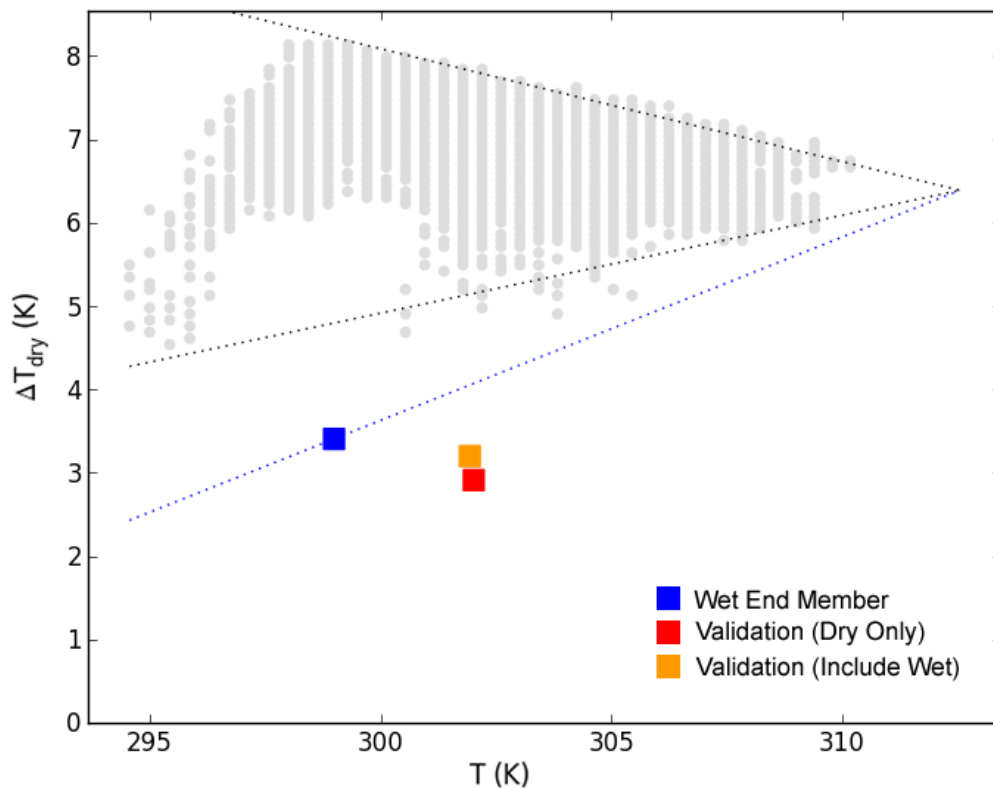
Figure 3.2.7: Example of Wet Pixel Calibration

70

Producing the wet "end member" involves first finding wet pixels and then estimating the sensible heat (or ΔT) for these wet pixels. The value used as the wet "end member" is simply the average H (or ΔT) and T_s for these pixels. Three methods for finding wet pixels are used 1) Above *NDVI* Threshold 2) Below *NDVI* Threshold, and 3) Unsupervised Classification. The Above *NDVI* Threshold method aims to find well watered vegetation pixels. This method assumes that the top p_{above} percent of *NDVI* values in the image are made up of well watered vegetation pixels. Once a value for p_{above} is chosen, the (1- p_{above})-th percentile of *NDVI* is determined as a threshold *NDVI*. The wet pixels are then found by choosing all pixels with *NDVI* greater than the threshold *NDVI*. The Below *NDVI* method is similar to the previous method, but it aims to find pixels made up of open water. It assumes that the bottom p_{below} percent of *NDVI* values in the image are made up of open water pixels. Similar to before, a value for p_{below} is chosen and the p_{below}-th percentile of *NDVI* is determined as the threshold *NDVI*. The wet pixels are then found by selecting all pixels with *NDVI* less than the threshold *NDVI*. The third method uses an unsupervised classification to find open water pixels. The classification method used could be any type of classification but the unsupervised method is used because it was already performed when masking out water during roughness length calculations.

The Below *NDVI* Threshold method and Unsupervised Classification method have the same goal of detecting water pixels. The advantage of the Below *NDVI* Threshold method is that it is much simpler to execute, but the disadvantage of the method is p_{below} must be provided. The same problem exists for the Above *NDVI* Threshold method. Therefore, it is necessary to analyze the sensitivity of the algorithm to

71

p_above and p_below parameters. *Bias* and *MAE* error of the algorithm using p values varying

from 0 to 100% were calculated and compared for each study area. Another option that is

tested is using absolute values of *NDVI* for a threshold to detect water. This option was

not used for Above *NDVI* because *NDVI* of healthy vegetation can be highly variable

across study areas.

The second part of finding the wet "end member" is to find the sensible heat of

the wet pixels found using one of the methods above. Estimating the sensible heat of the

wet pixels is limited because of a lack of weather data and surface parameters. In Florida

the Priestly Taylor equation was found to perform as well or better than the more

complex Penman-Monteith equation over a variety of land cover types (Douglas et al.

2009). Therefore, the Priestly Taylor approach is adopted because it only requires

temperature. Sensible heat is determined by subtracting the *ET* calculated using the

Priestly-Taylor equation (Priestley and Taylor 1972) from the available energy:

$$H_\text{wet} = A_\text{retrieved} \, (1 - \alpha_\text{PT} \, \Delta / (\Delta + \gamma)) \qquad\qquad 3.2.36)$$

where H_wet is the sensible heat for the wet pixels, α_PT is the Priestly-Taylor coefficient, Δ

is the rate of change of saturation vapor pressure with respect to temperature for the

current temperature and γ is the psychrometric constant. Δ and γ (both in units of kPa/K)

are calculated using:

$$\Delta = \mathrm{d}e_\text{sat} / \mathrm{d}T = 4283.58 / (T_\text{s} - 30.11)^2 \, e_\text{sat} \qquad\qquad 3.2.37)$$

$$e_\text{sat} = 0.6109 \, e^{\,-17.625 \, (T\text{s} - 273.15) / (T\text{s} - 30.11)} \qquad\qquad 3.2.38)$$

$$\gamma = C_\text{p} \, P / \lambda_\text{v} / \mathrm{MW}_\text{ratio} \qquad\qquad 3.2.39)$$

where T_s is the satellite retrieved surface temperature in K, e_sat is the saturation vapor

pressure (Alduchov and Eskridge, 1996), C_p is the specific heat capacity of air, P is the

pressure of the air, λ_v is the latent heat of vaporization and MW_{ratio} is the ratio of the molecular weight of water vapor to dry air. Although C_p, P and λ_v are not strictly constant, it is typically assumed that γ is constant for a given elevation. For the study areas in this dissertation it is assumed that $\gamma=0.07$ kPa/K. Although air temperature is usually used in the Priestly-Taylor equation, for open water or well watered vegetation it could be assumed that surface temperature is close to air temperature.

The difficulty in using equation 3.2.36 is deciding which value of α_{PT} to use. The standard value for α_{PT} is 1.26. It was necessary to analyze the range of values in our actual study areas. α_{PT} was calculated for all available stations for each study area using:

$$\alpha_{PT} = EF_{tower} (\Delta + \gamma) / \Delta \qquad\qquad 3.2.40)$$

From this the mean and standard deviation of α_{PT} was determined for each month. This provided an idea about the range of α_{PT} that could exist. It also provided an idea about α_{PT} over vegetation of varying soil moisture conditions since stations were situated over rain-fed vegetation. It was also necessary to examine the range of α_{PT} that would exist for open water. To achieve this, ET was simulated using the Penman-Monteith equation (Penman 1948, Monteith 1965) in order to simulate flux tower ET:

$$ET = (\Delta(T_a) A_{simulated} + g_a (e_{sat}(T_a) - e)) / (\Delta(T_a) + \gamma) \qquad\qquad 3.2.41)$$

where e is the actual vapor pressure, $e_{sat}(T_a)$ and $\Delta(T_a)$ are saturated vapor pressure and derivative of e_{sat} with respect to temperature calculated using air temperature T_a, and $A_{simulated}$ is the simulated clear sky available energy. It is necessary to simulate the clear sky available energy over water since the flux tower measurements were not necessarily cloud free. $A_{simulated}$ was simulated using equations 3.2.10 and 3.2.11. Down-welling clear

sky solar radiation was calculated using equation 3.2.16 with zenith angle calculated

based on latitude, day of year and local solar time (Wolf, 1968;Allen et al, 1998):

$$\theta_{hour} = 15 \ (LST - 12) \tag{3.2.42}$$

$$\delta = 23.43 \ \sin(360/365*DOY\text{-}79.64) \tag{3.2.43}$$

$$\theta = \cos^{-1}[\sin(\theta_{latitude}) \ \sin(\delta) + \cos(\theta_{hour}) \ \cos(\theta_{latitude}) \ \cos(\delta)] \tag{3.2.44}$$

where θ_{hour} is hour angle in degress, LST is the local solar time in hours (0-24 hours), δ is

the solar declination, $\theta_{latitude}$ is the latitude in degrees, DOY is the day of year, and θ □is

the solar zenith angle. α was assumed to be equal to 0.05 where the effect of low angle of

incidence on albedo is neglected. Net long wave radiation was calculated using

(Mecikalski, 2010):

$$R_{net,LW} = \sigma \ T_a^4 \ (.34 - .14 \ e^{.5}) \tag{3.2.45}$$

where T_a is air temperature measured by weather station. G/R_n was assumed to be 0.10

which is a very rough estimate since this value can be highly variable for open water

compared to land. In equation 3.2.6, g_a was calculated using a $z_o = 0.0001$ m. Finding g_a

requires a solution which alters the Monin-Obukhov length L until the L produced from

resulting u^* and H matches the guess.

   Simulated α_{PT} values for water were created using available station data for all

study areas. The resulting mean and standard deviation of α_{PT} was determined for each

month. This provided an idea of the range of α_{PT} that could exist.

3.2.8 Validation of Actual Evapotranspiration

   In addition to validating the algorithm with respect to evaporative fraction, it is

also important to validate with respect to actual instantaneous evapotranspiration.

Instantaneous ET at time of satellite overpass is used in validation instead of daily value

because LANDSAT alone does not provide information about daily available energy. Producing actual evapotranspiration from the model is as simple as multiplying the retrieved *EF* by the retrieved available energy. Determining the actual instantaneous evapotranspiration measured by the tower that can be compared to the satellite is not totally straight forward. As explained above, flux measurements using the eddy covariance method can have a lot of errors. Therefore it is necessary to correct the *ET* measurements by multiplying the available energy by the *EF* as described in section 3.1.1. In addition to the error inherent in assuming that the ratio of fluxes is accurate, there are other problems with using the tower available energy for estimating the tower *ET*. The available energy that is multiplied by *EF* must be that which is averaged over the eddy covariance footprint, but the footprint of radiometer measuring radiation is much smaller than the eddy covariance footprint. Figure 3.2.8 shows the footprint function which describes the source of radiation measured by the radiometer of the flux towers. This footprint function is based on a simple model in which the weight decreases away from the radiometer proportional to cosine of the angle (θ_r) between the vertical and the line of sight from radiometer to source area (Schmid, 1997):

$$w_{o,i} = \cos \theta_{r,\, i}{}^4 = 1/(z^2 + x_i^2)^2 \tag{3.2.46a}$$

$$w_i = w_{o,i} / \Sigma \, w_{o,i} \tag{3.2.46b}$$

where w_i is the weight function for cell i, z is the height of tower, and x_i is the distance to the base of the tower. Two of the cosine factors are a result of the source and target being angled to the line of sight while the other two cosine factors area a result of the spreading of the radiation away from the source. The resulting footprints based on the heights of stations used in this study are typically not much bigger than one LANDSAT pixel.
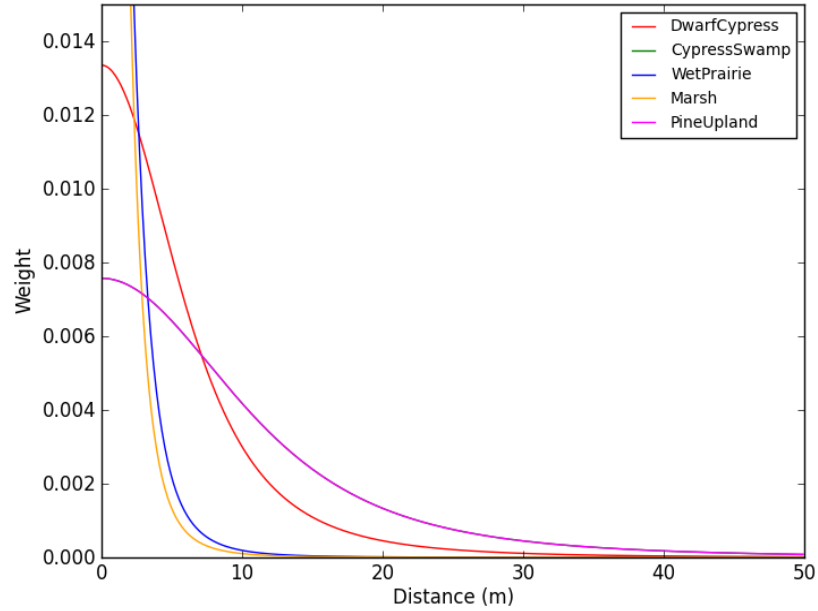
Figure 3.2.8: Radiometer Footprint Modeled for Big Cypress

In order to estimate the available energy averaged over the eddy covariance footprint, the satellite retrieved available energy will be corrected using the tower available energy. A very basic correction will be applied which assumes that the difference in energy between tower and the satellite measurement does not change when it scaled up from radiometer footprint to the eddy covariance footprint:

$$\overline{A}_{tower,EC} = \overline{A}_{retrieved,EC} + \overline{A}_{tower,RAD} - \overline{A}_{retrieved,RAD} \qquad 3.2.47)$$

where the subscript "retrieved" represents the energy estimated using satellite image, the subscript "tower" represents the energy measured by the tower (or what it is simulated to be over a larger footprint), the subscript EC means the energy is averaged over the eddy covariance footprint, and the subscript RAD means the energy is measured over the radiometer footprint. This correction produces a ground based energy which produces an *ET* which can be compared to the satellite retrieved *ET*.

The tower and retrieved energy averaged over radiometer footprint were compared for each study area. For most study areas there were day to day differences in

76

scatter due to different conditions opposed to a systematic offset or scale. Therefore, the simple correction explained above was used instead of performing a regression between RAD scale tower and retrieved energy over multiple days. The available energy calculated using equation 3.2.47 was multiplied by the tower based *EF* to produce tower based *ET* which was compared to the retrieved *ET*. The same criteria used in Section 3.2.6 for comparing evaporative fraction is used for comparing *ET* also. In addition, retrieved energy is multiplied by tower *EF* in order to look at the effect that the relationship between *EF* errors and energy have on *ET* errors. For example, if *EF* errors are large when energy is small, the resulting *ET* error will be minimized compared to the same *EF* error when energy is larger. This metric does not account for manner in which errors in retrieving available energy affect *ET* errors.

3.2.9 A Note On Heterogeneity and Similarity Theory

Monin-Obukhov similarity theory was derived for homogenous environments, yet the nature of our evaportranspiration environment relies on hetergenous environments. *ET* mapping would not be necessary if the environment was a homogenous environment in the first place. It is possible to test the implication of this contradiction using techniques such as large eddy simulations which are considered suitiable for modeling boundary layer fluxes over heterogeneous terrain (Avisar et al, 1998; Avissar & Schmidt, 1998; Bohrer, 2009; Albertson & Parlange, 1999; Albertson et al, 2001). Efforts have been made to incorporate large eddy simulations in to the remote sensing of *ET* (Albertson et al, 2001), but their implemation is not within the scope of this dissertation. Applications of SEBAL and METRIC have been shown to produce acceptable results

(Allen et al, 2007; Bastiaanssen et al, 2005; Gowda et al, 2008) and this dissertation
follows them while realizing the above.

3.3 Sensitivity Testing

3.3.1 Determining the Effect of Wind Speed

For testing the algorithm so far the wind speed at blending height, u_{blend} or u_{200},
was supplied to the algorithm from the eddy covariance data. Since the goal of the
satellite retrieval is to operate independently of the flux tower data, the effect of not
knowing the wind speed must be analyzed. The equation for calculating sensible heat can
be rewritten:

$$H = u_{200}\ C_H\ \Delta T \qquad\qquad 3.3.1)$$

where C_H is the bulk aerodynamic coefficient for heat which is equal to g_a / u_{200}. Now
instead of using ΔT as the dependent value in the calibration, the value $u_{200}\ \Delta T$ can be
used which can be determined by calculating H/ C_H (instead of H/g_a). This leads to an
alternate equation to calibrate:

$$u_{200}\ \Delta T = a_c + b_c\ T_S \qquad\qquad 3.3.2)$$

This is the same thing as multiplying the original calibration equation by u_{200}. Since u_{200}
is spatially constant it is absorbed by the calibration coefficients. Therefore, the
calibration process has the ability to detect information about wind speed which is
embedded in the slope of the line representing calibrated sensible heat. In fact, splitting g_a
into u_{200} and C_H was only done for demonstration purposes. When calculating ΔT_{dry},
energy was divided by g_a and therefore divided by a constant u_{200}. Therefore coefficients
a and b will carry the value of u_{200} in their denominators. When the calibrated equation is
multiplied by g_a again to find ET, the u_{200} in the g_a in the numerator will cancel the u_{200} in

the denominator. If the value of u_{200} guessed for the scene is wrong, it will just cancel out in the end. The information about the actual wind speed is still embedded in the coefficients. But this is only true for neutral conditions. When conditions are unstable, the stability corrections ψ_M and ψ_H must be used. ψ_m and ψ_h are functions of Monin-Obhukov length L which is a function of the friction velocity $u*$ which is a function of wind speed u_{200}. Since C_H and g_a depend on ψ_m and ψ_h in a nonlinear fashion (and therefore u_{200} in a nonlinear fashion), u_{200} will not cancel out when it comes to non-neutral conditions. Therefore testing the effect of uncertainty in wind speed is basically due to the effect that wind speed has on instability.

A simple approach is taken in which u_{200} is assumed to be equal to the average value for each study area. u_{200} is averaged on a monthly basis first to see if there are any strong seasonal variations. If seasonal variability is not a large factor then annually averaged u_{200} is used. A more complex approach would be to use an outside data source for the wind such as the Florida Automated Weather Network (FAWN). These data are available in an operational sense, but it turned out that it did not seem necessary to incorporate them at this time.

3.3.2 Testing Sensitivity to Temperature, Energy and Roughness

The sensitivity of the algorithm due to perturbations in temperature and available energy were calculated. In contrast to the validation procedures which compared retrieved values to individual stations on the ground, these sensitivity tests will compare entire maps produced using unperturbed inputs to maps produced using perturbed inputs. In this manner the sensitivity of the algorithm can be determined for the majority of the study area where eddy covariance stations are unavailable. The sensitivity tests are

performed separately for temperature and energy. The temperature is perturbed by some uniform amount across the entire study area. This new temperature map is then used to calibrate the model and produce a new *EF* and/or *ET* map from this new calibration and perturbed temperature map. The perturbed map is then compared to original map at the image and pixel level. To compare the maps at the image level the *Bias* error between the maps is used. To compare at the pixel level the *MAE* error is used:

$$Bias = \Sigma\ EF_{\text{perturbed},i} - EF_{\text{original},i} \qquad\qquad 3.3.3)$$

$$MAE = \Sigma\ |\ EF_{\text{perturbed},i} - EF_{\text{original},i}\ | \qquad\qquad 3.3.4)$$

where $EF_{\text{perturbed},i}$ is *EF* in cell *i* for the map created using perturbed values and $EF_{\text{original},i}$ is *EF* in cell *i* for the map created using original values. *Bias* is considered "image" level because it represents the difference between the averages of the images. The *MAE* is considered "pixel" level because it represents the deviation that an individual pixel experiences on average. Typically the terminology *Bias* and *MAE* are used when comparing a prediction to observations. Here the original map is thought to be the observation while the perturbed map is the prediction due to some error in a parameter. The situation has been idealized such that the originally retrieved map is considered the truth while the map that would actually be retrieved or predicted is assumed to be altered solely due to some uncertainty in temperature or energy. At each perturbation level, the *Bias* and *MAE* error for each useable scene in the study area was determined. The *Bias* and *MAE* values of all useable scenes in the study area was then used to calculate a mean and standard deviation of both *Bias* and *MAE* at each perturbation level:

$$\overline{\text{Bias}} \; = \Sigma \; Bias_i \, / \, n \qquad\qquad\qquad\qquad\qquad\qquad 3.3.5a)$$

$$\sigma_{\text{bias}} = \Sigma \; (Bias_i \, - \, \overline{\text{Bias}} \,)^2 / \, n \qquad\qquad\qquad\qquad\qquad 3.3.5b)$$

$$\overline{\text{MAE}} \; = \Sigma \; MAE_i \, / \, n \qquad\qquad\qquad\qquad\qquad\qquad 3.3.6a)$$

$$\sigma_{\text{MAE}} = \Sigma \; (MAE_i \, - \, \overline{\text{MAE}} \,)^2 / \, n \qquad\qquad\qquad\qquad\qquad 3.3.7b)$$

where $Bias_i$ is the bias for scene i in the study area for the current perturbation level, and

MAE_i is the MAE for scene i in the study area for the current perturbation level.

This process was repeated for temperature perturbations ranging from -10 K to +10 K. In the available energy case, two types of perturbations were used. The first type was a uniform perturbation as was done for temperature and the second type was a perturbation equal to a constant fraction of the current value. The fractional perturbation was repeated in the range of -50% to +50% and the uniform perturbation was repeated in the range of -200 to +200 W/m^2. The sensitivity of ET to energy was also produced in the same manner.

The sensitivity of the algorithm to roughness length was also determined. This is an important effect to analyze because roughness length is one of the more difficult variables to estimate in the algorithm. The same basic methodology used for temperature and energy as described above was used. The roughness length was given a uniform perturbation ranging from -1 m to +1 m. The perturbation in the negative direction was forced to result in a minimum roughness length of 0.0001. Another test was conducted which forced the roughness length to be a constant value across the map instead of making the perturbation value constant across the map. During the validation process a model variation was tested in which atmospheric conditions were considered neutral but

roughness length varied. This case assumes that roughness is constant but instability of atmosphere is allowed to vary. In effect it is testing whether roughness length can be ignored as long as instability is included in the model. This is different than assuming that conductance of the atmosphere is constant allowing sensible heat to be proportional to temperature alone.

3.4 Data Fusion of LANDSAT and MODIS resolution imagery

Since the objective of this research was to test the effect of resolution and not the effect of sensor differences, MODIS resolution imagery was simulated by aggregating 120 m LANDSAT thermal resolution into 1 km blocks. Fused thermal images were created for every image in the series of available images based on neighboring images. It is also necessary to find available energy for the fused day which requires albedo (α) and ground heat flux fraction (%G). It was assumed that these values changed more smoothly in time than temperature so they were linearly interpolated between neighboring scenes. For finding wet pixels, the minimum *NDVI* method was used. *NDVI* was linearly interpolated between neighboring scenes based on the assumption that it changes smoothly in time for wet areas. An *ET* map was then created for each fused scene and compared to the *ET* map retrieved using actual thermal image. The fusion methods tested and error analysis used to evaluate them is described below.

3.4.1 Data Fusion Techniques

Six data fusion algorithms 1) Simple Interval 2) Simple Ratio 3) Double Sided Proportion 4) Similar Temperature 5) Similar *ET* 6) Similar *EF* and four interpolation methods 1) Nearest Neighbor *ET* 2) Linear *ET* 3) Nearest *EF* 4) Linear *EF* were used to produce *ET* maps. Figure 3.4.1 defines the various scenes used in the fusion process. L_C

is the target LANDSAT resolution scene that is being estimated which simulates a "missing" day. The other five scenes are sources of information that can be combined in order to estimate L_C. M refers to the simulated MODIS resolution. These coarse MODIS resolution pixels will often be referred to as "blocks" in the future.
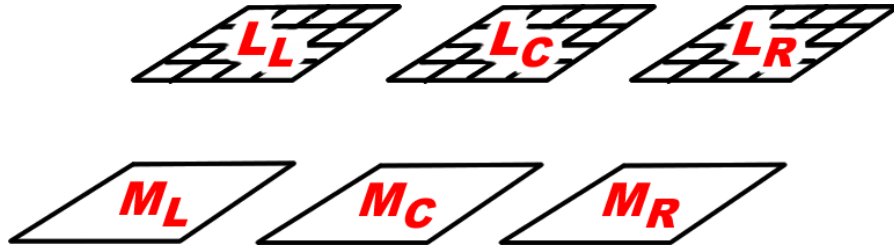
Figure 3.4.1: Diagram Defining Scenes in Data Fusion Process

1) *Simple Interval*: The Simple Interval method is the simplest method used for fusing temperature. It is the starting point for all of the other methods. It is a single sided technique in which only the data from the neighboring scene which is nearest in time is used. Depending on which side is closer the following equations are used:

$$L_C = L_L + (M_C - M_L) = L_R - (M_R - M_C) \tag{3.4.1}$$

This technique can often lead to "blockiness" because every LANDSAT pixel in the same block will experience the same change.

2) *Simple Ratio:* The Simple Ratio is the same as Simple Interval except instead of adding an interval to initial value, a ratio is multiplied by initial value:

$$L_C = L_L \, M_C/M_L = L_R \, M_C/M_R \tag{3.4.2}$$

3) *Double Sided Proportion:* This method uses all five pieces of data in the fusion process. It is based on the assumption that the ratio of the change from L =>C to the change from L=> R for MODIS and LANDSAT is proportional to each other. This proportionality can be rewritten as:

$$L_C = L_L + (L_R - L_L) \, (M_C - M_L) / (M_R - M_L) \tag{3.4.3}$$

The advantage of this technique is that it allows the individual pixels in the same block to change differently. Basically the block change from L=>C for each pixel is now weighted by the LANDSAT change from L=>R. If the resulting change from L=>C for each pixel is aggregated over the entire block, it must equal the block change from L=>C. This is accomplished by normalizing the LANDSAT change by block change from L =>R. This method works if the pixels in the same block do not change directions at different times. An example situation in which this method would break down follows. Assume one pixel is over water and the other is over land. If the change is from late fall to winter to spring, land will get colder and warmer while water will continue to be cool due to cold reservoir of water stored in lake. If equation 3.3.3 is to hold, then the ratio of the change in the 1st period to change in both periods must be constant for both surfaces. But this will not occur because although the 1st period for both might be similar, the total of both periods are much different because net changes over land will be much less or in different direction compared to water. Another problem with Double Side Proportion occurs when M_R - M_L is small which can lead to unrealistically large or small temperatures. In order to solve this problem, the temperature is forced to fall within the minimum or maximum coarse scale temperature for day of interest (using all M_C blocks in image).

4) *Similar Temperature:* This method searches all neighboring blocks in order to find that which is the most similar in temperature. The criteria used for similarity is

$$S = | L_L - M_L | = | L_R - M_R | \qquad 3.4.4)$$

where S is the similarity criteria. It uses the right vs. left side depending on whichever is closer in time to center. Once the block is found in which s is minimum for the LANDSAT pixel of interest L_L, (M_C - M_L) from that block is added to the L_L via equation

3.3.1. This technique does not produce the "blockiness" of Simple Interval because each pixel has its own change from an area which is similar to that pixel. Figure 3.4.2 is useful for understanding the concept. In this example the background white area is changing from white to gray while black is remaining constant. The pixel of interest is in a block which is a mixture of black and white. Therefore if the change of this block is used, it will produce less change because black is remaining constant. In the Similar Temperature method, the change of the pure white block near the pixel of interest is used because it will reflect the true change from white to gray.
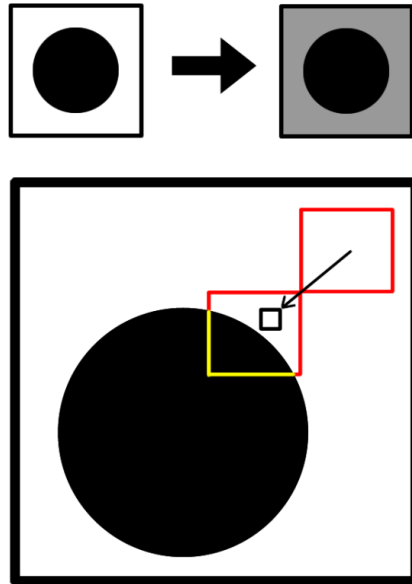
Figure 3.4.2: Diagram Explaining Similar Neighbor Method

A possible problem with the similarity approach can occur if the L_L is close to M_L, but M_L is not a homogenous block. In this case, only the mean state of the block is similar to L_L. Therefore, the change of this block might not reflect the change of a "pure" pixel. To account for this, homogeneity of the block should be included along with similarity of the block. This can be accomplished by representing the purity of the block with the mean absolute deviation:

$$MAD = \overline{\mid L_L - M_L \mid} \qquad\qquad 3.4.5)$$

This can be used to produce a new criterion based on similarity and homogeneity:

$$S_H = S + w\ MAD \qquad\qquad 3.4.6)$$

where S is the similarity criterion from equation 3.4.4 and w is a weight which determines the importance of homogeneity relative to similarity. If w is 0 then only similarity matters and as w becomes very large only homogeneity matters. Since both similarity and homogeneity are important, w should be some intermediate value. Determining the optimal weight value is not a trivial exercise. A universal weight value almost surely does not exist. The optimal weight value under different scenarios with respect to different type of errors is examined by varying the weight value and performing the Similarity and Homogeneity data fusion.

A problem with using temperature to find areas of similar change is that surfaces with similar temperature are not necessarily similar surfaces. For example, dry pixels can be cool because of a high albedo, while wet pixels could be the same temperature due to evaporative cooling. These two surfaces could change differently as time evolves.

5) *Similar ET:* This method attempts to solve the problem just discussed by finding areas of similar *ET* instead of temperature. Surfaces with similar *ET* should change similarly as time evolves. This method should more accurately find similar surfaces than using similar temperatures. It should be noted that once the similar block is found based on *ET*, the change in temperature is used for that block. This is because the change in *ET* is not known. *ET* is just used to locate the block to use for change.

6) *Similar EF:* This method is just a slight variation of Similar *ET* which uses evaporative fraction for similarity instead of *ET*.

86

In addition to data fusion techniques, simple interpolations are also used 1) Nearest Neighbor *ET* 2) Linear Interpolation of *ET* 3) Nearest Neighbor *EF* 4) Linear Interpolation of *EF*.

1) *Nearest Neighbor ET*: *ET* map which is nearest in time to the desired day is substituted for that day. This is the most simple method of all and used as a type of "sanity" check.

2) *Linear Interpolation of ET*: *ET* maps are linearly interpolated in time between the neighboring *ET* maps.

3) *Nearest Neighbor EF*: First, *EF* for desired day is determined from the nearest neighbor in time. *EF* is then multiplied by available energy of the desired day to find *ET*. The available energy for desired day is determined the same way as before with the fusion techniques except the temperature required for determining upwelling long wave is not fused. Instead, the temperature is simply linearly interpolated in time.

4) *Linear Interpolation of EF*: *EF* is linearly interpolated between neighboring *EF* maps and then multiplied by the available energy as with Nearest *EF*.

These methods are much simpler than any of the data fusion methods because they do not require an additional *ET* retrieval. They are included to determine the value of the more complicated fusion efforts which require additional higher temporal resolution data.

3.3.2 Evaluating Performance of Data Fusion Techniques

The data fusion techniques described above will be evaluated at two different scales 1) Image Scale and 2) Pixel Scale. For larger scale hydrological applications, the

Image Scale results will be of interests. For agricultural applications where individual fields are of interest, Pixel Scale results will be more pertinent.

1) Image Scale: This consists of finding the mean of the actual image retrieved and the mean of the fused image. These mean values will then be compared over time. The *Image Scale Bias* is defined as the difference between the mean *ET* of the images averaged over a time series of images. This represents the error in estimating *ET* at the image scale over longer time scales. *Image Scale MAE* is the absolute value of this difference averaged over a time series. This represents the error in estimating *ET* for the entire image at the daily time scale.

2) Pixel Scale: This refers to comparing *ET* for each individual pixel in the image in order to produce a map of *Bias* and *MAE* error. This is performed by averaging over the time series for each individual pixel. These maps can be aggregated in space in order to find the *Average Pixel Scale Bias* and the *Average Pixel Scale MAE*. The *Average Pixel Scale Bias* is the absolute value of each individual pixel's *Bias* averaged over the entire image. It should be noted that is necessary to use absolute value of the *Bias* or else the result would be identical to the *Image Scale Bias*. This is because the order of temporal vs. spatial aggregation does not matter. By taking the absolute value, the direction of the *Bias* is lost, but it still retains information about the average magnitude of an individual pixel's *Bias*. This represents the average error in estimating *ET* for an individual pixel over longer time scales. The *Average Pixel Scale MAE* is the individual pixel's *MAE* averaged over the entire image. This represents the average error in estimating *ET* for an individual pixel over daily time scales.

It is important not to include neighboring *ET* maps in the aggregations in time discussed above. If neighboring *ET* maps are included it will produce overly optimistic results. For example if the first map is created from change between first and second map and second map is created from change between second and first map, they will cancel when aggregated together to produce zero *Pixel Scale Bias*. This mutuality does not always occur but it will still happen enough to make the results appear to be too good. In order to produce more conservative results, sequences are created in which every other *ET* map in the time series is included. The result is two sequences in which the first begins with the first image and the second begins with the second image.

The temporal variability of data fusion errors was also investigated. Fused *ET* maps were compared to actual *ET* maps as a function of time. Also, the difference between the mean of *ET* maps was analyzed as a function of the time between the estimated map and the nearest neighbor (Δt_{min}). The spatial variability of the errors was also investigated by producing *Pixel Scale Bias* and *MAE* maps. The effect of these errors was realized by comparing *ET* map actually retrieved to fused *ET* maps.

4. Results and Discussion

4.1. Data Preprocessing

4.1.1 Analysis of Effects of Gaps on Calculation of Daily Averaged *EF*

Table 4.1 shows the average number of gaps along with the number of gap free days among useable clear sky scenes for each of the eddy covariance flux stations. The Disney and Big Cypress stations do not have any days that were gap free. Analysis of Disney hourly data shows that gaps systematically appear during non-daylight hours. This leaves Everglades, Gainesville and Kennedy for use in the analysis of the effect of gaps on daily *EF*. Donaldson station was chosen for further analysis because of the large number of gap free days and low average number of gaps. Everglades Short Hydro-period Marsh was chosen because it exhibited gaps in a different pattern than Donaldson as shown in Figure 4.1.1. The Short Hydro Marsh has more gaps during non-daylight hours. Figure 4.1.1 shows the probability of a gap occurring as a function of time for all of the flux data (not just useable clear sky scenes). For testing effect of gaps on daily *EF*, flux data from all days is used because it increases the number of gap free days compared to Table 4.1.1. Figure 4.1.2 shows the effect that increasing the number of gaps has on the computation of daily *EF*. This plot shows the *Bias* and *MAE* between daily *EF* calculated from fluxes with simulated gaps applied to gap free days and the actual daily *EF* for those gap free days. The manner in which the gaps are positioned is very important. This is shown by comparing the errors due to clustered gaps (green) with errors due to random gaps (blue). Random gaps do not significantly affect the results

90

until many gaps are added to the data while the clustered gaps produce large errors for a

small number of gaps. These simulations of ideal conditions can be used to describe the

nature of the actual gaps. The errors calculated using actual gaps from the data applied to

gap free days is shown in red. The plot shows that the errors using actual gaps locations

are somewhere between clustered and random for Short Marsh, but closer to clustered for

Donaldson. Also the plots shows the average number of gaps for Short Marsh to be

around 30 while average number of gaps for Donaldson to be around 15. This is

interesting because when using actual gaps (red line), both scenarios have similar *MAE* at

about 0.1. A possible explanation to this is that Donaldson has more clustered gaps. If

Donaldson was more in between clustered and random the *MAE* would be about 0.05.

Table 4.1.1: Average Number of Gaps and Gap Free Days among Useable Scenes

Study Area	Station	$\overline{N}_{gaps}$	$N_{gap\ free}$
Big Cypress	Cypress Swamp	11.5	0
Big Cypress	Dwarf Cypress	26	0
Big Cypress	Pine Upland	19.8	0
Big Cypress	Wet Prairie	27.3	0
Disney	Grassland	33.1	0
Everglades	Long Marsh	14.2	1
Everglades	Mangroves	0	3
Everglades	Short Marsh	19	1
Gainesville	Austin Cary	15.9	3
Gainesville	Donaldson	5.6	18
Gainesville	Mize	4.2	12
Kennedy	Scrub Oak	6.3	11
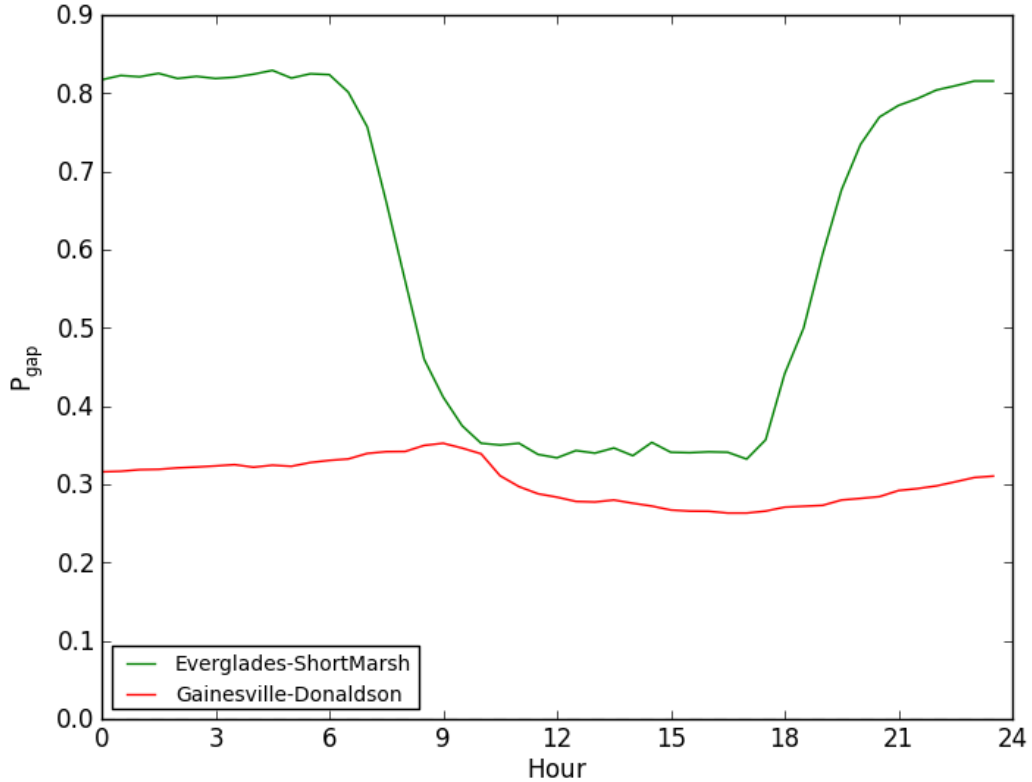
Figure 4.1.1: Probability of Gap Occurrence as Function of Time
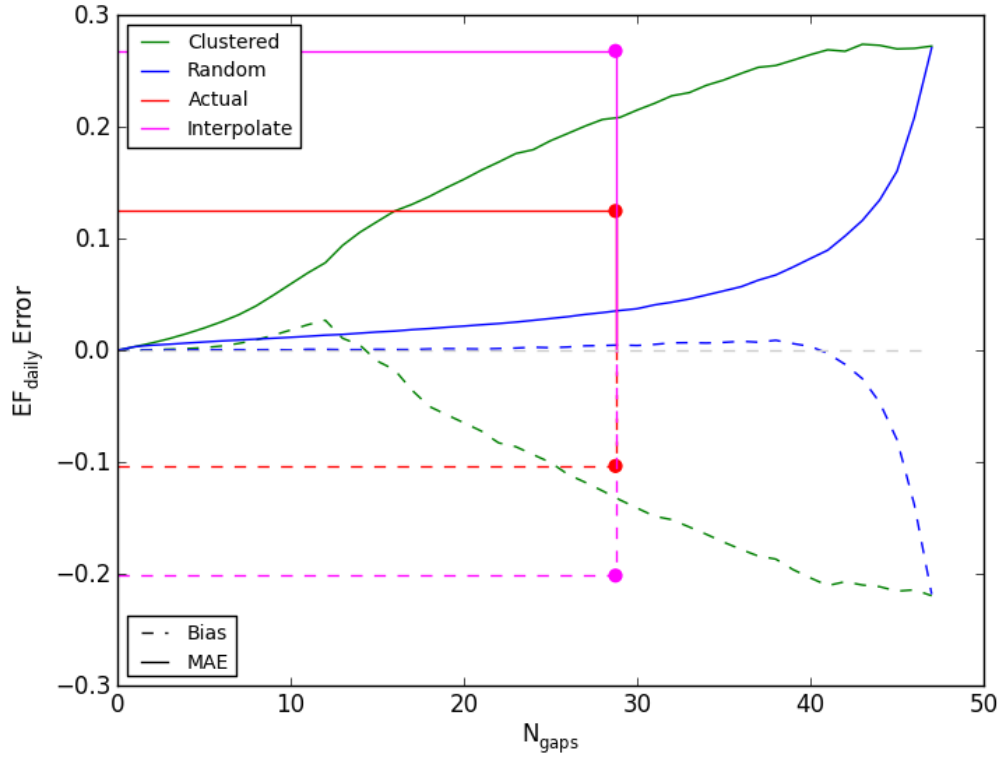
Figure 4.1.2: Effect of Gaps on EF_{daily} from Simulations for Everglades, Short Marsh
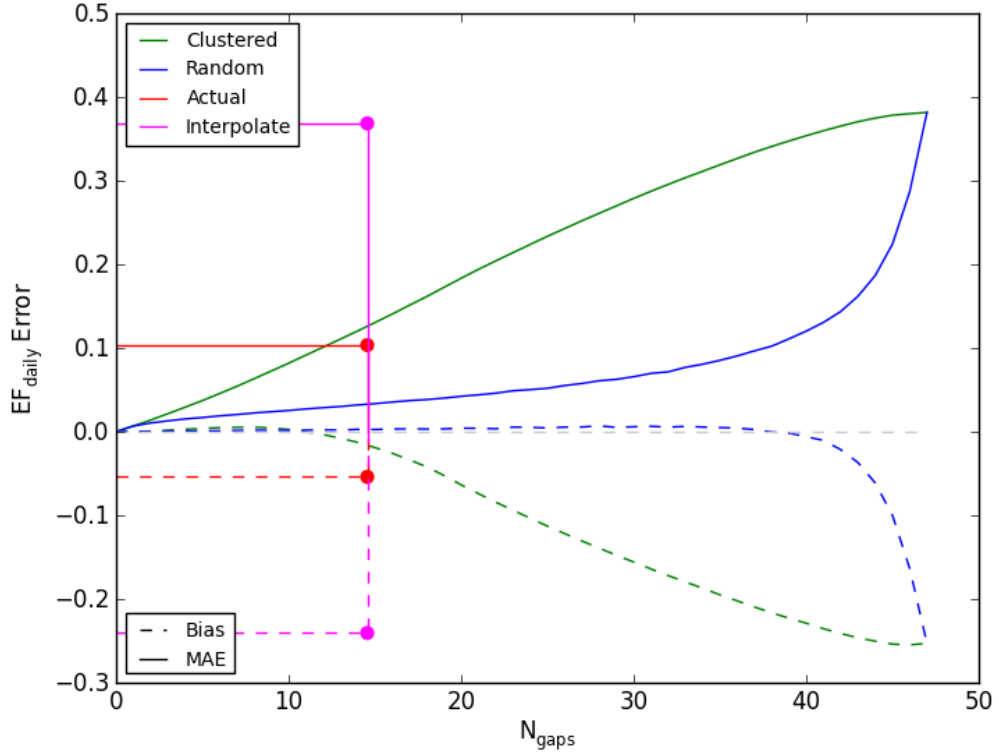
Figure 4.1.3: Effect of Gaps on EF_{daily} from Simulations for Gainesville, Donaldson

4.1.2 Analysis of Relationship between Daily EF and Satellite Overpass EF

The relationship between daily *EF* and satellite overpass *EF* was analyzed using flux data from only useable clear sky scenes and flux data from all measurement days. This could help in comparing the effect of cloudiness on the relationship. This comparison is somewhat limiting though due to the low availability of useable clear sky scenes. The relationship between daily *EF* and *EF* averaged over a window around satellite overpass was also analyzed in order to test whether window averaged *EF* could be used as proxy for daily *EF*. This could be useful because window averaged *EF* would have less of a chance of having gaps and could therefore be used to represent daily *EF* for comparison with satellite retrieved *EF*.

Table 4.1.2 shows the errors produced when comparing daily *EF* to overpass *EF* and window *EF* for gap free days among useable clear sky scenes. This shows significant *Bias* for both overpass and window *EF*. This means that using overpass or window *EF* as a proxy for daily *EF* would significantly underestimate daily *EF*. This does not seem to support the use of satellite retrieved *EF* as an estimate for daily *EF*. Figures 4.1.4 and 4.1.5 show scatter plots of daily *EF* vs. overpass and window *EF* for each study area in Table 4.1.2. These plots show that for all study areas a significant amount of variation exists among the difference between daily *EF* and overpass or window *EF*. Therefore it is not just a simple calibration between the two which could allow for correction. In order to further investigate why daily *EF* is so much larger than overpass *EF*, an extreme case which occurred on Nov 11, 2003 at Kennedy Scrub Oak was analyzed. In that case the daily *EF* = 0.85 while the overpass *EF*= 0.36. The reason the daily *EF* was so large was because a large amount of sensible heat was being supplied into the surface at night. The sensible heat that was lost to atmosphere during the day was equal to 1565 W/m^2 while

the amount of heat gained by the atmosphere during the night was equal to 1358 W/m^2. During the day the latent heat consumed by surface was 1152 resulting in only a moderate *EF* during the day equal to 0.42. During the night the latent heat at the surface is quite small and available energy lost by the surface is being resupplied by sensible heat from atmosphere. The reason the daily *EF* is so large is because the extra energy supplied at night via sensible heat from atmosphere nearly cancels that which is lost in the day. Therefore, most of the available radiation energy supplied to surface over the 24 hour cycle is being consumed by latent heat.

In order to correct for the problem just described, the correction using equation 3.1.3 was used to find a corrected overpass *EF*. As shown in Table 4.1.2, this correction cut the *Bias* and *MAE* in half for Everglades. For Gainesville and Kennedy it was more effective in reducing bias but only reduced *MAE* minimally. Figure 4.1.6 shows a scatter plot of the improvements due to the correction. Also reported in Table 4.1.2 are reductions in *Bias* and *MAE* when the corrected overpass *EF* was now being compared to the daily *EF* calculated using the alternate method consisting of correcting fluxes using equation 3.1.1 at each time step before summing. Everglades was not affected by this modification, but Gainesville and Kennedy were affected. This change is reflected in scatter plot shown in Figure 4.1.7. The effect of the differences in daily and overpass *EF* would have on the resulting actual daily *ET* in mm is also shown in Table 4.1.2. Figure 4.1.8 shows daily *ET* vs. overpass *ET* and 4.1.9 shows alternate daily *ET* vs. corrected overpass *ET*. In these figures the reduction in scatter using the alternate daily *ET* and corrected overpass *EF* is very evident. These results would suggest that correcting the overpass *EF* would increase the ability for overpass *EF* to estimate daily *ET*. It was not

95

intended that the inclusion of the alternate daily *EF* and *ET* calculation would determine

whether it was a better estimate. It was included in order to demonstrate that some of the

difference between overpass and original daily *EF* is due to problems with calculating

daily *EF* due to energy balance closure problems.

Table 4.1.2: *Bias* and *MAE* Errors between Daily *EF* and Overpass or Window *EF*
For Gap Free Days among Useable Clear Sky Scene

Study Area	Comparison	Bias	MAE	Bias (mm)	MAE (mm)
Everglades	EF_{daily} vs. $EF_{overpass}$	0.209	0.209	1.144	1.144
Everglades	EF_{daily} vs. EF_{window}	0.192	0.192	1.036	1.036
Everglades	EF_{daily} vs. $EF_{Acorrected}$	0.101	0.125	0.537	0.694
Everglades	$EF_{daily\ alternate}$ vs. $EF_{Acorrected}$	0.106	0.121	0.535	0.645
Gainesville	EF_{daily} vs. $EF_{overpass}$	0.115	0.127	0.488	0.57
Gainesville	EF_{daily} vs. EF_{window}	0.107	0.12	0.462	0.543
Gainesville	EF_{daily} vs. $EF_{Acorrected}$	0.069	0.115	0.268	0.526
Gainesville	$EF_{daily\ alternate}$ vs. $EF_{Acorrected}$	0.05	0.094	0.176	0.43
Kennedy	EF_{daily} vs. $EF_{overpass}$	0.118	0.125	0.47	0.518
Kennedy	EF_{daily} vs. EF_{window}	0.123	0.127	0.496	0.52
Kennedy	EF_{daily} vs. $EF_{Acorrected}$	0.076	0.098	0.28	0.401
Kennedy	$EF_{daily\ alternate}$ vs. $EF_{Acorrected}$	0.043	0.061	0.151	0.266
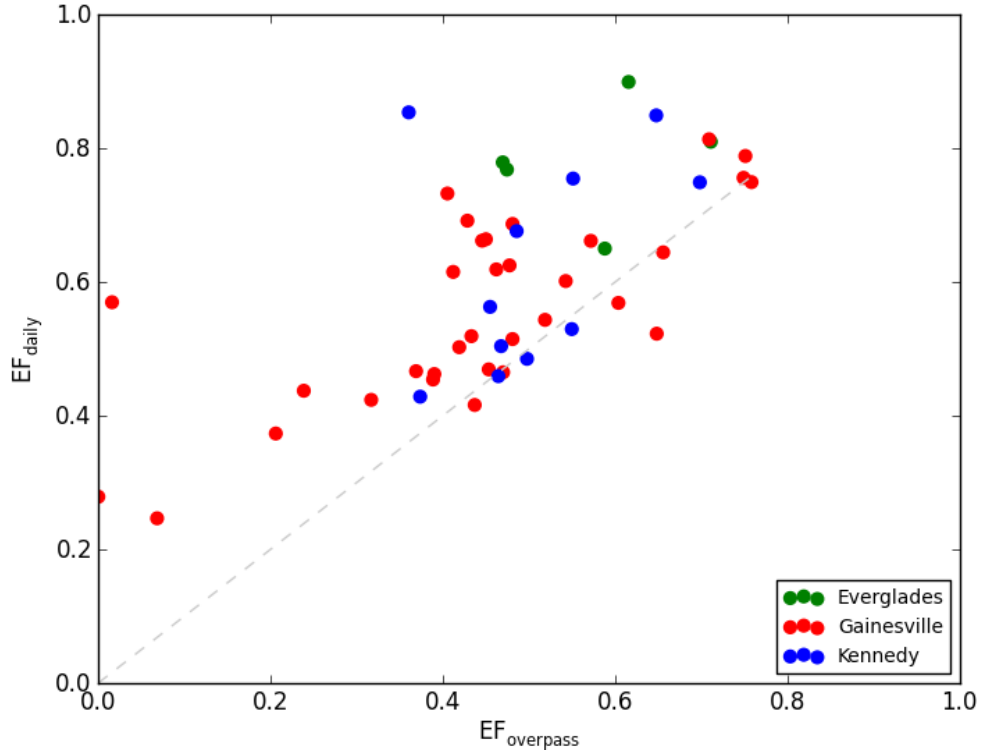
Figure 4.1.4: Study Area Plot of EF_{daily} vs. $EF_{overpass}$ on Gap Free Useable Clear Sky Days
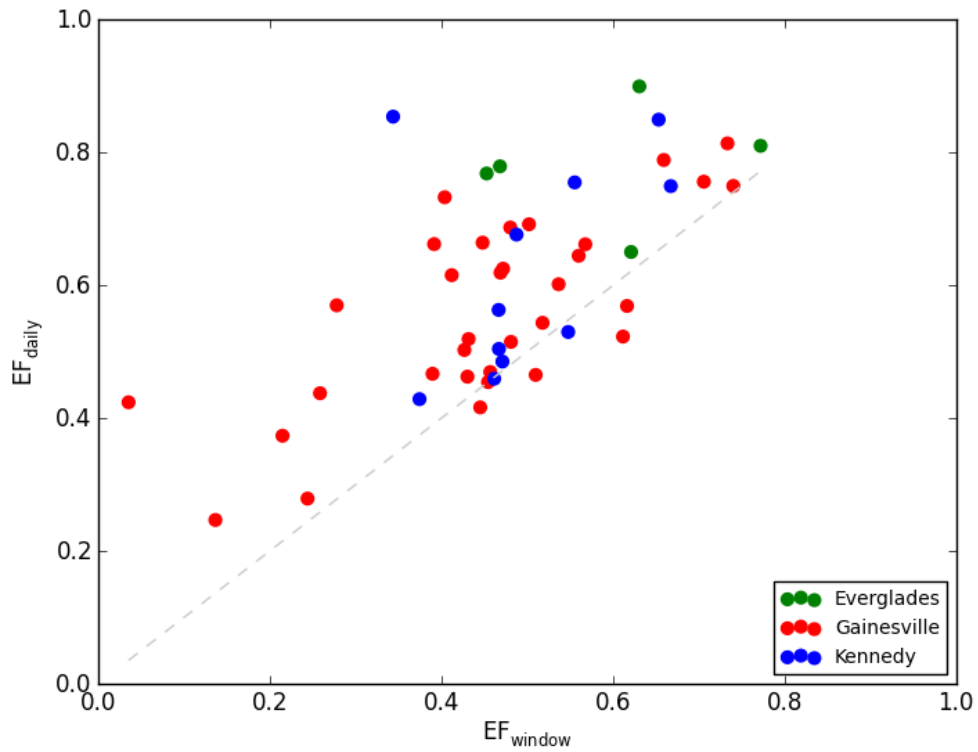
Figure 4.1.5: Study Area Plot of EF_{daily} vs. EF_{window} on Gap Free Useable Clear Sky Days
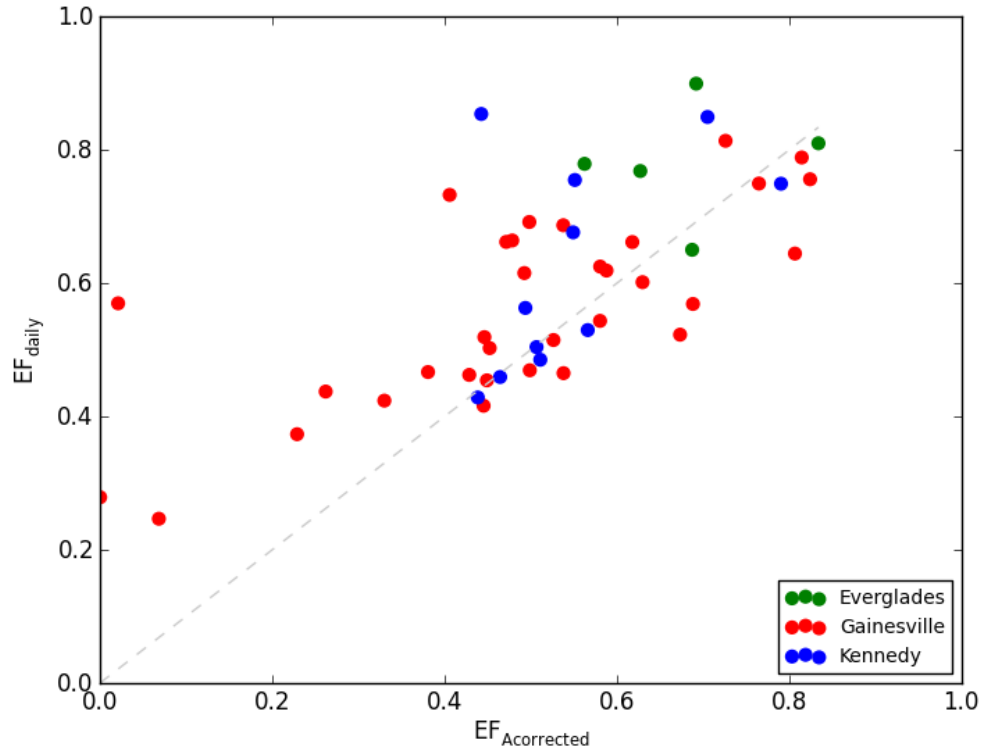
Figure 4.1.6: Study Area Plot of EF_{daily} vs. $EF_{corrected}$ on Gap Free Useable Clear Sky Days
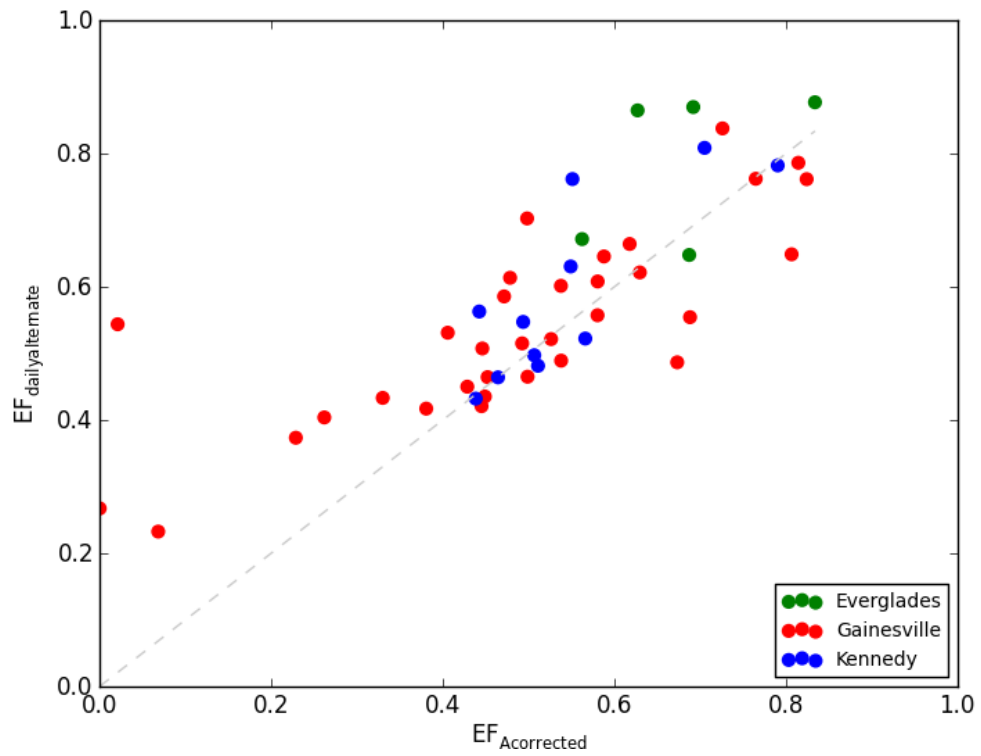
Figure 4.1.7: Alternate EF_{daily} vs. $EF_{corrected}$ on Gap Free Useable Clear Sky Days
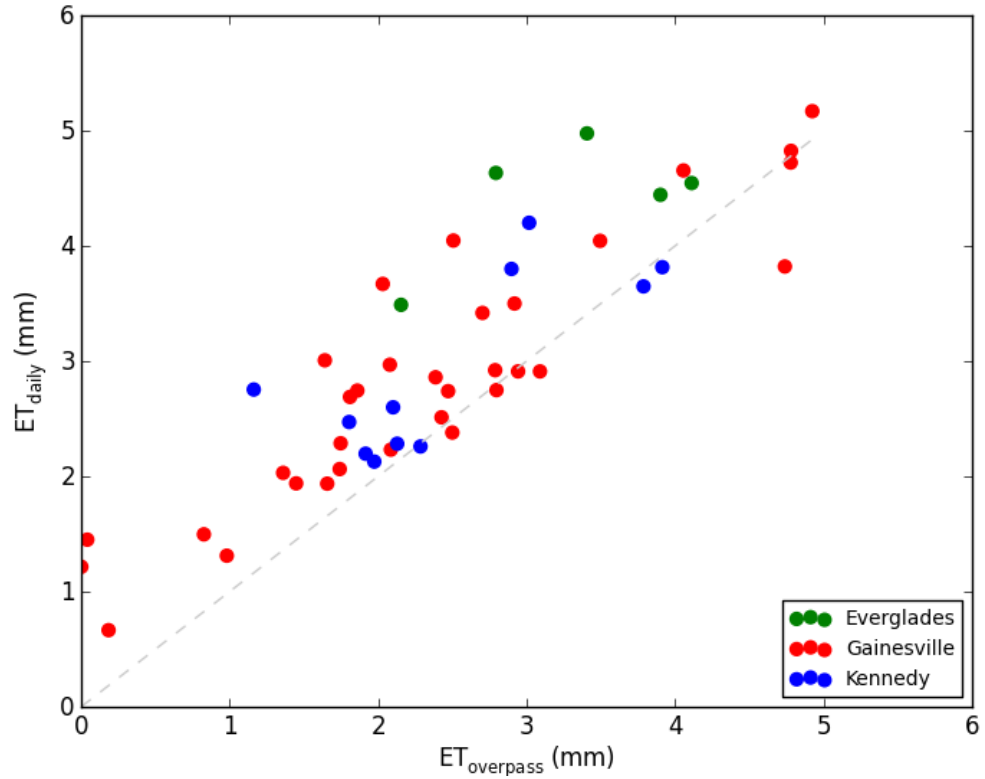
Figure 4.1.8: Study Area Plot of ET$_{daily}$ vs. ET$_{overpass}$ on Gap Free Useable Clear Sky Days
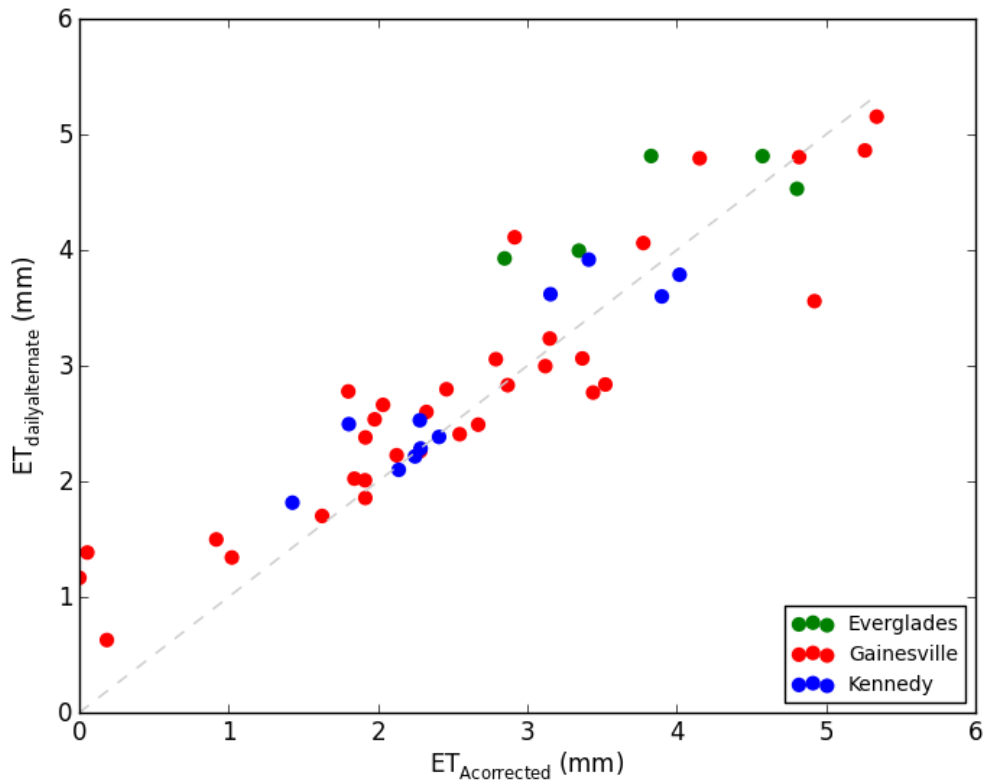
Figure 4.1.9: Alternate ET$_{daily}$ vs. ET$_{corrected}$ on Gap Free Useable Clear Sky Days

Next the relationship between daily *EF* and overpass *EF* or window *EF* is analyzed using all available flux measurements. Because only 6 gap free days existed for Short Marsh Everglades, only the results for Donaldson are reported. Table 4.1.3 shows the *Bias* and *MAE* errors broken up seasonally. This shows that summer and spring seem to produce the best relationships. In this case spring looks even a bit better than summer which could be due to the increased presence of clouds in summer which should limit the relationship. Figure 4.1.10 shows a scatter plot of daily *EF* to overpass *EF* grouped by season for Donaldson. These figures show lots of scatter for all seasons although winter and fall seem to have more extreme cases. The total *Bias* = 0.161 and *MAE* = 0.236 for daily *EF* vs. overpass *EF*. This is much larger than the *Bias* = 0.115 and *MAE* = 0.127 for Gainesville during useable clear sky days. Figure 4.1.11 show the scatter plots of the daily *EF* to overpass *EF* of all useable clear sky scenes which are colored by season. This plot seems to suggest that there is a better relationship between daily *EF* and overpass *EF* during the summer but spring is fairly close also. This comparison is not very robust though due to the limited amount of summer data points.

Table 4.1.3: Seasonal *Bias* and *MAE* Errors between EF_{daily} and $EF_{overpass}$ or EF_{window} For Gap Free Days among All Available Donaldson Flux Measurements

StudyArea	Station	Season	Comparison	Bias	MAE
Gainesville	Donaldson	Winter	EF_{daily} vs. $EF_{overpass}$	0.2381	0.2537
Gainesville	Donaldson	Winter	EF_{daily} vs. EF_{window}	0.2448	0.2505
Gainesville	Donaldson	Spring	EF_{daily} vs. $EF_{overpass}$	0.0827	0.112
Gainesville	Donaldson	Spring	EF_{daily} vs. EF_{window}	0.0934	0.1042
Gainesville	Donaldson	Summer	EF_{daily} vs. $EF_{overpass}$	0.1143	0.1251
Gainesville	Donaldson	Summer	EF_{daily} vs. EF_{window}	0.1175	0.1226
Gainesville	Donaldson	Fall	EF_{daily} vs. $EF_{overpass}$	0.1719	0.1831
Gainesville	Donaldson	Fall	EF_{daily} vs. EF_{window}	0.181	0.1848
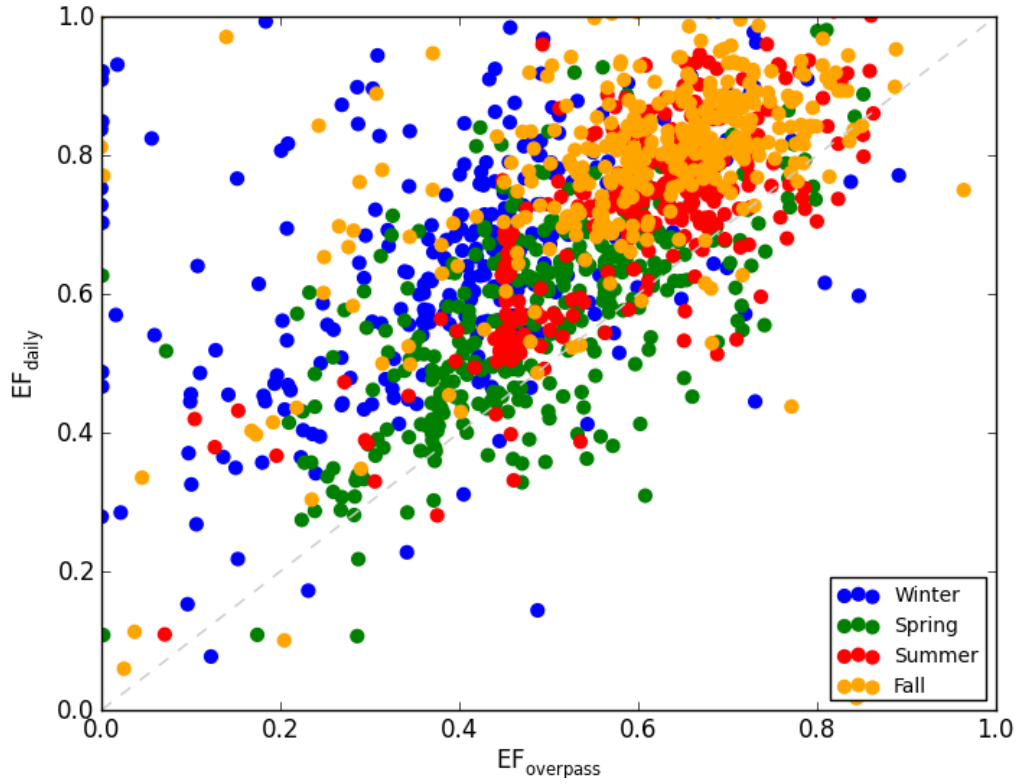
Figure 4.1.10: Seasonal *EF*_{daily} vs. *EF*_{overpass} on All Gap Free Days for Donaldson
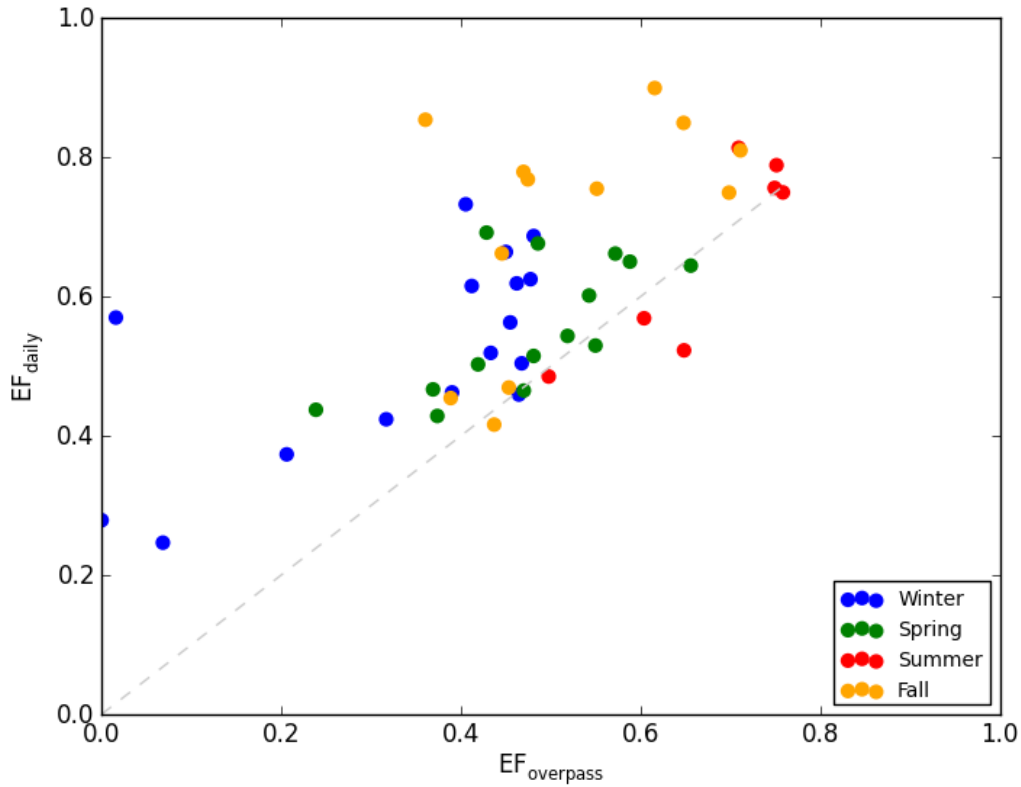
Figure 4.1.11: Seasonal *EF*_{daily} vs. *EF*_{overpass} on All Gap Free Useable Clear Sky Days

This comparison was intended to be used to test the effect of cloudy skies on the errors. This could possibly support the idea that more clouds would decrease the relationship between daily *EF* and overpass *EF*. On the other hand the sample of cloud free days is small and more cloud free days would need to be collected in order to produce more robust results. Similar to the clear sky data, this data also does not support the use of window *EF* or satellite retrieved *EF* as a proxy for daily *EF*. A better solution would be to apply satellite retrieved *EF* to the period when available energy is positive during the day, and then set *ET* equal to zero during the night when calculating a daily *ET* value.

4.2 Validation of Dry Pixel Calibration

Bias and *MAE* produced from comparing retrieved *EF* to eddy covariance *EF* is shown in Figure 4.2.1. The *Bias* and *MAE* errors for every study area are shown as a function of model and boundary variation. The *ΔT* vs. *T* model performed the best based for all study areas except Big Cypress. For Big Cypress the *H* vs. *T* model worked the best. Based on *MAE*, the Disney study area appears to work similar for *ΔT* vs. *T* regardless of whether neutral conditions are assumed, but neutral conditions actually produce a negative correlation between observed and predicted. It is also interesting to note that while Disney has the second lowest *MAE* it has a very low correlation. The Even Bins Threshold Fit boundary variation is generally the best method for all model variations. For the optimal model variation of each study area Even Bins Threshold Fit is the best method for all study areas. It should also be noted that cloud filtering was applied to all cases and albedo filtering was applied to the Kennedy and Everglades study areas. Table 4.2.1 reports the optimal model and boundary variation and associated statistics for

each study area. The results for the Homestead and Mangroves study areas which are

inside the Everglades study area are also shown. A detailed analysis of the results for

each study area follows.
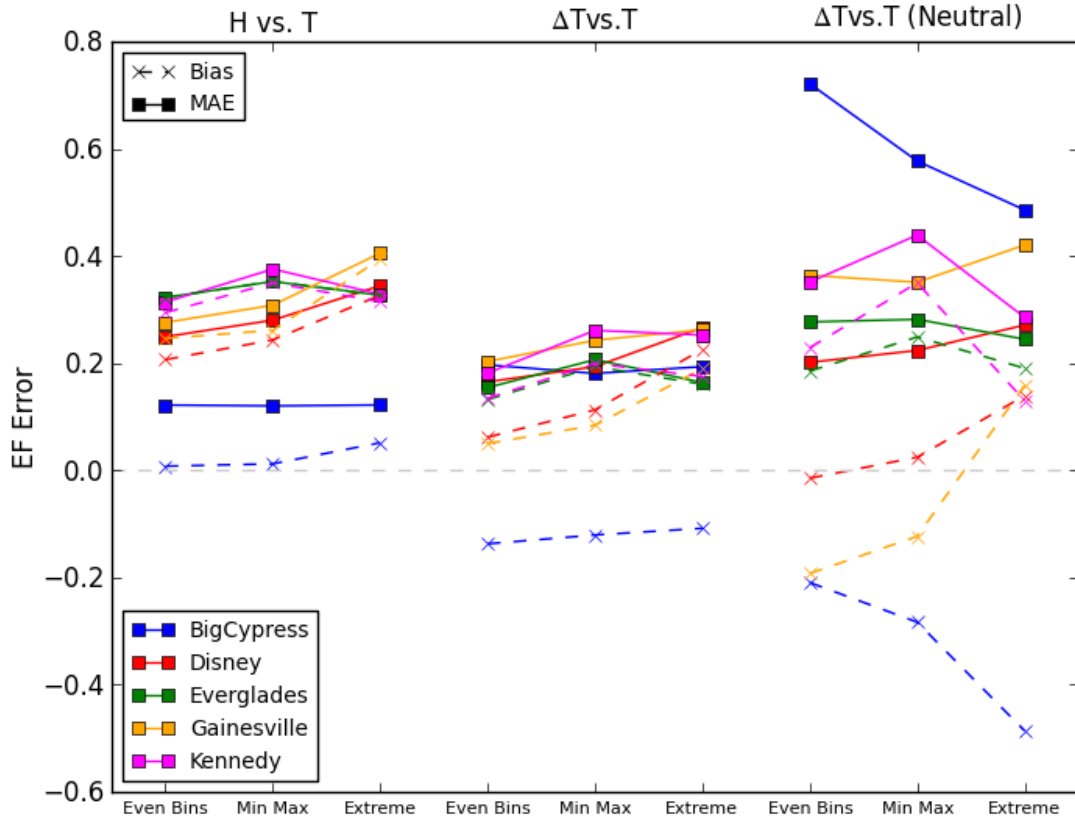
Figure 4.2.1: *EF Bias* and *MAE* **vs. Model and Boundary Variations for each Study Areas**

Table 4.2.1: Optimal Model and Boundary Variations for each Study Area

Study Area	Model	Boundary	α Filter	Bias	MAE	MAD	ρ	N
BigCypress	H vs. T	Even Bins		0.022	0.114	0.114	0.442	14
Disney	ΔT vs. T	Even Bins		0.062	0.165	0.154	-0.045	21
Everglades	ΔT vs. T	Even Bins	Yes	0.132	0.154	0.128	0.683	10
Gainesville	ΔT vs. T	Even Bins		0.05	0.203	0.199	0.2	65
Kennedy	ΔT vs. T	Even Bins	Yes	0.134	0.181	0.151	0.48	24

4.2.1 Big Cypress Dry Pixel Validation

Figure 4.2.2 shows the relationship between *EF* retrieved from satellite and tower *EF* for the optimal variation from Table 4.2.1 consisting of *H* vs. *T* model and Even Bins boundary variation. Excluding the minimum and maximum *EF* tower points, the range of retrieved *EF* is about 0.2 while the range of tower *EF* is about 0.4. Figure 4.2.3 shows the results for the *ΔT* vs. *T* model and Even Bin Threshold Fit. This model is capable of producing more of a range in *EF* retrieved values, but it also severely underestimates *EF* at times. This leads to a higher *MAE* and *Bias* error compared to *H* vs. *T* model. Figure 4.2.4 shows the variation of the difference between retrieved *EF* and tower *EF* vs. time. 9 out of the 14 validation points are within +/- 0.1 *EF*. The 2 largest residual are on Feb 8, 2010 at the Pine Upland station when *EF* was abnormally small and Oct 19, 2009 at the Dwarf Cypress station when *EF* was abnormally high. On Oct 19, 2009 the Cypress Swamp *EF* measurement drastically reduced by -0.25 *EF* compared to Oct 3, 2009. The scene with the lowest errors on average was April 23, 2008 in which all of the residuals were within +/- 0.1 *EF*. The scene with the highest errors on average was Oct 19, 2009. Figure 4.2.5 shows the plot of available energy vs. temperature for the best case scenario on April 23, 2008 using Even Bins Threshold Fit. This plot demonstrates the method for detecting the dry pixel calibration points which are shown as the black points on the bottom boundary. The red points are the validation sensible heat values from towers which come close to the fit of the sensible heat vs. temperature relationship determined from calibration points. The geographical location of the calibration points within the study area is shown on Figure 4.2.7. The majority of the points are located at the airport but there are also points at areas that were determined to be cleared out using Google

Maps. Figure 4.2.7 shows the plot of available energy vs. temperature for the worst case scenario on October 19, 2009. The reason the algorithm does so poorly on this day could be because of the large range of sensible heat and *EF* values. It is very possible that this range of values could be due to problems with the eddy covariance measurements on this day.
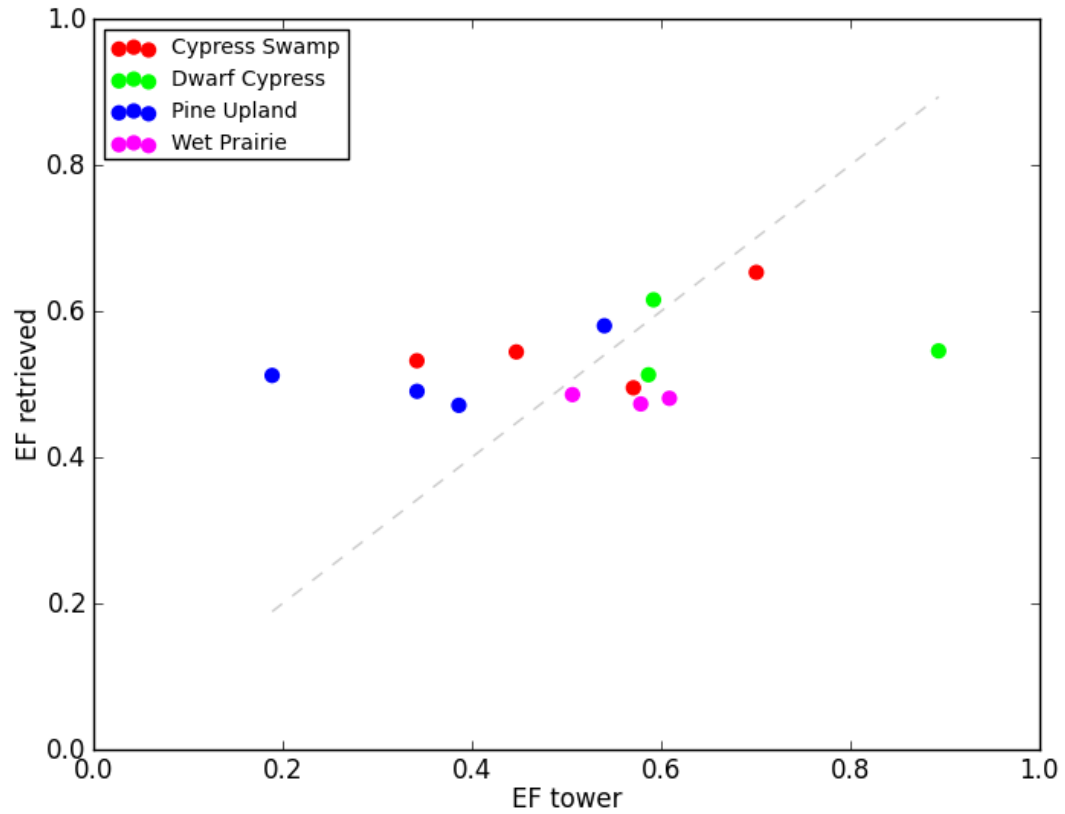
Figure 4.2.2: *EF* **retrieved vs.** *EF* **tower for Big Cypress Optimal Variation**
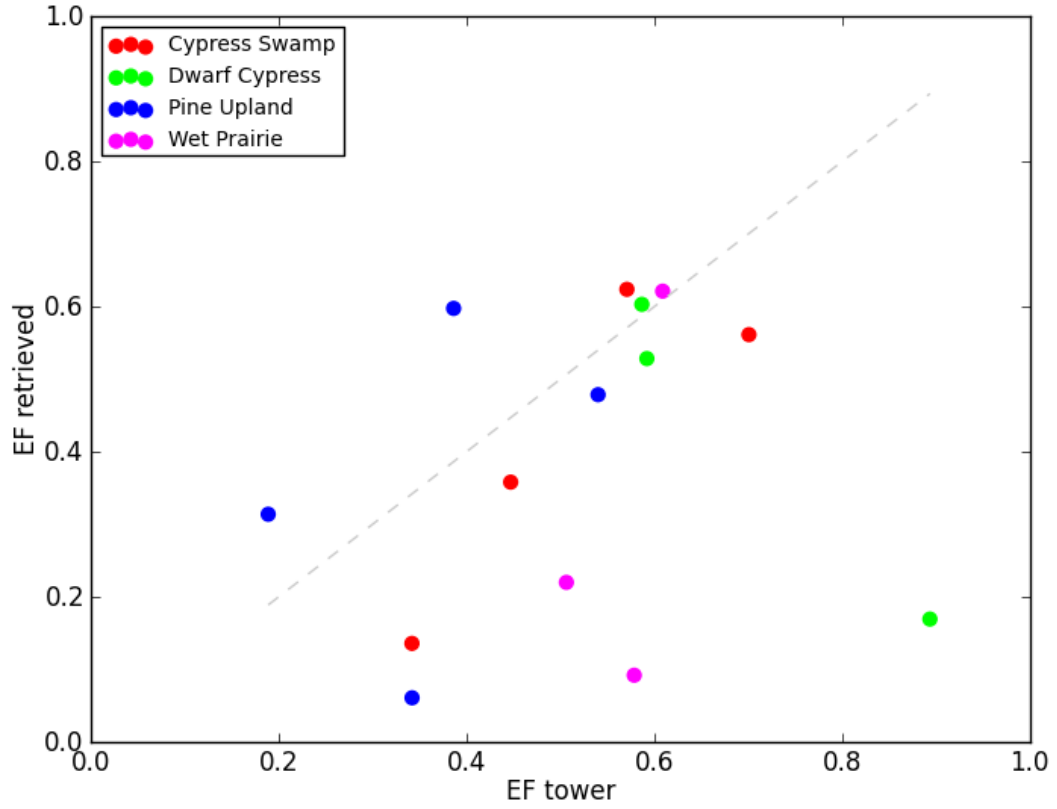
Figure 4.2.3: *EF* retrieved vs. *EF* tower for Big Cypress *ΔT* vs. *T* Model
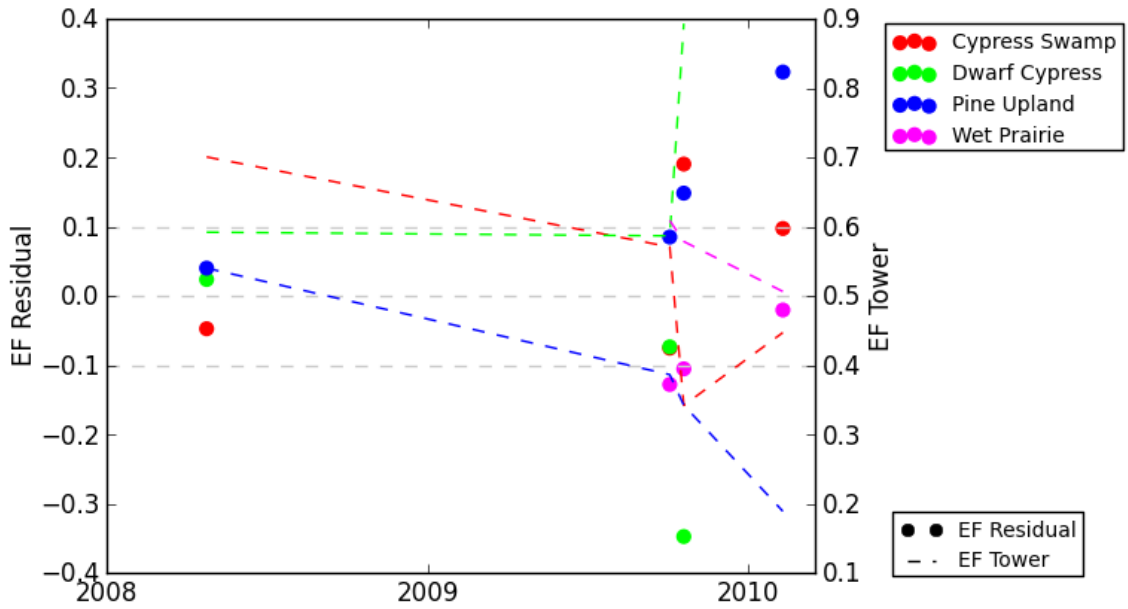
Figure 4.2.4: *EF* residual and *EF* tower vs. Year for Big Cypress Optimal Variation

106
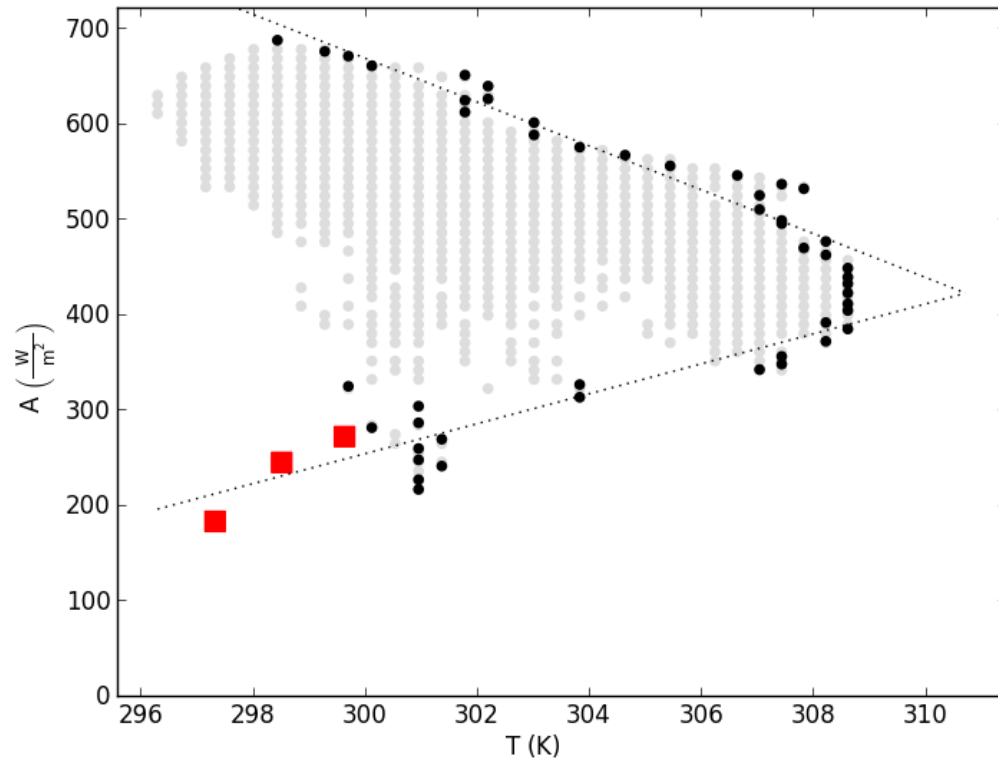
Figure 4.2.5: Available Energy vs. Temperature for Big Cypress on April 23, 2008
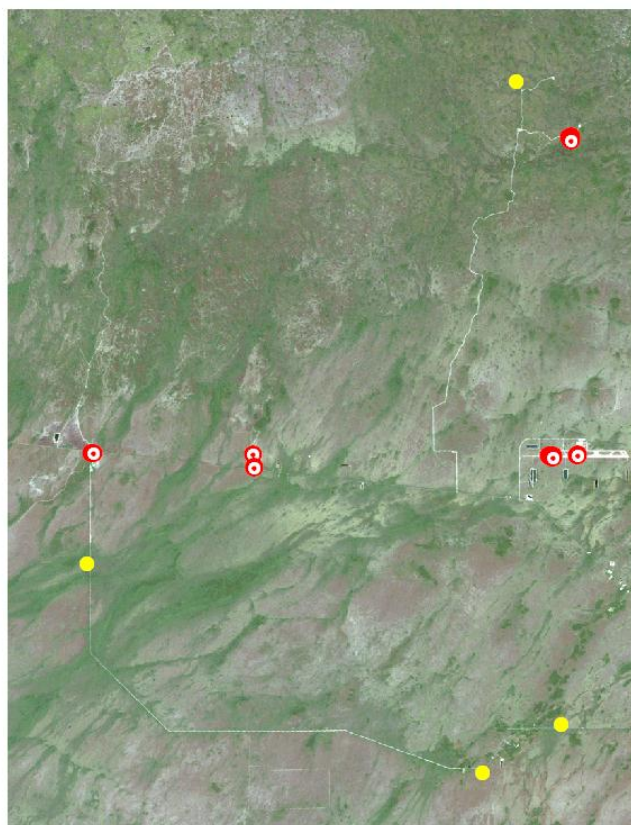
Figure 4.2.6: Automatically Detected Calibration Points on April 23, 2008

107
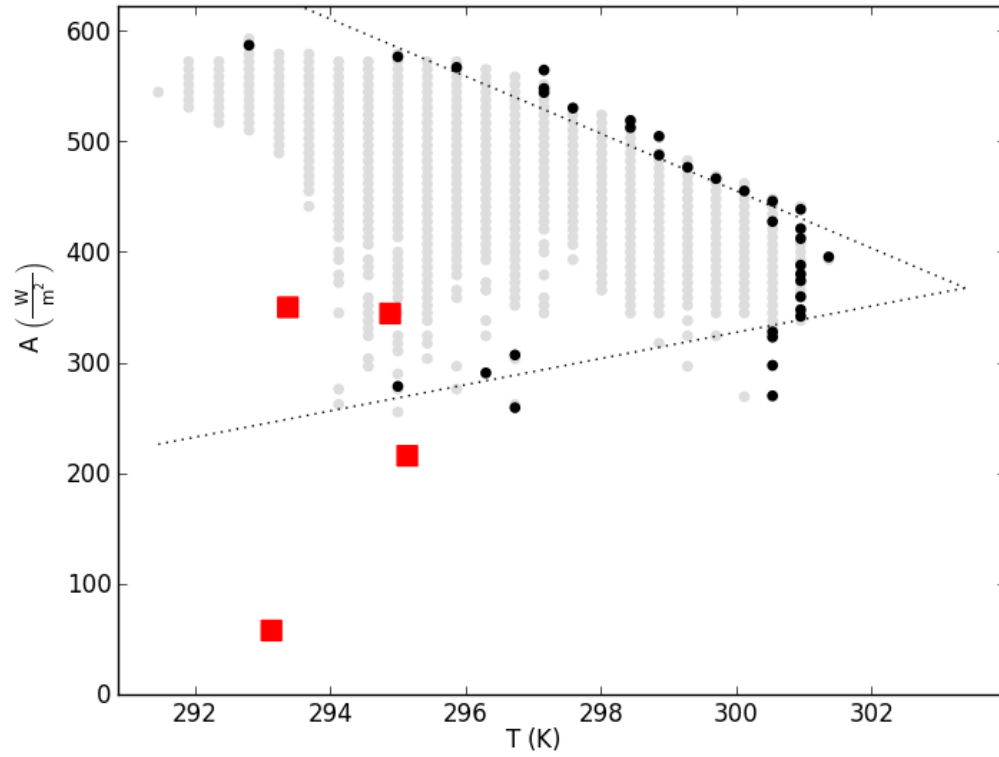
Figure 4.2.7: Available Energy vs. Temperature for Big Cypress on October 19, 2009

4.2.2 Disney Wilderness Preserve Dry Pixel Validation

Figure 4.2.8 shows the relationship between retrieved *EF* from satellite and tower

EF for optimal variation in Table 4.2.1. When tower *EF* is less than 0.3 the algorithm

overestimates *EF* but when tower *EF* is more than 0.6 the algorithm underestimates *EF*.

As noted earlier when examining Figure 4.2.1, the *ΔT* vs. *T* neutral case appeared to have

errors similar to the optimal case. Figure 4.2.9 demonstrates that this result is misleading

due to the negative correlation (R=-0.551) between retrieved *EF* and tower *EF*. Figure

4.2.9 shows the residuals of *EF* vs. time along with tower *EF* for each season. 9 out of the

21 validation points have an *EF* residual greater than +/- 0.1. Winter, spring and fall

scenes produced 1/2, 3/8 and 1/3 of their residuals outside of the +/- 0.1 window

respectively. Because of the small number of validation points it is difficult to judge any

one season to be any better than any other.
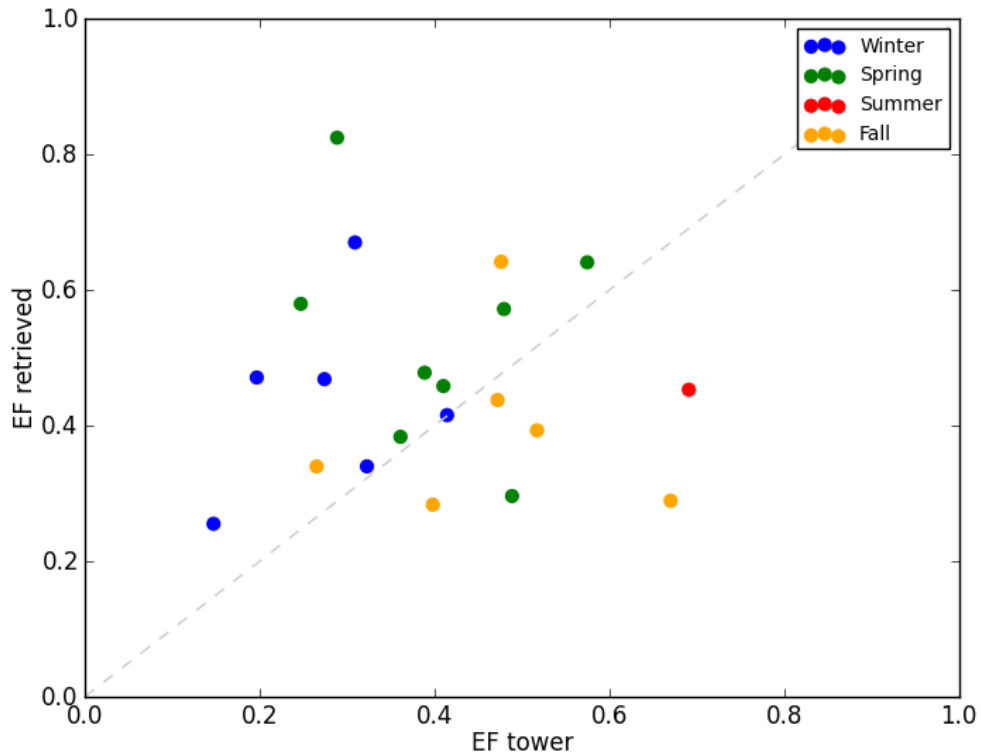
Figure 4.2.8: *EF* retrieved vs. *EF* tower for Disney Optimal Variation
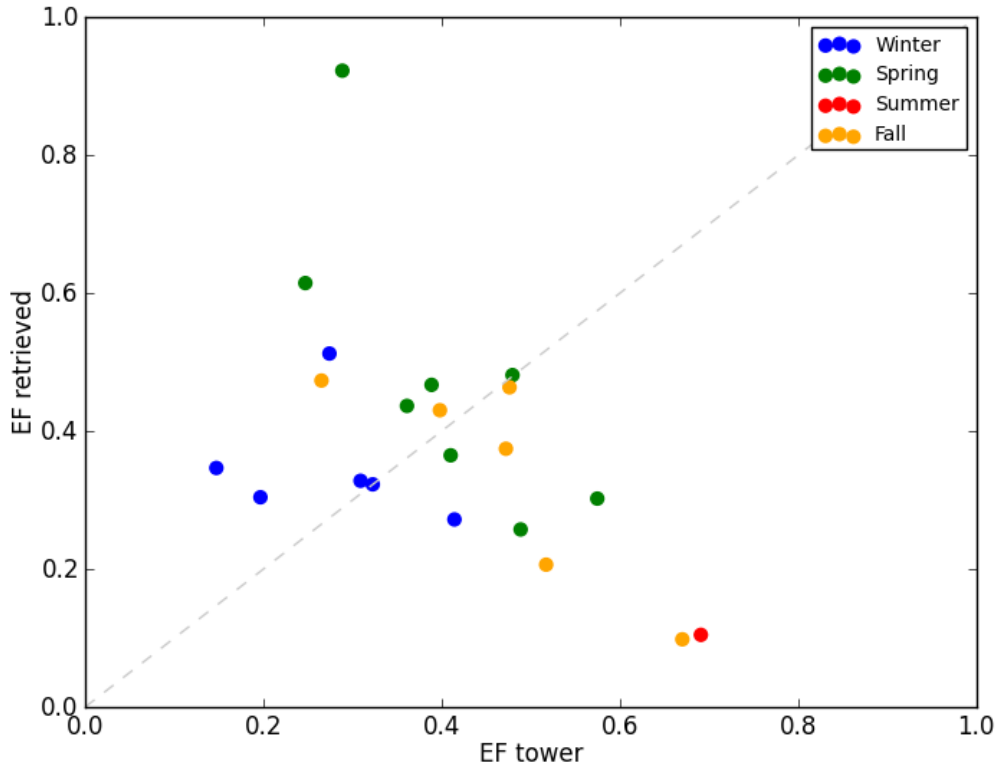
Figure 4.2.9: *EF* retrieved vs. *EF* tower for Disney *ΔT* vs. *T* neutral
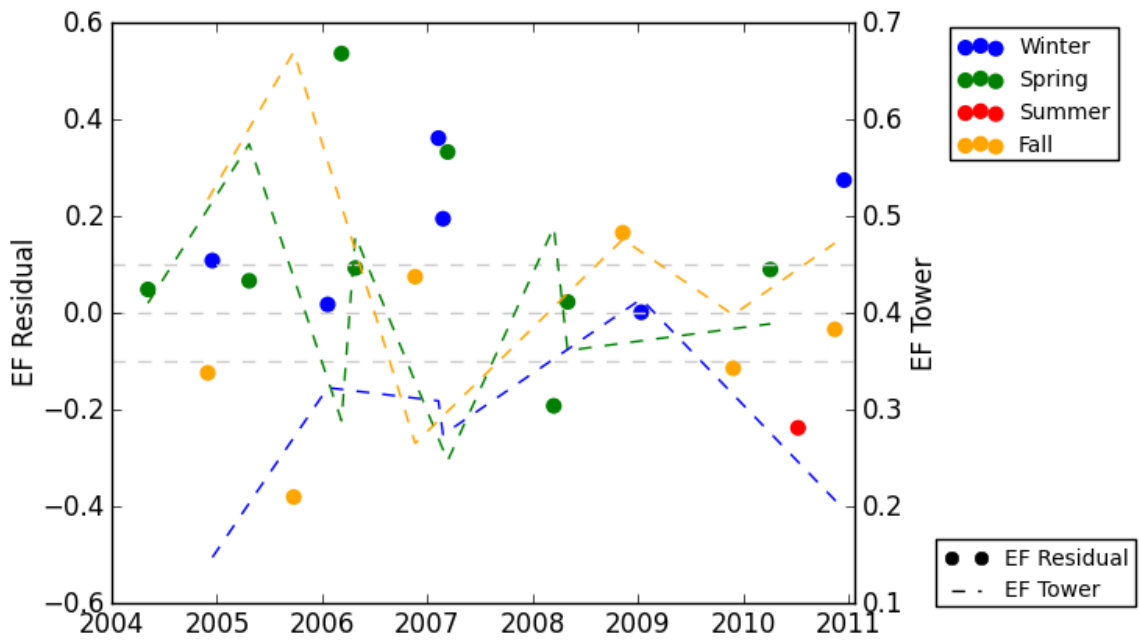
Figure 4.2.10: *EF* residual and *EF* tower vs. Year for Disney Optimal Variation

For the Disney study area, two variations of the extent were considered. The first extent was much smaller and did not include the developed area to the west. The second extent was larger and included the developed area. The increase in the size of the extent and inclusion of the developed area had a large impact on the calibration results. Figure 4.2.11 and 4.2.12 shows plots of ΔT_{dry} vs. T for both extents on April 30, 2008. For the small extent there are apparently not any dry pixels available because ΔT_{dry} vs. T lower boundary was much larger than the validation point shown on Figure 4.2.11. If the lower boundary pixels are not dry then ΔT_{dry} is not equal to actual ΔT as assumed in the algorithm. The true dry lower boundary would be 1-*EF* time the predicted boundary. Figure 4.2.12 shows the results for the larger extent where dry pixels exist. Now the validation point agrees with the predicted boundary because of the introduction of the developed area to the west which apparently contains dry pixels. Figure 4.2.13 shows the geographical location of the automatically detected calibration points for both extents. It shows that none of the points considered dry when using the small extent were considered dry when using the large extent. Most of the actual dry pixels on the image were located in the developed area in the western part of study area. For the remainder of the analysis the Disney study area is chosen to be that with the larger extent.
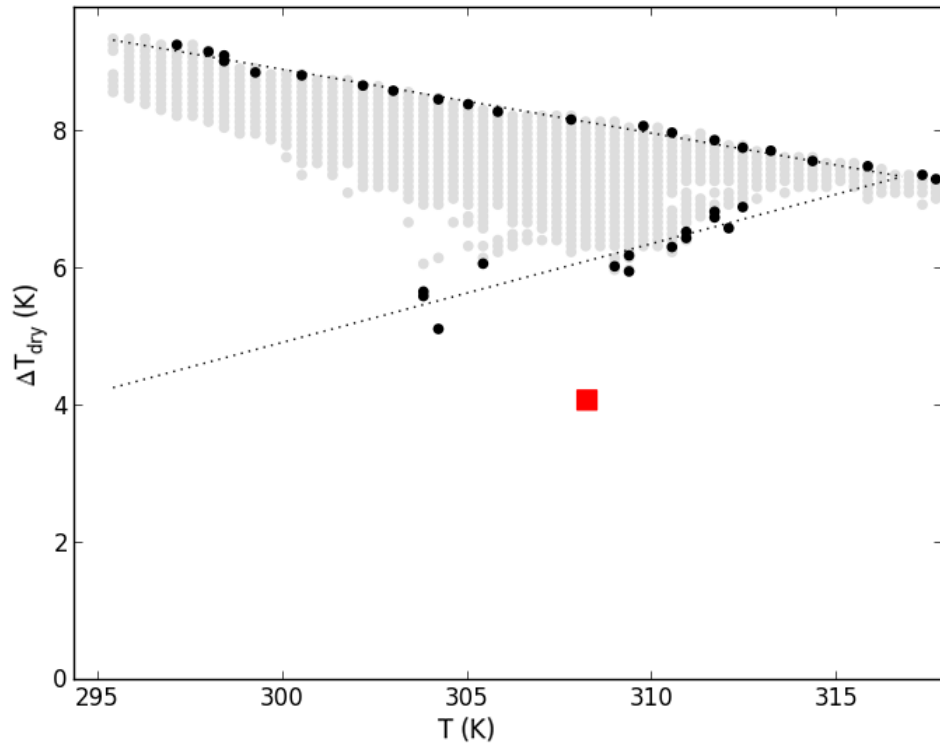
Figure 4.2.11: ΔT$_{dry}$ vs. Temperature for Small Extent Disney on April 30, 2008
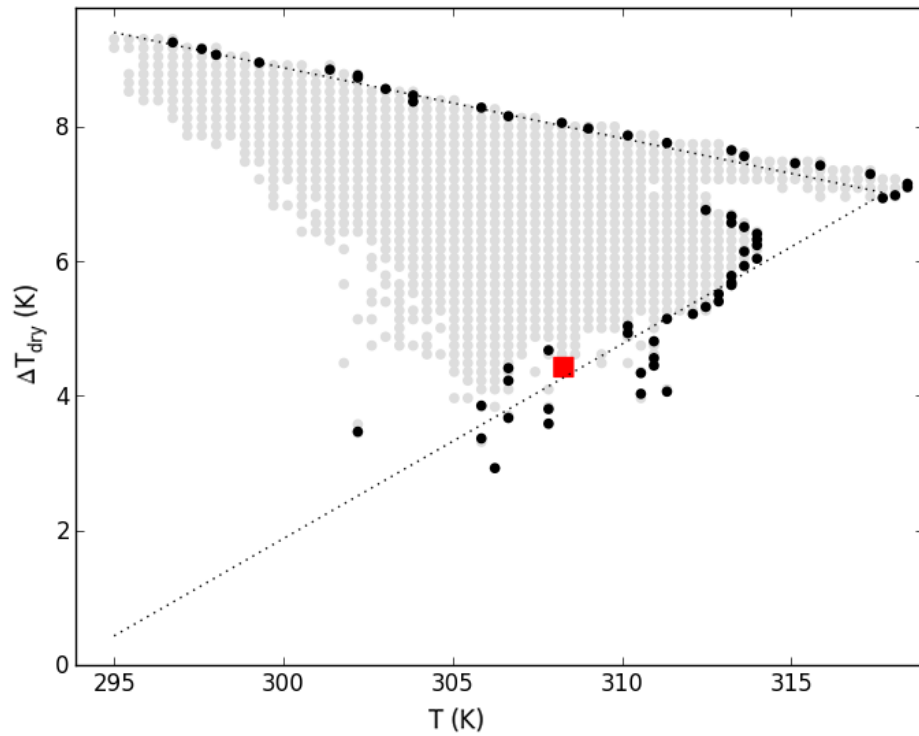
Figure 4.2.12: ΔT$_{dry}$ vs. Temperature for Large Extent Disney on April 30, 2008
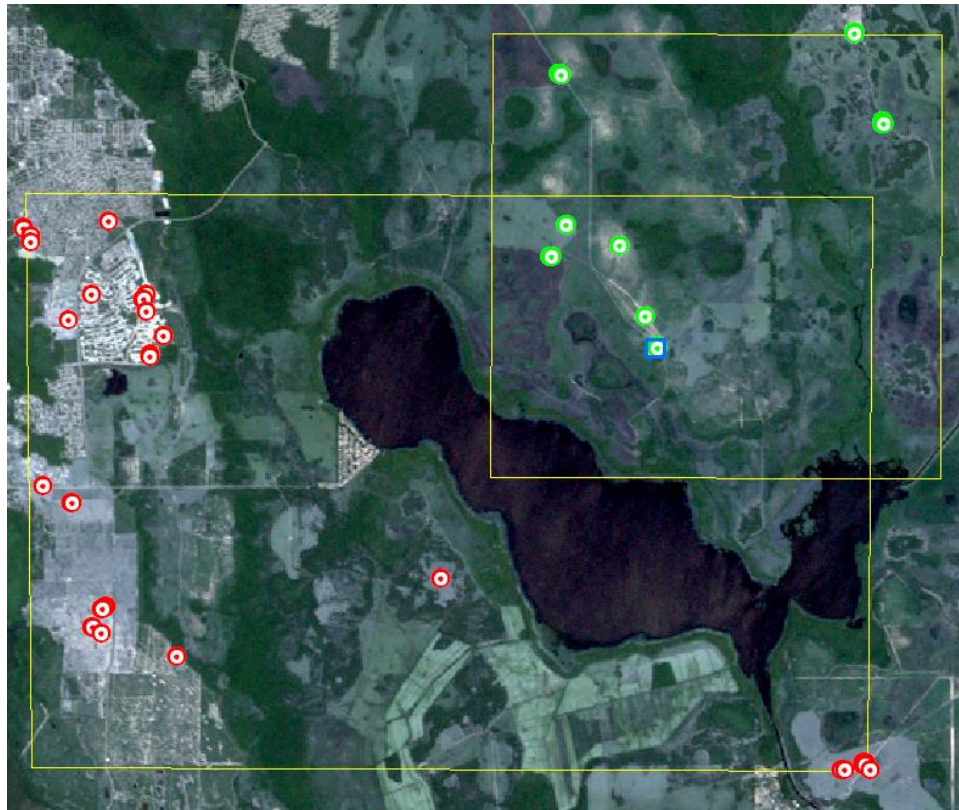
Figure 4.2.13: Automatically Detected Calibration Points for Disney on April 30, 2008

4.2.3 Everglades Dry Pixel Validation

Figure 4.2.14 shows the results of Everglades study area when the entire

Everglades extent is used for calibration. In this case the optimal variation was ΔT vs. T

with Even Bin Threshold Fit and albedo filtering. Filtering albedo improved *Bias*/*MAE*

from 0.227/0.231 to 0.132/0.154. Figure 4.2.15 shows the difference between retrieved

and tower *EF* vs. year in which 6 out of 10 scenes have error within +/- 0.1 *EF*. The

reason for the increase in accuracy after filtering albedo is shown in Figures 4.2.16 and

4.2.17. When large albedo surfaces are allowed it results in very low ΔT_{dry} lower

boundary values which underestimates sensible heat with respect to validation points in

red. Figure 4.2.17 demonstrates the manner in which the removal of the high albedo

surfaces alters the lower boundary.
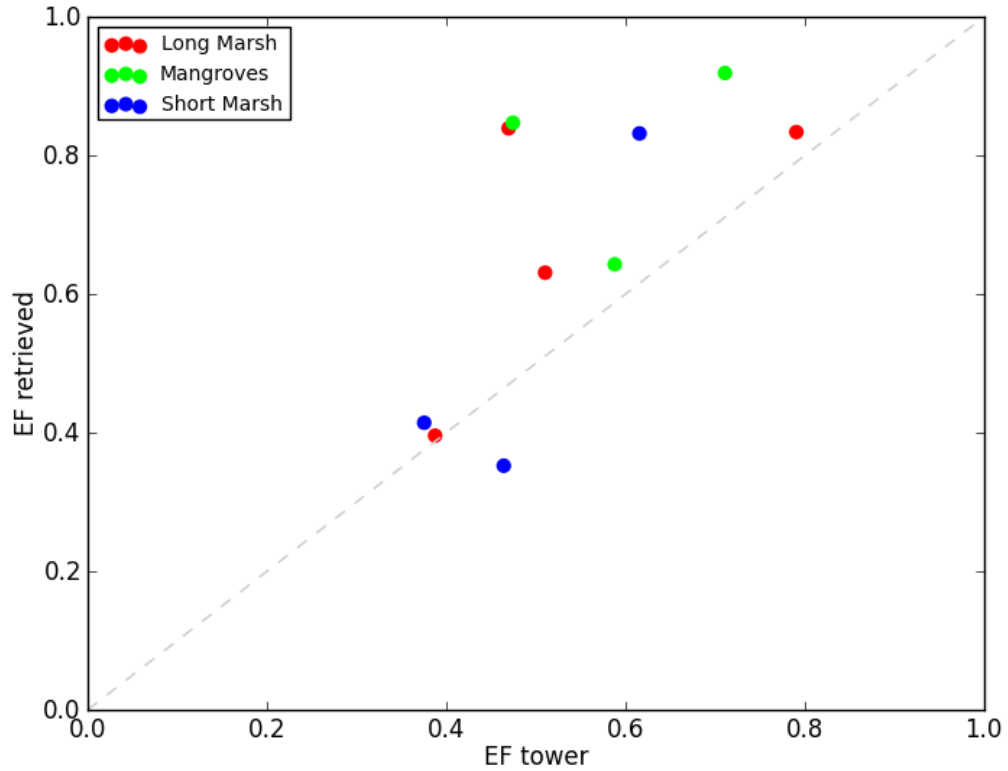
Figure 4.2.14: Optimal *EF* retrieved vs. *EF* tower for Everglades Full Extent
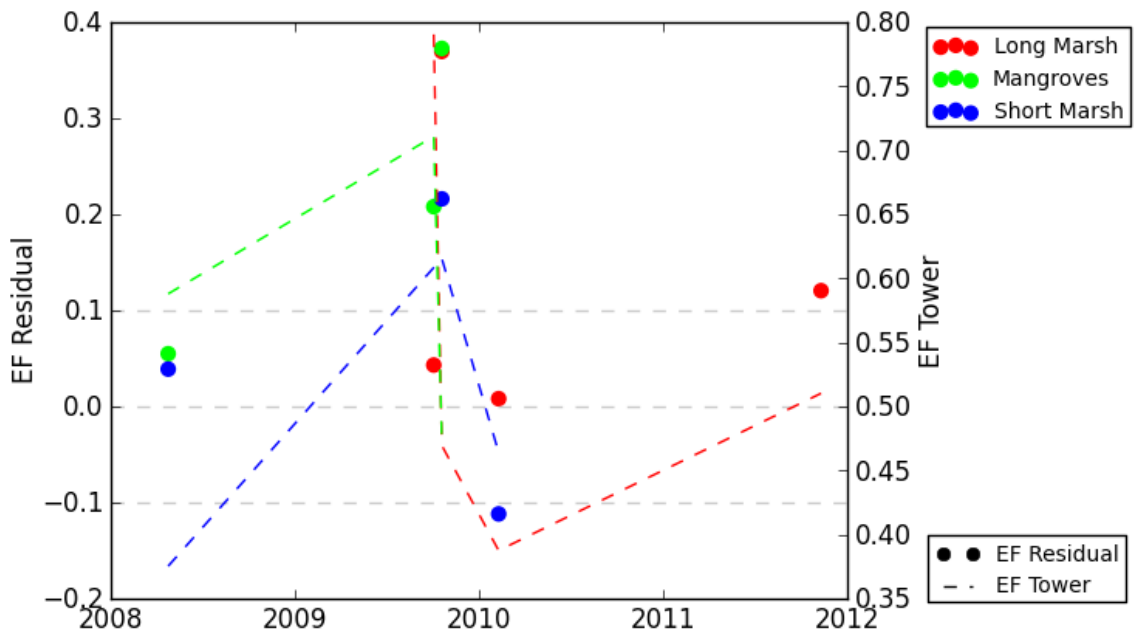
Figure 4.2.15: *EF* residual and *EF* tower vs. Year for Everglades Optimal Variation
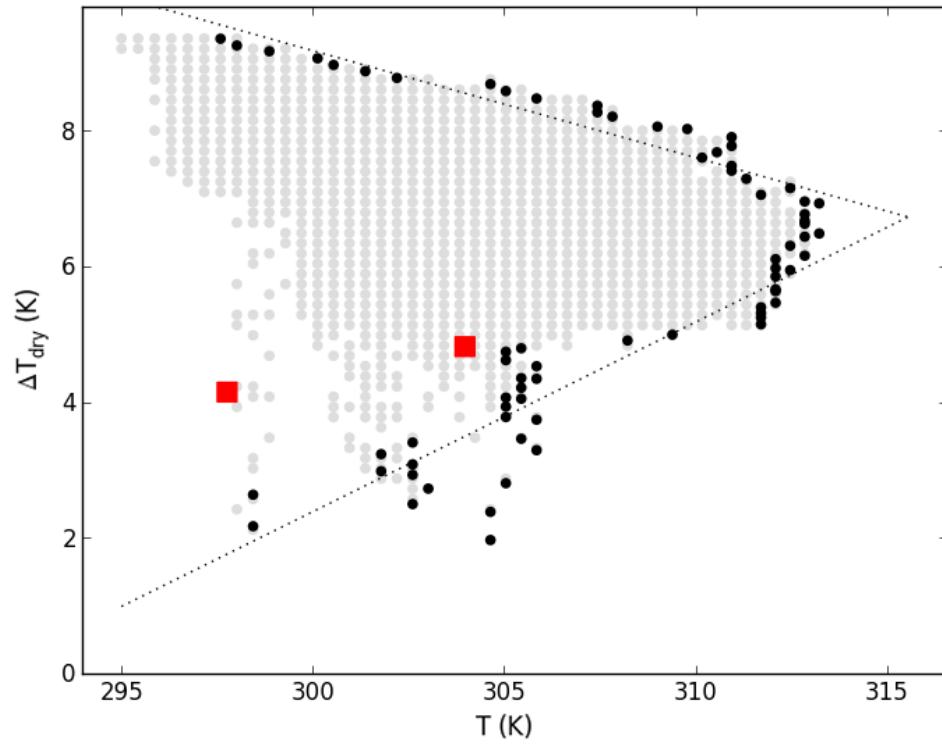
Figure 4.2.16: ΔT$_{dry}$ vs. Temperature for Everglades, April 23, 2008 Without Filtering α
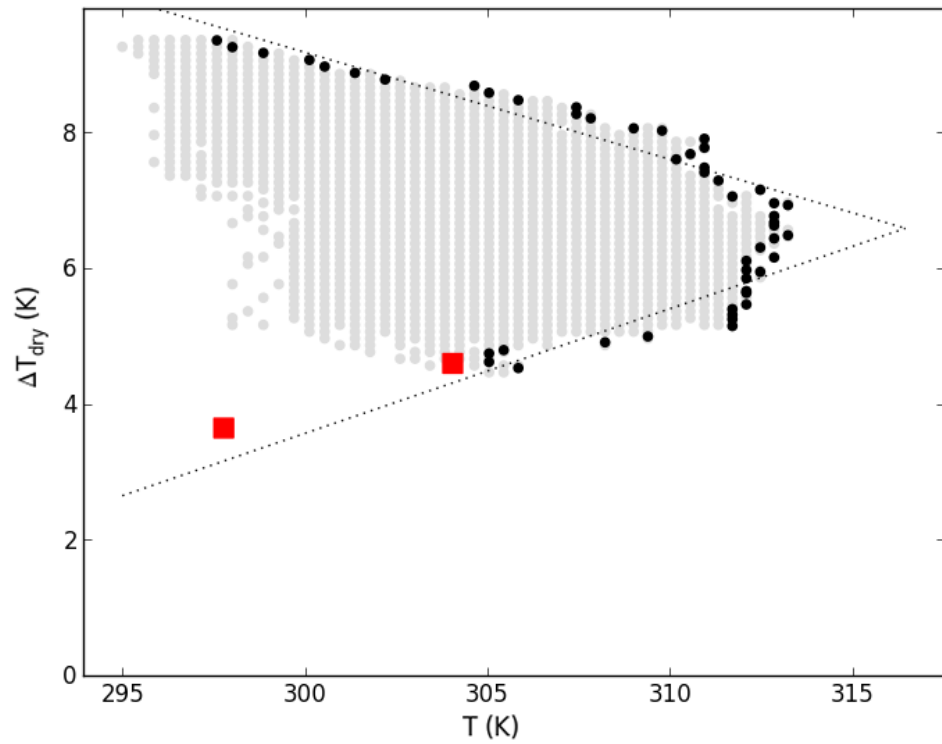
Figure 4.2.17: ΔT$_{dry}$ vs. Temperature for Everglades, April 23, 2008 With Filtering α

115

Figure 4.2.18 shows the results when algorithm was performed on the Mangroves and Homestead extents separately. Processing extents separately increased *MAE* only slightly from 0.154 to 0.176, but the *Bias* was greatly reduced from 0.132 to 0.023. Using the Mangroves extent separately leads to an underestimation of *EF*. The *MAE* calculated using only Mangrove points increases slightly from 0.212 to 0.218 when using Mangrove extent instead of full extent. The dry calibration points automatically detected for both study areas on April 23, 2008 is shown in Figure 4.2.19. It would have seemed initially that using the full extent would have performed better because the Mangroves extent did not include truly dry pixels as shown in Figure 4.2.20 for October 3, 2009. The lower boundary has very high ΔT_{dry} for correspondingly low temperatures which indicates the absence of dry pixels resulting in a severe overestimation of sensible heat evident in the corresponding underestimation of *EF*. Surprisingly, using the full extent did not improve the results much because now sensible heat was being under estimated as shown in Figure 4.2.21. It is interesting to note that as the predicted sensible heat decreases, the validation ΔT increases. This is because buoyancy decreases with sensible heat which decreases conductivity of the atmosphere which increases validation ΔT. The algorithm can be very sensitive to the effect of sensible heat on atmospheric conductivity. Figure 4.2.21 also shows better agreement for Long Marsh than Mangroves. This could possibly be because Long Marsh is closer to the dry calibration points found in Homestead area. This could suggest that the problem with using full extent for retrieving Mangrove *EF* is because Mangroves are too far from Homestead dry pixels.
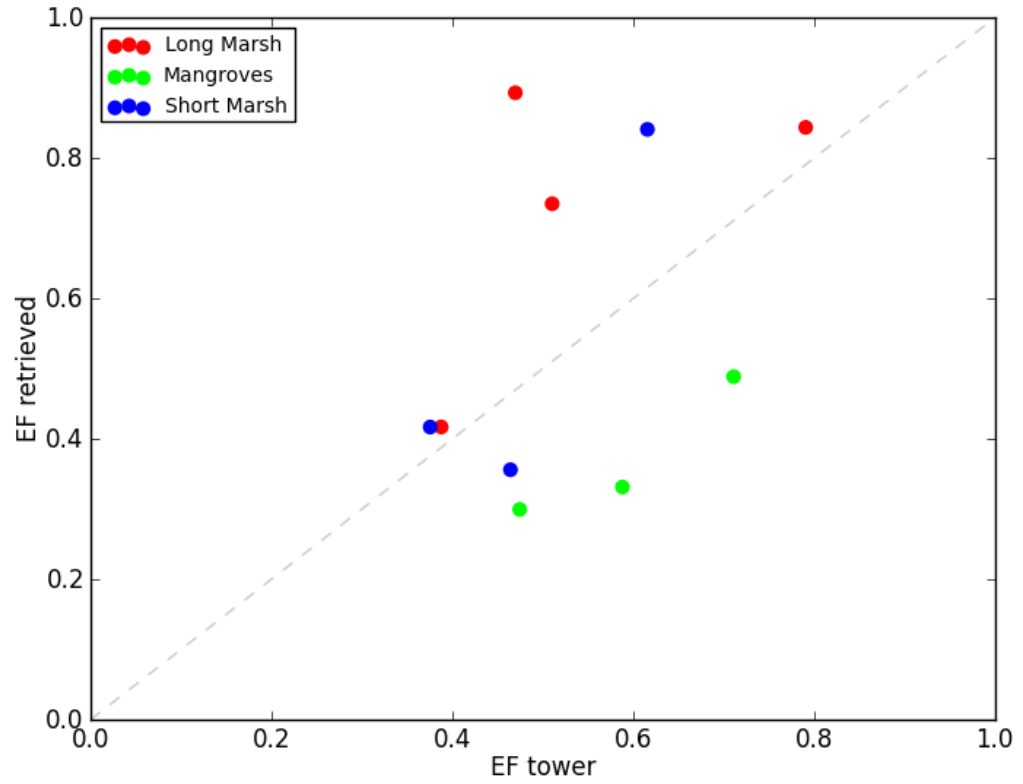
Figure 4.2.18: Optimal *EF* retrieved vs. *EF* tower for Homestead/Mangroves Extents
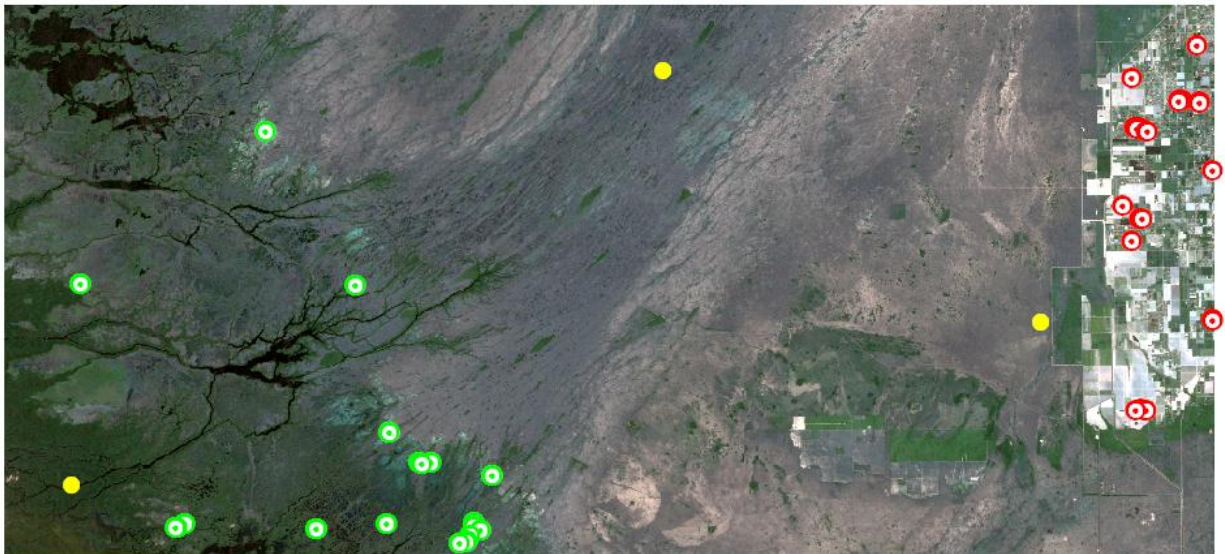
Figure 4.2.19: Automatically Detected Calibration Points for Everglades on April 23, 2008
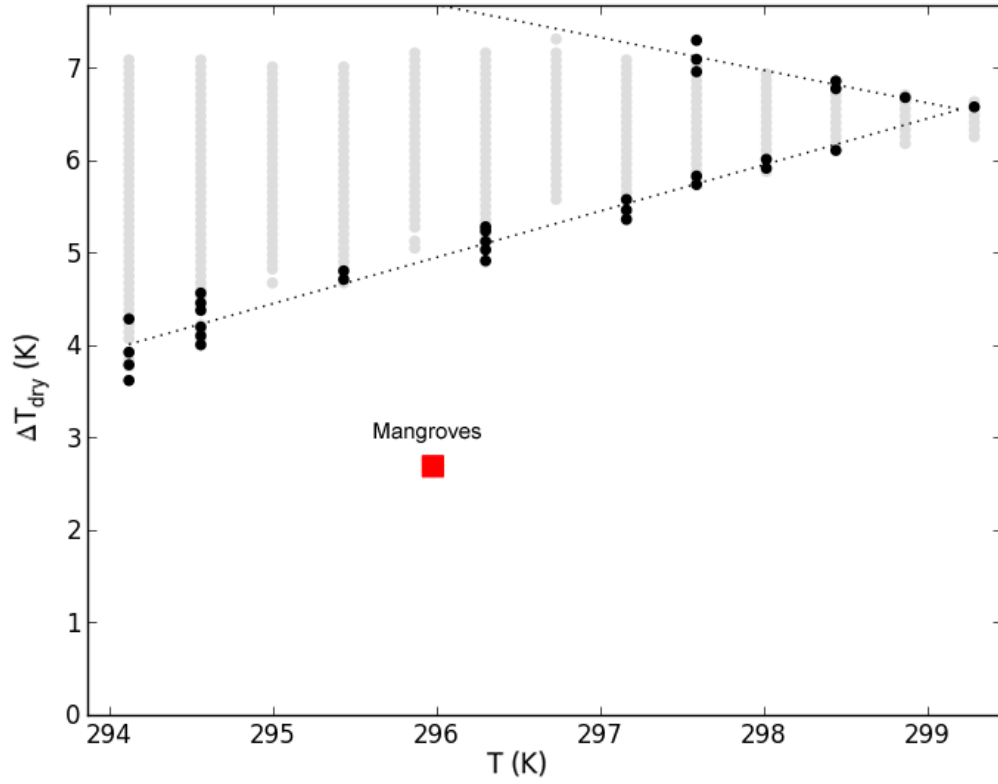
Figure 4.2.20: *ΔT*dry vs. *T* for Everglades on Oct 3, 2009 using Mangroves Extent
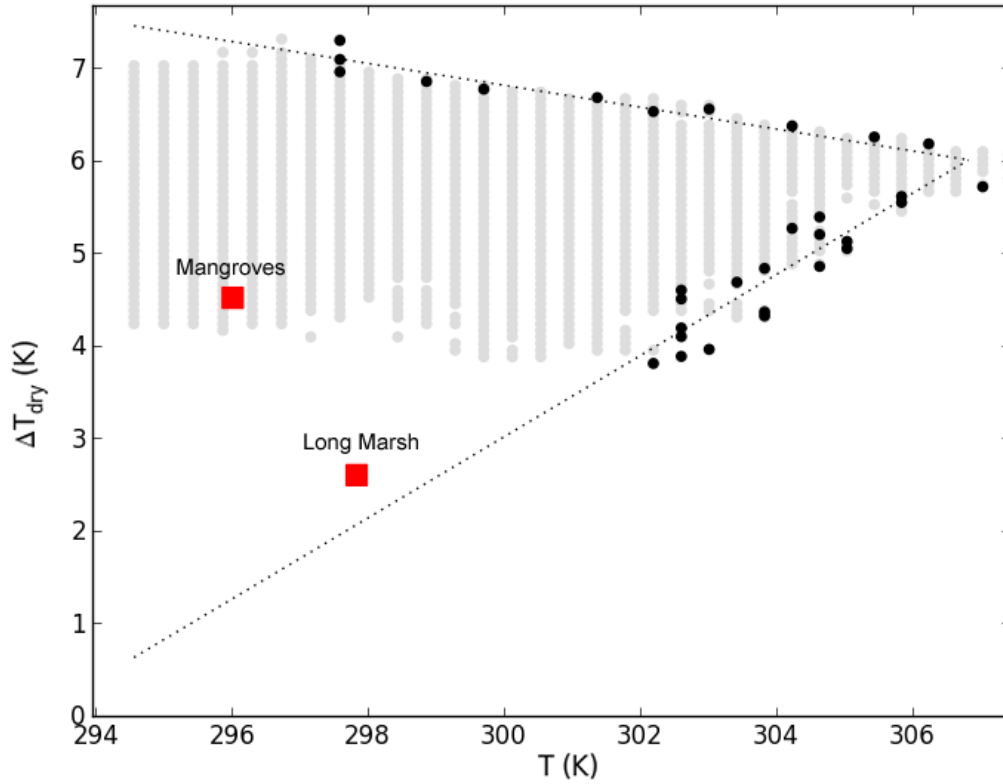
Figure 4.2.21: *ΔT*dry vs. *T* for Everglades on Oct 3, 2009 using Full Extent

4.2.4 Gainesville Dry Pixel Validation

Figures 4.2.22 and 4.2.23 show the comparison of retrieved vs. tower *EF* for

Gainesville study area classified by station and season respectively. The optimal variation

is *ΔT* vs. *T* with Even Bin Threshold Fit. A large number of validation points were

available due to the large number of useable scenes combined with 3 available stations.

Figure 4.2.24 shows the variation of error and tower *EF* with time. Based on the tower,

EF is lowest for winter and highest for summer while spring and fall produce *EF* in the

0.4 to 0.6 range. A high degree of error between retrieved and tower *EF* is produced for

the Gainesville study area. Only 21 of the 65 validation points have an error within +/-

0.1 *EF* and 35 of the 65 validation points produced an error within +/- 0.2 *EF*. Table 4.2.1

reports errors for the optimal variation grouped by station and season. When broken up

by station *Bias* and *MAE* are fairly similar except for Mize is less biased and Austin

Carey has a little less *MAE*. Donaldson only has about 25% of validation points within

+/- 0.1 *EF* while Austin Carey has about 40%. When broken up by season, more

interesting patterns emerge. The *MAE* produced for summer is considerable less than it is

for other seasons. The *Bias* for spring is much larger than the other seasons and fairly low

for both summer and fall. The *Bias* in winter is nearly zero, but the *MAE* is large.
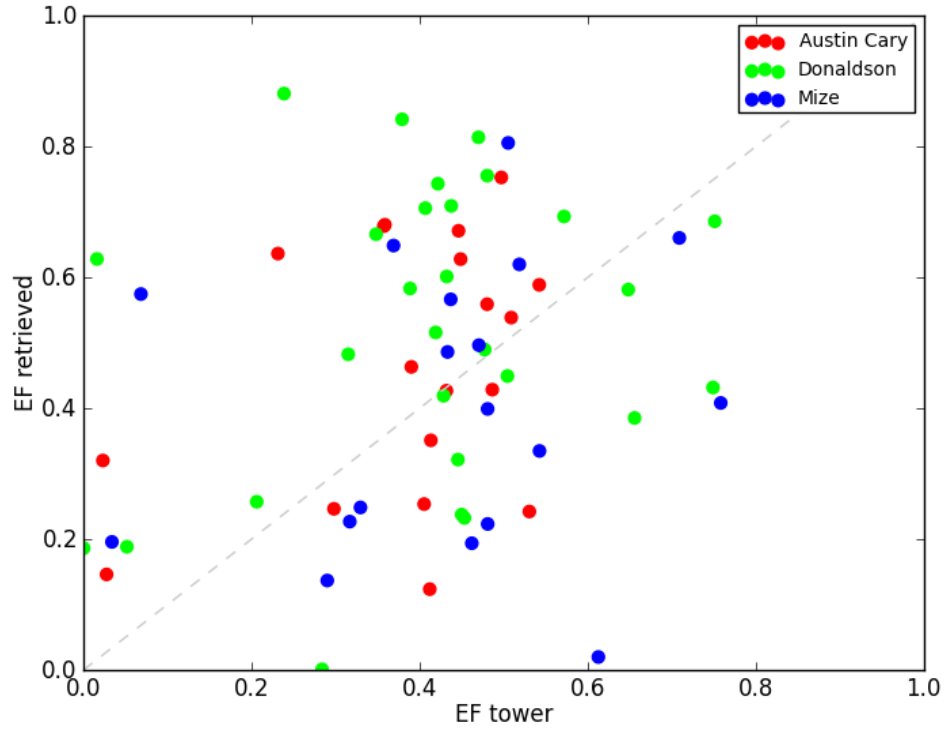
Figure 4.2.22: Optimal *EF* retrieved vs. *EF* tower for Gainesville by Station
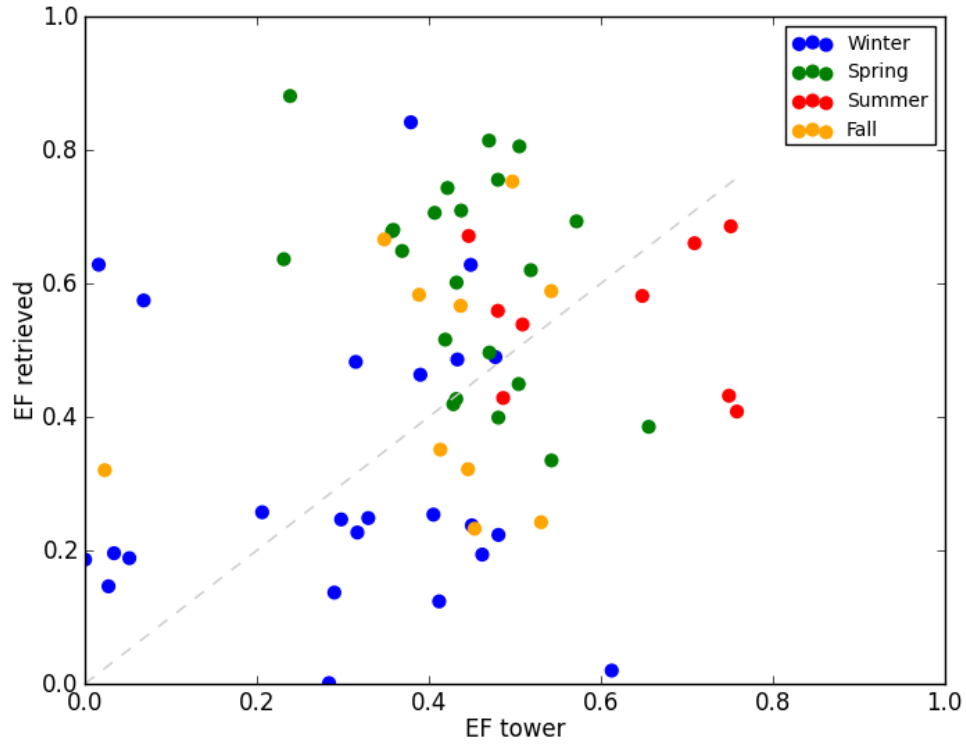
Figure 4.2.23: Optimal *EF* retrieved vs. *EF* tower for Gainesville by Season
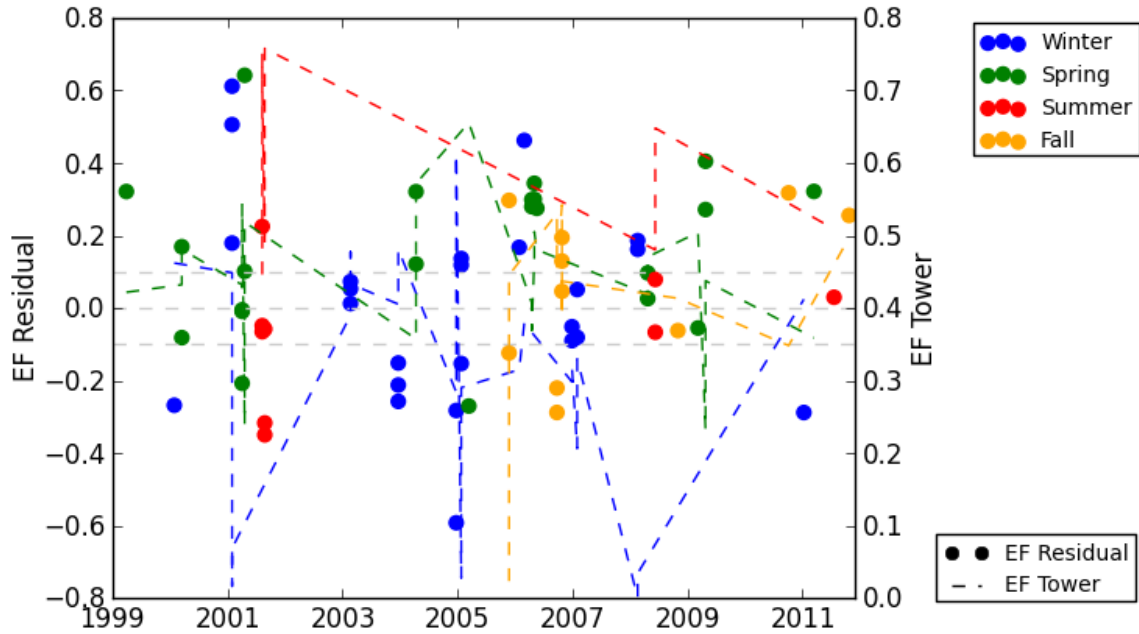
Figure 4.2.24: Optimal *EF* residual and *EF* tower vs. Year for Gainesville

Table 4.2.2: Errors for Optimal Gainesville Variation Grouped by Station and Season

Group	Bias	MAE	$N_{|\Delta EF| < 0.1}$	$N_{|\Delta EF| < 0.2}$	N_{Total}
AustinCary	0.076	0.171	8	11	19
Donaldson	0.109	0.225	7	14	28
Mize	-0.032	0.205	6	10	18
Winter	0.012	0.215	7	15	24
Spring	0.167	0.224	6	9	22
Summer	-0.064	0.138	6	6	9
Fall	0.054	0.194	2	5	10
Total	0.06	0.204	21	35	65

Figure 4.2.25 and 4.2.26 show the effect of not accounting for the variation of atmospheric conductivity (g_a) in the algorithm. The black lower boundary line in Figure 4.2.25 represents the calibrated relationship for H vs. T where $H = g_a (T_s - T_a)$. This line describes the relationship between H and T for a relatively small g_a which is associated with a smooth bare surface. The red validation points are associated with rough slash pine surface with a large g_a. The red dashed line represents the relationship between H and T if the slope of the line g_a was increased to reflect that which is appropriate for slash pine. This results in a much better agreement between model and tower measurements. A unique relationship between H and T does not exist, but the slope of the relationship varies depending on g_a. Figure 4.2.26 shows the ΔT vs. T model which accounts for g_a because $\Delta T = H / g_a$. Now that g_a is accounted for there is a better agreement between retrieved H and tower H. This would suggest that determining the roughness length in order to calculate g_a is important in situations in which roughness is variable.

Figure 4.2.27 and 4.2.28 shows the variation in the land cover of the Gainesville study area between March 14, 2000 and April 21, 2008. Between these dates some areas have been cleared of vegetation while in other areas vegetation was allowed to grow back. The position of the automatically detected calibration points are also shown on these figures. The figures demonstrate the manner in which the position of the dry pixels appears to successfully reflect changes in the landscape.
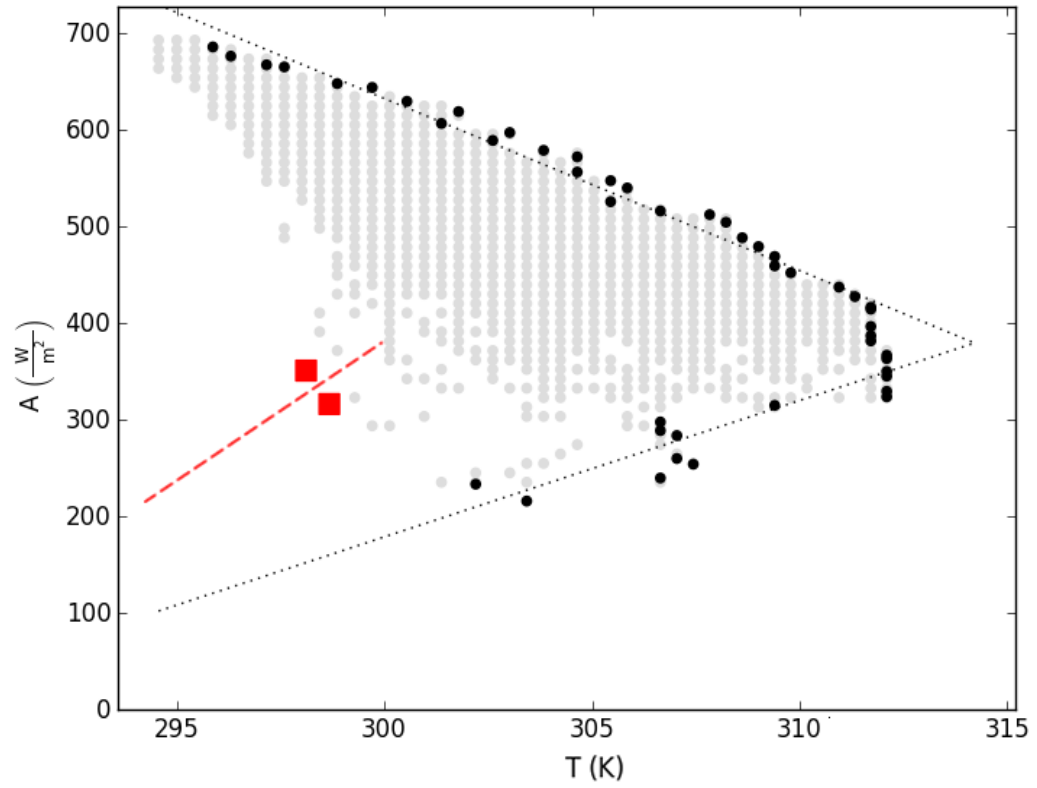
Figure 4.2.25: *A* vs. *T* for Gainesville on April 21, 2008
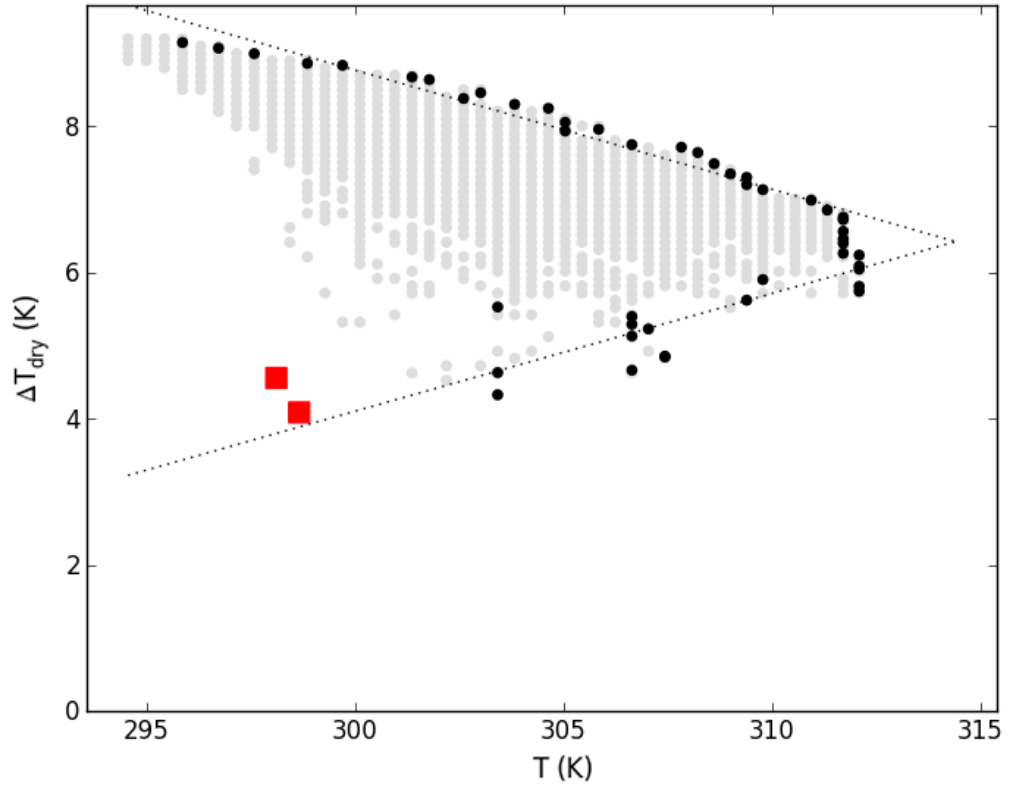
Figure 4.2.26: *ΔT*dry vs. *T* for Gainesville on April 21, 2008

123

Figure 4.2.27: Automatically Detected Calibration Points for Gainesville on April 21, 2008
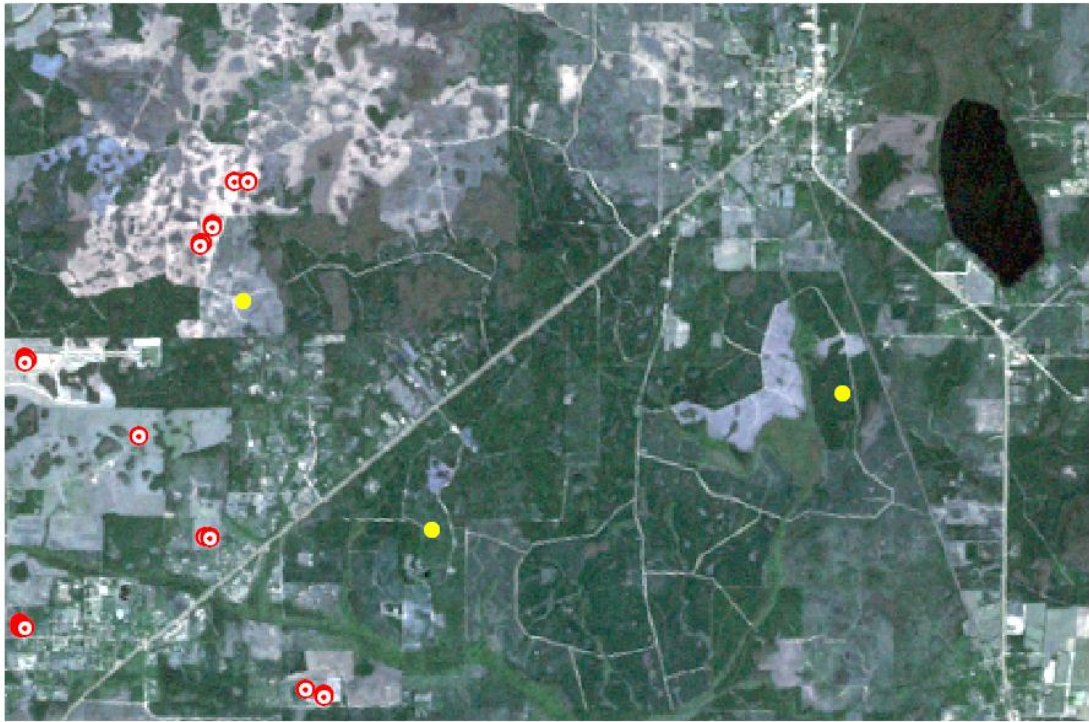
Figure 4.2.28: Automatically Detected Calibration Points for Gainesville on March 14, 2000

4.2.5 Kennedy Space Center Dry Pixel Validation

Figure 4.2.29 shows the comparison of retrieved vs. tower *EF* for Kennedy study

area grouped by season for the optimal variation. This optimal variation is ΔT vs. *T*, Even

Bin Threshold Fit, with albedo filtering applied to the default smaller extent. Figure

4.2.30 shows the variation of error and tower *EF* with time. Based on the tower, *EF* is

quite similar across seasons but this could be misleading because the number of available

points is small. Among the 24 available scenes there are 10 scenes which have an error

within +/- 0.1 *EF*. The algorithm was applied to both the large and small extent with and

without albedo filtering. For all cases ΔT vs. *T* model and Even Bin Threshold Fit

boundary was used. The best case scenario is shown in Figure 4.2.29 and 4.2.30 while the

worst case scenario is shown in Figure 4.2.31. This shows that the algorithm severely

under estimates sensible heat and over estimates *EF* over the large extent when albedo is

not filtered. Many times the *EF* was forced to be one because the calibration resulted in

negative sensible heat values at the validation sites. The optimal case also over estimated

sensible heat more often on average but not as severely. Table 4.2.3 summarizes the

errors for the four different variations of extent and albedo filtering. This shows that the

cases when albedo was filtered produced the best results and the smaller extent produced

better results than the large extent.
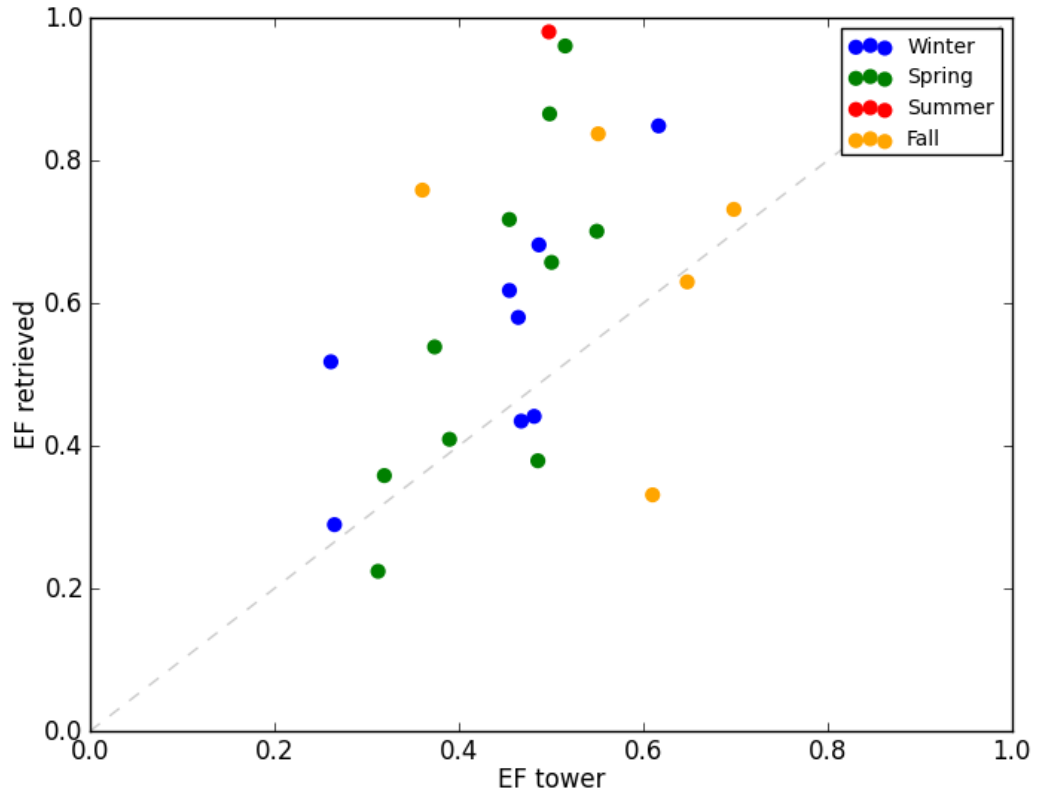
Figure 4.2.29: Optimal *EF* retrieved vs. *EF* tower for Kennedy by Season
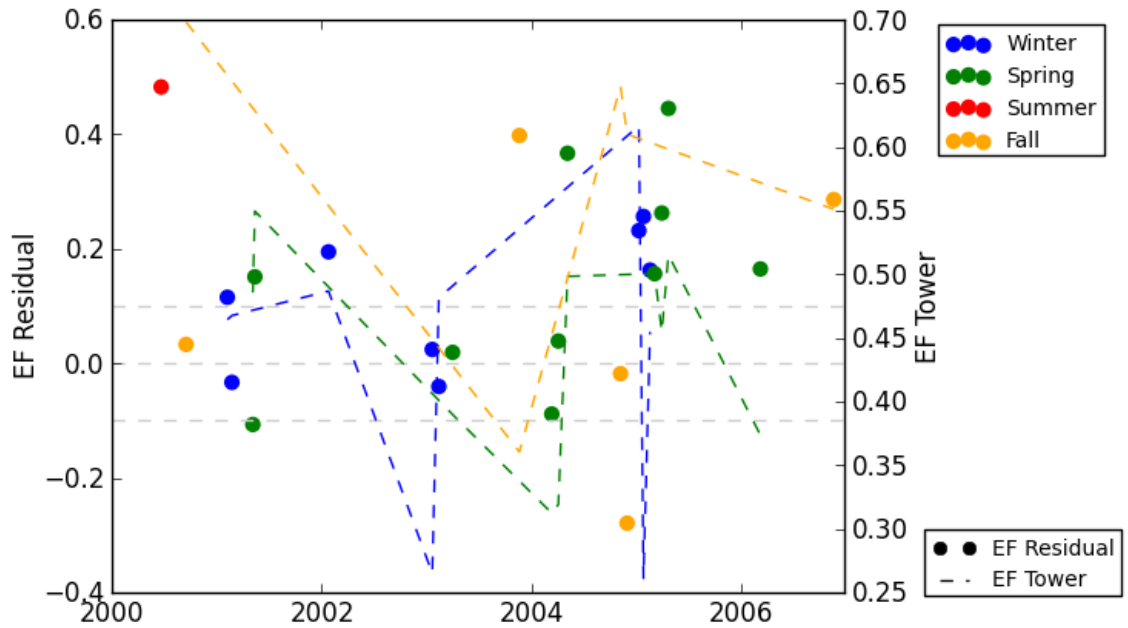
Figure 4.2.30: Optimal *EF* residual and *EF* tower vs. Year for Kennedy
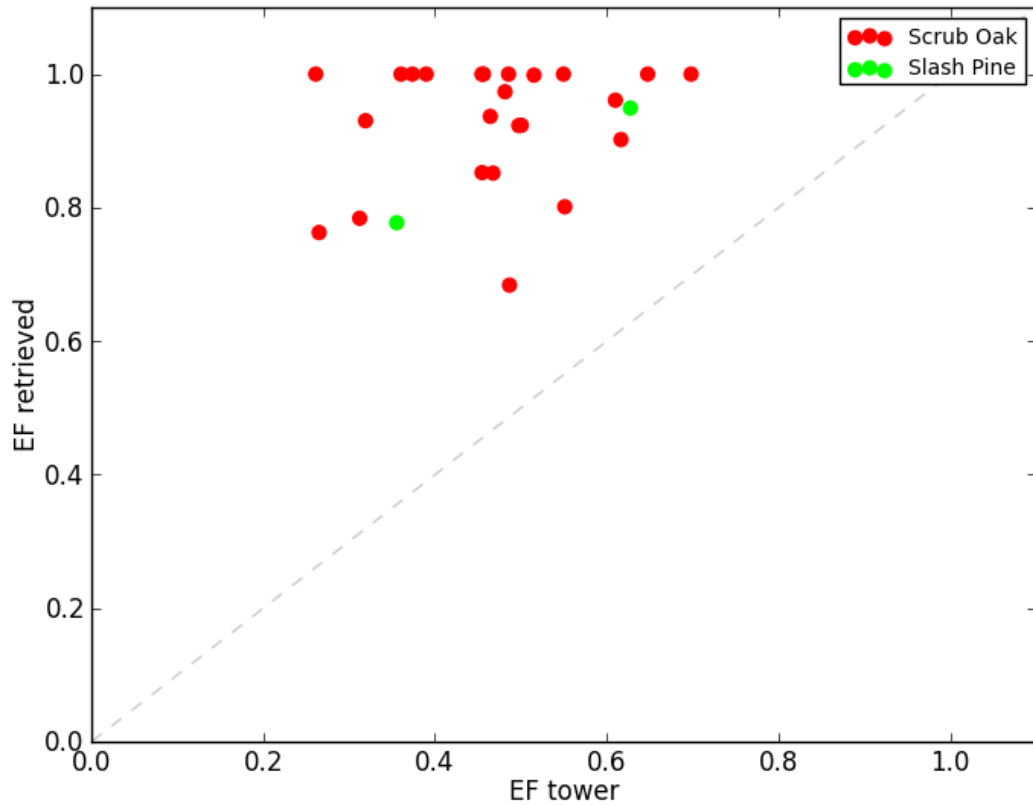
Figure 4.2.31: Optimal *EF* retrieved vs. *EF* tower for Kennedy Large Extent

Table 4.2.3: Errors for Kennedy with Varying Extents and Filtering

Extent	Filter α	Bias	MAE
Large	No	0.454	0.454
Small	No	0.333	0.333
Large	Yes	0.184	0.232
Small	Yes	0.134	0.181

Figure 4.2.32 and 4.2.33 show the effect of filtering albedo on the calibration. Figure 4.2.32 did not filter albedo which led to an under estimation of sensible heat compared to the validation point. When filtering of albedo was applied in Figure 4.2.33, it increased the sensible heat so that better agreement with the validation point was produced. Figure 4.2.34 shows the calibration points used when filtering was and was not performed. The red calibration points were detected in both cases, the green calibration

points were detected in the non-filtered case, and the magenta calibration points were detected in the filtered case. A large amount of overlap is noticeable in the image along the runway. The points unique to the non-filtered case consisted of some high albedo man made surfaces to the south which appeared to be white roofs after inspection via Google Maps. The points unique to the filtered case were found in the north and were made up of natural non vegetation surfaces which looked recently dried out. These points were the darkest and hottest of the dry surfaces. Figure 4.2.35 demonstrates the inability of the algorithm to produce an accurate sensible heat when the large extent was used. In this case, even though filtering of albedo was used the larger extent affected the results in a negative way. Some warmer surfaces shifted the sensible heat down which led to an underestimation of sensible heat. This could probably be due to a tendency for the atmosphere to vary more near the coast where the boundary layer is changing from marine conditions to terrestrial conditions. Figure 4.2.36 shows the calibration points detected for both small extents (red points) and large extents (green points) while filtering albedo for both. The calibration points used with the large extent were in different locations to the south. The yellow box defines the small default extent. It would have been helpful to compare the predicted *EF* using large extent calibration to the Slash Pine station but the flux tower only produced two useable points as shown in Figure 4.2.31. This analysis demonstrates the sensitivity of the algorithm to the extent. If the small extent was increased just enough to bring the large manmade surface to the south into the extent, the results could be greatly altered.
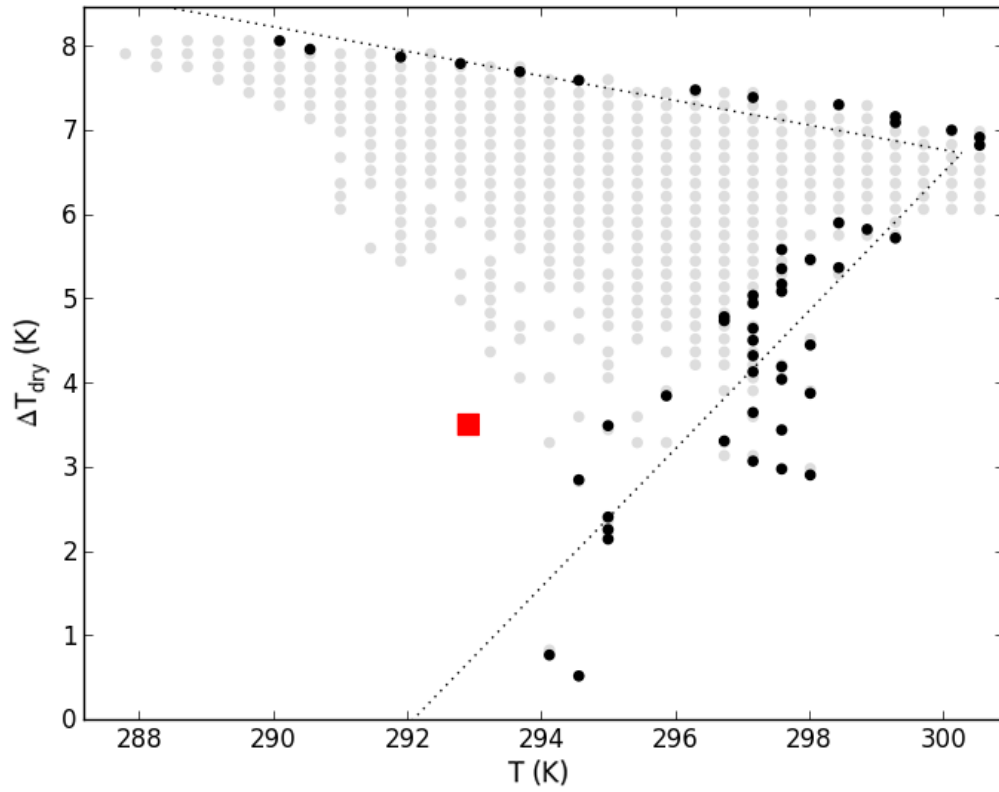
Figure 4.2.32: *ΔT*$_{dry}$ vs. *T* for Kennedy with No Filter α on April 1, 2003
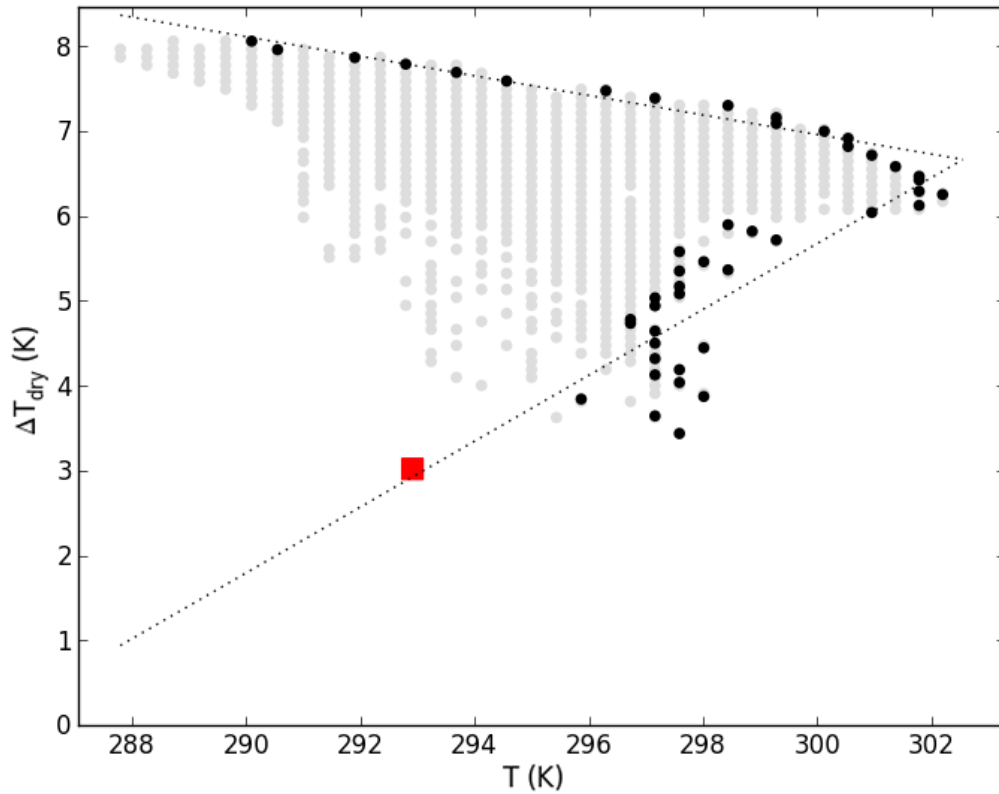
Figure 4.2.33: *ΔT*$_{dry}$ vs. *T* for Kennedy with Filter α on April 1, 2003

Figure 4.2.34: Calibration Points Detected for Kennedy Small Extent on April 1, 2003
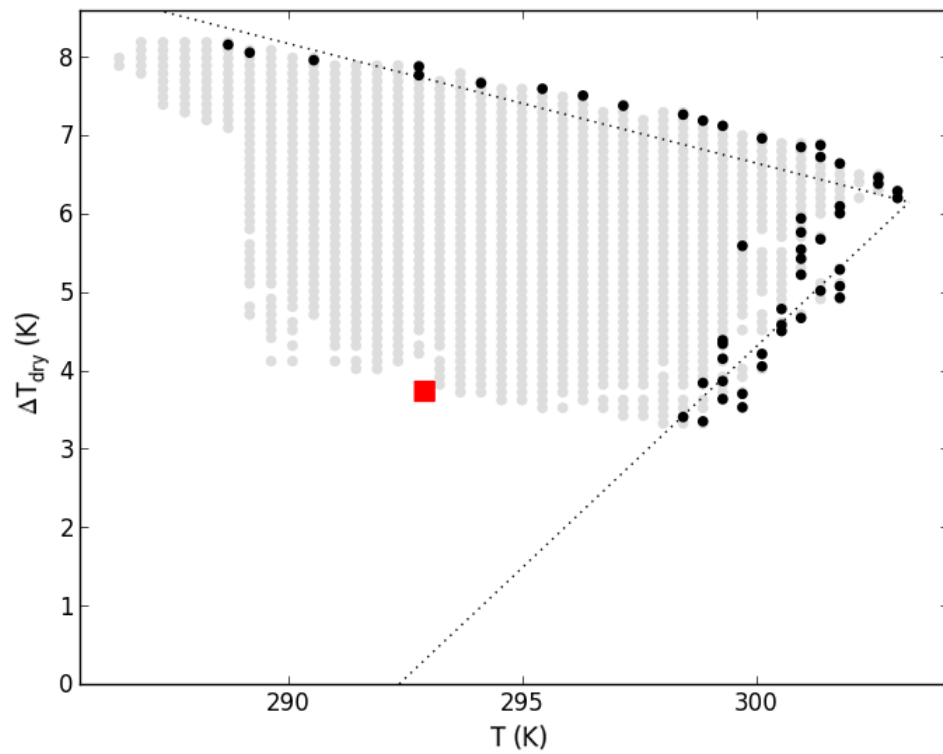
Figure 4.2.35: ΔT_{dry} vs. T for Kennedy Large with Filter α on April 1, 2003

130
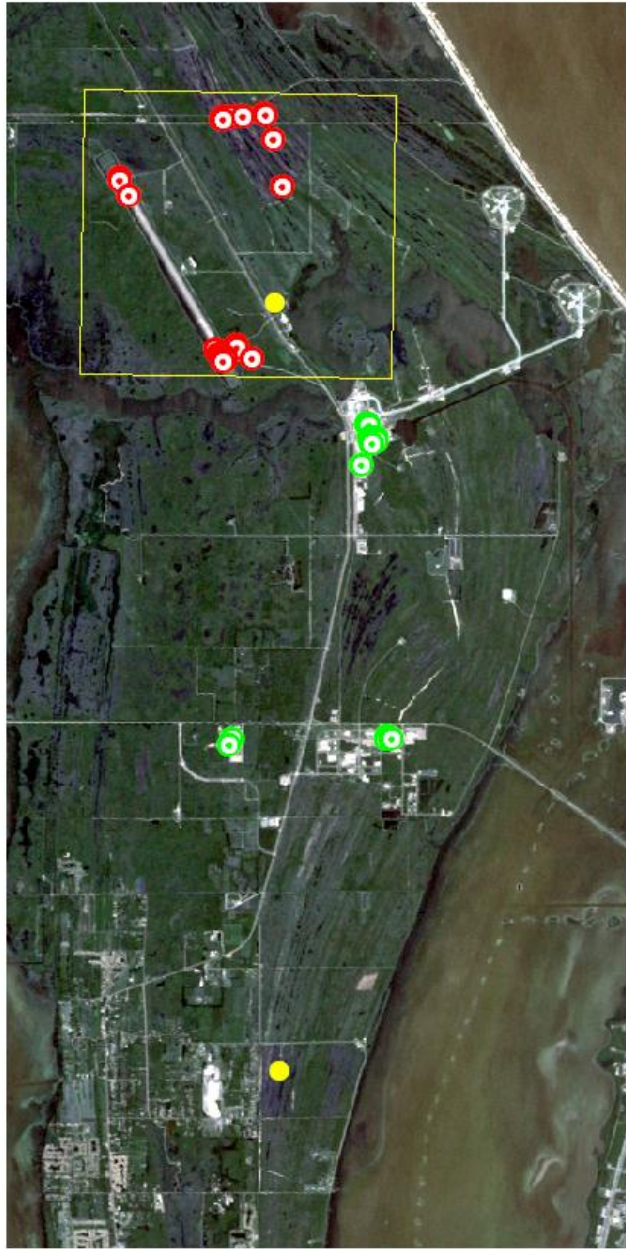
Figure 4.2.36: Calibration Points Detected for Kennedy Large and Small on April 1, 2003

4.3 Incorporating Wet Pixels into Calibration

4.3.1 Investigation of Priestly Taylor Coefficient

The Priestly Taylor coefficient α_{pt} was analyzed using all flux tower data and also using the Penman-Monteith model over water as described in methodology section. Big Cypress was not included in the analysis because only flux tower data for day of satellite overpass was available. Figure 4.3.1 shows the variability of α_{pt} for each month and each study area. It shows the mean value along with the mean plus two standard deviations. The mean α_{pt} has seasonal variability peaking in fall and reaching minimum in spring. The standard deviation of α_{pt} is the largest in the winter. The mean α_{pt} remains below 1.0 for all study areas, but mean plus two standard deviations can reach as high as 1.5 for Gainesville. The mean α_{pt} plus two standard deviations remains fairly constant at around 1.25 for Everglades and is below 1.2 for Disney and Kennedy. Because the flux towers are measuring vegetation, this information was used to estimate α_{pt} needed to estimate the sensible heat of the wet pixels. Originally the standard value of $\alpha_{pt} = 1.26$ was used but this severely overestimated latent heat and underestimated sensible heat. The top *NDVI* values used to find wet pixels should represent well watered vegetation and therefore the mean values were not used because they included all vegetation states in their calculation. It would be better to use an intermediate value between the highest values and the mean values. A value of $\alpha_{pt} = 1$ was assumed based on the assumption that the energy term would be greater than the aerodynamic term for wet conditions. This is not necessarily true as shown in Figure 4.3.1. It would have been possible to estimate a α_{pt} value specific to study area and time of year for use in the algorithm, but the aim of

the algorithm is to operate independently of the flux towers. Investigation of α_{pt} based on flux towers was a check to determine the possible range of α_{pt}.

Figure 4.3.2 shows the variation of α_{pt} based on values simulated for water as described in methodology section. In this case there is a lot less variation of α_{pt} with α_{pt} varying from 1.03 for smallest mean value and 1.15 for largest mean plus two standard deviations. For vegetation the mean state did not necessarily reflect well watered vegetation. Open water doesn't have this problem so the mean state should reflect the mean evaporation. The mean α_{pt} varies from about 1.03 to about 1.07. A value of 1.05 could have been applied in calibration based on simulation, but $\alpha_{pt} = 1$ was adopted as before. This assumes that the energy term would be much greater than the aerodynamic term over water.
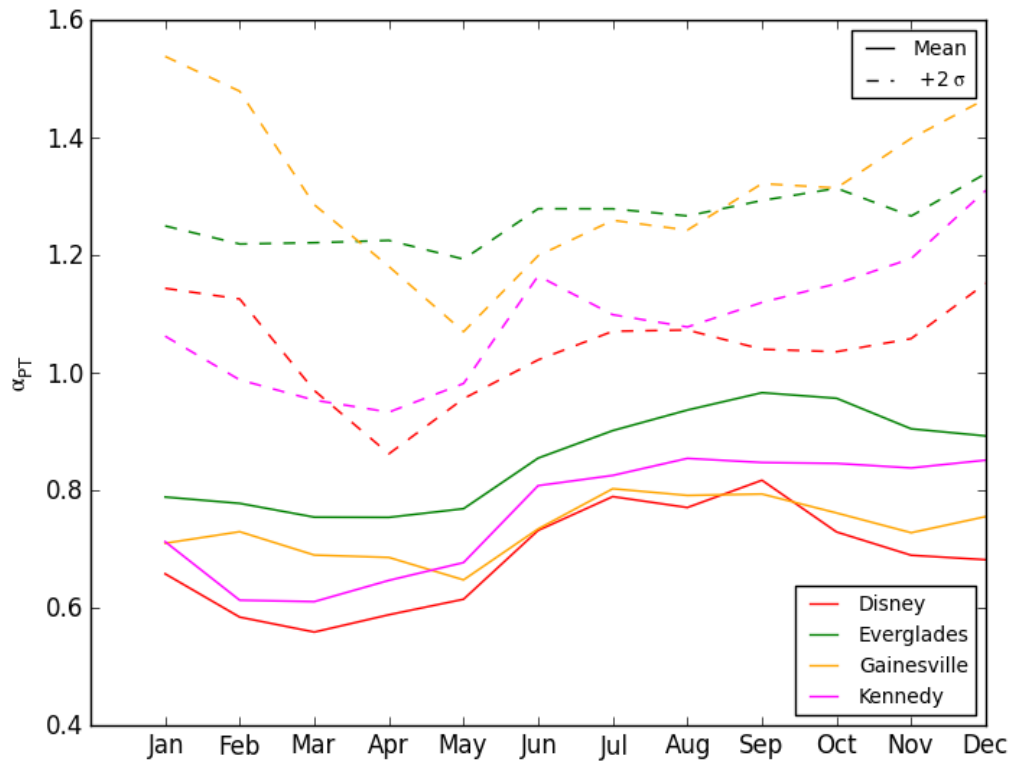
Figure 4.3.1: Monthly Variation of α_{pt} from flux towers

133
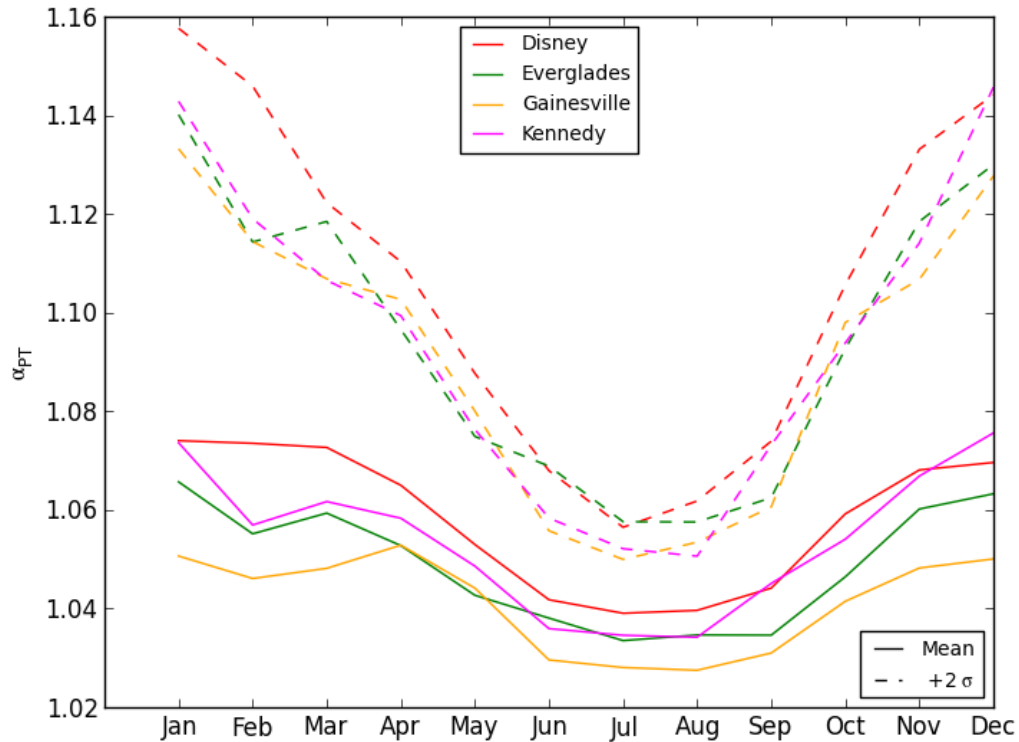
Figure 4.3.2: Monthly Variation of α_{pt} from Simulation over Water

4.3.2 Validation of Calibration Which Includes Wet Pixels

Wet pixels were introduced to the calibration and the method in which wet pixels were detected was varied. The method used for finding the boundary in the dry pixel part of the calibration was Even Bin Threshold Fit. This was chosen because the dry pixel validation determined that it was the best method for all study areas. Albedo filtering was used for Kennedy and Everglades as with optimal dry pixel only calibration. The three methods of detecting wet pixels are unsupervised classification, keeping pixels below *NDVI* threshold and above *NDVI* threshold. The threshold value is the proportion of the total pixels that will be considered wet pixels. The calibration was performed on threshold value ranging from 0 to 100%. The resulting errors produced from these optimal thresholds are plotted in Figure 4.3.3. The unsupervised classification did not require a threshold value. It should be noted that the best case scenarios shown in Figure

134

4.3.3 can be difficult to achieve because it requires knowledge of the optimal threshold. For example, the neutral case with above *NDVI* threshold appears to produce decent results, but Figure 4.3.4 reveals the large variation in optimal threshold value among study areas. For the threshold approach to be useful, it would be necessary for the errors to be minimized over a larger range that could be estimated before running calibration. For example, it would seem that some range of low values would all contain well watered vegetation and some small value could be uniformly applied. In reality this isn't the case as shown for Kennedy and Disney which produce minimum errors for arbitrary threshold values. A simple approach would be to only include the wet pixel with the absolute maximum *NDVI*. For Big Cypress this produced the smallest error in Figure 4.3.4 and could be a valid approach. Another case in which the best case scenario offers unattainable results is for ΔT vs. T with below *NDVI* threshold as shown in Figure 4.3.5. In that case Disney and Everglades produce good results, but once again the optimal threshold value is not stable and would be hard to predict beforehand. For Gainesville the approach is feasible if the wet pixel was assumed to be that with absolute minimum *NDVI* value. Another simple approach is to assume that the maximum *NDVI* of wet pixels is equal to zero. This should do a decent job of finding a good sample of open water pixels. The calibration was performed using the H vs. T model and setting the maximum *NDVI* threshold directly instead of using a percentile value. The threshold *NDVI* value was varied from -0.5 to 0.5. Figure 4.3.6 shows that minimum values exist over a wide range of *NDVI* thresholds less than zero making zero a good choice of threshold. This behaves similar to using the unsupervised classification and demonstrates the ability of the threshold to find open water wet pixels.

135
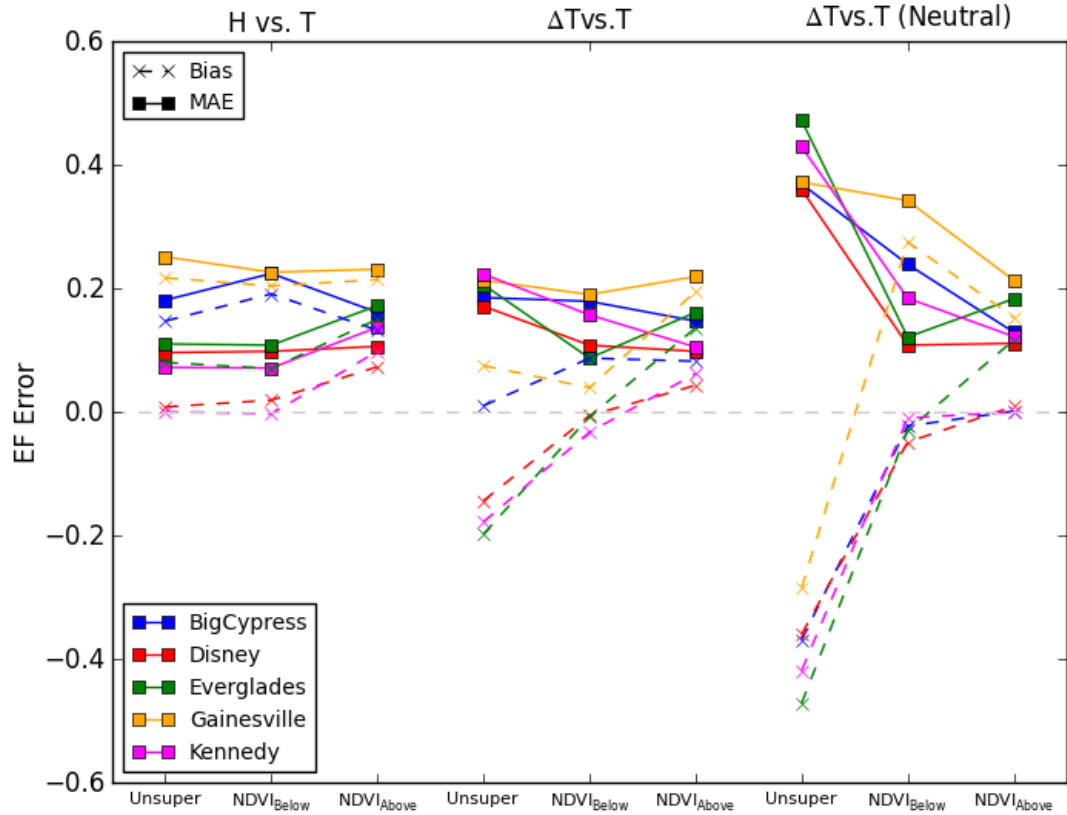
Figure 4.3.3: *Bias* and *MAE* Error of All Models and Wet Pixel Type for Each Study Area
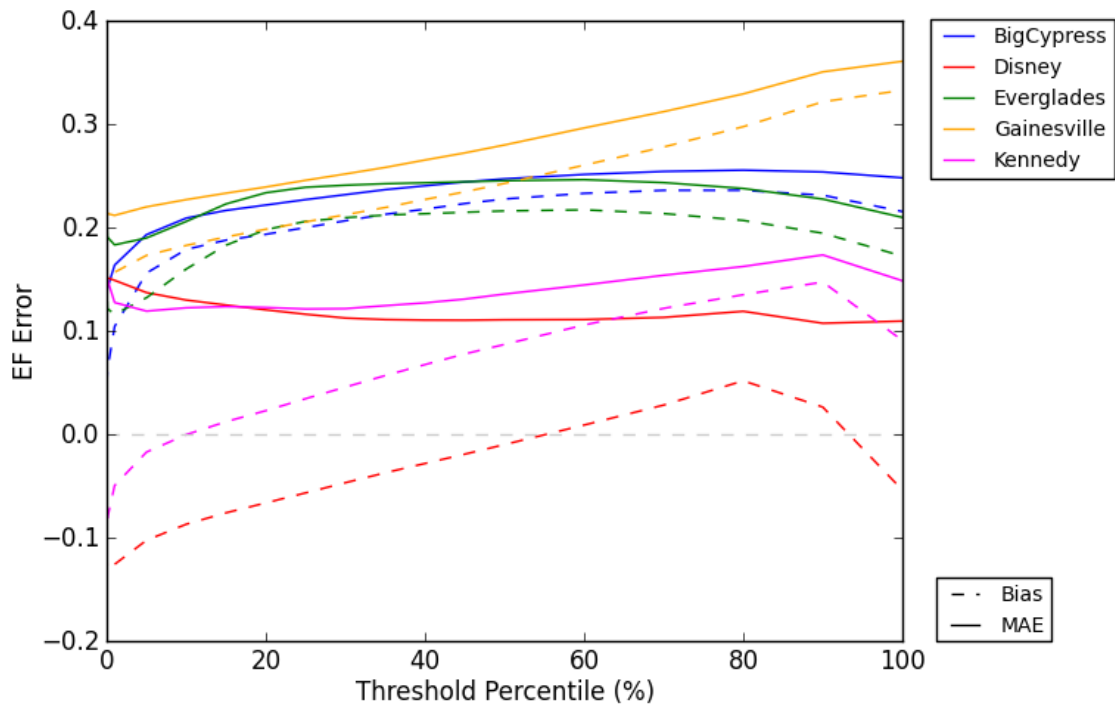
Figure 4.3.4: Variation of Errors for *ΔT* vs. *T* Neutral and Above *NDVI* Threshold
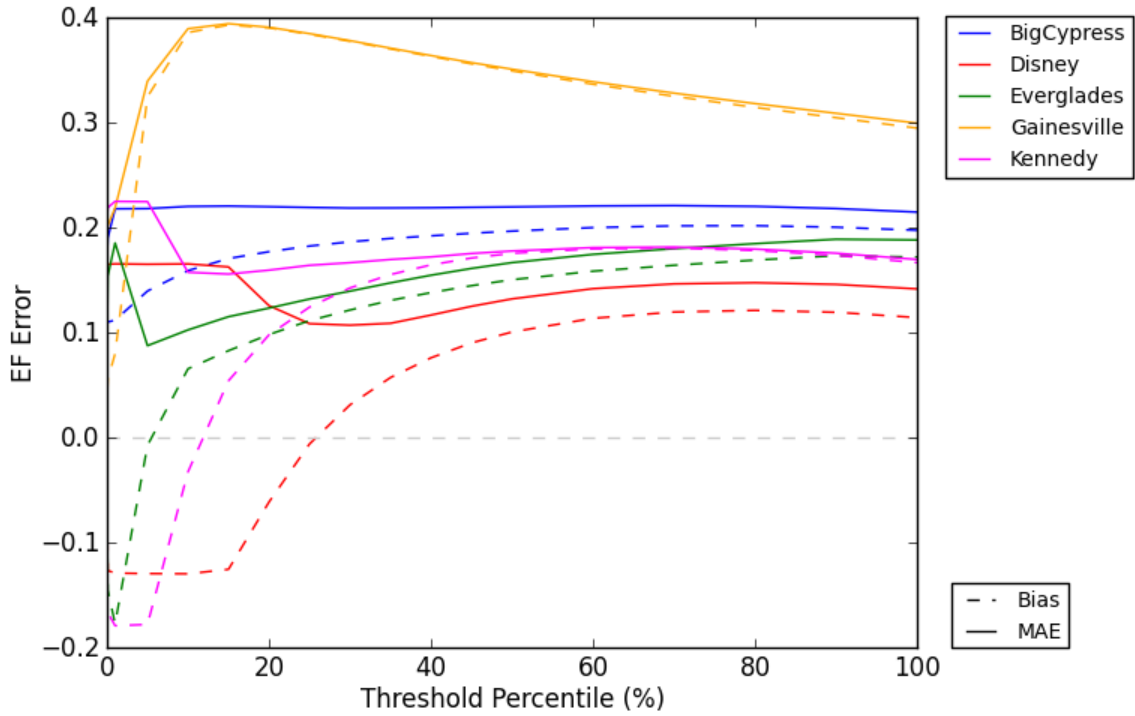
Figure 4.3.5: Variation of Errors for *ΔT* vs. *T* Model and Below *NDVI* Threshold
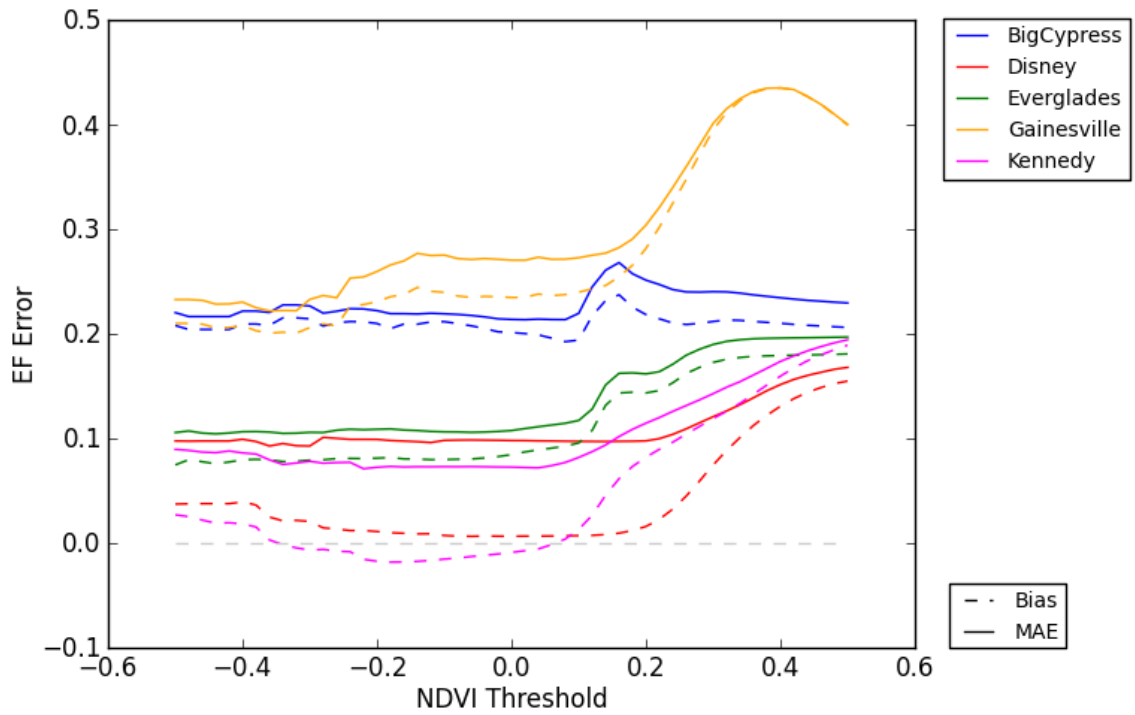
Figure 4.3.6: Variation of Errors for *H* vs. *T* Model and Absolute *NDVI* Threshold

137

Since threshold values would be difficult to determine, $NDVI_{min}$ and $NDVI_{max}$ were used instead. The optimal variations shown in Table 4.3.1 were determined using these extreme thresholds. The errors reported in Table 4.3.1 demonstrate an increase in performance due to the introduction of wet pixels into the calibration for some cases. The Big Cypress and Gainesville study areas did not see much of an enhancement due to the addition of wet pixels. Disney, Everglades and Kennedy did see a big change. Kennedy Space Center experienced the largest change in both *Bias* and *MAE*. The optimal variation for these three study areas is *H* vs. *T* using unsupervised classification to find wet pixels. It should be noted that using Unsupervised and *NDVI*=0 as thresholds produced very similar results for these three study areas. The simplest way to incorporate wet pixels into the calibration would be to use *NDVI*=0 in order to avoid performing an unsupervised classification. In this dissertation the unsupervised classification was already performed in order to mask out water when determining roughness length, but in practice the *NDVI* =0 threshold method would be simpler. In regards to Big Cypress and Gainesville, introducing wet pixels into the calibration did not matter very much.

Table 4.3.1: Optimal Variations after Including Wet Pixels in Calibration

Study Area	Model	Classification	Bias	MAE	MAD	ρ	ΔBias	ΔMAE
BigCypress	ΔT vs. T (Neutral)	$NDVI_{max}$	0.001	0.129	0.129	0.415	-0.021	0.015
Disney	H vs. T	Unsupervised	0.008	0.096	0.095	0.609	-0.054	-0.069
Everglades	H vs. T	Unsupervised	0.08	0.11	0.087	0.605	-0.052	-0.044
Gainesville	ΔT vs. T	$NDVI_{min}$	0.055	0.19	0.185	0.236	-0.005	-0.014
Kennedy	H vs. T	Unsupervised	0.004	0.072	0.072	0.593	-0.13	-0.109

Figures 4.3.7-4.3.11 shows scatter plots of retrieved *EF* to tower *EF* for all five study areas using optimal variation after wet pixels were added to the calibration. A very good relationship was produced for Disney, Everglades and Kennedy. Big Cypress produced a fairly good fit. Although the *Bias* and *MAE* did not change much from dry pixel alone, a larger range of retrieved *EF* was produced. The Gainesville results still produced a large amount of error even after the wet pixels were added.
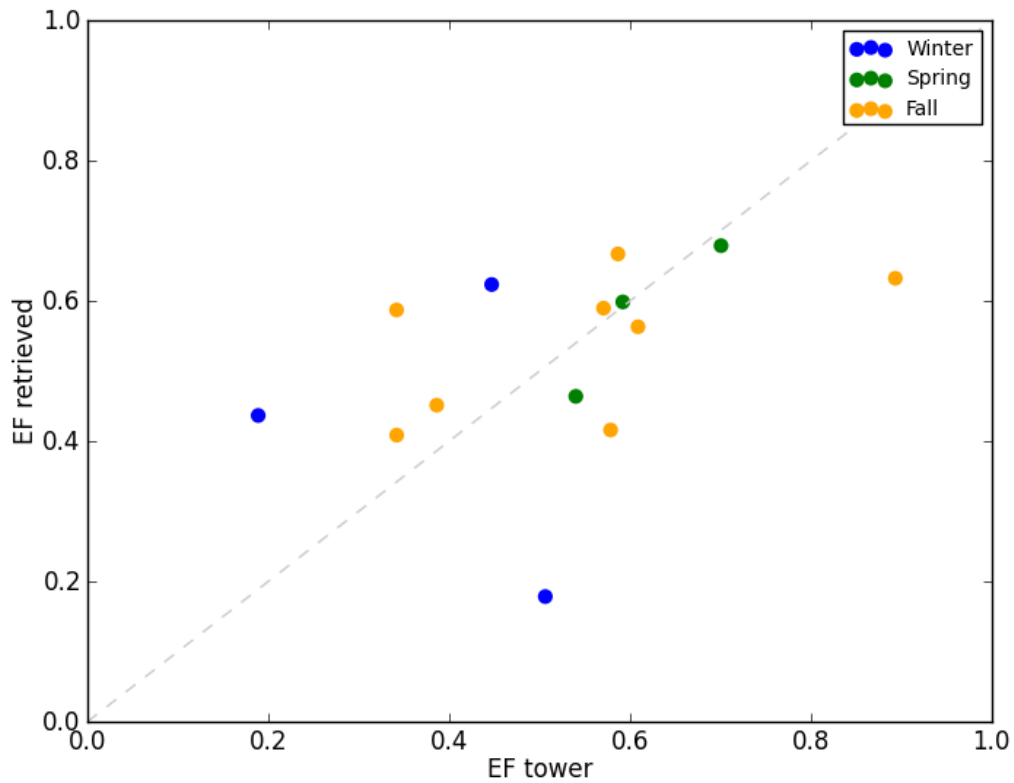
Figure 4.3.7: Optimal *EF* Retrieved vs. *EF* Tower for Big Cypress by Season
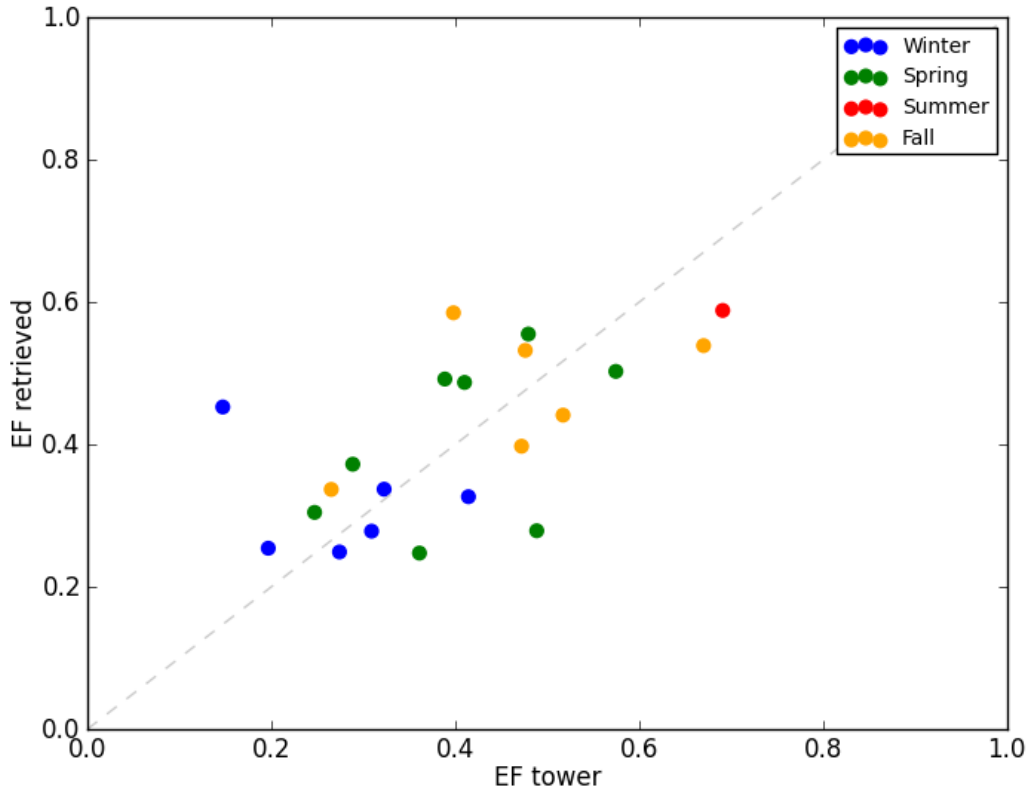
Figure 4.3.8: Optimal *EF* Retrieved vs. *EF* Tower for Disney by Season
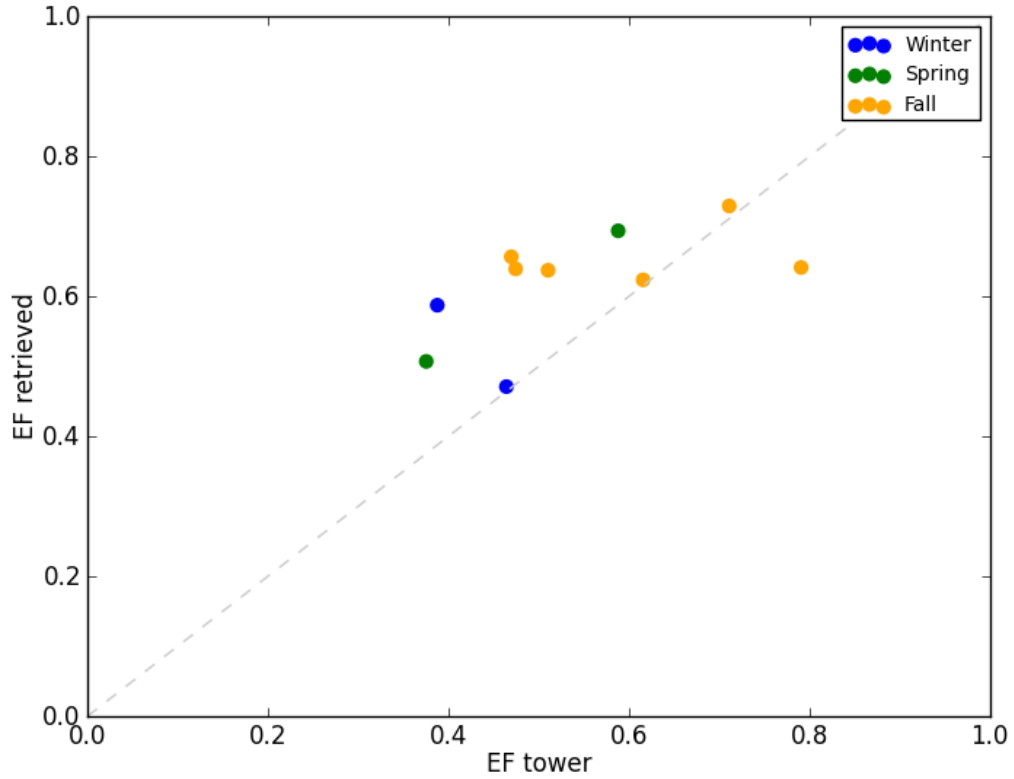
Figure 4.3.9: Optimal *EF* Retrieved vs. *EF* Tower for Everglades by Season

140
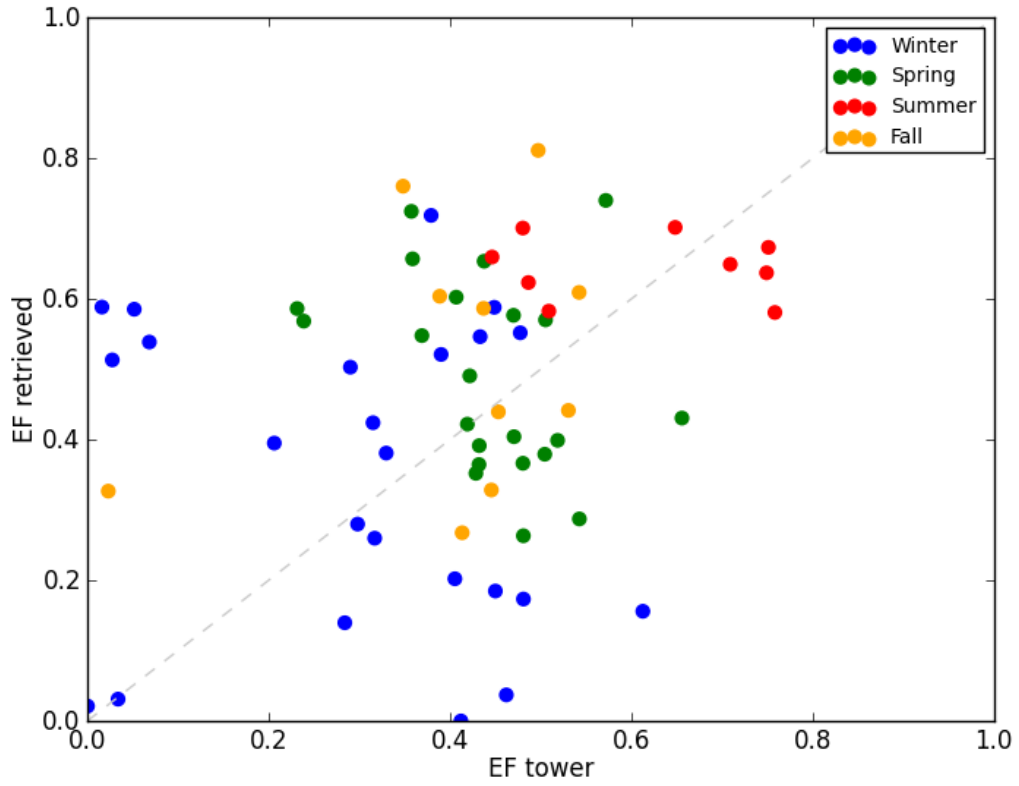
Figure 4.3.10: Optimal *EF* Retrieved vs. *EF* Tower for Gainesville by Season
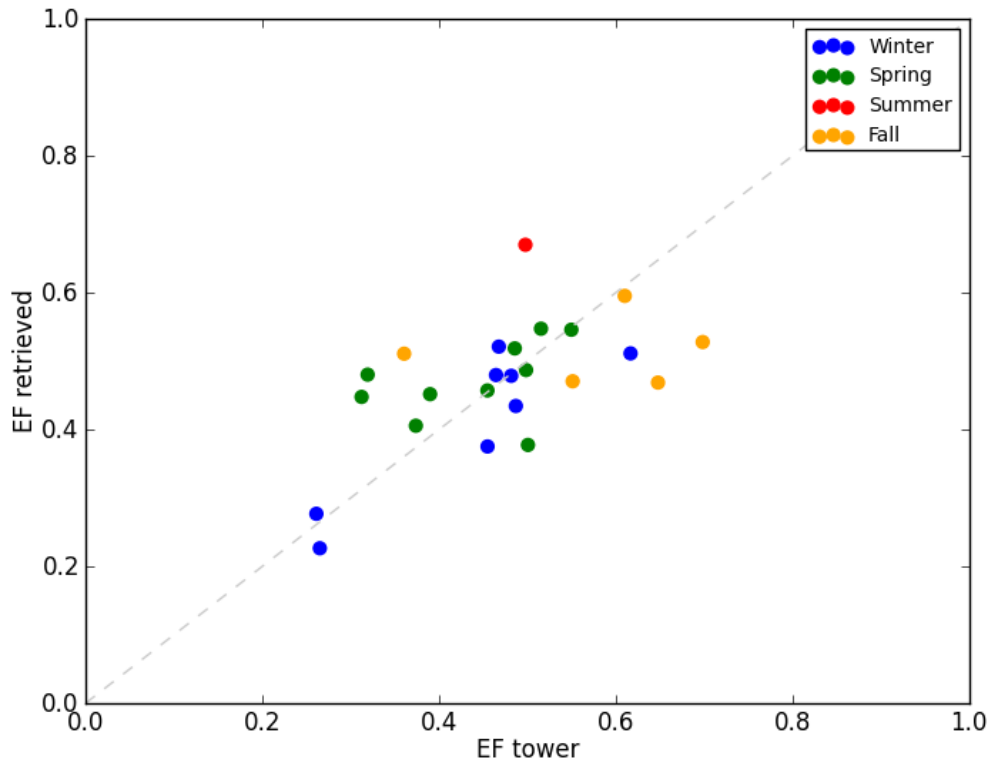
Figure 4.3.11: Optimal *EF* Retrieved vs. *EF* Tower for Kennedy by Season

4.3.3 Comparison of Dry Only Calibration to Calibration Including Wet Pixels

The results for optimal variations of both dry only calibration and that which includes wet pixels is shown in Figure 4.3.12. The figure shows very little difference for Big Cypress and Gainesville in terms of *Bias* and *MAE*. Big Cypress experienced a slight decrease in *Bias* when wet pixels were introduced and slight increase in *MAE* while Gainesville experienced a slight decreases in *MAE*. Disney, Kennedy and Everglades were affected strongly by the introduction of wet pixels into the algorithm. The Kennedy study area experienced the greatest reduction in both *Bias* and *MAE*. The introduction of wet pixels for Disney resulted in a very low *Bias* and *MAE* less than 0.1. The Everglades was also improved except the *Bias* is still a significantly positive number while the *MAE* is similar to Disney and Kennedy. The low bias error for most of the study areas is a good sign in terms of aggregating *ET* over monthly or seasonal periods. Although there might be significant errors at the daily time scale as described by *MAE*, the daily errors should sum to acceptable values as shown by small *Bias* errors. It should be noted that the scenes in this study are skewed toward the dry season. Therefore, higher temporal resolution imagery such as MODIS would need to be fused with LANDSAT in order to investigate the performance of the algorithm at monthly or seasonal time scales.
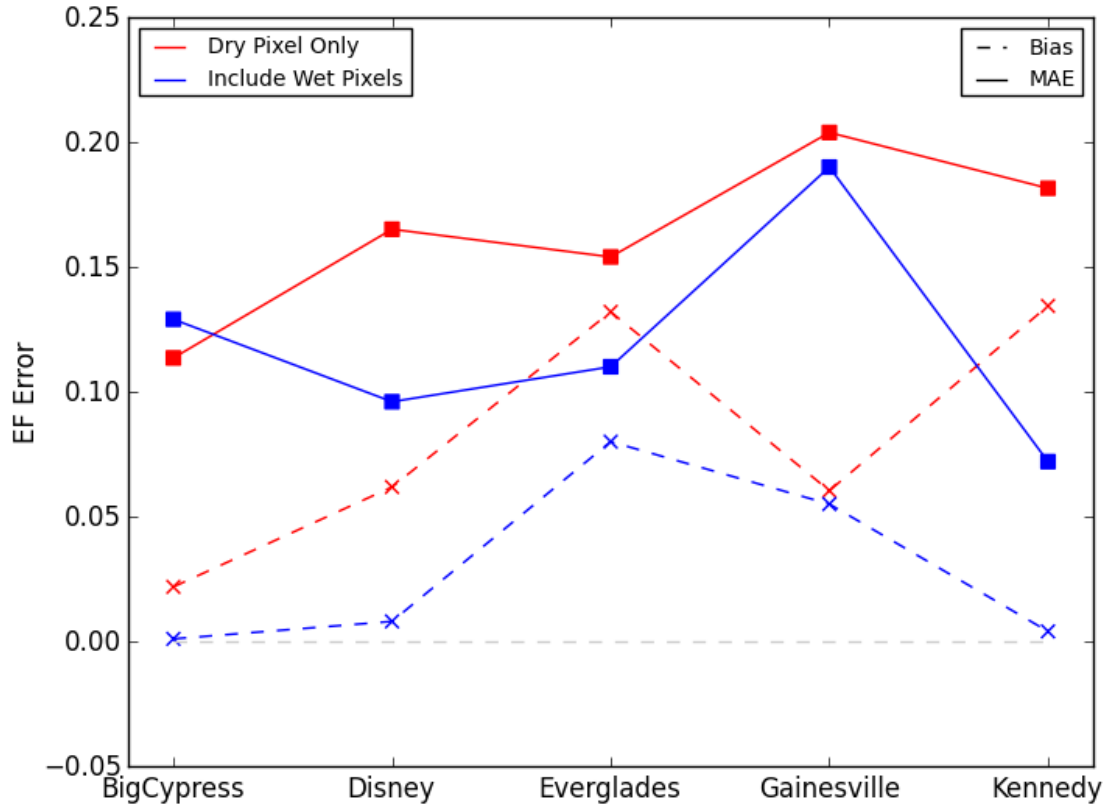
Figure 4.3.12: Comparison of Dry Pixel Only to Including Wet Pixels in Calibration

4.4 Mapping Spatial Variability of Evaporative Fraction

Maps of *EF* were produced for the optimal variations reported earlier. For Big

Cypress and Gainesville the optimal dry pixel only calibrations shown in Table 4.2.1

were used. For Disney, Everglades and Kennedy the optimal dry with wet pixel

calibrations shown in Table 4.3.1 were used. The *EF* maps from all of the useable days

were averaged to produce a mean *EF* map for each study. The absolute deviation with

respect to the mean map was averaged to produce a mean absolute deviation (*MAD*) map

for each study area. These maps are shown in Figures 4.4.1 – 4.4.10. It should be noted

that these average maps do not represent a climatological average for the study area

because the sample of satellites scenes is small. Also the scenes only represent clear sky

days so that some seasons are represented more heavily than other seasons. These maps

143

are shown in order to demonstrate the ability of the algorithm to measure the spatial

variability of *EF* in the landscape. The mean maps say something about spatial variability

of *EF* while the *MAD* maps say something about the manner in which the temporal

variability of *EF* varies in space.
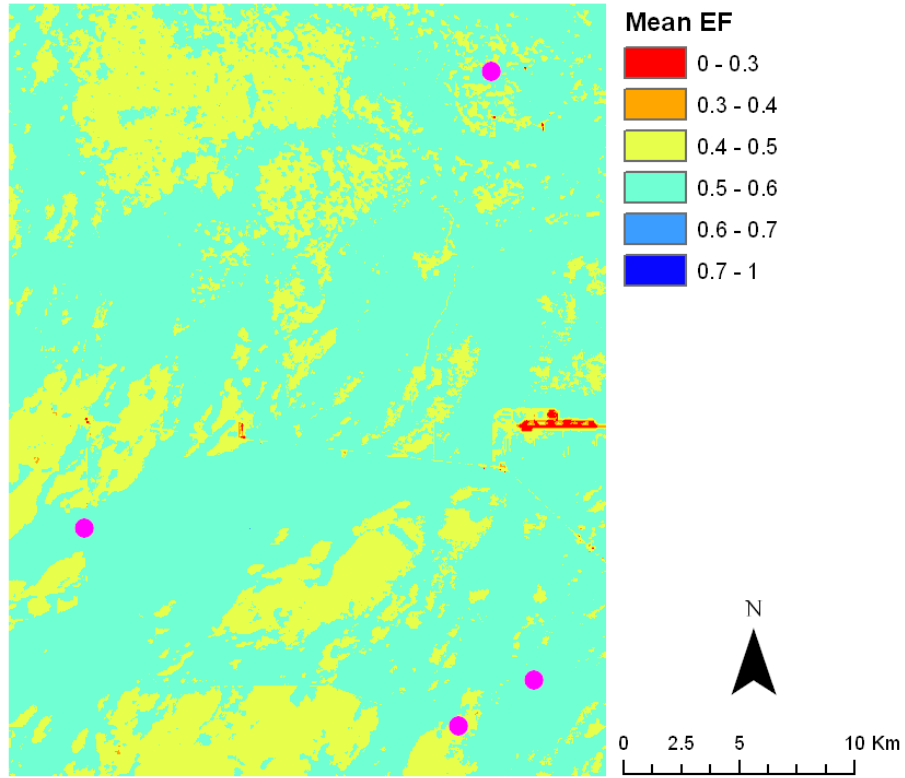
Figure 4.4.1: Mean *EF* for Big Cypress Using Optimal Dry Pixel Calibration
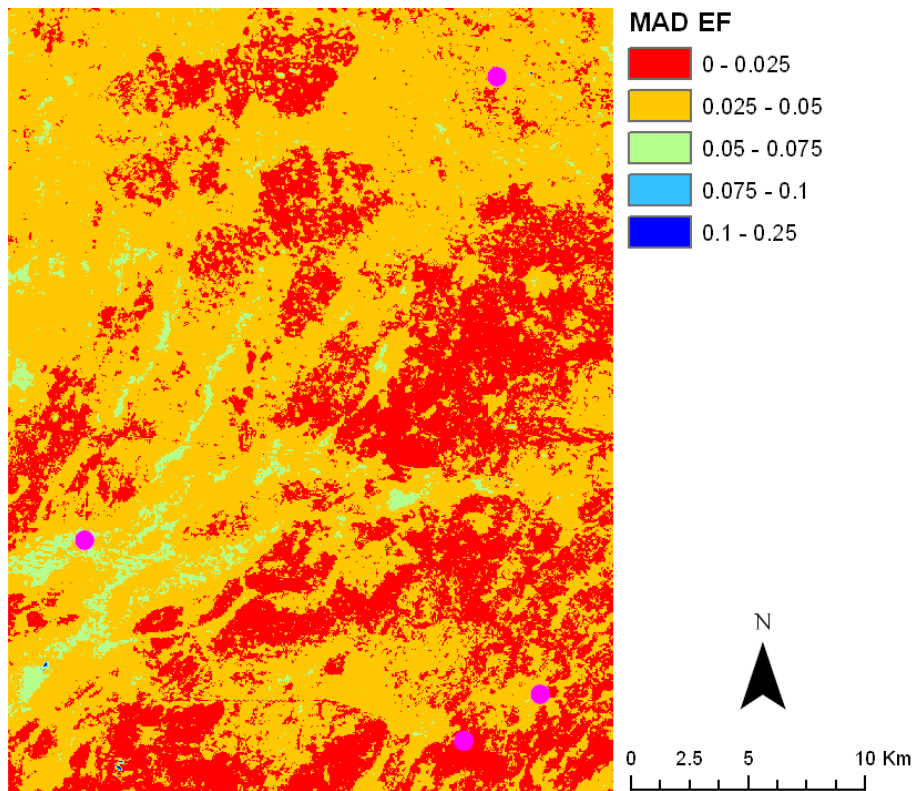
Figure 4.4.2: MAD *EF* for Big Cypress Using Optimal Dry Pixel Calibration

145
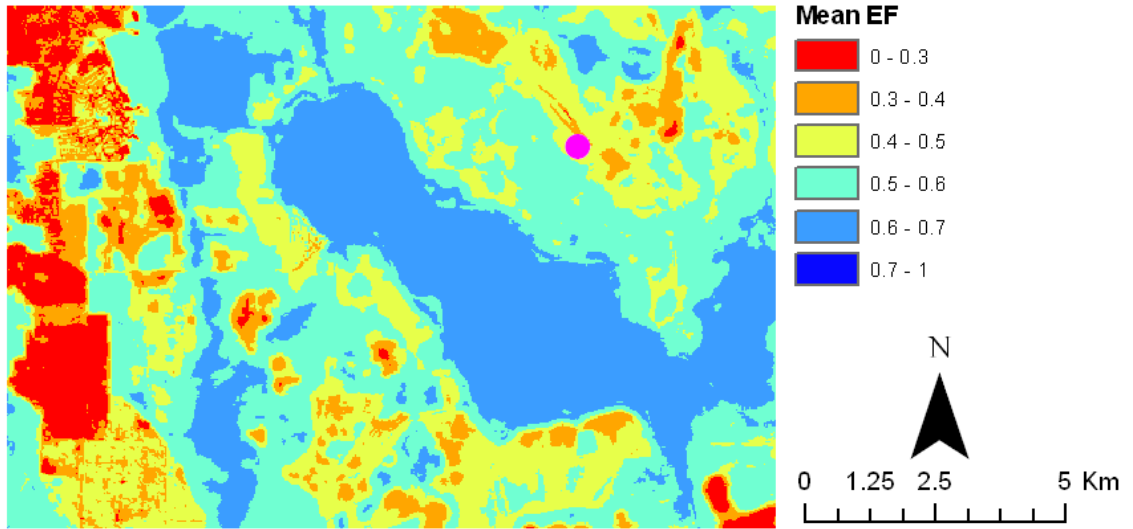
Figure 4.4.3: Mean *EF* for Disney Using Optimal Dry and Wet Pixel Calibration
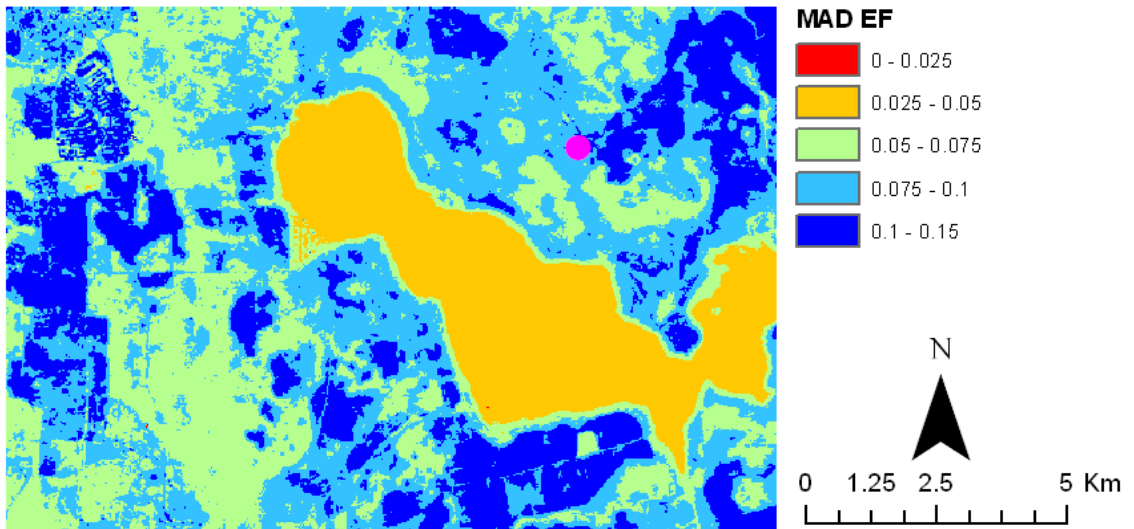
Figure 4.4.4: MAD *EF* for Disney Using Optimal Dry and Wet Pixel Calibration

146
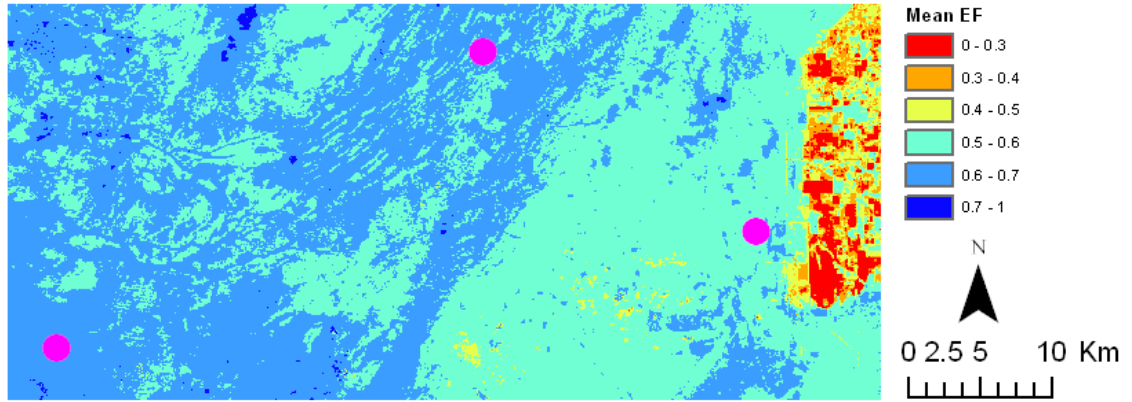
Figure 4.4.5: Mean *EF* for Everglades Using Optimal Dry and Wet Pixel Calibration
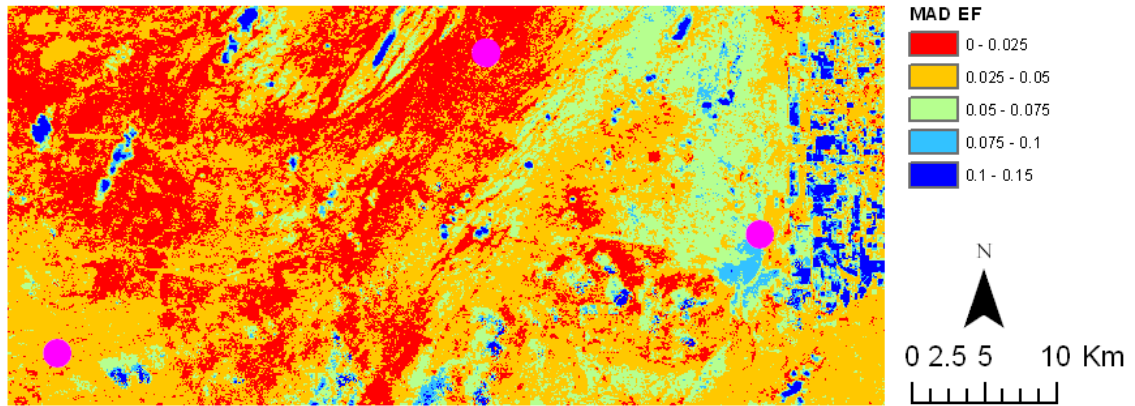
Figure 4.4.6: MAD *EF* for Everglades Using Optimal Dry and Wet Pixel Calibration
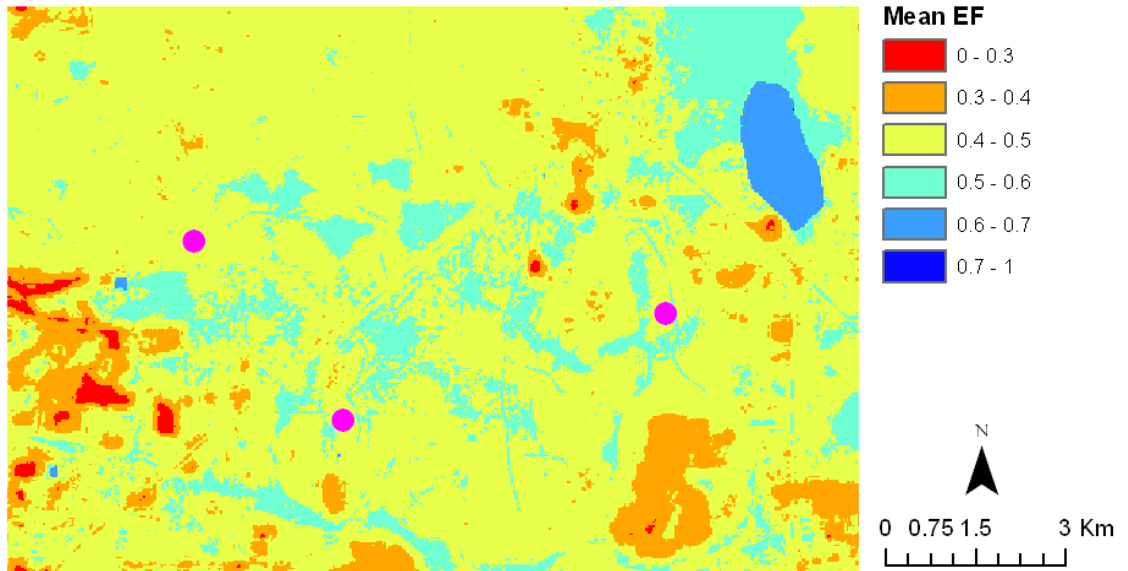
Figure 4.4.7: Mean *EF* for Gainesville Using Optimal Dry Pixel Calibration
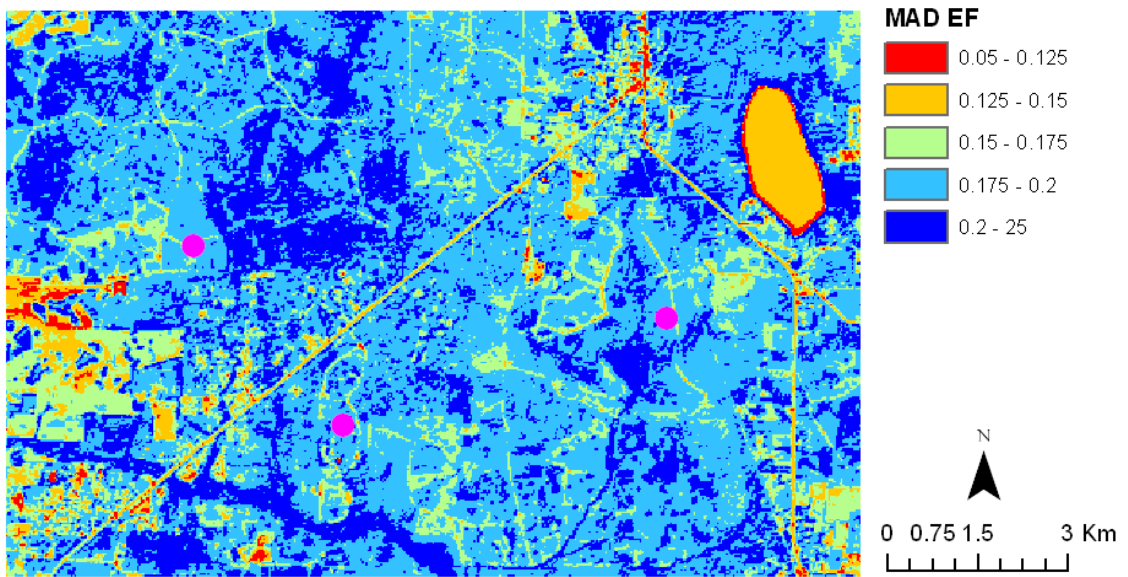
Figure 4.4.8: MAD *EF* for Gainesville Using Optimal Dry Pixel Calibration
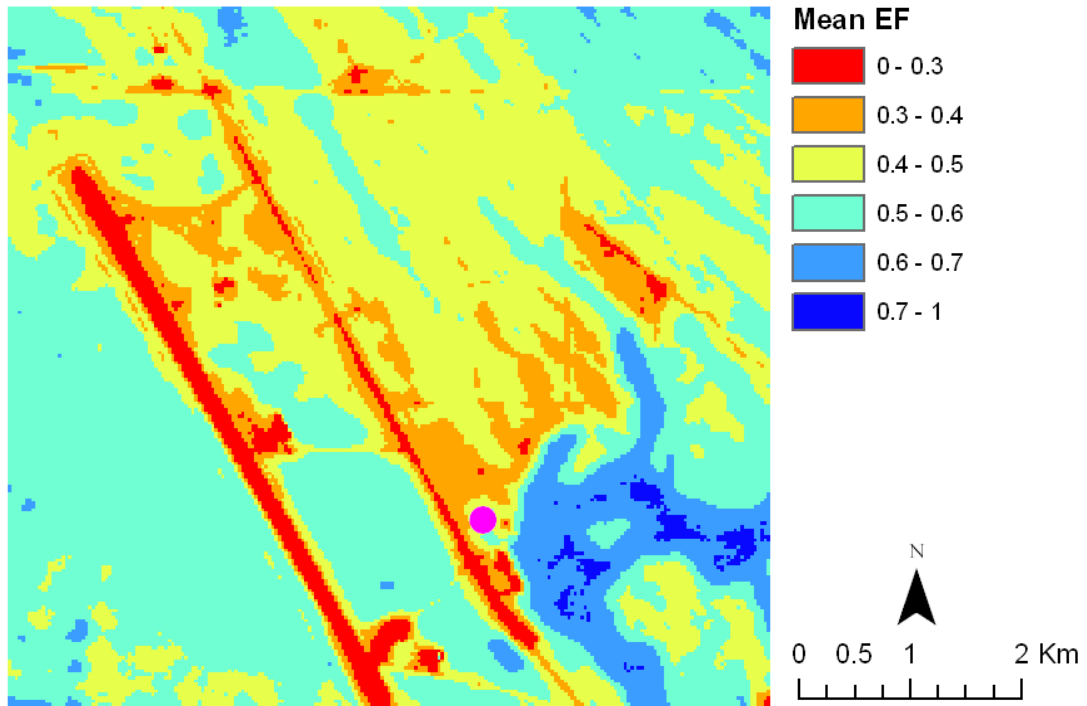
Figure 4.4.9: Mean *EF* for Kennedy Using Optimal Dry and Wet Pixel Calibration
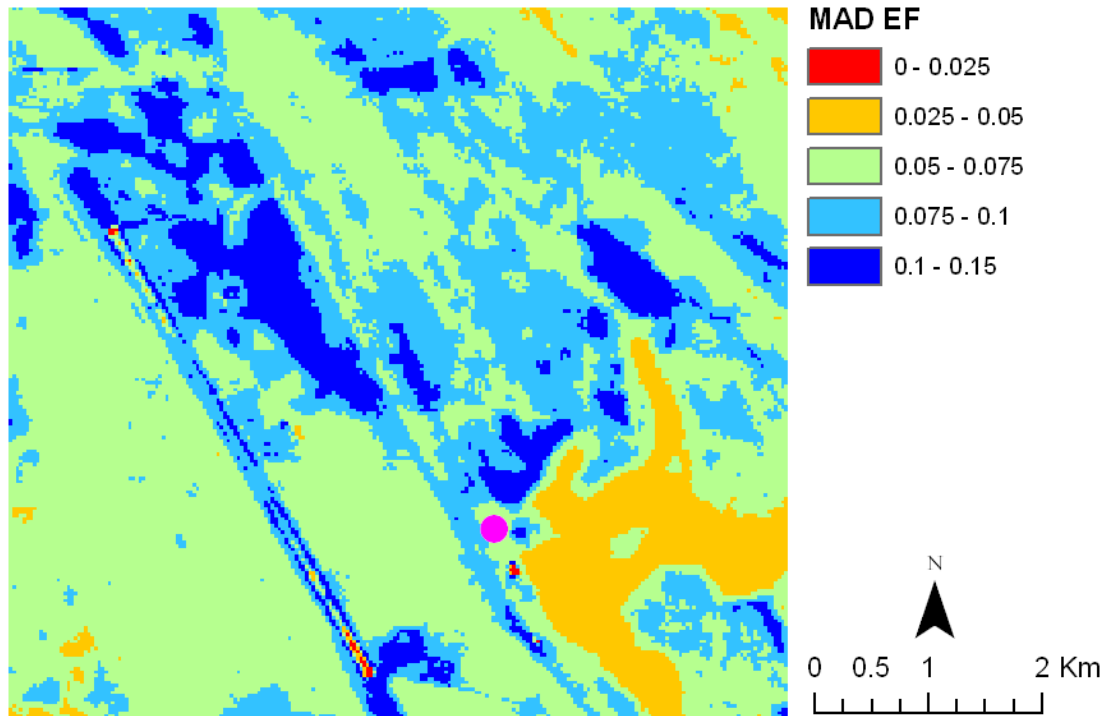
Figure 4.4.10: MAD *EF* for Kennedy Using Optimal Dry and Wet Pixel Calibration

The spatial variability of Big Cypress as shown in Figure 4.4.1 is not very large. *EF* ranges from 0.4 to 0.6 except for the airport and other dry areas. The temporal variability of *EF* produced is less than 0.05 for most of the study area. The Cypress swamp area is experiencing the highest temporal variability based on the limited number of scenes available for Big Cypress. Disney has a high degree of spatial variability because of the developed area to the west which is very dry and the lake which has a high *EF*. The flux station is located in an area of intermediate *EF*. The temporal variability *EF* for the Disney study area varies spatially from 0.025 to 0.15. The lake has the least temporal variability while the dry areas have larger temporal variability. It would seem that the dry areas would have a low variability in *EF* because *EF* should be close to zero in dry areas. This could be an indication of the algorithm to overestimate *EF* in dry areas or possibly these areas are not completely dry. The Everglades study area contains large *EF* values with low spatial variability other than the agricultural area to the east. The temporal variability is largest in the east in dry parts of agricultural area. It should be noted that since there is a small number of scenes available for Big Cypress and Everglades, these maps do not represent the actual variability of *EF*. For Gainesville, features such as the lake, runoff areas, and chronically disturbed areas are distinguished from the areas of typical vegetation shown in yellow. For the majority of the scene, the average *EF* is fairly smooth because of the long time period of scenes that were used. However, the land surface is constantly changing as timber is cleared but over the time period used the vegetation in these areas grow back and the disturbance is not very evident on the mean *EF* map. Some of this variability of the land surface conditions should be reflected in the high temporal variability of *EF* observed, but a portion is also

150

due to changes in the atmospheric conditions. Since the lake is not experiencing any change in surface type, the temporal variability is only made up of change in atmospheric conditions. The higher temporal variability of vegetation compared to the lake is due to change of vegetation conditions in the landscape. The Kennedy Space Center study area shows a large degree of spatial variability. The runway and open water feature clearly distinguish themselves. Also there is a disturbed area with low *EF* near the middle of the scene. The temporal variability is similar to Disney in that the dry areas have more variability than the vegetated areas. This would make sense for the disturbed areas which are impervious and could be experience variability in moisture content, but for the runway it is probably due to errors in the algorithm.

Figure 4.4.11 demonstrates the spatial and temporal variability of the *EF* maps produced for Gainesville study area using the optimal dry pixel only calibration method. Figure 4.4.7 and 4.4.8 shows maps of the *EF* and absolute deviation of *EF* averaged over time. Figure 4.4.11 shows the *EF* and the absolute deviation of *EF* which has been spatially averaged instead. The blue points represent the average *EF* of each scene and the red points measure the mean absolute deviation of *EF* for each scene. The blue line is the average of all the blue points while the red line is the average of all the red points. The variability of the blue points represents the temporal variability of the mean state of each scene. This variability can be quantified by taken the mean absolute deviation of the blue points producing the constant value shown in green. The red points represent the spatial variability of *EF* for each scene and the red line represent the average spatial variability. The green and red line can be used to compare the spatial and temporal variability of *EF* for the useable clear sky scenes. For the Gainesville case shown in

151

Figure 4.4.11, the temporal variability is more than twice the spatial variability. Figure

4.4.12 shows the temporal and spatial variability values for all study areas from maps

produced using optimal variation. The largest temporal variability is for Gainesville while

the lowest is for Big Cypress and Everglades. For Big Cypress the spatial and temporal

variability are very similar. For all other cases except Gainesville the spatial variability is

greater than the temporal variability. Figure 4.4.13 shows this type of spatial and

temporal variability but for instantaneous actual *ET* at time of satellite overpass. This

shows that temporal variability has increased relative to spatial variability. It would seem

that when available energy was multiplied by *EF* the spatial variability of actual *ET*

would be accentuated because darker areas (more energy) should be wetter (more *EF*)

than lighter areas (less energy). Figure 4.4.13 implies that this effect is counteracted by

the manner in which the temporal variability of available energy is more than the spatial

variability of available energy.
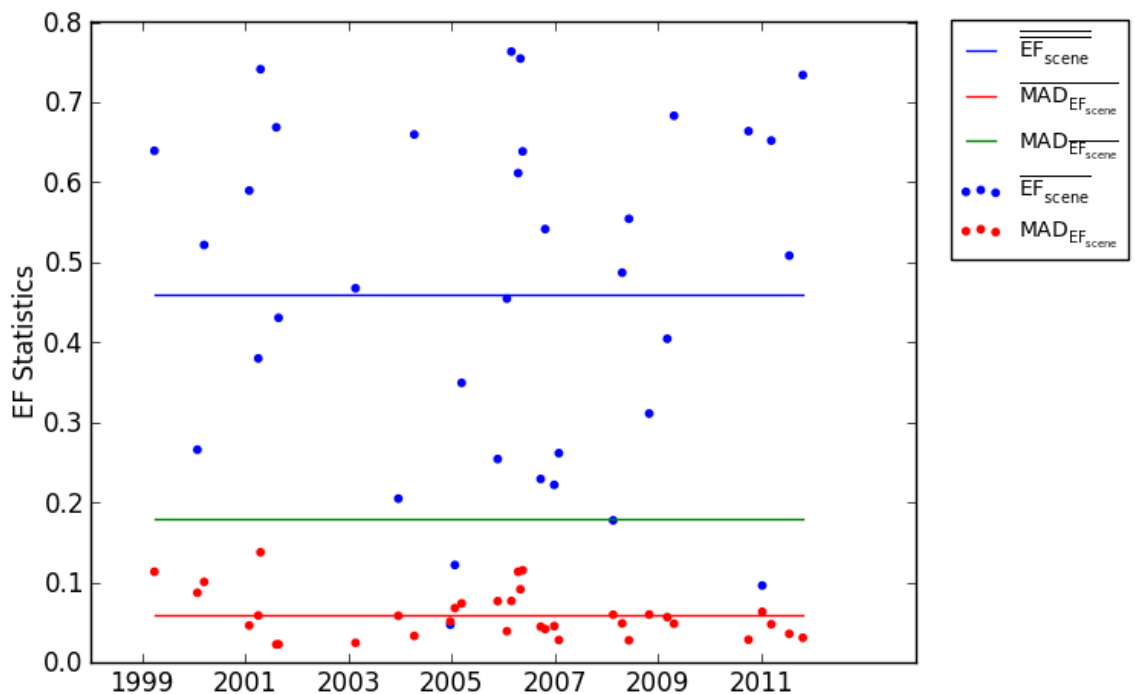
Figure 4.4.11: Spatial and Temporal Variability of Gainesville Optimal Variation
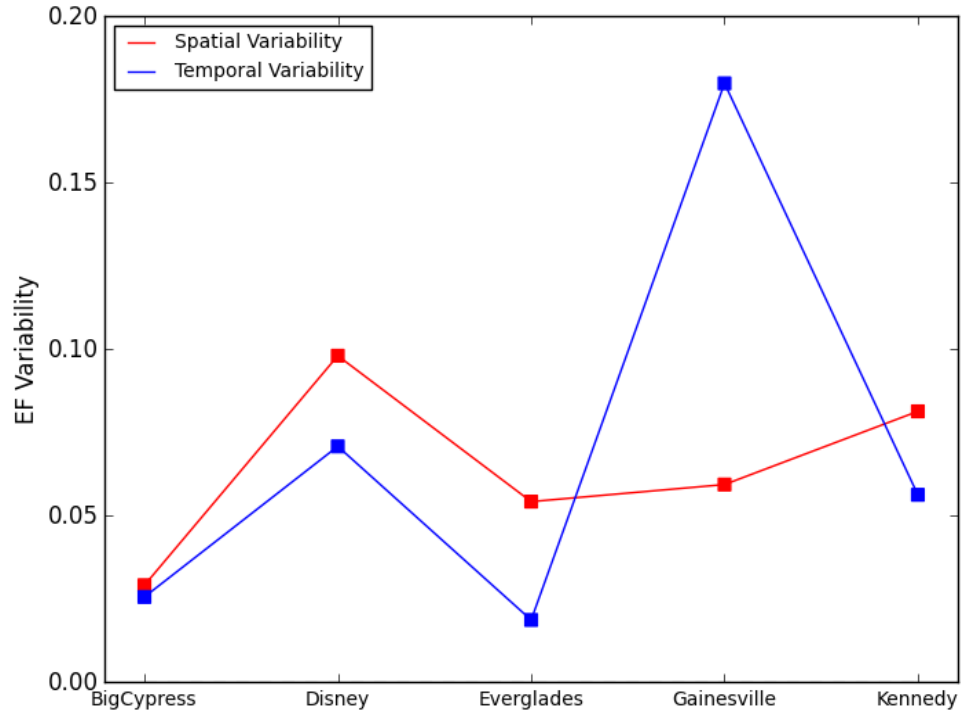
Figure 4.4.12: Spatial and Temporal Variability of Study Area's Optimal Variations
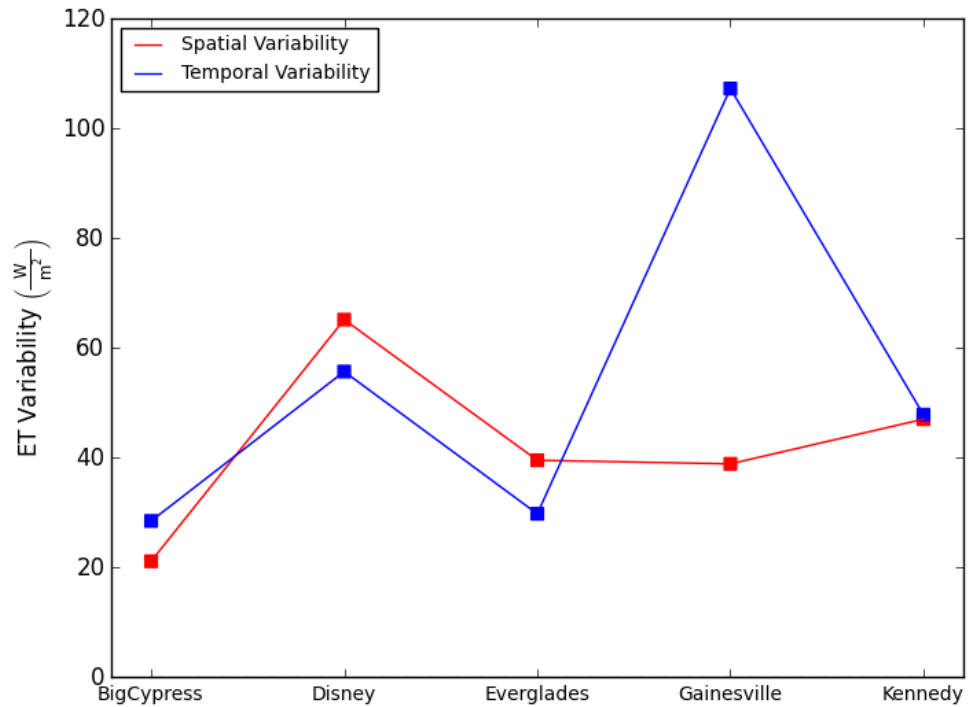
Figure 4.4.13: Spatial and Temporal Variability of Study Area's Optimal Variations

Figure 4.4.14a shows the mean *EF* map for the Mangrove extent when the
calibration points came only from the Mangrove extent. Figure 4.4.14b shows the mean
EF map for the Mangrove extent when the calibration points only came from the full
Everglades extent. The full extent variation was optimized considering all Everglades
validation points while the Mangrove extent variation was optimized only considering
Mangroves. The optimal Everglades variation is the same as used in *EF* map above and
the optimal Mangroves variation is *ΔT* vs. *T*, Even Bins, with $NDVI_{min}$ wet pixel. The *EF*
error for the Mangrove stations when using full extent is *Bias*=*MAE*=0.096 and the *EF*
error when using Mangrove extent is *Bias*=-0.03 and *MAE*=0.104. The extreme
difference in maps between the two cases reveals the problem of judging the success of
mapping algorithm using flux towers. Although the map in which calibration points only
came from Mangrove extent seemed to fit the Mangrove stations better, the map that was
produced does not seem likely. Figure 4.4.14a has a large portion of the landscape with
very low *EF* which does not seem sensible for such a wet environment. This problem is
most likely due to the absence of dry calibration points in the Mangroves extent.
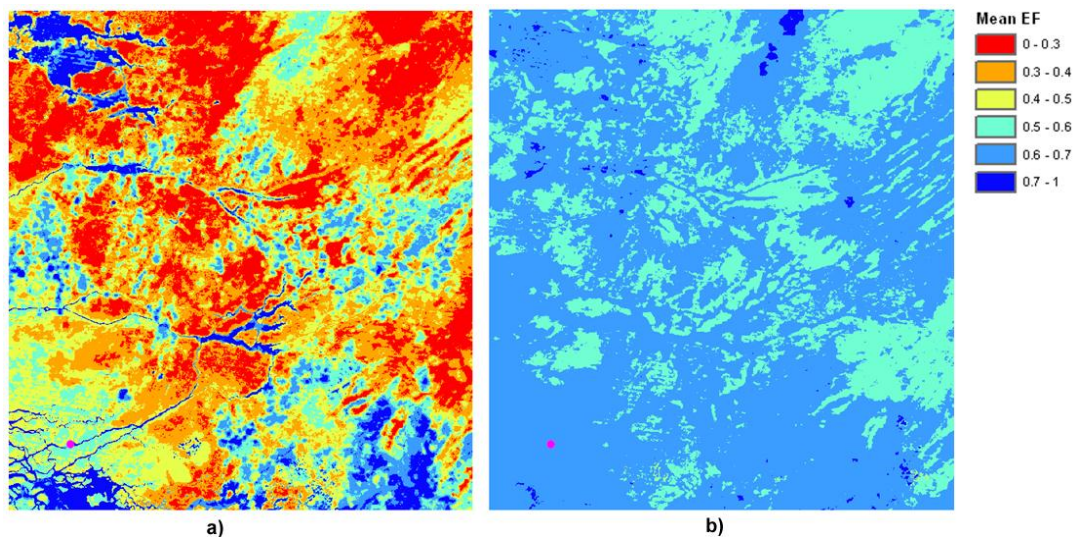
**Figure 4.4.14: Difference in Mean *EF* Maps for Mangroves Extent When
Calibration Points Chosen from Different Extents**

4.5 Validation using Instantaneous Actual Evapotranspiration

    4.5.1 Comparison of Satellite Available Energy to Tower Available Energy

    Figures 4.4.1-4.4.5 compare the available energy estimated by the radiometer at the eddy flux station to the available energy estimated using the satellite imagery averaged over the radiometer footprint. As discussed previously in methodology section, the radiometer footprint is not much larger than size of LANDSAT pixel. The satellite consistently overestimates energy for Big Cypress as shown in Figure 4.4.1. There does not seem to be a pattern based on a particular station, but wet prairie seems to have the most agreement. No seasonal pattern is obvious other than the error increasing as the available energy is reduced. The most likely reason for the overestimation of available energy by the satellite is because the algorithm did not account for the energy being stored in the water. The amount of energy stored in standing water that exists in Big Cypress can result in a substantial reduction in available energy. The measurements of available energy for the tower accounted for this process (Shoemaker et al, 2011). There is a very good agreement between satellite and tower for Disney as shown in Figure 4.4.2. There is a small tendency for the satellite to underestimate the energy as available energy increases. A similar pattern occurs for Kennedy as shown in Figure 4.4.3 except the underestimation is more extreme. All of the spring measurements are significantly underestimated by the satellite. The underestimation for Kennedy could possibly be due to an underestimation of down welling long wave radiation by the satellite. The satellite algorithm did not take into account the increase in precipitable water that should occur near the coast. For the Everglades, Figure 4.4.4 shows different patterns depending on station. The energy at the Mangroves stations are consistently overestimated, while the

155

Long and Short Marsh are underestimated most of the time. The winter points have small error while the underestimation of the other Marsh points intensifies as available energy increases. For Gainesville the energy is both over estimated and underestimated as shown in Figure 4.4.5. There is no clear difference between stations except Austin Carey seems to show the most agreement. Summer and fall produce less error than winter and spring. Table 4.5.1 shows a summary of the errors for each study area. Disney and Kennedy show significant *Bias*, but small variability around this bias. The *MAE* for Kennedy is much larger than *MAE* for Disney. Gainesville produced an acceptable *MAE* and small *Bias*. Big Cypress and Everglades produced a large *MAE* but Everglades have very little *Bias* compared to the *Bias* for Big Cypress. These errors should have a significant effect on the actual *ET* calculation, but the intent of the algorithm was to produce evaporative fraction *EF* which could be multiplied by sources of daily available energy which would be more accurate. LANDSAT only offers snapshots of available energy which are required for calculating *EF*. In a future section the sensitivity of the estimation of *EF* to available energy is investigated. Still, it was important to look at the results of actual *ET* because of the correlation and interaction of *EF* and Energy could lead to different optimal retrieval variations.
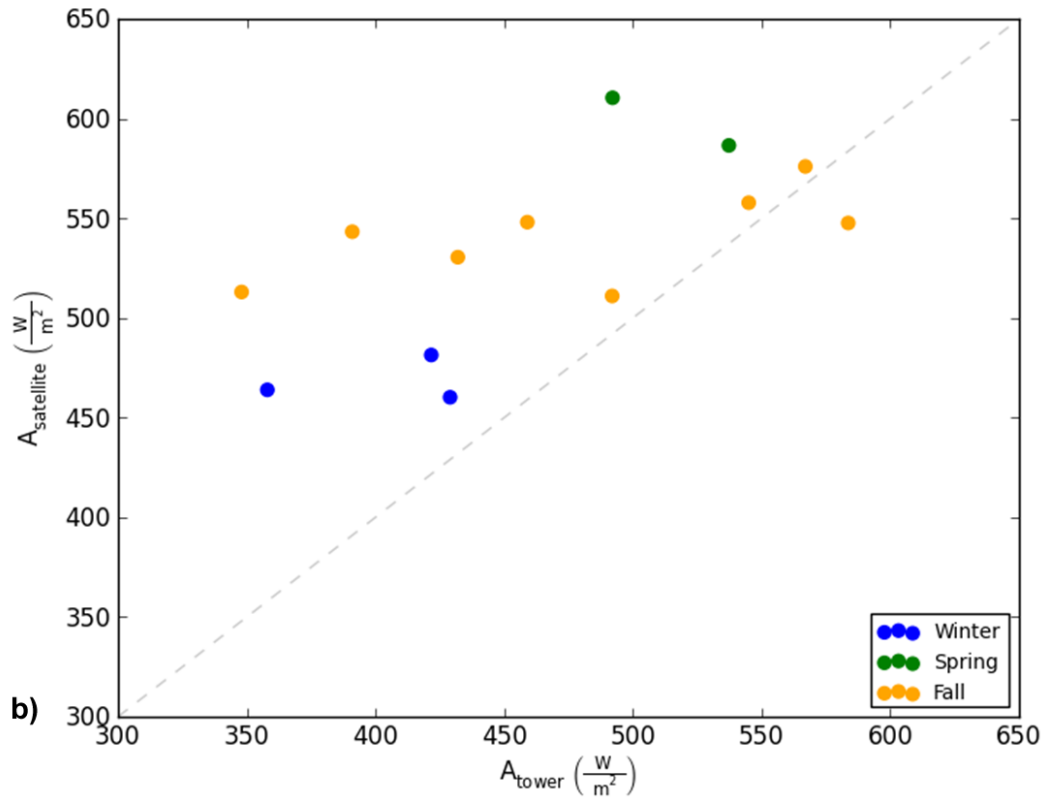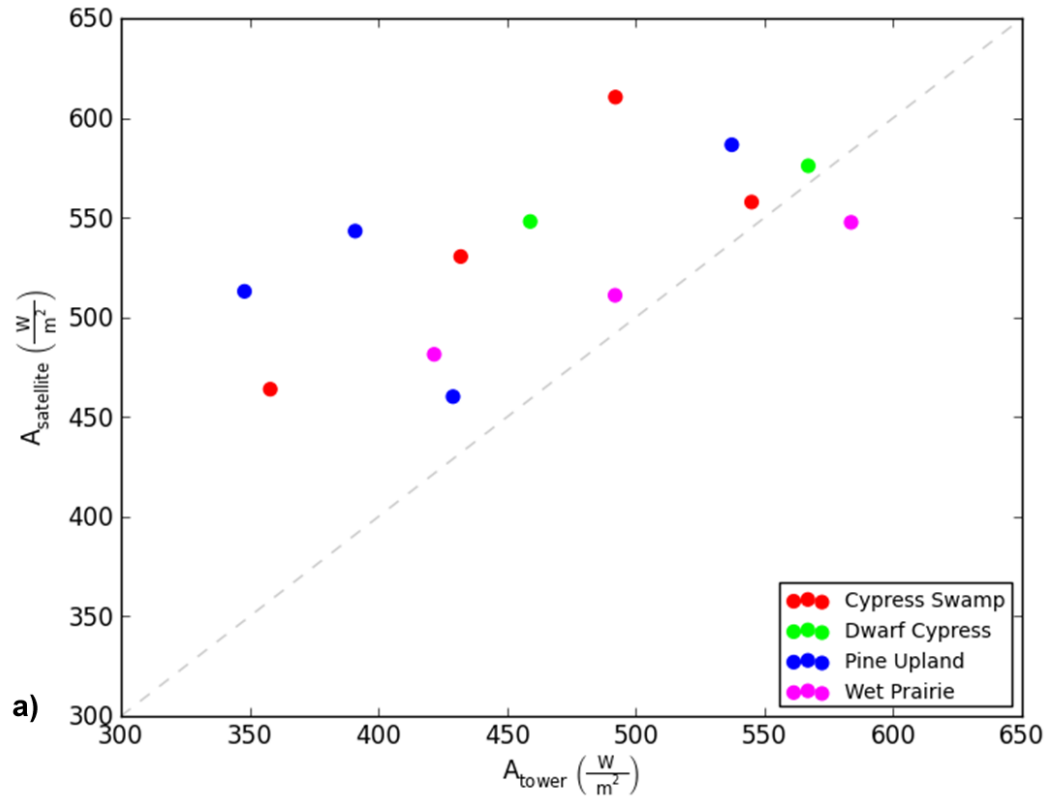
Figure 4.5.1: Big Cypress Available Energy$_{Satellite}$ vs. Available Energy$_{Tower}$
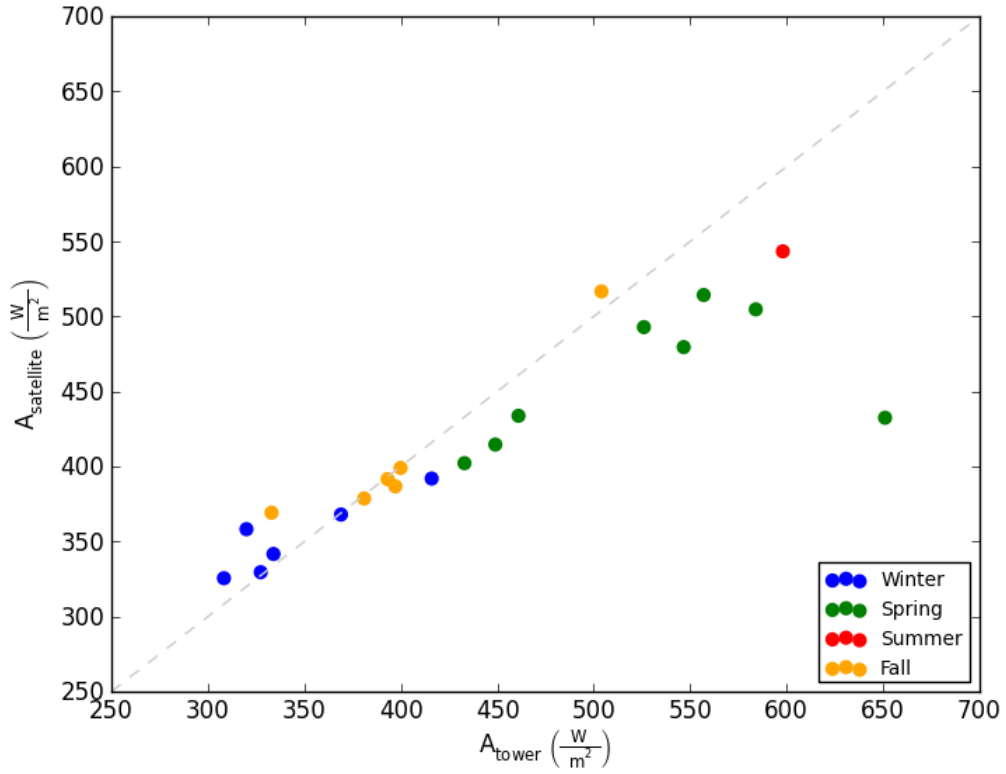
Figure 4.5.2: Disney Available Energy_{Satellite} vs. Available Energy_{Tower}
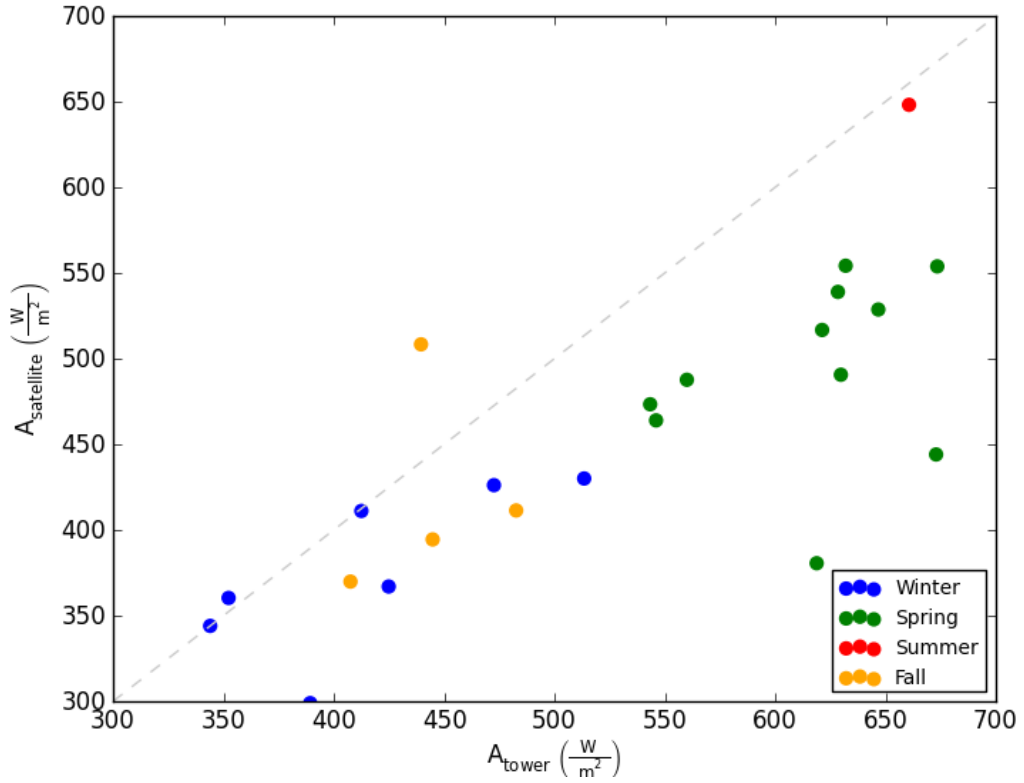
Figure 4.5.3: Kennedy Available Energy_{Satellite} vs. Available Energy_{Tower}
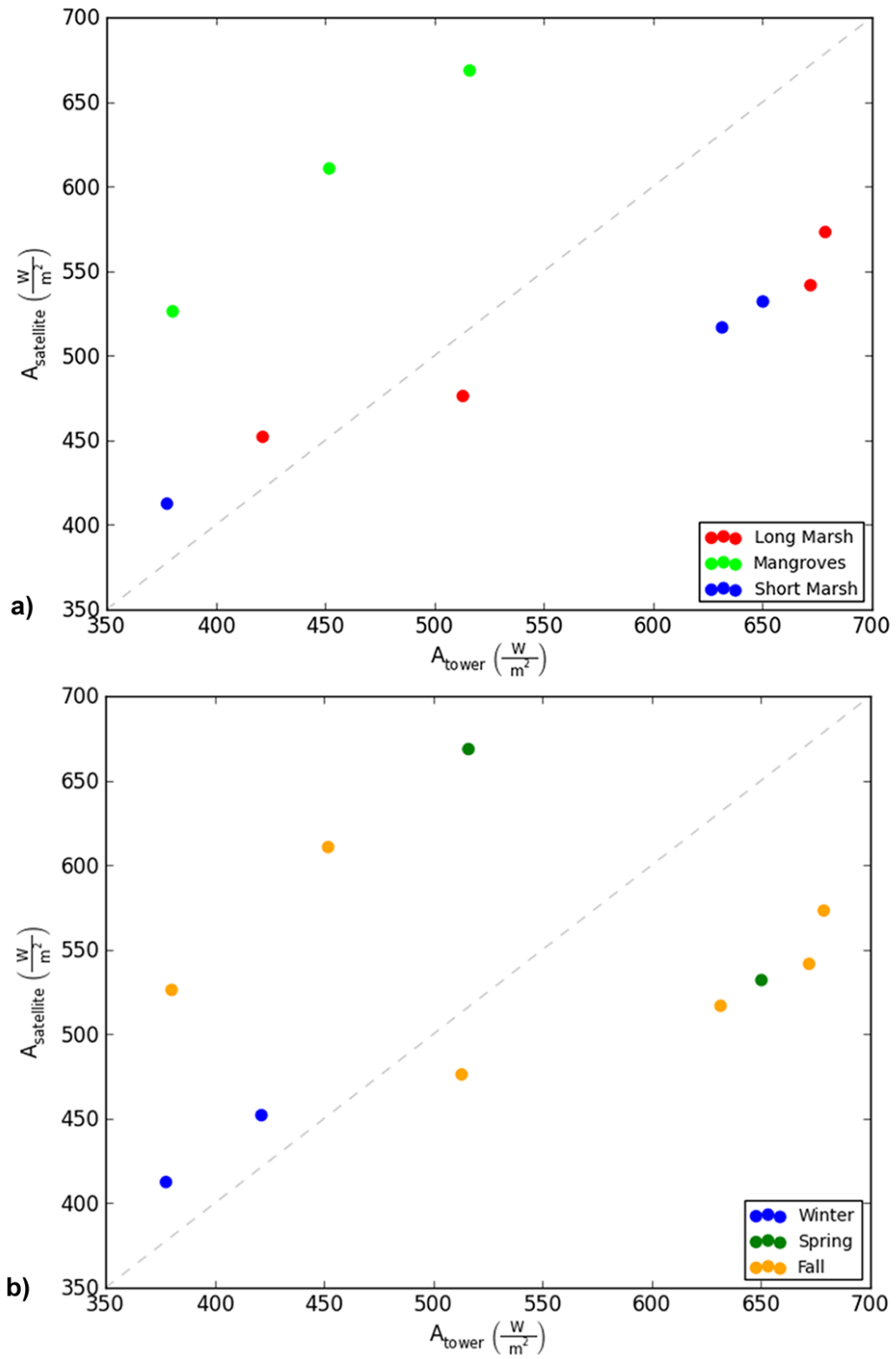
Figure 4.5.4: Everglades Available Energy$_{Satellite}$ vs. Available Energy$_{Tower}$

Figure 4.5.5: Gainesville Available Energy_{Satellite} vs. Available Energy_{Tower}
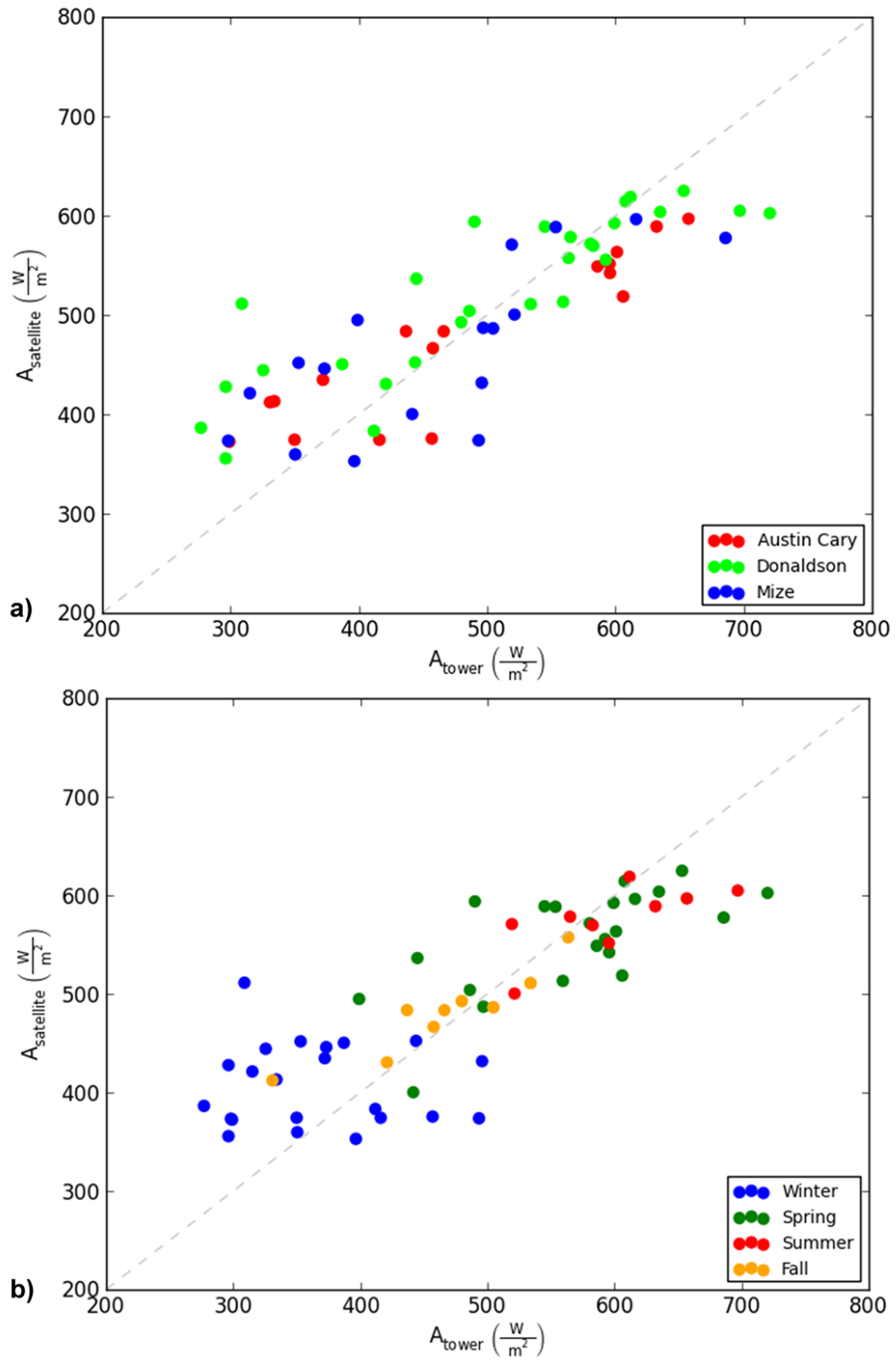
Figure 4.5.5: Gainesville Available Energy$_{Satellite}$ vs. Available Energy$_{Tower}$

Table 4.5.1: Errors between Satellite and Tower Available Energy for All Study Areas

Study Area	Bias ($^{W}/_{m^2}$)	MAE ($^{W}/_{m^2}$)	ρ
BigCypress	93.693	98.838	0.145
Disney	-24.464	35.342	0.88
Everglades	1.7	102.843	0.326
Gainesville	12.498	56.022	0.833
Kennedy	-74.564	81.24	0.777

4.5.2 Comparison of Satellite Instantaneous *ET* to Tower Instantaneous *ET*

The goal of the retrieval algorithm in this dissertation was to retrieve *EF* values which could be multiplied by external sources of daily averaged available energy. Because actual *ET* is the desired result for most users, it should be used as the criteria for comparing calibration variations. This can lead to different results because of 1) correlation between the errors in *EF* and available energy 2) errors in available energy itself. The comparison of *ET* retrieved from satellite to that measured by the flux tower was done using the instantaneous *ET* retrieved at the time of the satellite overpass. Daily averaged *ET* would be more useful to most parties, but converting the snapshot of *ET* produced by satellite imagery to daily *ET* would produce additional error. Therefore, instantaneous *ET* is used so that the error due to the various calibration techniques can be isolated from the errors due to extrapolating to daily *ET*.

Figure 4.5.6 shows the variation of the *Bias* and *MAE* errors in instantaneous *ET* when the dry pixel only calibration was used. For each study area, the results for all model and boundary variations are shown. The *ΔT* vs. *T* model variation is the best for almost all study areas. There is little variation in *MAE* with respect to the boundary type for *ΔT* vs. *T*, while a bit more variation exists for the *Bias* error. The best variation all

around would be *ΔT* vs. *T* with Even Bins. Table 4.5.2 shows the optimal results using the dry pixel only calibration. For Big Cypress and Gainesville the Min Max boundary was better than Even Bins, but the difference wasn't large. Optimizing with respect to *ET* instead of *EF* resulted in the model variation changing from *H* vs. *T* to *ΔT* vs. *T* for Big Cypress. Both models had similar *MAE* but *Bias* is 50.5 W/m² for *H* vs. *T* compared to -14.9 W/m² for *ΔT* vs. *T*. For Kennedy and Disney the neutral model had low errors but the ρ values were much less than *ΔT* vs. *T*.
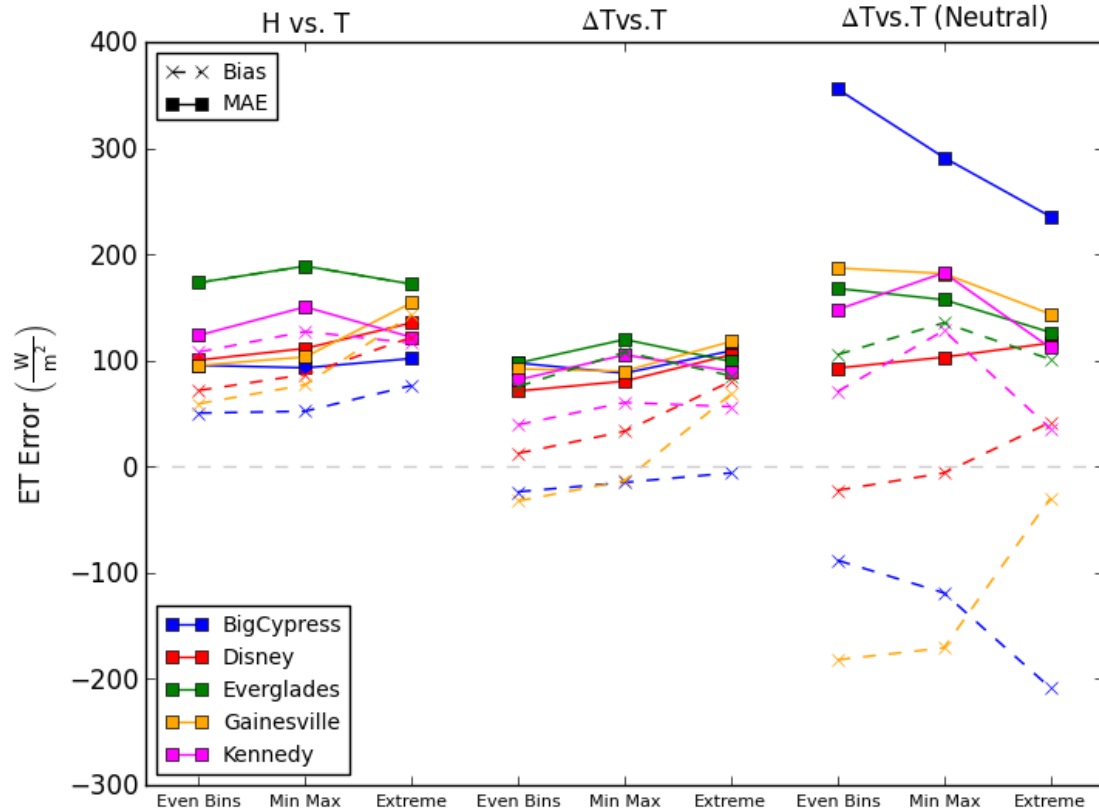
Figure 4.5.6: *Bias* **and** *MAE ET* **Error of All Models and Boundary Types**

Table 4.5.2: Optimal Variations of Dry Pixel Only Calibration Based on Actual ET

Study Area	Model	Boundary	α Filter	Bias ($^W/_{m^2}$)	MAE ($^W/_{m^2}$)	ρ
BigCypress	ΔT vs. T	Min Max		-14.876	87.982	0.334
Disney	ΔT vs. T	Even Bins		12.504	71.236	0.336
Everglades	ΔT vs. T	Even Bins	Yes	75.307	97.608	0.622
Gainesville	ΔT vs. T	Min Max	Yes	-13.219	89.992	0.491
Kennedy	ΔT vs. T	Even Bins	Yes	39.417	81.756	0.69

Figure 4.5.7 shows the variation of the *Bias* and *MAE* errors in instantaneous *ET* when wet pixels were introduced to the calibration. The results seem to vary among study areas more in this case. For Disney and Kennedy the *H* vs. *T* model is better for most variations. For Kennedy, *ΔT* vs. *T* and *NDVI*$_{Above}$ is similar for *MAE* but *Bias* is 23.4 W/m^2 for *ΔT* vs. *T* compared to -4.6 W/m^2 for *H* vs. *T*. For Everglades *H* vs. *T* with Unsupervised or *NDVI*$_{Below}$ is very similar to *ΔT* vs. *T* with *NDVI*$_{Below}$ except *Bias* is a bit lower and *MAE* a bit higher for *ΔT* vs. *T*. Gainesville is clearly the best using *ΔT* vs. *T* with *NDVI*$_{Below}$. It turns out that for Big Cypress the neutral model with *NDVI*$_{Above}$ produced the best result. It was comparable to other models for *MAE* but *Bias* is 48.4 W/m^2 for neutral compared to 55.4 W/m^2 for *ΔT* vs. *T*.
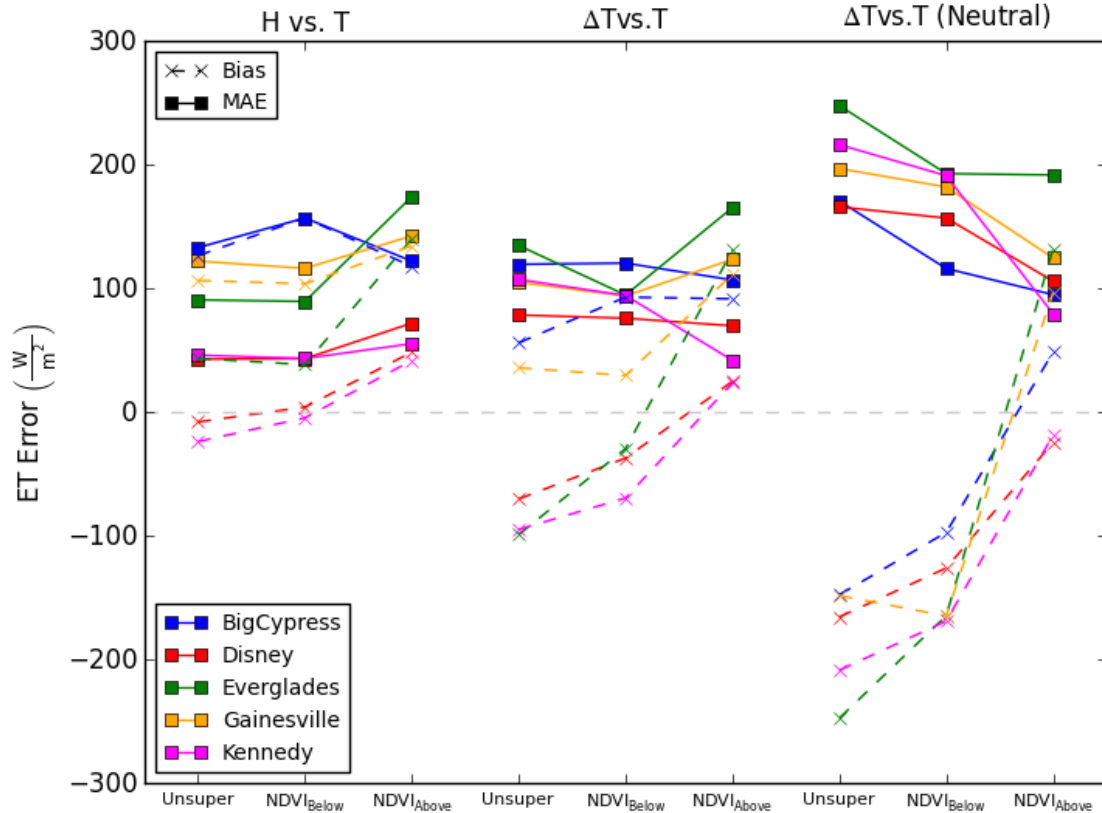
Figure 4.5.7: *Bias* **and** *MAE ET* **Errors of All Models and Wet Pixel Types**

Table 4.5.3: Optimal Variations after Including Wet Pixels Based on Actual ET

Study Area	Model	Classification	Bias ($^W/_{m^2}$)	MAE ($^W/_{m^2}$)	ρ
BigCypress	ΔT vs. T (Neutral)	$NDVI_{max}$	48.444	94.789	0.418
Disney	H vs. T	$NDVI_{min}$	4.068	43.138	0.761
Everglades	H vs. T	$NDVI_{min}$	37.709	87.94	0.471
Gainesville	ΔT vs. T	$NDVI_{min}$	28.51	92.378	0.535
Kennedy	H vs. T	$NDVI_{min}$	-4.601	43.186	0.778

Figure 4.5.8 compares the optimal variations based on actual *ET* of the dry pixel only calibration to the calibration which includes wet pixels. For Disney, Kennedy and Everglades both *Bias* and *MAE* errors were reduced. Even after adding the wet pixels, the algorithm is still significantly biased towards overestimating *ET* for Everglades. For Big Cypress and Gainesville, including wet pixels increases the *Bias* error significantly but

only increases *MAE* by a small amount. Table 4.5.4 lists the dry pixels only or wet pixels included algorithm which produced the final optimal variation. It also shows the *Bias* and *MAE* errors as a fraction of the average tower *ET*. For Disney and Kennedy the *Bias* as a fraction is less than about 2%, but for *MAE* the fraction is rather large. For the other 3 study areas the *MAE* becomes very large and the *Bias* becomes as large as 13% for Everglades. Although the *MAE* errors are larger, it is encouraging that the *Bias* error is low for many of the cases. The *MAE* reflects the manner in which the algorithm can predict *ET* for a specific day, but the *Bias* reflects the ability of algorithm to predict *ET* averaged over longer periods. A low *Bias* error would suggest that the algorithm could perform decently at producing daily or possibly seasonally averaged *ET*. Based on this, the algorithm would have potential for estimating long term *ET* for Disney and Kennedy. For Big Cypress and Gainesville it would underestimate long term *ET* and considerably overestimate *ET* for the Everglades. It should be noted that the sample of data used to test the algorithm was uneven in time and therefore the *Bias* measured might not be as representative of long term *ET* error as desired. Also, the quantity of data when divided by season is not large enough to get an accurate value of seasonal *ET* error. Figures 4.5.9-4.5.13 show scatter plots of retrieved *ET* vs. tower *ET* for each of the study areas. For Big Cypress the results are plagued by 4 outlying instances of error. For Everglades, the overestimation of *ET* by algorithm can be clearly seen. For Disney and Kennedy low errors can be seen, but for Gainesville a large amount of error is evident. For Gainesville the error is fairly unbiased except for summer in which the algorithm underestimates *ET*.
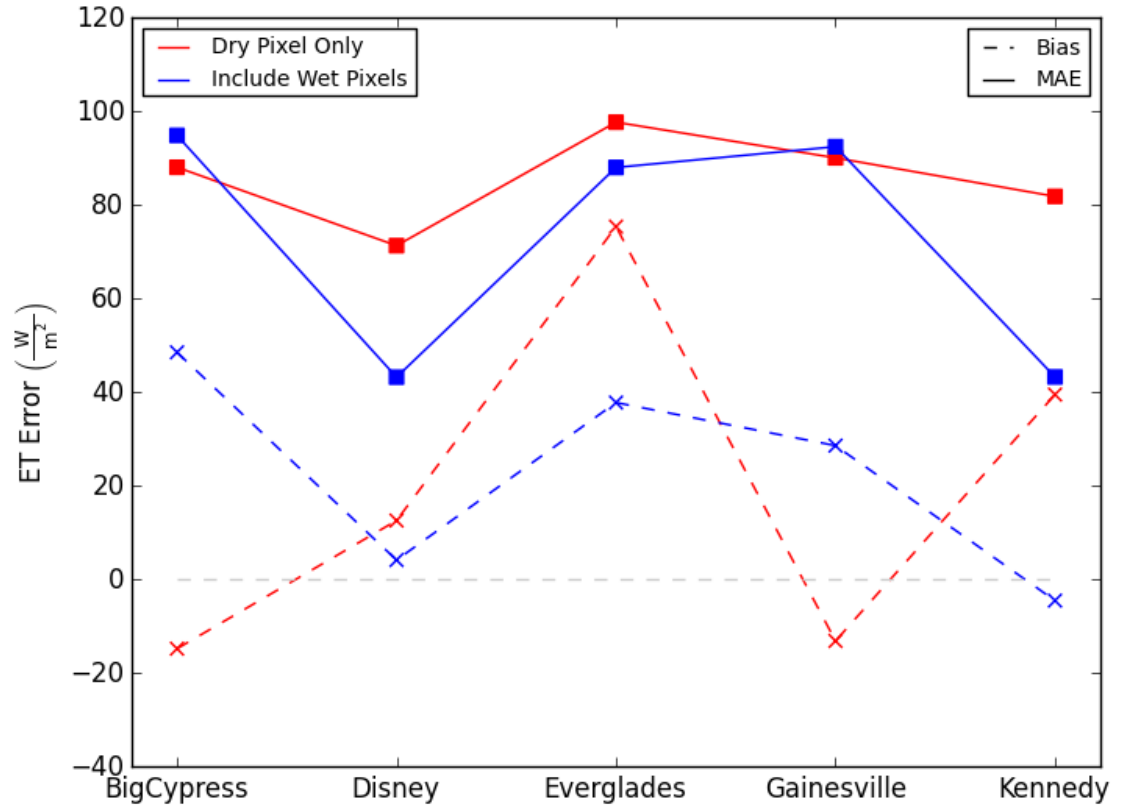
Figure 4.5.8: Comparison of Dry Only To Including Wet Pixels in Calibration for ET

Table 4.5.4: Optimal Variations for *ET* and *ET* Errors Relative to Mean Tower *ET*

Study Area	Model	Boundary	α Filter	Classification	$\overline{ET}$ (W/m²)	$Bias/\overline{ET}$	$MAE/\overline{ET}$
Big Cypress	ΔT vs. T	Min Max		None	235.4	-0.063	0.374
Disney	H vs. T	Even Bins		$NDVI_{min}$	185.2	0.021	0.223
Everglades	H vs. T	Even Bins	Yes	$NDVI_{min}$	287.9	0.131	0.307
Gainesville	ΔT vs. T	Min Max	Yes	None	207	-0.064	0.434
Kennedy	H vs. T	Even Bins	Yes	$NDVI_{min}$	248.3	-0.017	0.161
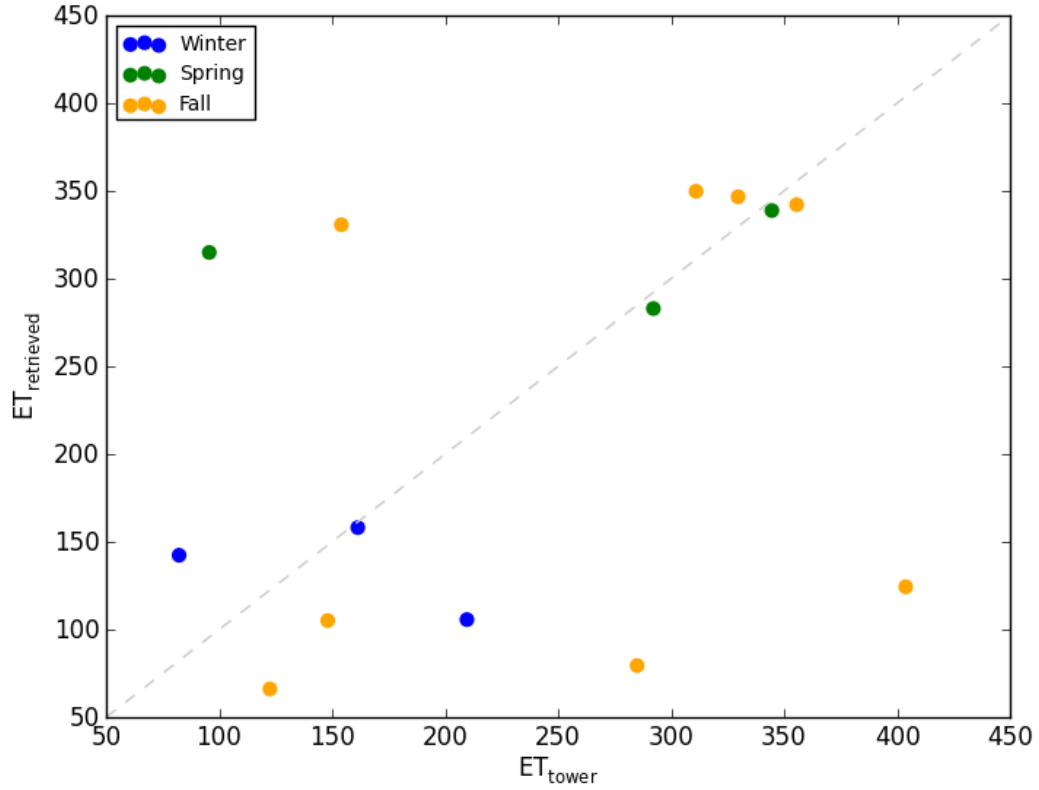
Figure 4.5.9: Optimal *ET* Retrieved vs. *ET* Tower for Big Cypress by Season
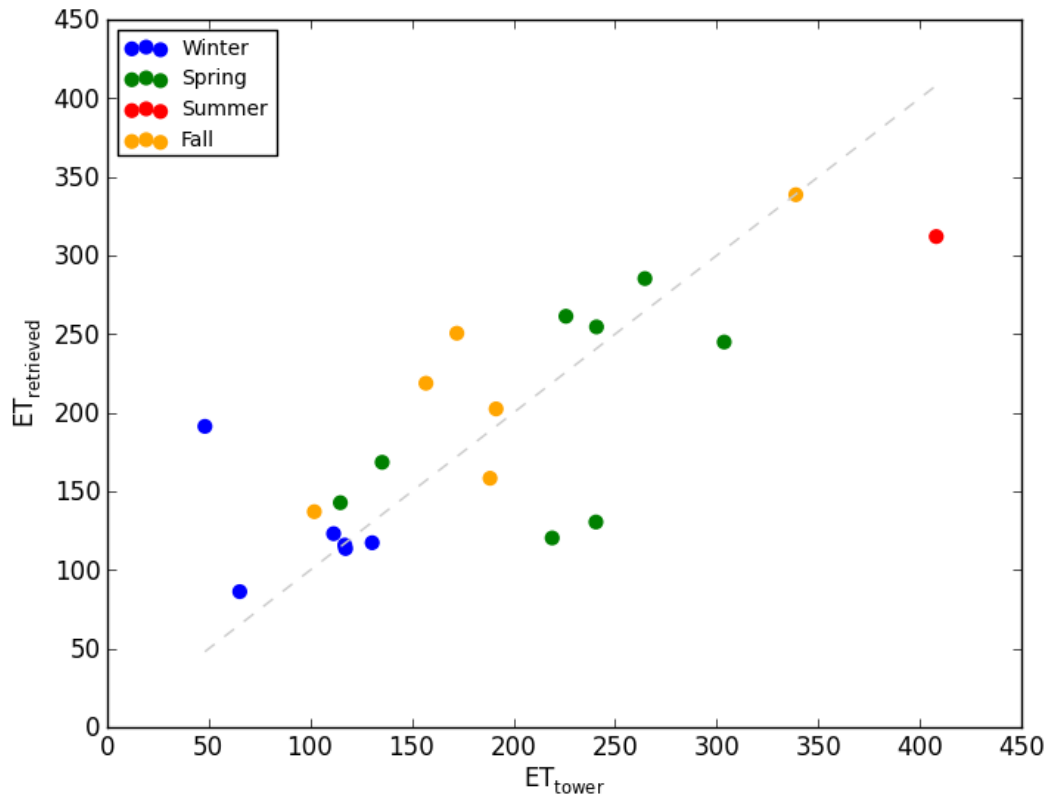
Figure 4.5.10: Optimal *ET* Retrieved vs. *ET* Tower for Disney by Season
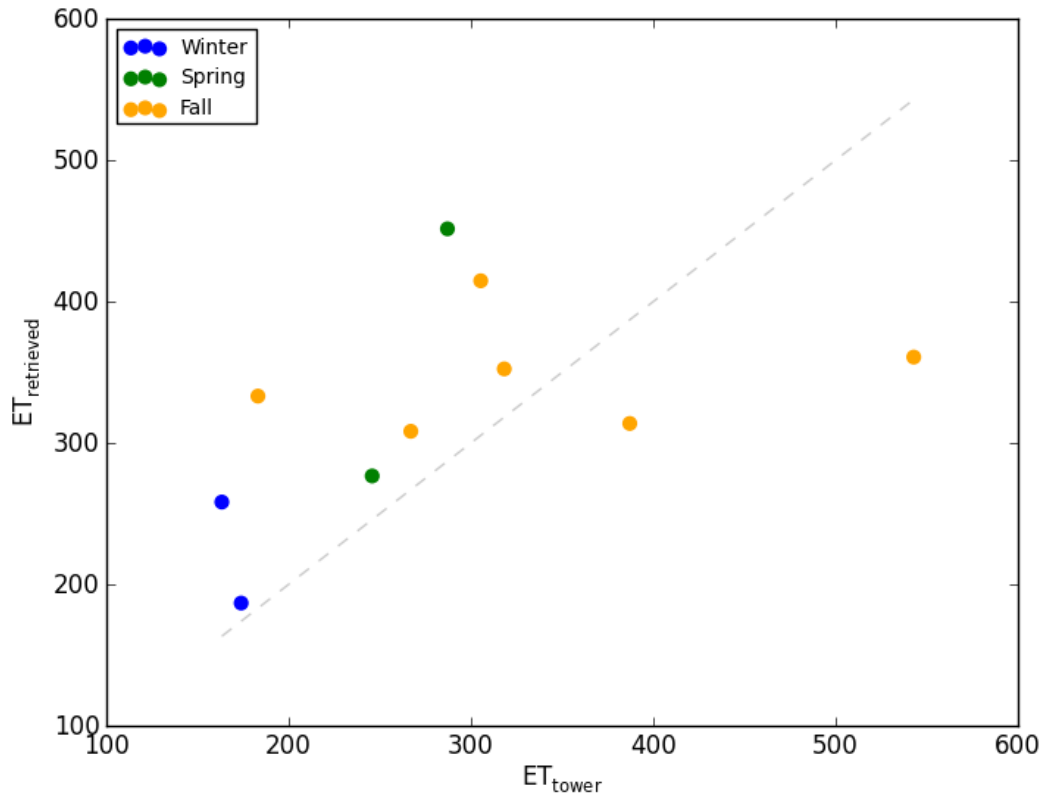
Figure 4.5.11: Optimal *ET* Retrieved vs. *ET* Tower for Everglades by Season
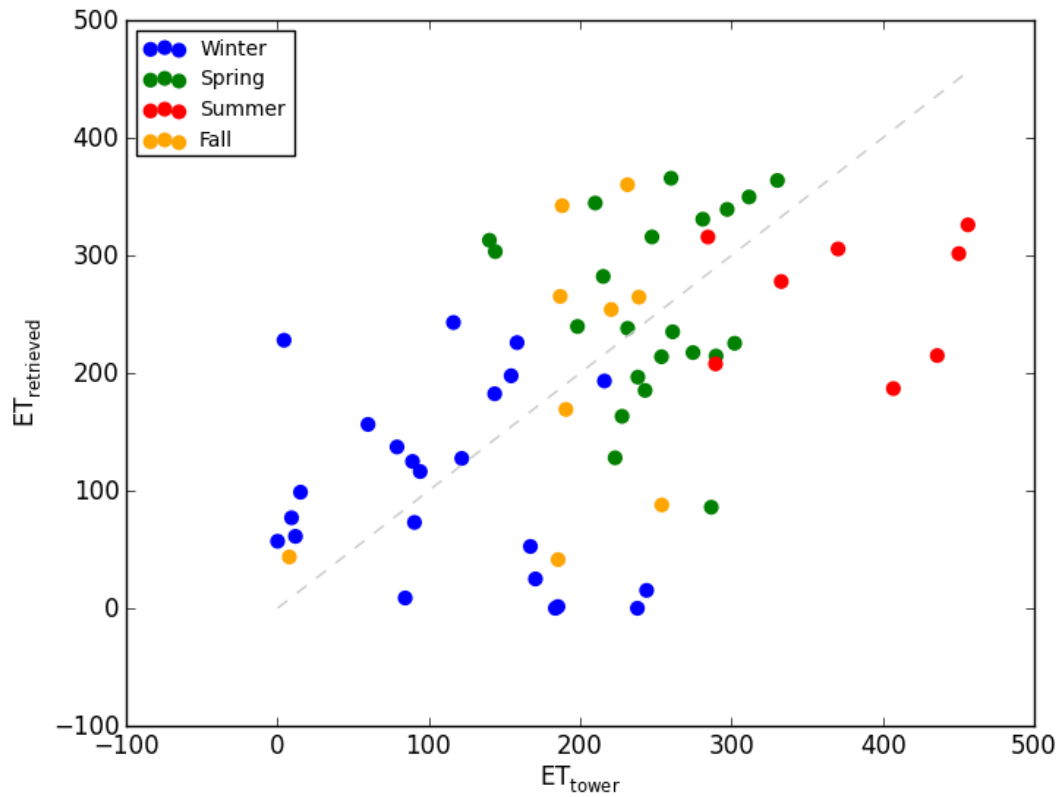
Figure 4.5.12: Optimal *ET* Retrieved vs. *ET* Tower for Gainesville by Season

168
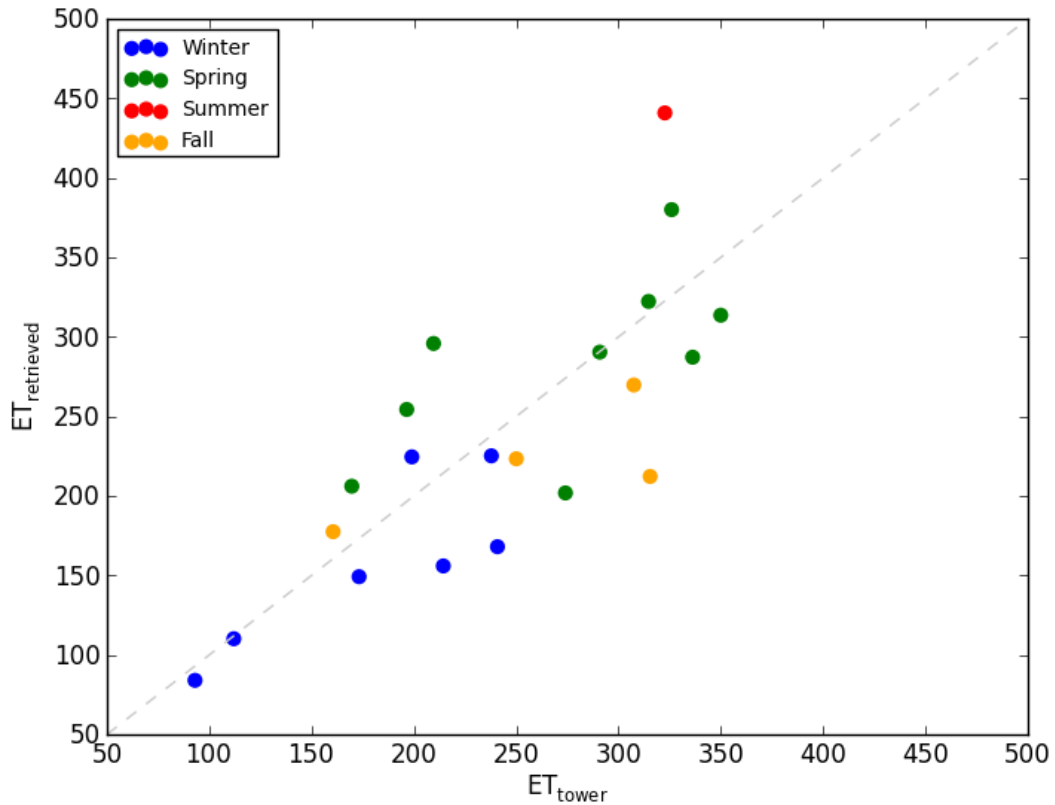
Figure 4.5.13: Optimal *ET* Retrieved vs. *ET* Tower for Kennedy by Season

4.5.3 Investigation of the Effect of Errors in Available Energy on Actual *ET*

Some interesting results were produced when the effect that errors in retrieving

available energy had on *ET* were analyzed. To estimate *ET* at the tower, available energy

was multiplied by evaporative fraction. In order to analyze the effect of errors in

available energy on *ET*, the available energy at the tower was calculated in two ways. In

the first case, the available energy from satellite was used to get *ET*. In the second case,

the available energy from the tower was used to get *ET*. The subsequent errors calculated

using the first tower *ET* would not include errors in retrieving available energy while the

errors using the second tower *ET* would include errors in retrieving available energy. The

difference between the errors would demonstrate the effect of errors in retrieving

available energy on retrieving *ET*. Figure 4.5.14 shows the change in the absolute value

of the *Bias* and *MAE* errors for all variations in each study area. A positive change means the *ET* error is increased due to energy errors while negative means *ET* error actually decreases *ET* error. It would seem that the errors due to retrieving available energy algorithm would always increase the resulting errors for retrieving *ET* but this is not always the case. This effect is more pronounced for the *Bias* error but it even occurs for *MAE*.

Figure 4.5.15 examines this effect in more detail using Kennedy Space Center as an example with *H* vs. *T*, Even Bins and $NDVI_{min}$ wet pixels variation. This figure shows the difference between errors produced when tower energy is used minus when satellite energy is used for each validation point. The error in energy for some points moves in an opposite direction of the errors in evaporative fraction which leads to a reduction in the absolute value of the error. It is possible for the errors in *ET* to be divided into a component due to evaporative fraction errors and another component due to available energy errors:

$$\Delta ET = \Delta EF\ A_{satellite} + \Delta A\ EF_{tower} \qquad\qquad 4.5.1)$$

where ΔET is the difference between retrieved and tower *ET*, ΔEF is the difference between retrieved and tower *EF*, ΔA is the difference between the retrieved and tower available energy, EF_{tower} is the *EF* measured by flux tower, and $A_{satellite}$ is the available energy retrieved by satellite. This analysis is based on the simple correction which assumes that the difference between $A_{satellite}$ and A_{tower} over the eddy covariance footprint is same as that over the tower radiometer footprint. Figure 4.5.16 allows the visualization of this effect even better. When these components are of opposite signs, they will have the potential to counteract each other. The gray area on the figure shows the region in

which the errors in energy counteract the errors in *EF* in such a way that the absolute value of the resulting error is decreased. The gray area does not encompass an entire quadrant because if the error in energy is too large the *EF* error is counteracted so much that the error is increased in the opposite direction. In the Figure 4.5.16 it is obvious that many of the errors are producing a decrease in the absolute value of the error in the lower right quadrant. The result is a dampening of the effect of errors in energy on *ET* or even a decrease in the final *Bias* or *MAE* error. Figure 4.5.17 shows this dampening effect for the optimal variations listed in Table 4.5.4. The blue line show the *Bias* and *MAE* error if only errors in evaporative fraction are considered (ie. satellite energy used to calculated tower *ET*). The red line shows the *Bias* and *MAE* error if only errors in available energy are considered (ie. tower *EF* used to calculate satellite *ET*). The green line is the actual *Bias* and *MAE* error found when both effects are considered. For Big Cypress and Kennedy the *ET* error was actually reduced due to the effect of errors in available energy. For Disney the *Bias* error was reduced. The reduction in *Bias* error is because the errors due to energy are in the opposite direction of the errors due to *EF*. Only for the Everglades was the *MAE* noticeably increased due to the effect of energy errors. For Big Cypress errors in energy were similar to Everglades but they produced a decrease in *ET* error. For the other study areas a considerable amount of error due to energy is present but the effect on errors in *ET* is not large.
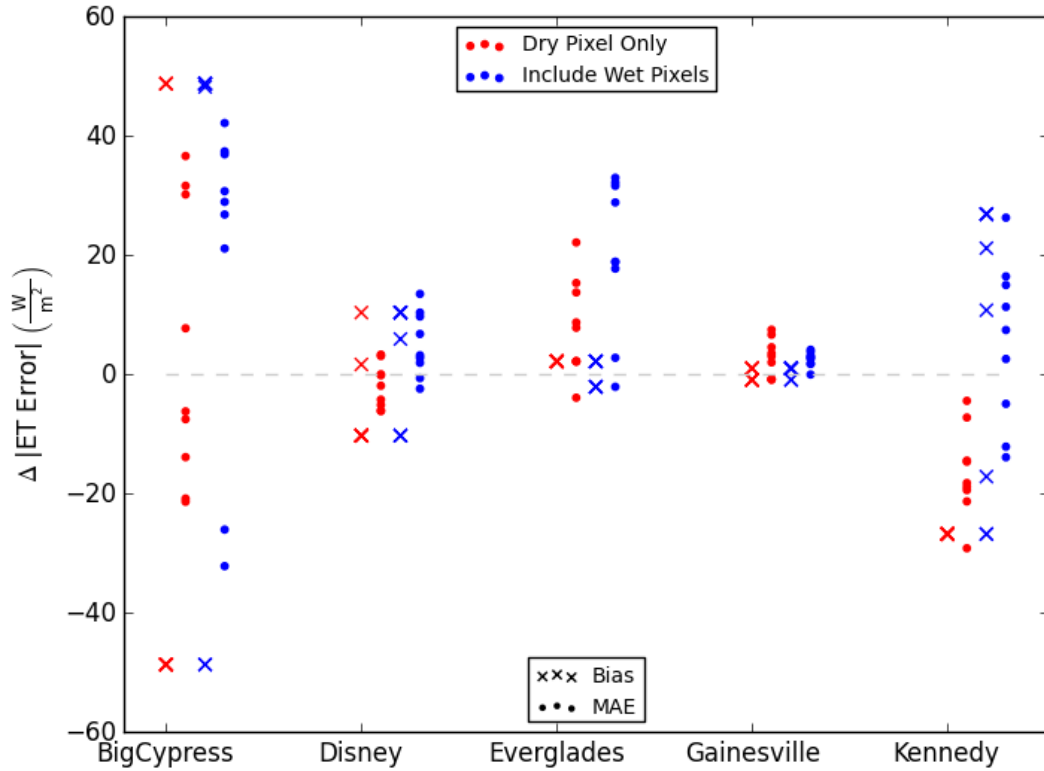
Figure 4.5.14: Effect of Errors in Energy on Errors in *ET* among Variations
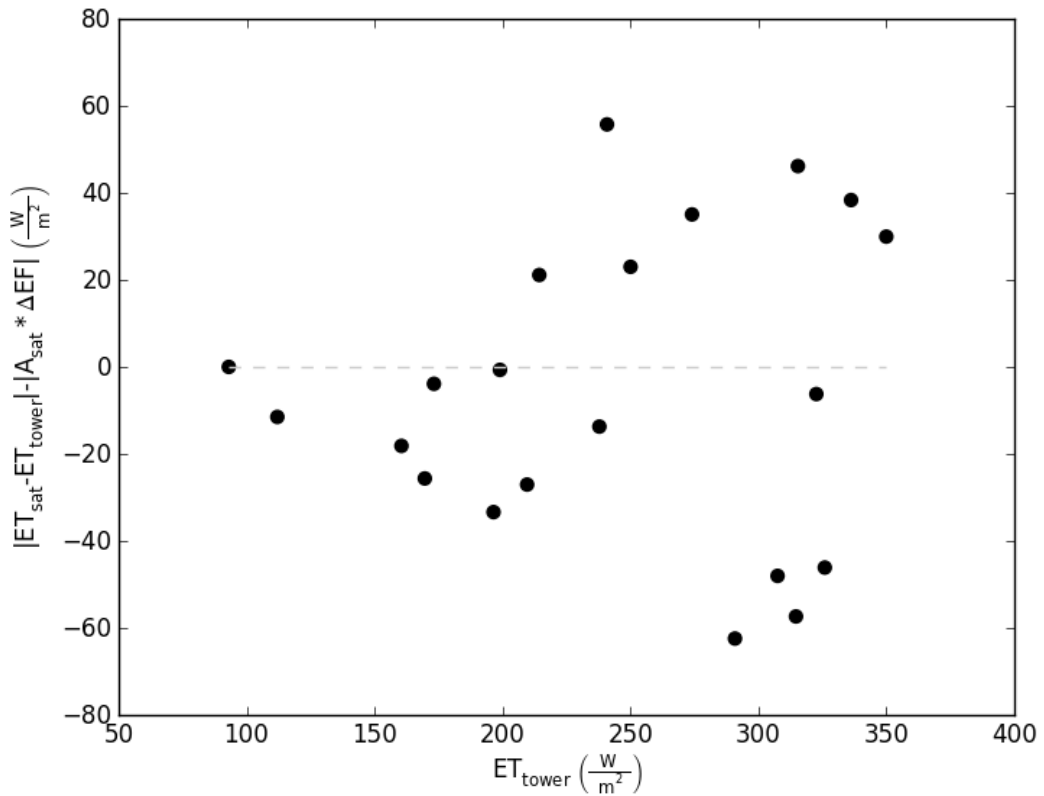
Figure 4.5.15: Effect of Energy Errors on *ET* Error for Kennedy, *H* vs. *T*, *NDVI*min
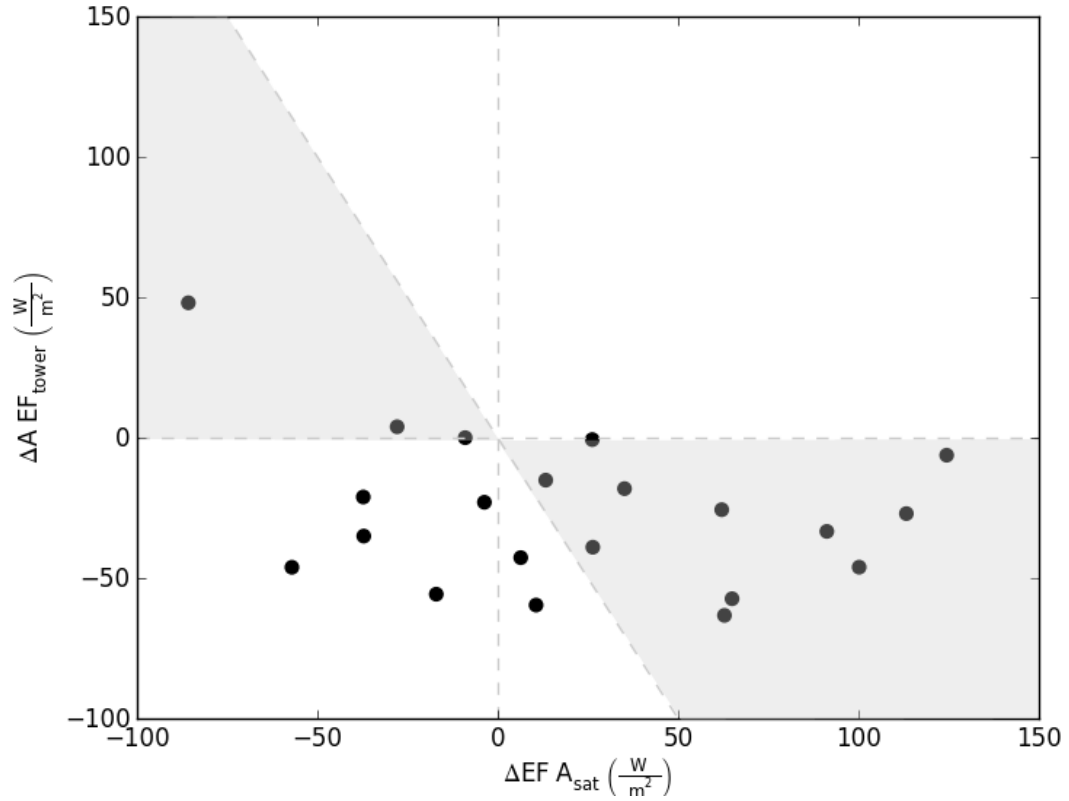
Figure 4.5.16: Counteracting *EF* and Energy Errors for Kennedy, *H* vs. *T*, *NDVI*$_{min}$
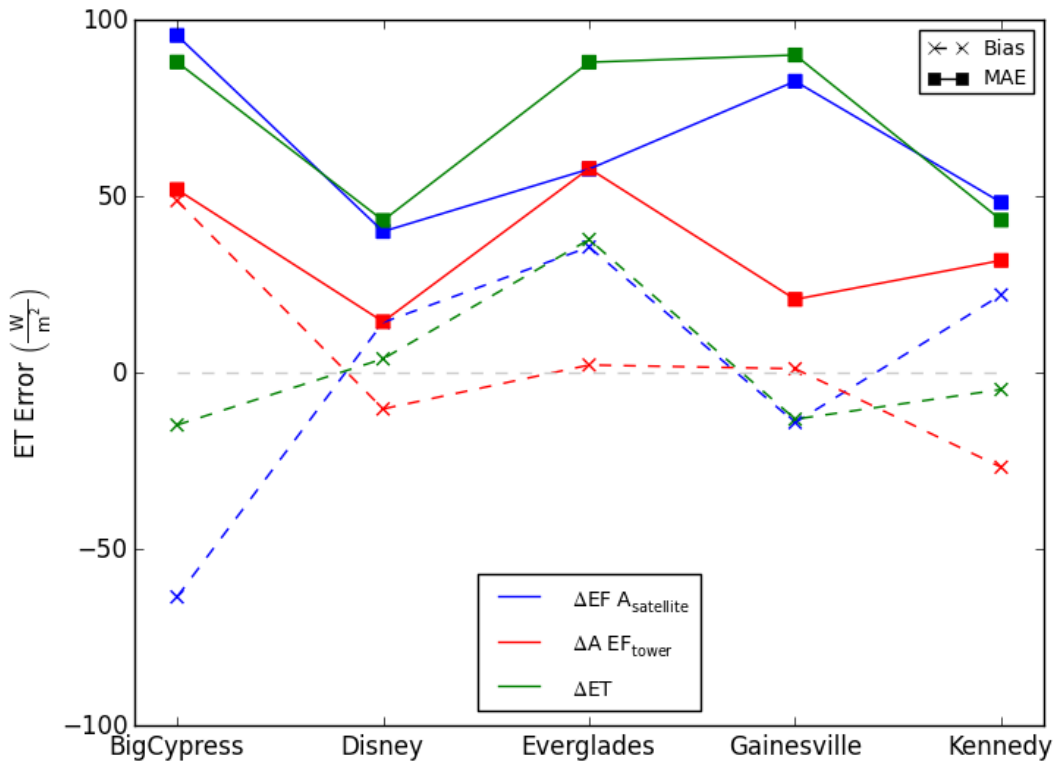
Figure 4.5.17: *ET* Errors for Optimal Variation with Counteracting *EF* and Energy Errors

173

4.6 Comparison of Calibration to Other Methods

4.6.1 Comparing Automated Calibration to Manual Calibration

A manual calibration was performed for the Kennedy study area using one dry and one wet pixel. The dry pixel was chosen to be on the air strip found in the image and the wet pixel was chosen to be in open water. These points were then used to calibrate the model using the same method that includes wet pixels. A comparison of the manual calibration to the optimal automated calibration is reported in Table 4.6.1. The automated calibration performs at least as well as the manual calibration. For the ΔT vs. T model the automated method performs much better. For the H vs. T model the MAE errors is only slightly less for the automated method, but the manual method is much more biased. It was not necessarily the goal of this dissertation to produce an automated calibration that was more accurate than the manual calibration. Instead, the goal is to produce an automated method that is similar in accuracy to the manual method. The value in developing the automated algorithm is that it is more operational and saves time.

Table 4.6.1: Comparison of Manual to Automated Calibration *ET* Error for Kennedy

Model	Calibration	Bias$_{ET}$ ($^W/_{m^2}$)	MAE$_{ET}$ ($^W/_{m^2}$)	ρ_{ET}
H vs. T	Auto	-4.8	43.2	0.778
H vs. T	Manual	-33.9	51	0.751
ΔT vs. T	Auto	23.4	41.7	0.818
ΔT vs. T	Manual	-111.9	122.6	0.795

4.6.2 Comparison to Other Studies in Florida

(Bhattarai et al, 2012) used a modified SEBAL method with LANDSAT data to retrieve daily and monthly *ET* values in Florida and validated it against USGS eddy covariance flux towers. The method used is very similar to that which is used in this

174

dissertation except manually identification of wet and dry pixels was used. Also, daily *ET* was determined by multiplying instantaneous *ET* by the ratio of daily *RET* to instantaneous *RET* calculated using FAWN weather station data. Another difference is that all of the scenes were during the growing season from mid May to mid September. In this study the Disney Preserve study areas was evaluated for 7/8/2004 and 7/24/2004. In this dissertation these scenes were not used because on 7/8/2004 the flux tower had gaps in the data while 7/24 had light clouds. Because this study used daily *ET* and this dissertation uses instantaneous *ET*, the relative error between studies is the only useful metric. The relative *MAE* error for 7/8/2004 and 7/24/2004 was around 5% and 30% respectively. This would be around 17% error on average compared to 22% for this dissertation. This is not a very robust comparison since only two Disney scenes were used in the Bhattarai et al. study. The Bhattarai et al. study used 3 other flux towers in Florida. The relative *MAE* error averaged over all four study areas was about 7% which is much better than this dissertation. It is difficult to determine whether this difference is due to using FAWN weather stations to get *RET*, using a manual calibration, or performing analysis with scenes only in the growing season.

The PT-JPL method was used to estimate monthly latent heat values and compared to the Mize eddy covariance station from the Gainesville study area. It should also be noted that the PT-JPL was used on MODIS data. An RMS and *Bias* error over a period between 2000 and 2003 was found to be about 25 and 3 W/m^2 respectively (Fisher et al, 2008, Mallick et al., 2013). The optimal error for instantaneous *ET* for method used in this dissertation for Gainesville is *MAE*=90 W/m^2 and *Bias*=-13 W/m^2. The low *Bias* suggests that if the method used in this dissertation was aggregated over the month, the

errors could be something closer to Fischer et al. 8 day *ET* estimated using the MODIS

ET product was validated over Donaldson which produced a *MAE* equal to about 0.5

mm/day (Mu et al, 2011). The average 8 day *ET* observed was about 2.7 mm/day

resulting in a 19% error. The relative *MAE* error in this dissertation for Gainesville was

about twice this at 43%, but the *Bias* error was only 6%. Aggregating over 8 days would

most likely reduce *MAE* error closer to *Bias* error.

Monthly estimates of *ET* using the SEBop method was compared to the Austin

Carey flux tower (Senay et al, 2013). This method produced RMS error equal to 62 mm.

In July, the tower measured latent heat due to *ET* was equal to about 90 W/m^2 while that

predicted by SEBop was about 190 W/m^2. In November, December and January the error

was very small. (Jiang et al, 2009) compared *EF* estimated using the triangle method with

AVHRR to four flux stations over sawgrass in South Florida. This produced a *Bias* error

equal to 0.05 and an *MAE* error equal to 0.16 compared to *Bias*=0.08 and *MAE*=0.11 for

optimal Everglades variation. In terms of daily *ET*, Jiang et al produced relative *Bias*

error equal to -21% and a relative *MAE* error equal to 31%. When estimating

instantaneous *ET* using the optimal Everglades variation, relative *Bias* error was equal to

13% and relative *MAE* error was equal to 31%. It should be noted that Jiang et al. used

the same surface based energy measurements in calculating both validation *ET* and

retrieved *ET*.

4.7 Investigation of the Effect of Wind

The effect of wind speed was investigated by setting the wind speed to a constant

value equal to the mean wind speed from the flux tower data. *H* vs. *T* does not depend on

wind speed so only *ΔT* vs. *T* model variation must be analyzed. Because the optimal

model variation for Gainesville study area was ΔT vs. T when tested against EF and ET, it was chosen for analysis. Also, the dry pixel only calibration was chosen for analysis because it was the optimal type for Gainesville with respect to ET. It was necessary to determine whether there was a large seasonal variability of wind speed at blending height (u_{blend}). Figure 4.7.1 shows the mean and standard deviation of u_{blend} for each month. All of the flux data available was used opposed to only using just the dates in which a clear sky image was available. The seasonal variability was not large enough to warrant using a monthly value for mean u_{blend}. Instead, the mean value over all months $u_{blend} = 3.57$ m/s was used.
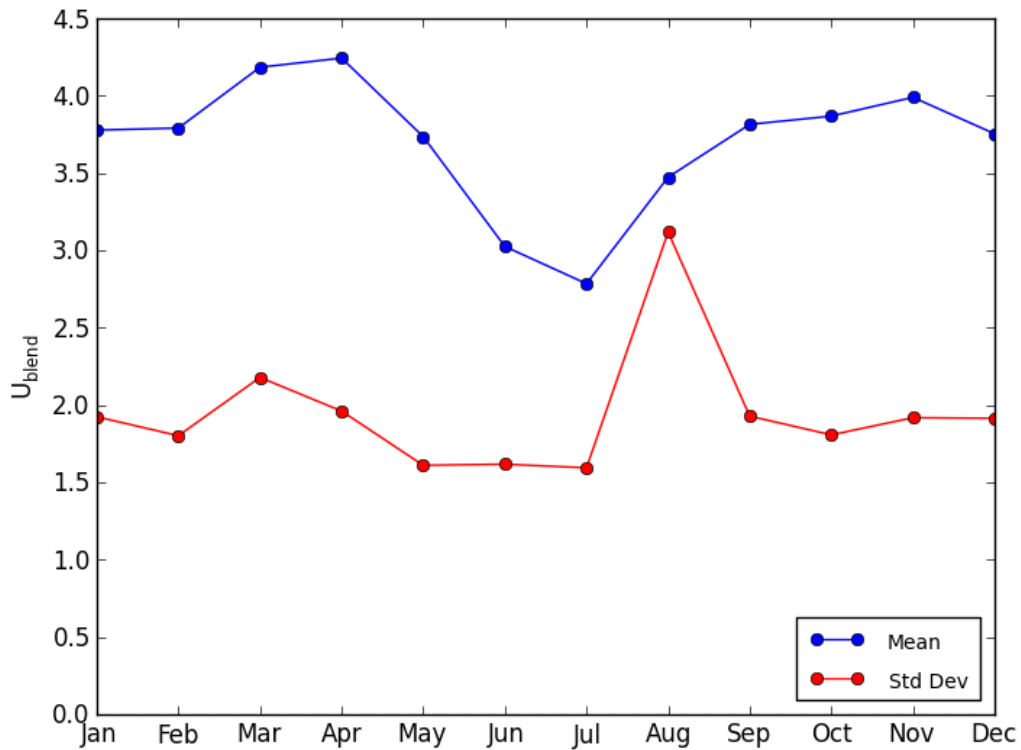
Figure 4.7.1: Mean and Standard Deviation of u_{blend} for Gainesville by Month

The results of using the mean u_{blend} in the dry pixel only calibration for Gainesville are summarized in Table 4.7.1. The original results using the actual u_{blend} from the day of the image is also shown for comparison. When mean u_{blend} is used the

177

Bias and *MAE* are actually reduced in some cases. Originally the optimal boundary variation was Even Bins. When mean u_{blend} is used the optimal boundary variation is now Min Max with a lower *Bias* and *MAE* for both *EF* and *ET* (highlighted in yellow). But, when using mean u_{blend} the correlation between retrieved and tower is reduced. For *EF* the correlation when using mean u_{blend} is very poor.

Table 4.7.1: Comparison of *EF* and *ET* errors if using actual u_{blend} vs. mean u_{blend}

Boundary	Wind Scenario	$Bias_{EF}$	MAE_{EF}	ρ_{EF}	$Bias_{ET}$ ($^W/_{m^2}$)	MAE_{ET} ($^W/_{m^2}$)	ρ_{ET}
Even Bins	Actual	0.06	0.204	0.23	37	100.1	0.514
Even Bins	Mean	-0.096	0.179	0.09	-47.3	86.4	0.446
Min Max	Actual	0.088	0.241	0.124	50.8	120.1	0.441
Min Max	Mean	-0.051	0.167	-0.081	-26.1	84.1	0.355
Extreme	Actual	0.19	0.263	0.275	100.7	135.4	0.494
Extreme	Mean	0.18	0.247	0.167	93.7	134.5	0.386

Figures 4.7.2-4.7.3 shows scatter plots of the retrieved *EF* vs. tower *EF* when using actual u_{blend} with Even Bins and mean u_{blend} with Min Max Bins respectively. A difference between the distributions of the errors is evident. For spring and fall the errors are reduced while for summer the errors are increased with a bias towards underestimation. The winter errors become more clustered where before they were more spread out. The *Bias* towards underestimation when using mean u_{blend} can be clearly seen on Figure 4.7.2. Also the range of *EF* that is retrieved when using u_{blend} is reduced from about 0.0-0.9 to 0.2-0.7. Therefore the performance when using u_{blend} is reduced negatively when *EF* is low or high. Since the validation data contains many intermediate values, using mean u_{blend} does not affect the results very drastically, but if more low and high *EF* was present in validation data it would have increased the total error considerably. Therefore, the actual reduction in *Bias* and *MAE* when using mean u_{blend}

does not mean it is better than using actual u_{blend}. A similar conclusion can be made based on using instantaneous ET shown in Figures 4.7.4-4.7.5. The retrieved ET seems to correlate to tower ET a bit better than using EF, but there is still a reduction in range of retrieved ET. The results for spring and fall are very good possibly because the range of observed ET is small for these seasons. For winter low ET is being overestimated while high ET is being underestimated. The failure of using mean u_{blend} in summer results in retrieved ET in summer being less than spring. Although tower ET ranges from 300 to 500 W/m^2, retrieved ET is consistently around 200 W/m^2. These could have severe implications because summer is the peak growing season.

Figures 4.7.6-4.7.7 show the variation in the residuals between retrieved and tower EF vs. u_{blend} when using actual u_{blend} with Even Bins and mean u_{blend} with Min Max Bins. A change in the relationship between the residuals and u_{blend} can be seen. When using the actual u_{blend}, a relationship between the error and wind is evident. For small winds there is a tendency for the algorithm to overestimate EF, while for larger winds there is a tendency for underestimation. When using mean u_{blend}, the relationship between error and wind disappears. The error for low wind becomes more negative while the error for high wind becomes less negative. The final results is that the errors using mean u_{blend} become similar to the errors produced when using actual u_{blend} for days when u_{blend} is close to mean u_{blend}. It is necessary to determine why this is occurring. When using mean u_{blend}, u_{blend} is being overestimated on days in which actual u_{blend} is small and underestimated when actual u_{blend} is large. Therefore, it is necessary to determine the effect that changes in wind speed have on retrieved EF. To do this it is convenient to look at the change in sensible heat (H) and its' component g_a and ΔT. The effect of wind on ET

was looked at for Donaldson on January 28, 2001 when u_{blend}=1.6 m/s. On this day the

EF was overestimated by about 0.6 using actual u_{blend}, but this was reduced to about 0.4

when using mean u_{blend}. Therefore, by increasing u_{blend} from 1.6 m/s to the mean value of

3.7 m/s the sensible heat retrieved by algorithm increased. Further analysis showed that

g_a increased from 46 to 69 W/m^2/K, while ΔT found using retrieved temperature

increased from 3.1 to 3.7 K. ΔT changed because the relationship between ΔT and T

changed when wind speed changed. In finding the relationship between ΔT and T, it was

assumed that $\Delta T = \Delta T_{dry}$ where ΔT_{dry} is equal to the ΔT over bare ground where all of the

available energy is being used as sensible heat. In order to find ΔT_{dry}, the available energy

is divided by the g_a found over bare ground. Since ΔT increased with u_{blend}, it means that

g_a must have decreased with u_{blend} since energy is constant. This seems a bit counter

intuitive since g_a actually increased with u_{blend} over the Donaldson surface. This is

occurring because g$_a$ depends not only on wind speed, but also on the instability of the

atmosphere. Figure 4.7.8-4.7.9 shows the relationship between g_a and u_{blend} for bare

ground and Donaldson on 1/28/2001. In both of these figures, g_a decreases with u_{blend} for

small u_{blend} and increases with u_{blend} for large u_{blend}. The threshold u_{blend} where g_a reaches

a minimum value varies depending on the roughness of the surface. Over Donaldson, the

threshold is much smaller than over bare ground. Therefore Donaldson g_a responded to

u_{blend} differently than bare ground on 1/28/2001 because it is on a different side of the

threshold when u_{blend} is between 1.6 to 3.7 m/s. By looking at the variation of friction

velocity (u^*) and Obukhov length (L), the variation of the threshold u_{blend} with roughness

can be explained. Donaldson is over slash pine which is a rough surfaces that results in a

large u^*. A large u^* results in very large L meaning that instability/buoyancy of the

atmosphere is not very important. Therefore, an increase in u_{blend} directly increases g_a.

Once the wind speed becomes very small, $u*$ becomes small enough that the instability of

the atmosphere becomes important (L becoming closer to zero). An increase in the

instability of the atmosphere results in an increase in g_a. Therefore, as u_{blend} continues to

decrease, the atmosphere becomes more instable, and g_a begins to increase. Over bare

ground the threshold u_{blend} is larger because the buoyancy/instability effect is achieved at

larger u_{blend}. This is because $u*$ is less for bare ground than for trees with the same u_{blend}.

For both surfaces the buoyancy effect becomes important around $u*=0.2$ which

corresponds to $u_{blend} < 1$ m/s for Donaldson but $u_{blend}=4$ m/s for bare ground. In

conclusion, this difference in the response of g_a to u_{blend} produces a change in EF in

negative direction for low actual u_{blend} but a change in EF in negative direction for high

actual u_{blend}.
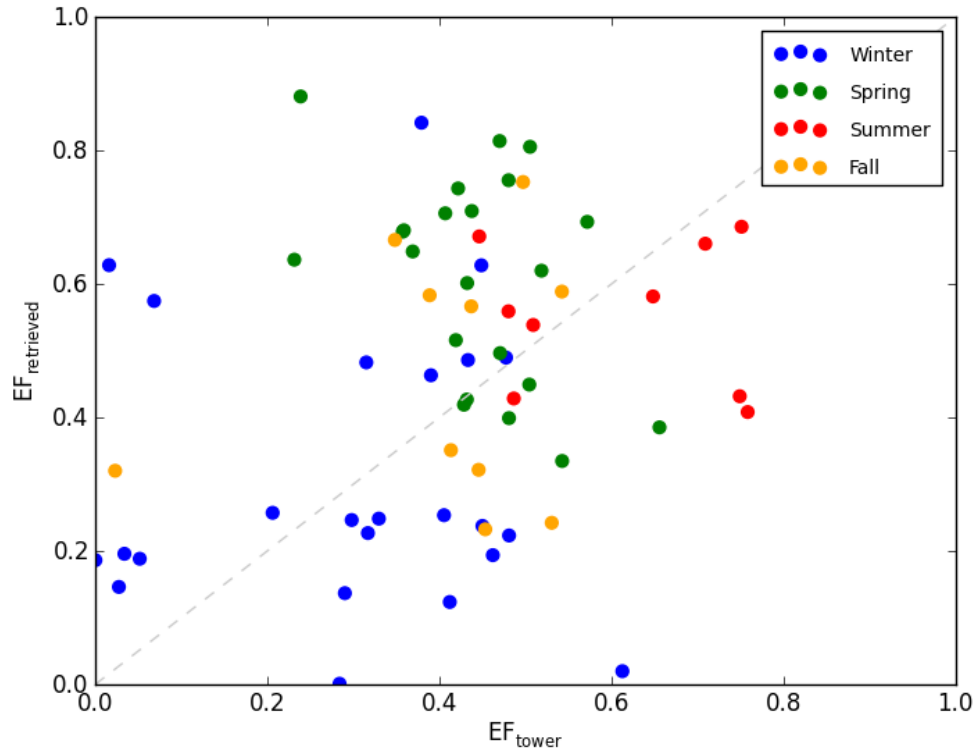
Figure 4.7.2: Retrieved *EF* vs. Tower *EF* using Actual U$_{blend}$ and Even Bins for Gainesville
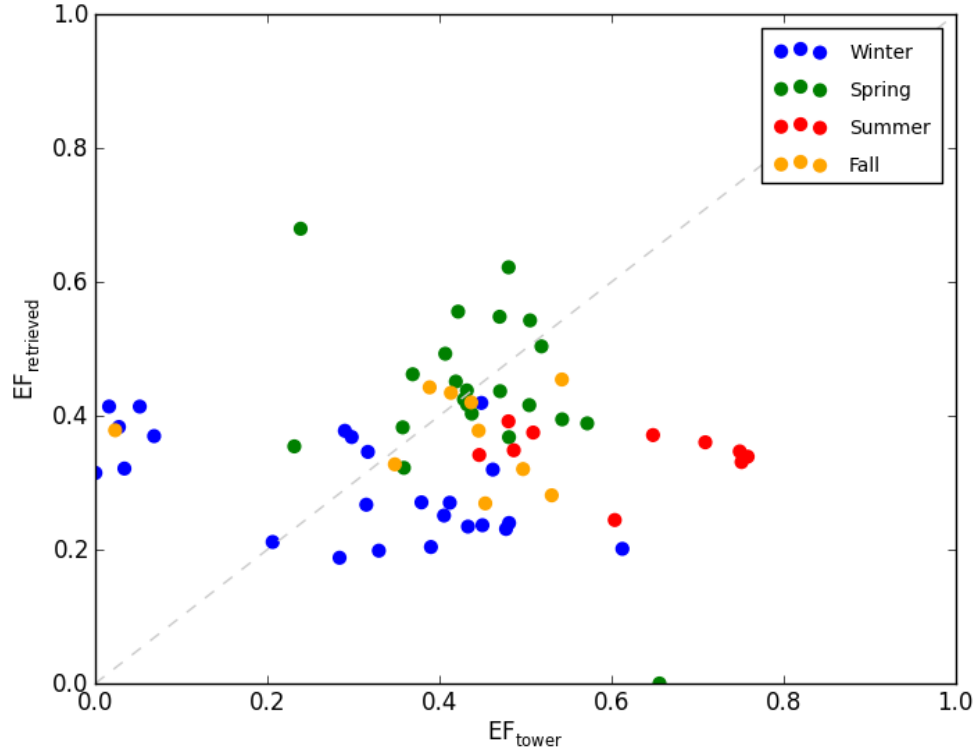
Figure 4.7.3: Retrieved *EF* vs. Tower *EF* using Mean U$_{blend}$ and Min Max for Gainesville
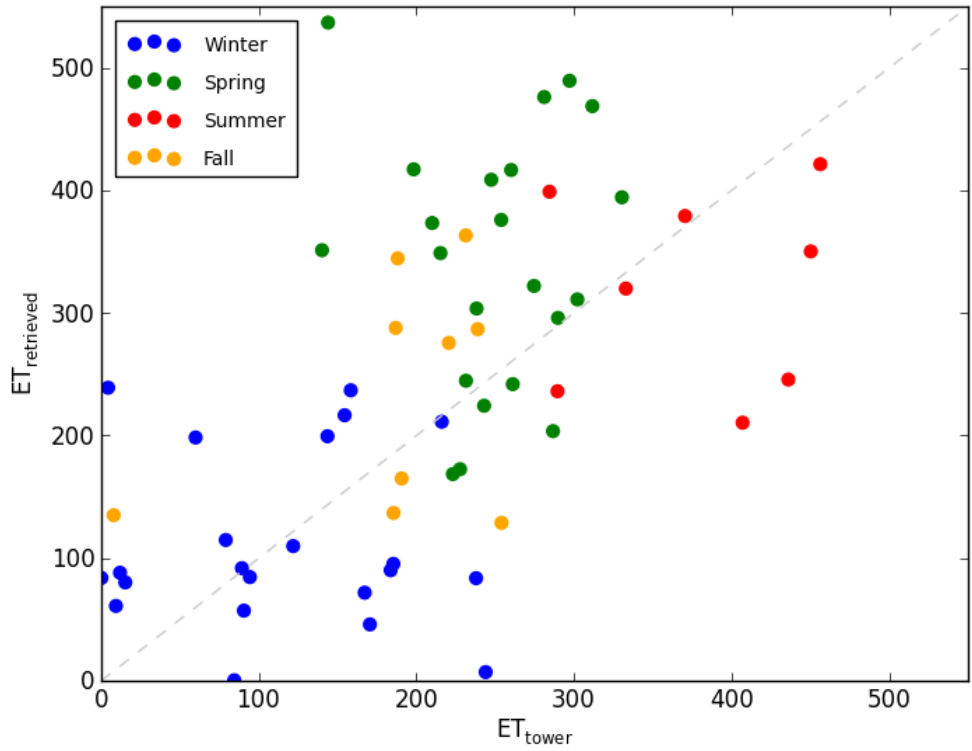
Figure 4.7.4: Retrieved *ET* vs. Tower *ET* using Actual u_{blend} and Even Bins for Gainesville
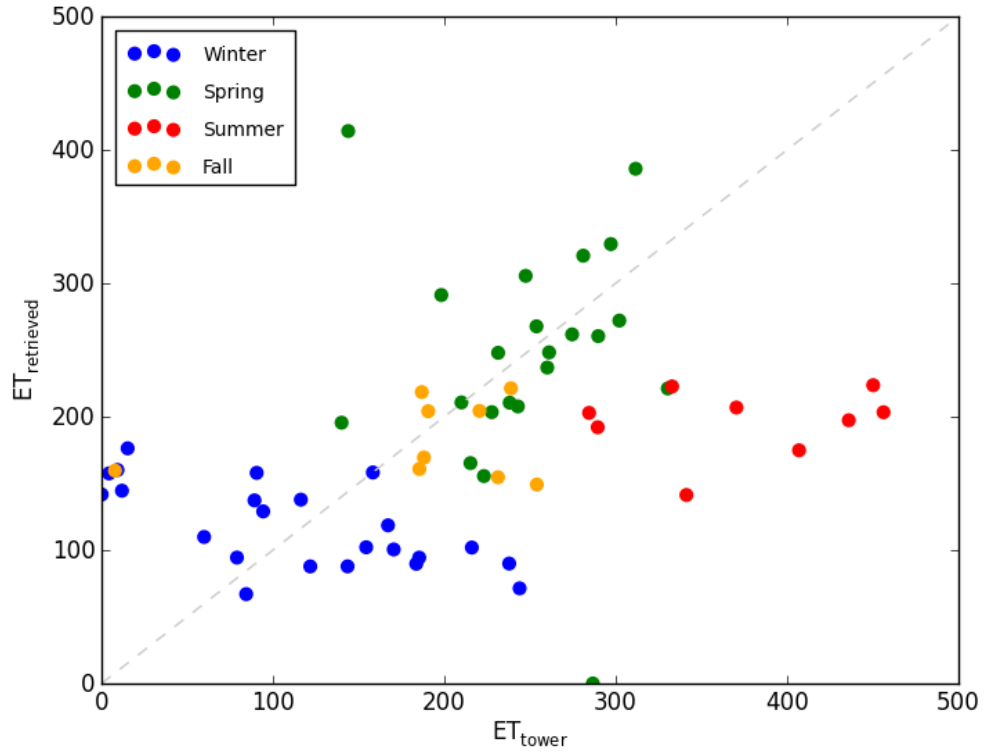
Figure 4.7.5: Retrieved *ET* vs. Tower *ET* using Mean u_{blend} and Min Max for Gainesville
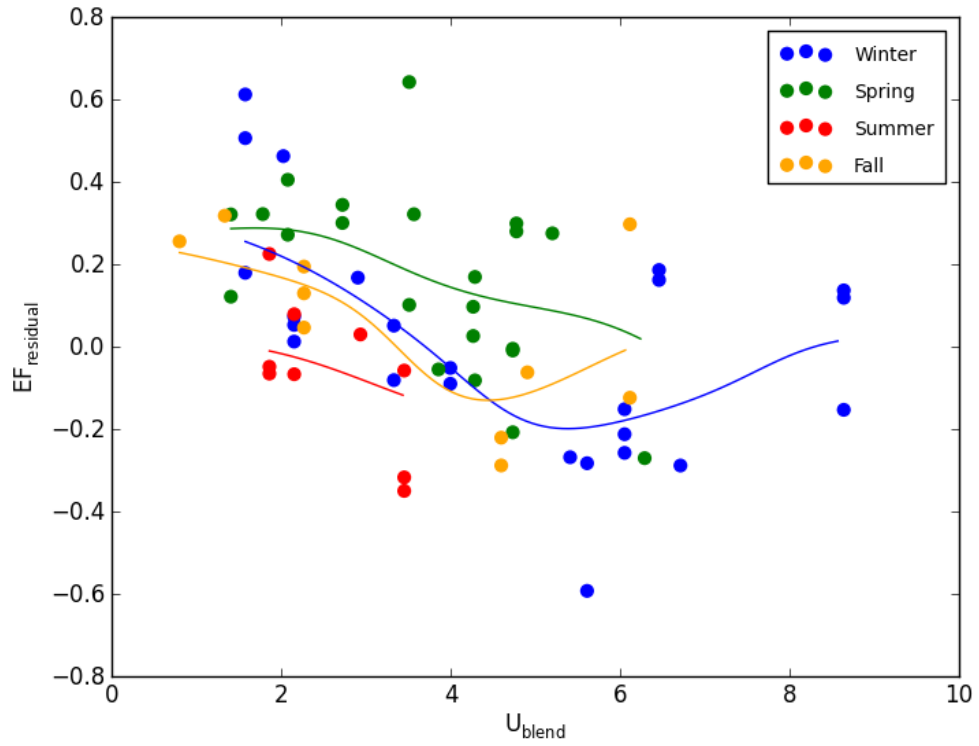
Figure 4.7.6: Relationship Between *EF* Error and u_{blend} using Actual u_{blend} for Gainesville
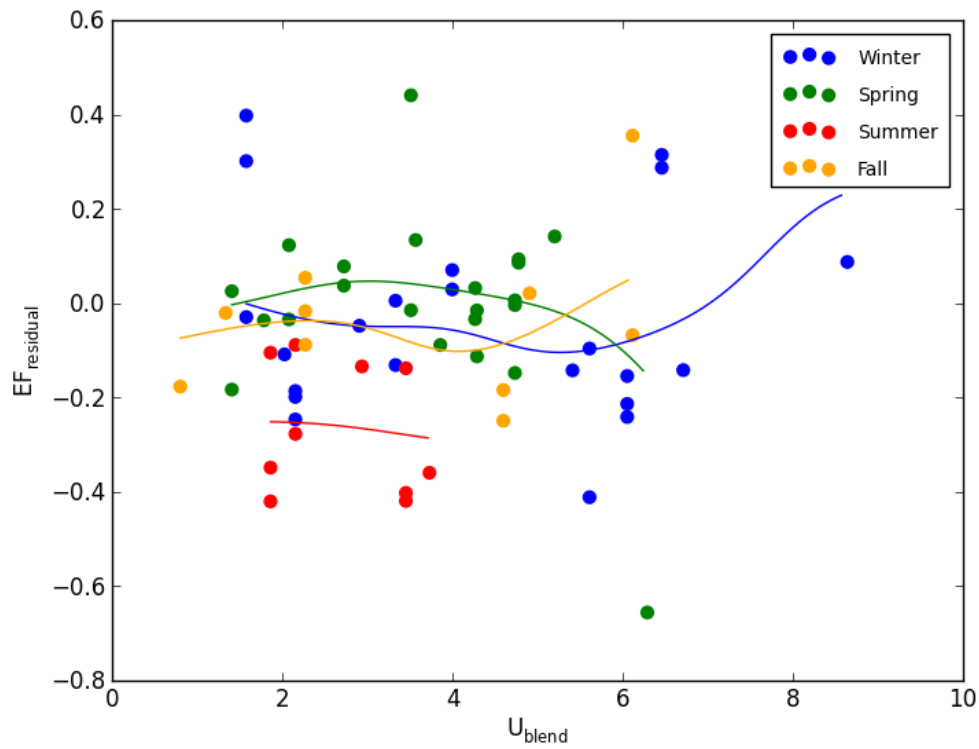
Figure 4.7.7: Relationship Between *EF* Error and u_{blend} Using Mean u_{blend} for Gainesville
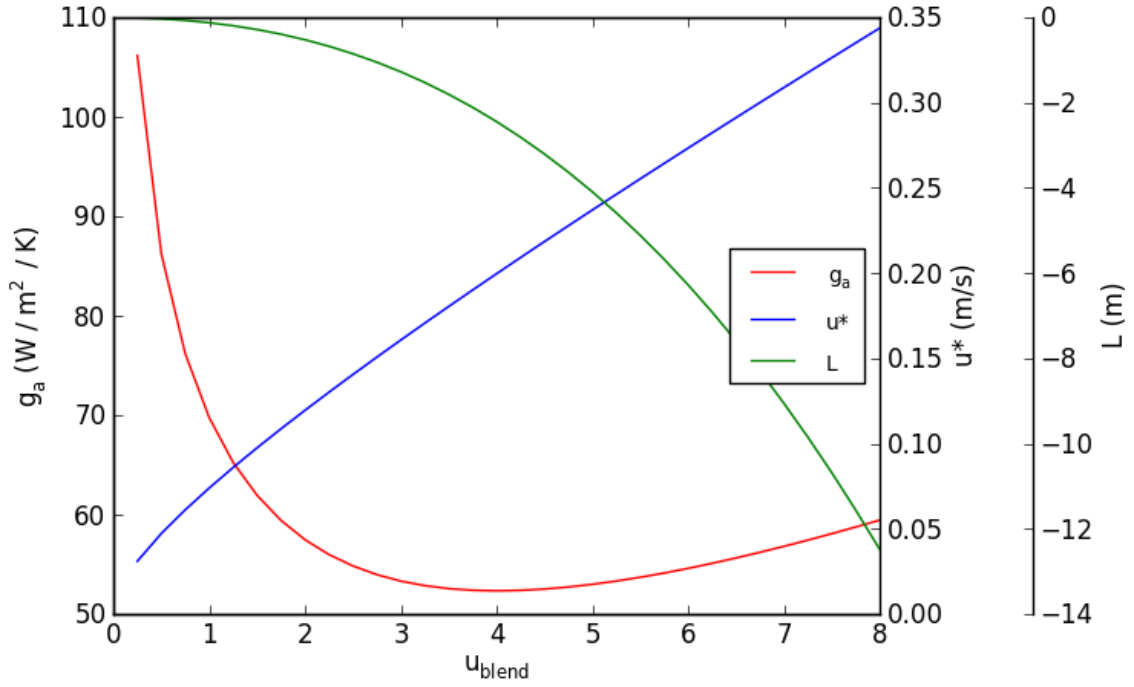
Figure 4.7.8: Effect of u_{blend} on g_a, u^* and L for Gainesville 1/28/2001 over Bare Ground
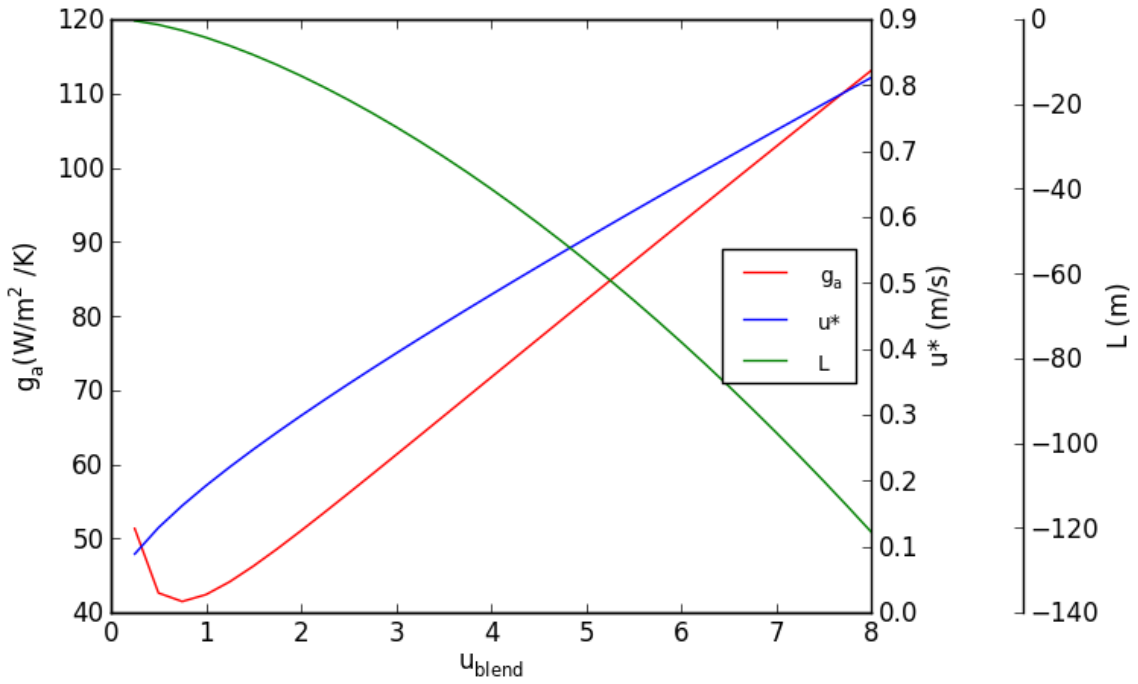
Figure 4.7.9: Effect of u_{blend} on g_a, u^* and L for Gainesville 1/28/2001 over Donaldson

4.8 Sensitivity Analysis for *ET* Remote Sensing Algorithm

    4.8.1 Sensitivity to Temperature and Available Energy

    The Disney study area was chosen to analyze sensitivity to temperature and available energy because it produced good results. Since the sensitivity analysis was testing the change in the entire retrieved *ET* map, it seemed appropriate to choose a study area which performed well. First the dry pixel only calibration using the *H* vs. *T* model was used to test the sensitivity of *EF* to temperature and available energy. The *Bias* and *MAE* of the difference between the original map and perturbed map was produced for each day. The mean and standard deviation of the *Bias* and *MAE* was then calculated for various perturbations. Because the temperature acts like an "index" in the calibration, perturbing the temperature of every pixel evenly did not produce a change in *EF*. When this simulation was conducted the *MAE* for *EF* change was less than 0.006 due to numerical precision issues. The perturbation of energy did produce a change in *EF*. Figure 4.8.1 shows the *Bias* and *MAE* of *EF* differences averaged over all scenes when the energy was perturbed by a percentage amount. It should be noted that the *MAE* should always be positive, but it was assigned the same sign as the *Bias* for visualization purposes. In addition, the standard deviation of the *Bias* and *MAE* for all scenes was added to and subtracted from *Bias* and *MAE*. Ideally *EF* should not be sensitive to changes in energy because the change in sensible heat relationship is proportional to changes in energy and therefore *EF* does not change. In other words, the energy used in the dry pixel calibration has changed by the same percentage as the energy which is divided by sensible heat to get *EF*. Figure 4.8.2 demonstrates why this ideal case does not occur. The actual perturbed case was created by increasing the energy of all of the

original pixels by 50%. These pixels were then used to find the boundary points (blue points). In the ideal case (green points), the energy of the original boundary points (red points) are increased by 50% instead. This produces a different set of boundary points and resulting relationship for sensible heat vs. temperature. Essentially when all of the data was stretched by 50%, it effectively reduced the bin size relative to the range of data which allowed more pixels into the boundary. This changed the nature of the relationship resulting in a difference in sensible heat of about 25 W/m^2. The *EF* of the actual perturbed case was reduced due to the increase in sensible heat relative to the ideal perturbation case.
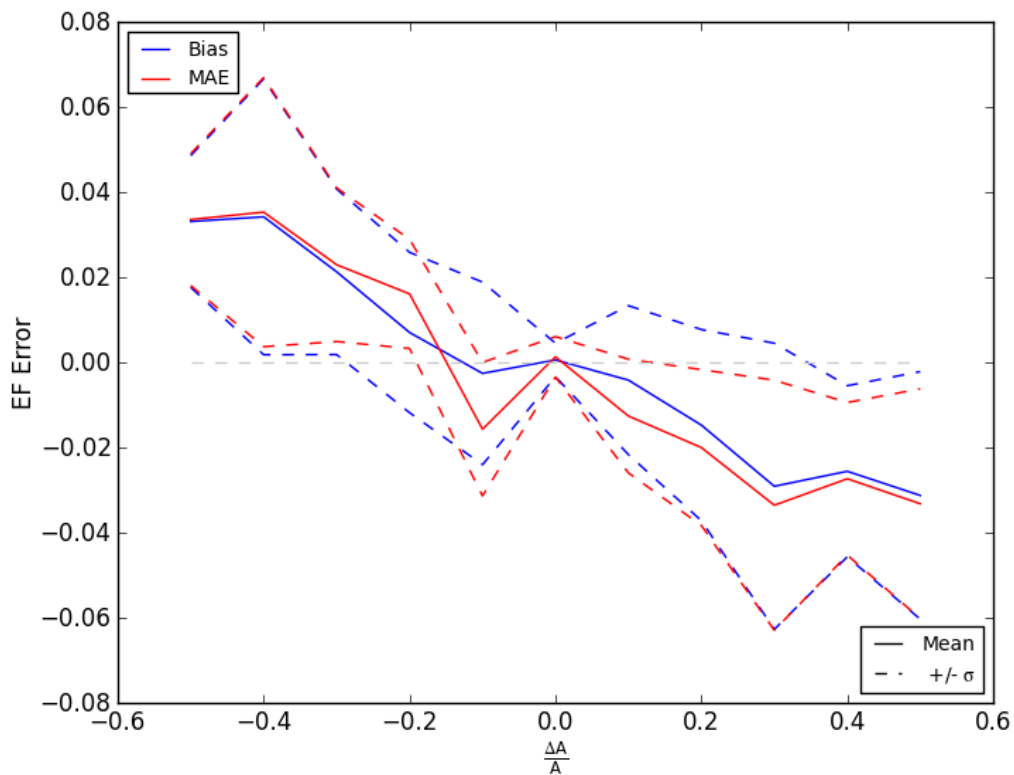
Figure 4.8.1: Sensitivity of *EF* to Available Energy Percent Change for Disney – Dry Only
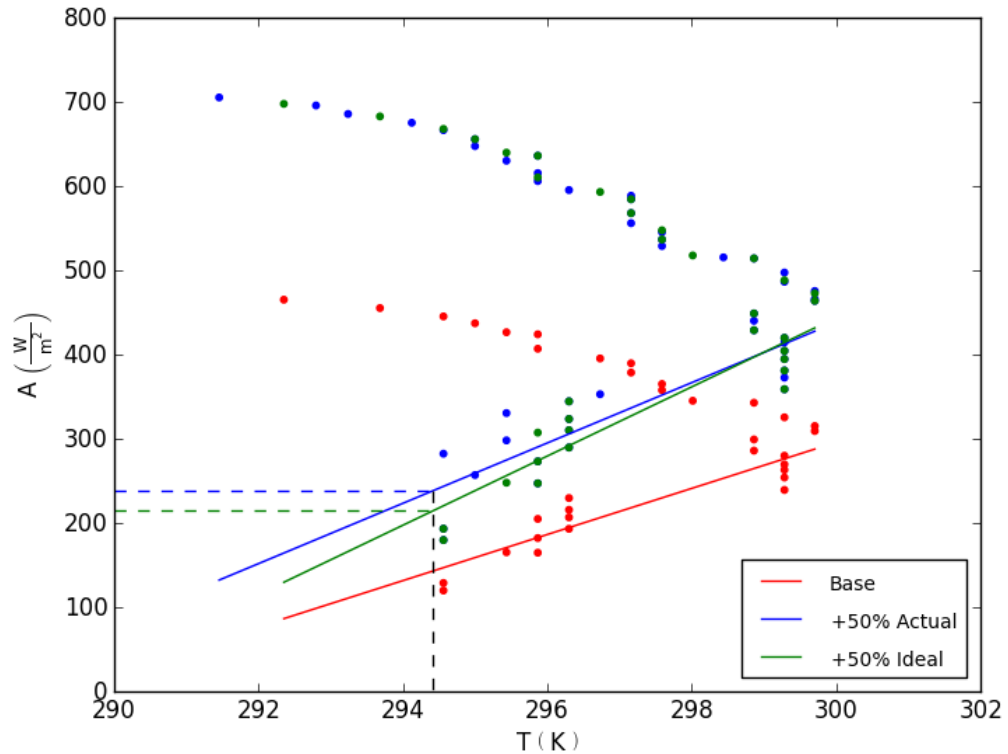
Figure 4.8.2: Sensitivity of *EF* to Available Energy Percent Change for Disney – Dry Only

A sensitivity analysis for the calibration which included wet pixels using the *H* vs.

T model for Disney was also conducted. The boundary variation was Even Bins and the

classification variation for wet pixels was $NDVI_{min}$. In contrast to the dry pixel only

calibration, *EF* was now quite sensitive to temperature as shown in Figure 4.8.3. Once

again *MAE* was given the same sign as the *Bias* error for visualization. This sensitivity is

a result of the temperature dependence of the Priestly-Taylor equation used to calculate

EF for the wet pixels. This means that an increase in temperature leads to an increase in

EF compared to the unperturbed situation. This is an important result because retrieving

surface temperatures are not very accurate. If the temperature was retrieved with an error

of +/-5 K, it could lead to an error of +/-0.05 *EF*. Therefore an increase in accuracy of

surface temperature retrieved by using platforms such as LANDSAT 8 with dual thermal

channels or ASTER with multiple thermal channels would have more of an effect on the

calibration that included wet pixels than it would on one using dry pixels only.
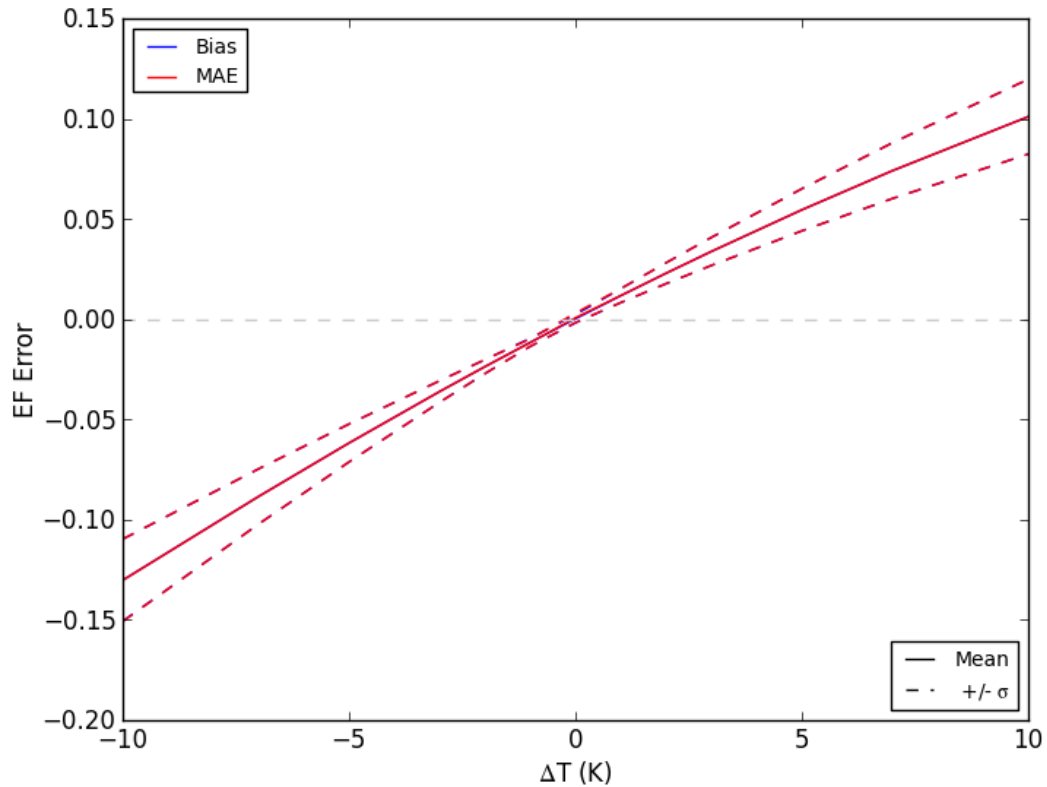
Figure 4.8.3: Sensitivity of *EF* to Temperature for Disney after Including Wet Pixels

Ideally, *EF* should not be sensitive to percent changes in available energy

following the argument made above for the dry pixel only calibration. This is because

both the wet and dry end members making up the numerator are changing by the same

proportion as the available energy making up the denominator of the *EF* calculation.

When the sensitivity analysis was performed, the difference in *EF* due to percent changes

in available energy is negligible with an error less than 0.005. For the dry pixel

calibration, the ideal case was not realized. When the wet pixels were included, the wet

and dry end member scaled similar to each other so that the ideal case was realized. The

binning issue which produced the different *H* vs. *T* relationships for the dry pixel

calibration does not affect the resulting dry end member. This can be seen in Figure 4.8.2

where the ideal and actual perturbed cases are different but the dry end members are nearly identical. Once again *MAE* was given the same sign as the *Bias* error for visualization. When absolute perturbations in available energy are used instead of percent changes, *EF* becomes sensitive to available energy as shown in Figure 4.8.4. In this case a change in energy in either direction can actually result in both positive and negative changes. The average change in *EF* for positive changes in energy is positive and vice versa. *EF* is also more sensitive to negative changes in energy. This can be explained using a simple analysis for the change in *EF* due to change in energy (*ΔA*). Using the linear relationship between sensible heat and temperature the following equation can be derived:

$$\Delta EF_i = \Delta A/(A_i+\Delta A)\ (w_i\ EF_{wet} - EF_i) \tag{4.8.1}$$

where *i* represents the ith pixel in the image, *ΔEF* is the difference between original and perturbed image, *ΔA* is the perturbation in available energy, *A* is the original available energy, *EF* is the original evaporative fraction, EF_{wet} is the evaporative fraction of wet end member using Priestly Taylor, and *w* is a weight linearly related to temperature so that it is zero at the dry end member temperature and 1 at the wet end member temperature. From this equation, it can be seen that the sign of the *ΔEF* for a given *ΔA* can be either positive or negative depending on the relationship between *EF*, *T* and EF_{wet}. It turns out that $w_i\ EF_{wet}$ is greater than EF_i on average. This equation also explains why the response for negative *ΔA* is more than positive *ΔA*. For example, ΔEF=1/2($w\ EF_{wet}$ − *EF*) when *ΔA* equal to *A* in the positive direction, but only a *ΔA* equal to *A*/3 in the negative direction is required to achieve the same *ΔEF*. This implies that the underestimation of energy would have more serious consequences than overestimation.

190

In many cases the energy was overestimated because the storage into the water column was not accounted for. In the case of Kennedy, energy was underestimated instead. In either direction the *EF* errors should be less than around 0.05 for a *ΔA*= 200 W/m^2 and less than 0.02 for *ΔA*= 100 W/m^2.
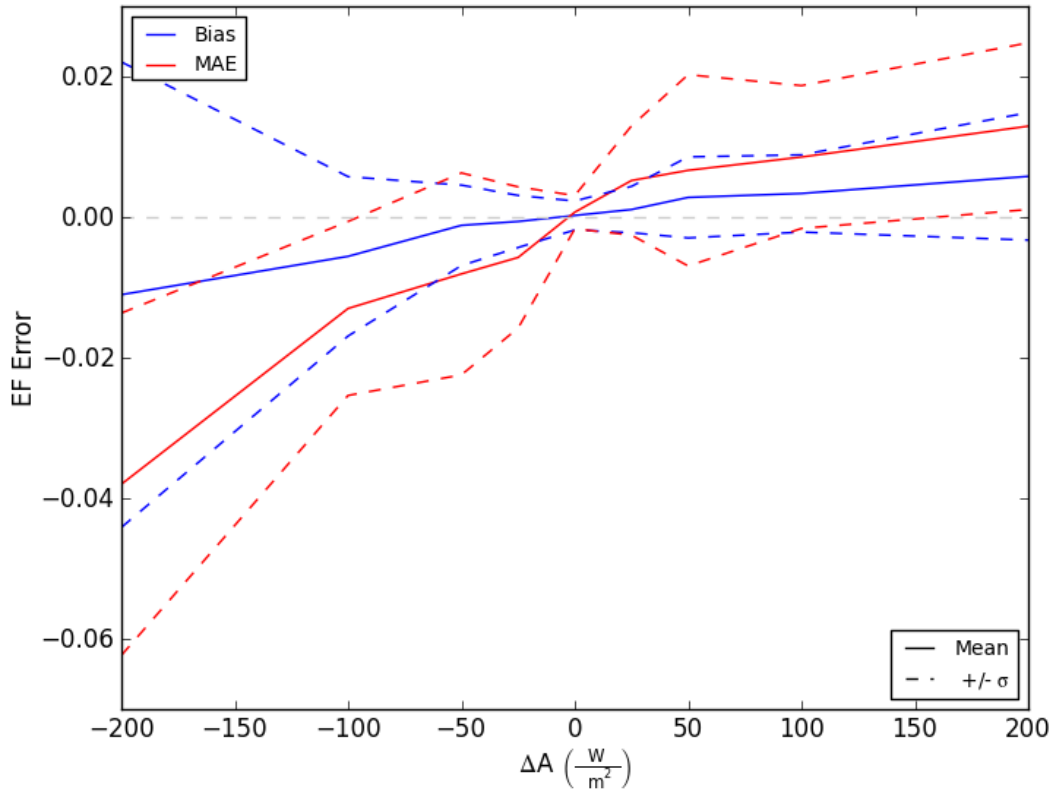
Figure 4.8.4: Sensitivity of *EF* to Energy for Disney after Including Wet Pixels

In regards to errors in available energy, the effect on actual *ET* is of more concern because it is directly related to available energy. Therefore it was important to also conduct a sensitivity analysis of actual *ET* to temperature and energy. This was done using the calibration which included wet pixels for Disney with Even Bins and *H* vs. *T*. The sensitivity of *ET* to temperature is mostly due to changes in *EF* while the sensitivity of *ET* to energy is mostly due to changes in energy since *ET=EF A*. Figure 4.8.5 shows the response of *ET* to changes in temperature where *MAE* has once again taken the sign

of the *Bias* error. It can be seen that the error is proportional to the *EF* error multiplied by something like the mean available energy for the scene. For example the mean *Bias*/*MAE* for ΔT=10 K is about equal to 40 W/m^2. This is equal to ΔEF=0.1 from earlier multiplied by mean energy of 400 W/m^2. Since the sensitivity of *EF* was larger to ΔT in the negative direction, sensitivity of *ET* was also larger in negative direction. For changes in energy, the sensitivity of *EF* was due to both changes in *EF* and energy but changes in energy dominated. Figure 4.8.6 shows sensitivity of *ET* to energy where *MAE* once again has taken the sign of *Bias*. For ΔA=+/- 200 W/m^2, ΔEF was on order of 0.03 which after multiplying this by mean energy of about 400 W/m^2 would produce a contribution of ΔET=12 W/m^2 due to change in *EF*. The remaining 100 W/m^2 is due to the change in energy itself which is equal to *EF* ΔA with *EF*=0.5.
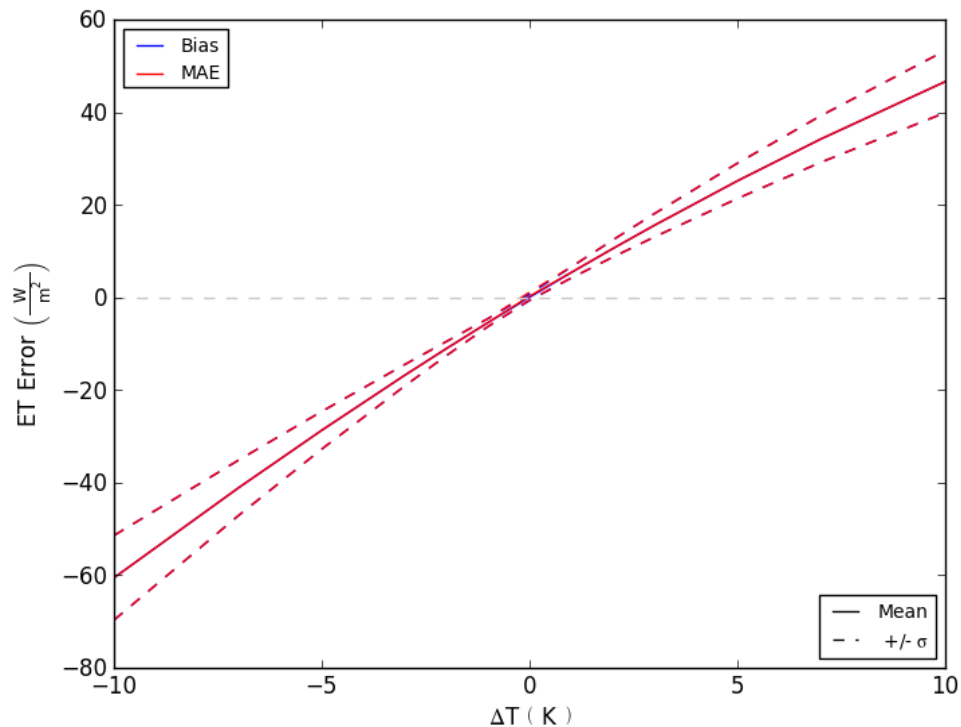
Figure 4.8.5: Sensitivity of *ET* to Temperature for Disney after Including Wet Pixels

192
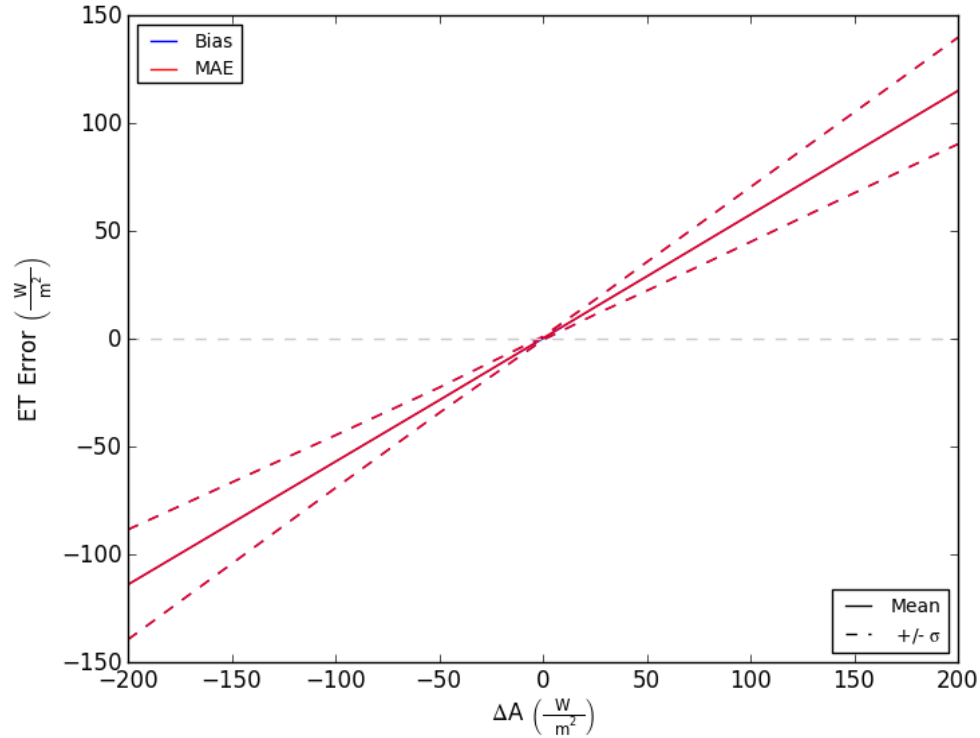
Figure 4.8.6: Sensitivity of *ET* to Energy for Disney after Including Wet Pixels

4.8.2 Sensitivity to Roughness Length

A sensitivity analysis for *EF* vs. roughness length was performed for the Gainesville study area. Gainesville was chosen because the *ΔT* vs. *T* method seemed to work the best for this study area and there are also a large number of useable scenes available for the study area. Even Bins was used along with the calibration which included wet pixels found using $NDVI_{min}$. The roughness length (z_o) was adjusted by +/- 1 m while forcing z_o to be at least 0.0001 m for perturbations in the negative direction. Figure 4.8.7 shows the *EF* errors for the difference between original and perturbation cases. *MAE* has taken the sign of the *Bias* error for visualization purposes. As z_o increases, *EF* decreases because estimated sensible heat increases with roughness. As z_o decreases the mean *MAE* and *Bias* for *EF* increases, but there are some scenes in which the *EF* actually decreases. Because of this the *Bias* is less than *MAE*. This can be

193

explained by looking at Figure 4.8.8 which shows the variation in sensible heat with z_o for bare ground on 3/28/1999. It is possible for the sensible heat to increase with decreasing z_o because the increasing instability of boundary layer ($|L|$ decreasing) increases turbulence more than the decreasing friction velocity ($u*$) reduces turbulence. It would seem that the original z_o for most pixels is similar to or greater than the z_o that produces minimum sensible heat. Therefore an increase in z_o will not result in a change in direction of the response of sensible heat to z_o. When z_o is reduced on the other hand, some of the pixels will cross this area of minimum sensible heat.

A back of the envelope calculation was performed to estimate the *EF* error produced due to errors in z_o in which z_o was estimated from vegetation height (h) using $z_o=h/10$. If it was assumed that LIDAR could detect vegetation height with an accuracy of about 1m, then the error in z_o would be on the order of 0.1 m. Figure 4.8.9 shows sensitivity of *EF* to z_o using a linear x axis. It shows that the error in *EF* would be somewhere around 0.02. If the roughness length was completely unknown on the other hand, very large errors could occur. Figure 4.810 shows a simulation using the same calibration variation as before, except the roughness length was assumed to be a constant value for the entire scene instead of incrementing each pixel. This can lead to large errors depending on the constant z_o which is used. If a small z_o is assumed then error in *EF* can be around 0.15, but assuming a large z_o will result in smaller errors within 0.05. This is occurring because most of the study area is made up of tress with large z_o so that the best guess would be something close to the majority z_o. Figure 4.8.11 shows the distribution of z_o in the landscape with the corresponding mode near $z_o=1$ m. It should be noted that

194

assuming constant roughness length is not the same as assuming constant g_a because of the effect of instability on g_a is still accounted for.
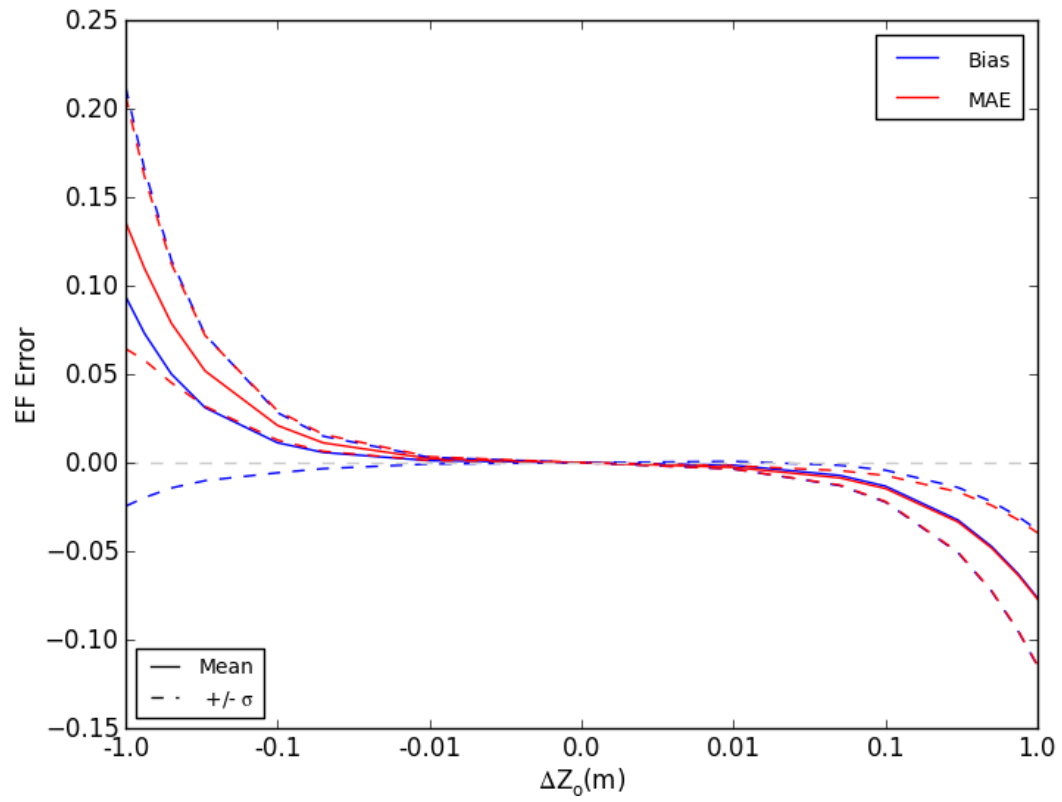
Figure 4.8.7: Sensitivity of *EF* to z_o for Gainesville

Figure 4.8.8: Effect of z_0 on H, u^* and L for Gainesville 3/28/1999 over Bare Ground
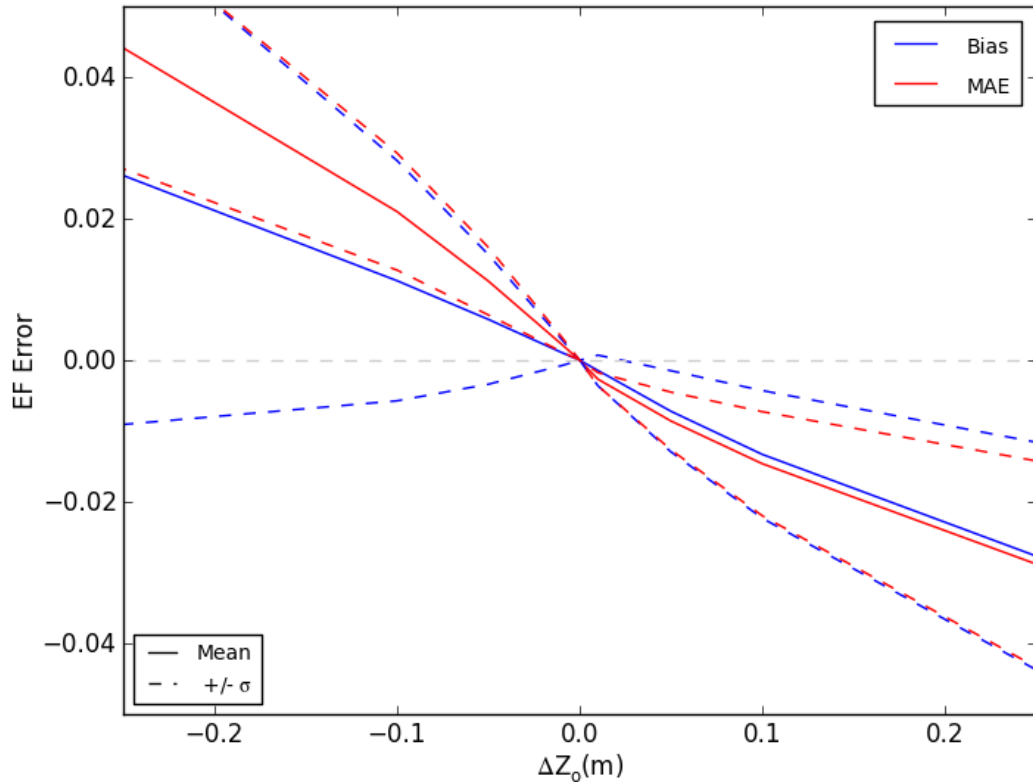
Figure 4.8.9: Sensitivity of EF to z_0 for Gainesville Linear Scale
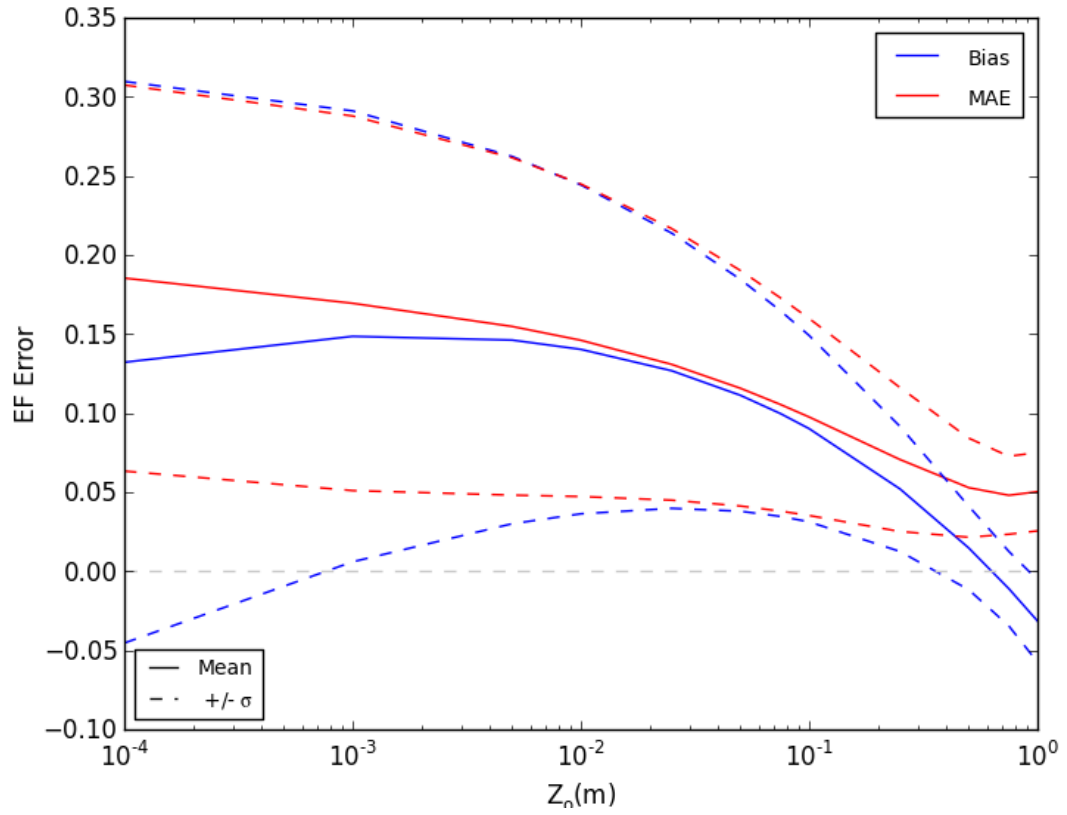
Figure 4.8.10: Effect of Using Constant z_o *EF* for Gainesville
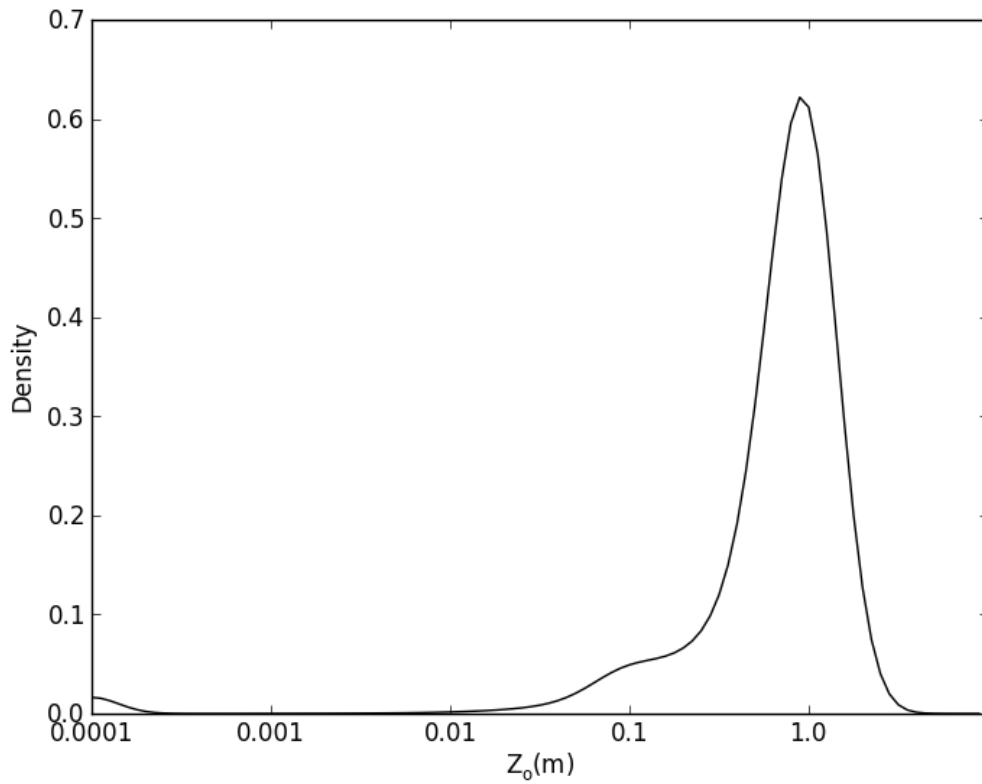
Figure 4.8.11: Distribution of z_o for Mean of All Scenes for Gainesville

4.9 Data Fusion of LANDSAT Imagery with Simulated MODIS Imagery

Six data fusion algorithms 1) Simple Interval 2) Simple Ratio 3) Double Sided Proportion 4) Similar Temperature 5) Similar *ET* 6) Similar *EF* and four interpolation methods 1) Nearest *ET* Neighbor Interpolation 2) Linear *ET* Interpolation 3) Nearest *EF* Neighbor Interpolation 4) Linear *EF* Interpolation were used to produce *ET* maps. Coarse scale imagery such as that produced from MODIS was simulated by aggregating 120 m LANDSAT thermal resolution into 960 m blocks. Fused images were created for every other image in the series of available images based on neighboring images which produced two sequences of images. The simulations were performed for Disney Preserve and Kennedy Space Center study areas using Even Bin Threshold Fit boundary variation in the calibration which included wet pixels detected using $NDVI_{min}$. Albedo values less than 0.5 were filtered out for Kennedy. Instantaneous *ET* was used for comparison between the fused and originally retrieved maps. Figures 4.9.1 and 4.9.2 show the image scale aggregate errors as a function of fusion/interpolation type for each study area and sequence. Image scale refers to comparing mean *ET* for the entire image. Image scale bias is the difference between the mean *ET* of the images averaged over the entire sequence. This represents the error in estimating *ET* for the entire image over long time scales. Image scale *MAE* is the absolute value of the difference between mean *ET* of the images averaged over the entire sequence. This represents the error in estimating *ET* for the entire image at the daily time scale.

Figure 4.9.1 shows a large variability in image scale *Bias* depending on whether the first run or second run of the sequence was processed. For Disney, the method which produced lowest image scale *Bias* for both runs was Similar *ET*, and surprisingly Linear

ET was also a close second. Nearest *EF* and Linear *EF* was the best for the first run. The worst methods were Nearest Neighbor and Double Sided Proportion. For Kennedy, the methods that used similar blocks for change did not work very well with respect to image scale *Bias* except for Similar *EF* on the first run. Double Sided Proportion performed the best for both runs and Nearest *ET* and Linear *ET* worked nearly as well. Nearest *EF* and Linear *EF* did well on the first run. Figure 4.9.2 shows the image scale *MAE* which has a more consistent pattern between runs compared to image scale *Bias*. For Disney, Similar *ET* and *ET* are the best for both runs, but Simple Interval and Ratio both work nearly as well. For Kennedy, Similar *ET*, Similar Temperature, Simple Interval, Simple Ratio and Linear *EF* performed the best on average.
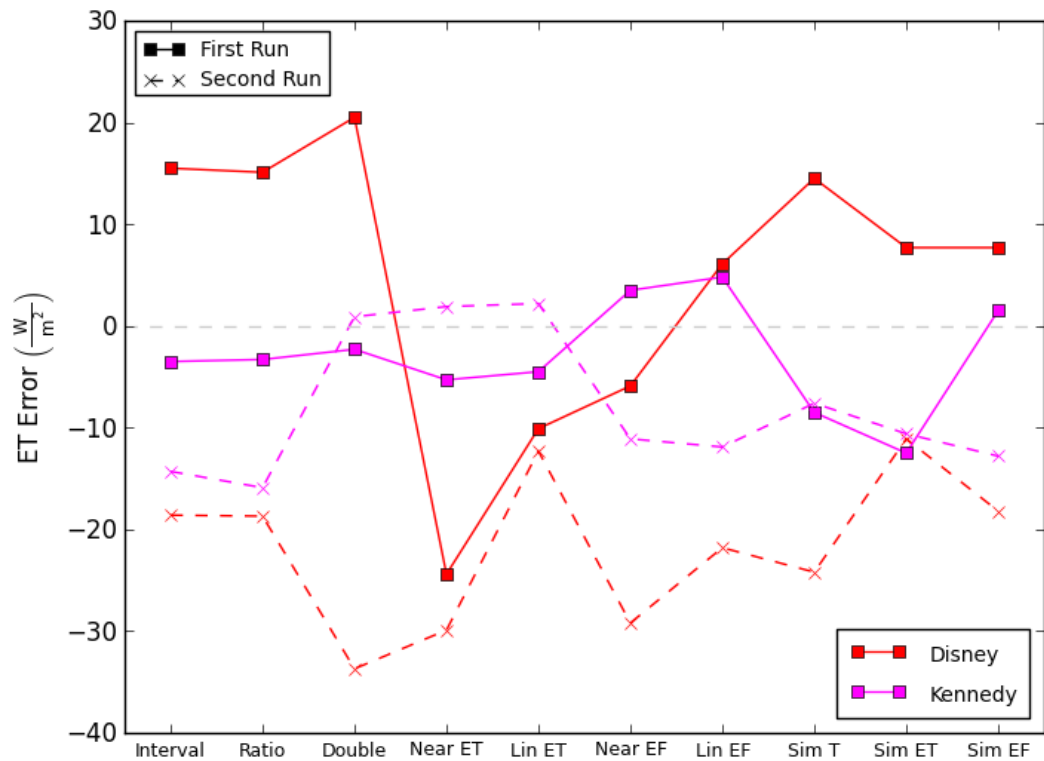
Figure 4.9.1: Image Scale *Bias* for Different Fusion Types
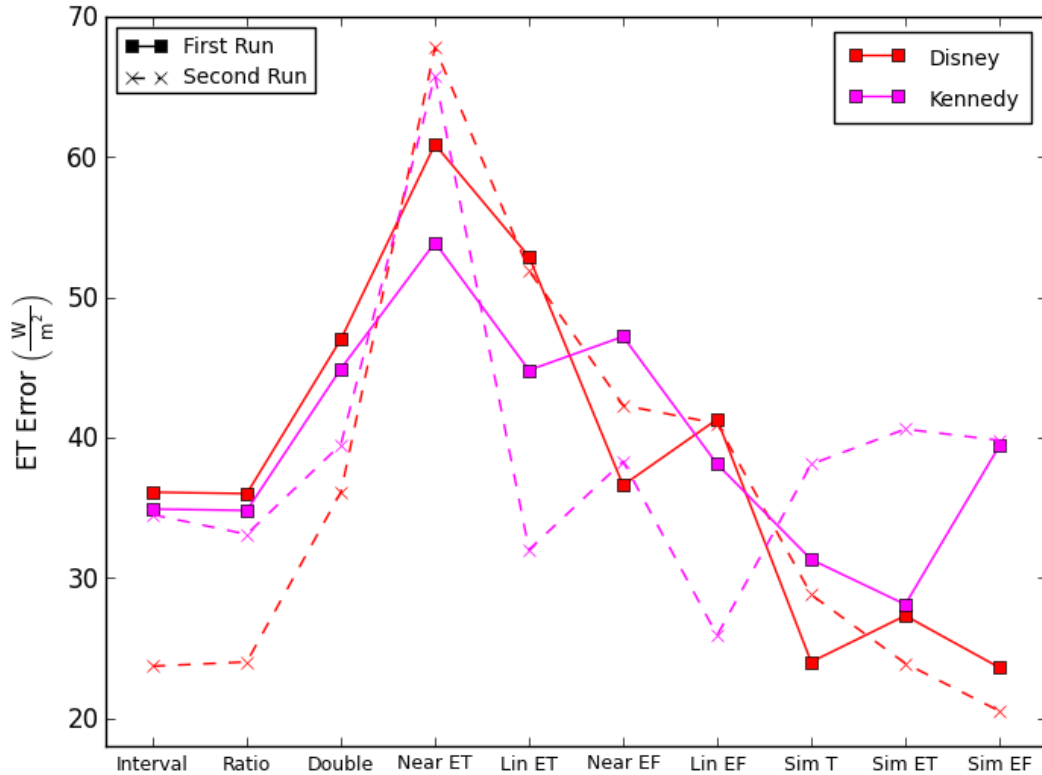
Figure 4.9.2: Image Scale *MAE* for Different Fusion Types

Figures 4.9.3 and 4.9.4 show the pixel scale aggregate errors as a function of

fusion/interpolation type for each study area and sequence. Pixel scale refers to

comparing *ET* over time for each individual pixel in the image in order to produce a map

of *Bias* and *MAE* error. Average pixel scale *Bias* is the absolute value of each individual

pixel's bias averaged over the entire image. This represents the average error in

estimating *ET* for an individual pixel over long time scales. The average pixel scale *MAE*

is the average of each individual pixel's *MAE* over the entire image. This represents the

error in estimating *ET* for an individual pixel at the daily time scale. Figure 4.9.3 shows a

more consistent pattern between the first and second run for pixel scale *Bias* compared to

image scale *Bias*. For Disney, the method which produced the lowest pixel scale *Bias*

consistently was Similar *ET*, but Nearest *EF* was the best for First Run. The worst

methods were Nearest *ET* and Double Sided Proportion. This outcome was similar to the

image scale *Bias*, except there is a larger magnitude of error. For Kennedy, all of the methods performed very similarly on average. Linear *ET* and Similar Temperature are the most consistent while Interval and Ratio varied the most. Figure 4.9.4 shows the pixel scale *MAE* which has a pattern similar to the image scale *MAE*. For Disney, Similar *EF* and *ET* are the best for both runs, but Simple Interval and Ratio both work nearly as well. For Kennedy, Similar *ET*, Similar Temperature, Simple Interval, Simple Ratio and Linear *EF* dif the best on average.

For both study areas and both sequences, Nearest *ET* clearly performed the worst with respect to *MAE*. While Linear *ET* and Double Sided Proportion had a wide range of results among study area and sequences, they did not perform as well on average compared to the other techniques with respect to *MAE*. A very interesting result is that Linear Interpolation proved to be as useful as more complicated fusion techniques. Linear *EF* had low *MAE* and Linear *ET* had low *Bias*. These methods could be useful depending on application, but the method which performed the most consistently across all study areas and sequences for both bias and *MAE* was Similar *ET*. Other methods worked better in certain instances, but the results for Similar *ET* did not vary much while having an acceptable amount of error. Table 4.9.1 shows the results for Similar *ET* next to the optimal variation for each study area and sequence. For each error type the minimum error was subtracted from error for each fusion type. This residual was summed over each error type for each fusion type to produce the optimizing criteria. The largest individual difference between Similar *ET* and optimal variation was within 2% and 5% for Disney and Kennedy respectively. Similar *ET* wasn't absolute best in all cases, but it was the most reliable.
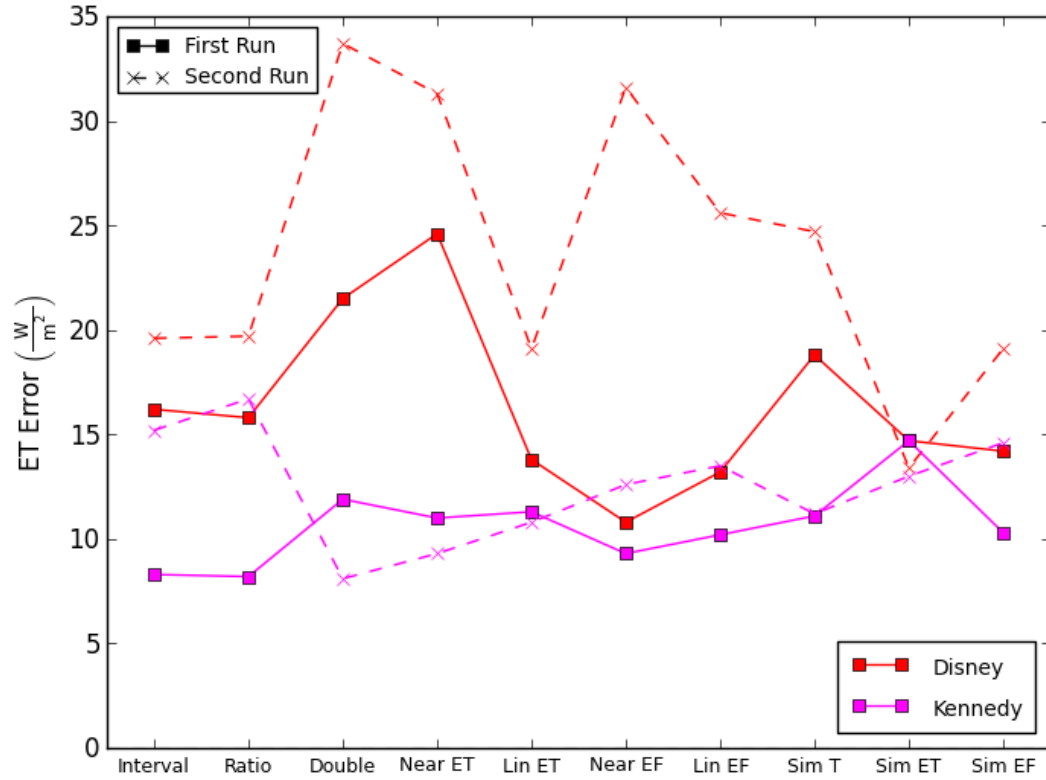
Figure 4.9.3: Average Pixel Scale *Bias* for Different Fusion Types
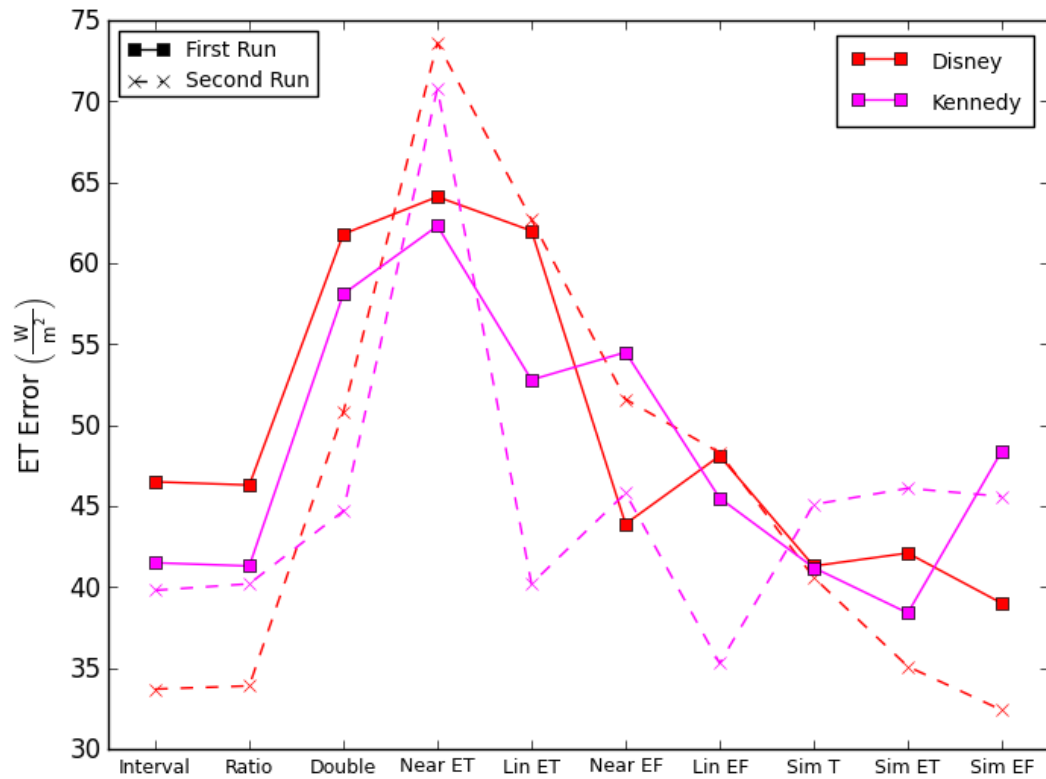
Figure 4.9.4: Average Pixel Scale *MAE* for Different Fusion Types

Table 4.9.1: Optimal Methods for Study Area and Run Combinations with Errors

Simulation			Image Scale		Pixel Scale	
Study Area	Run	Method	Bias ($^W/_{m^2}$)	MAE ($^W/_{m^2}$)	Bias ($^W/_{m^2}$)	MAE ($^W/_{m^2}$)
Disney	First	Similar ET	7.7 (2.9 %)	27.3 (10.3 %)	14.7 (5.5 %)	42.1 (15.8 %)
Disney	First	Similar EF	7.7 (2.9 %)	23.6 (8.9 %)	14.2 (5.3 %)	39.0 (14.7 %)
Disney	Second	Similar ET	-11.1 (-4.0 %)	23.9 (8.7 %)	13.4 (4.9 %)	35.1 (12.7 %)
Kennedy	First	Simple Ratio	-3.3 (-1.3 %)	34.8 (13.4 %)	8.2 (3.2 %)	41.3 (16.0 %)
Kennedy	First	Similar ET	-12.5 (-4.8 %)	28.1 (10.9 %)	14.7 (5.7 %)	38.4 (14.8 %)
Kennedy	Second	Linear ET	2.2 (0.9 %)	32.0 (13.0 %)	10.8 (4.4 %)	40.2 (16.4 %)
Kennedy	Second	Similar ET	-10.6 (-4.3 %)	40.6 (16.6 %)	13.0 (5.3 %)	46.1 (18.8 %)

4.9.1 Finding Similar and Homogenous Coarse Pixels for Data Fusion

Homogenity was included in addition to similarity as a criteria for finding blocks (coarse pixels) which contain the amount of change to be used for a target pixel. This requires a weight to determine the importance of homogeneity over similarity. Figure 4.9.5 shows the results of all error types and sequences as a function of this weight when *ET* was used in the search at Disney. A larger weight means homogeneity has more of an influence on choosing the block than similarity. A weight of zero returns the same results as Similar *ET*. As the weight becomes large, the change from the most homogenous block in the image is used for all pixels. For all of the simulations except for both bias types of the second run there is some intermediate weight which minmizes the error. The errors for both bias types of the second run are minimum for a weight equal to zero (ie. not including homogeneity). For the first run, both of the bias are at a minimum at a weight equal to about 1.25. For *MAE* the error is minium at a wieght equal to about 0.25. For most of the cases, including homogeniety only has the potential to reduce the errror by about 5 W/m^2, but it also has the potential to increase the error by more than 10 W/m^2. If homogeneity was to be included, a weight=0.25 would probably be the best

choice because at this point the negative effects on *Bias* has not been experienced yet, but the positve effects on *MAE* have been achieved.
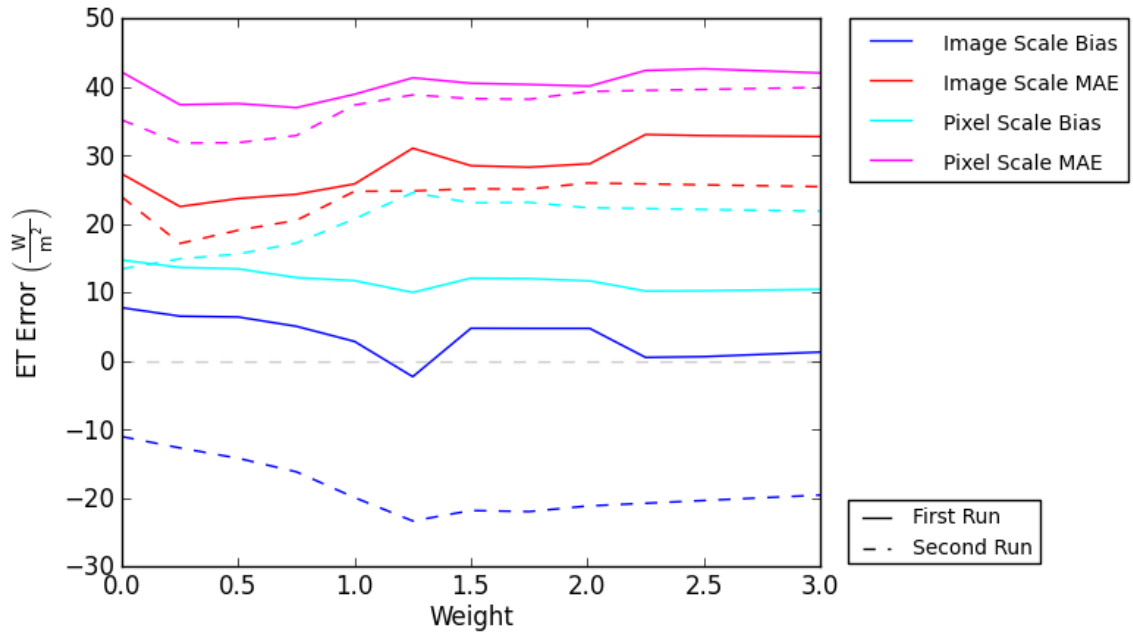
Figure 4.9.5: Variation of Errors with Homogeneity Weight for Disney Similar *ET*

4.9.2 Examination of the Temporal Variability of Data Fusion Errors

It is useful to examine the time series of differences between the actual *ET* map retrieved and the map produced using data fusion or simple interpolation. Figure 4.9.6 and 4.9.7 shows a time seires of the mean *ET* of the entire image for actual *ET* retreived, Linear *EF* and Similar *ET* fusion for Disney and Kennedy respectively. This represents differences at the image scale since mean *ET* of entire image is used. Similar *ET* and Linear *EF* are both able to reproduce peaks and valley of *ET* most of the time, but Similar *ET* is mabye a bit more consistent. Linear *EF* might not reproduce peaks and valleys of *EF*, but since energy for target day is accurate the resulting *ET* works. For Disney, the Similar *ET* fusion is better except for 2 or 3 days. For some days, Similar *ET* produced erratic values such as the 2 days in mid 2005. For Kennedy, Linear *EF* is even more sucessful, but Similar *ET* still reporoduces the time series a bit better except for 2 days.

204

Linear *EF* possible works better for Kennedy because the return period of LANDSAT is
8 days vs the standard 16 days because Kennedy is located where two scenes overlap.

Figure 4.9.8 shows the frequency distribution of the minimum time (Δt_{min}) between the
scene being estimated and the nearest neighbor for Disney and Kennedy. For Kennedy
the mean value is aboue 25 days while for Disney it is about 50 days. Also Disney has
much more variance in this Δt_{min} but Kennedy does have a large outlier at around 250
days.
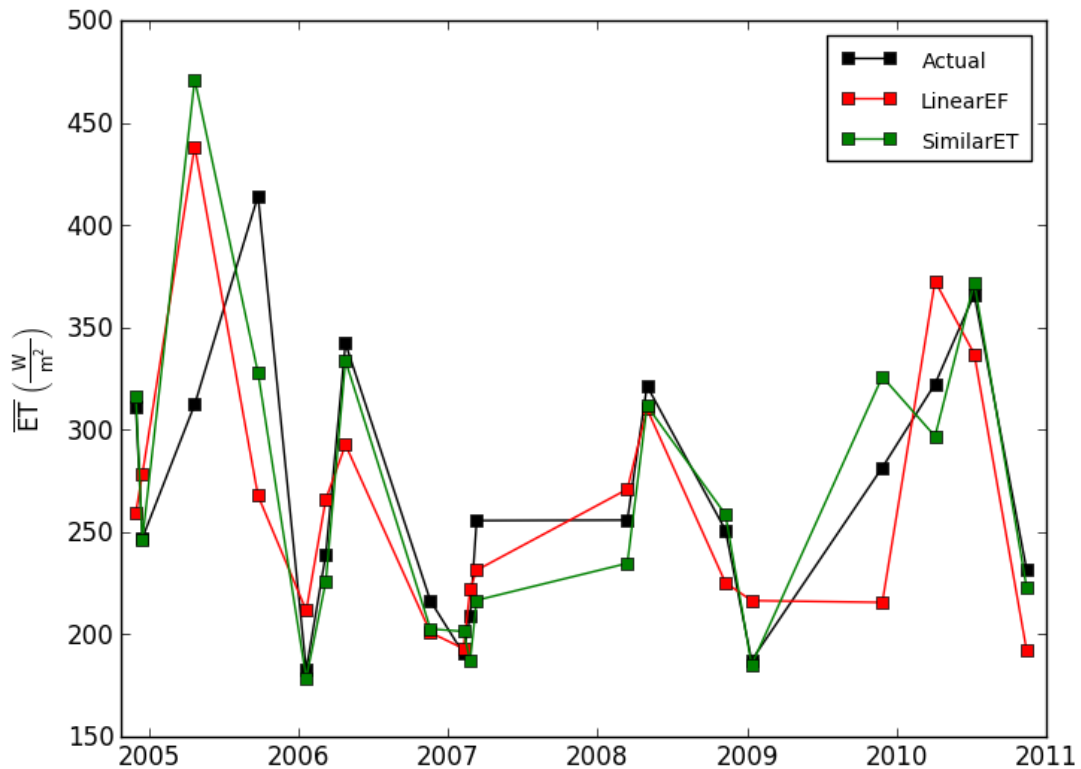
Figure 4.9.6: Mean *ET* vs. Time for Actual, Linear and Similar *ET* in Disney
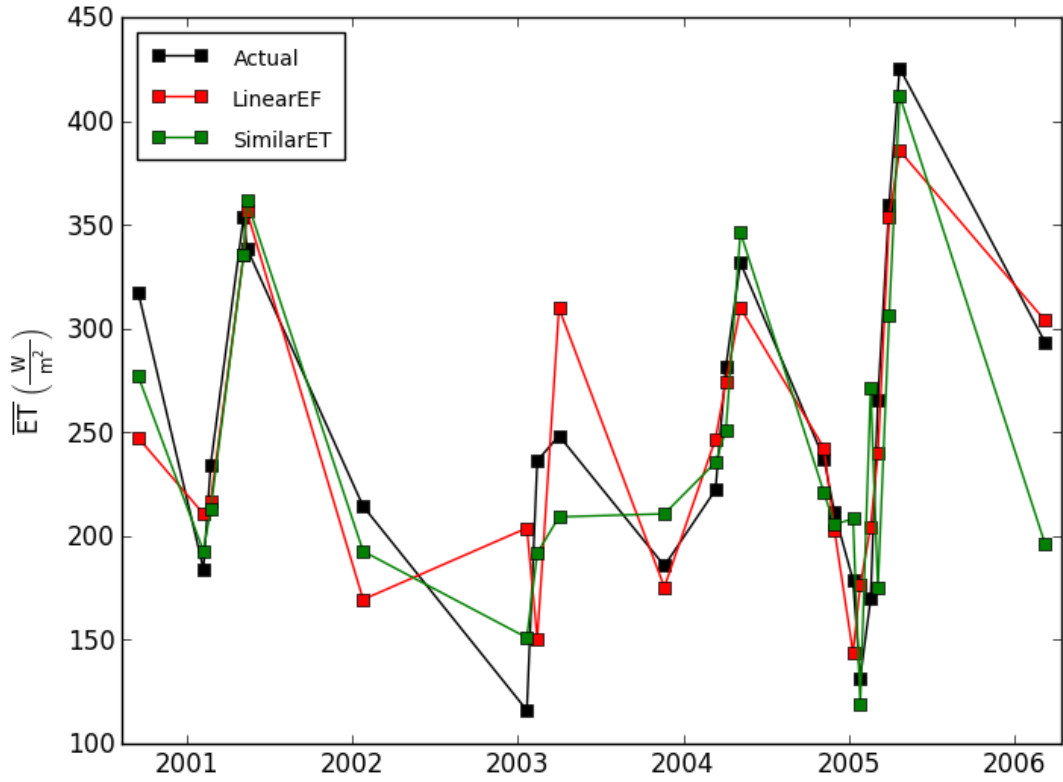
Figure 4.9.7: Mean *ET* vs. Time for Actual, Linear and Similar *ET* in Kennedy
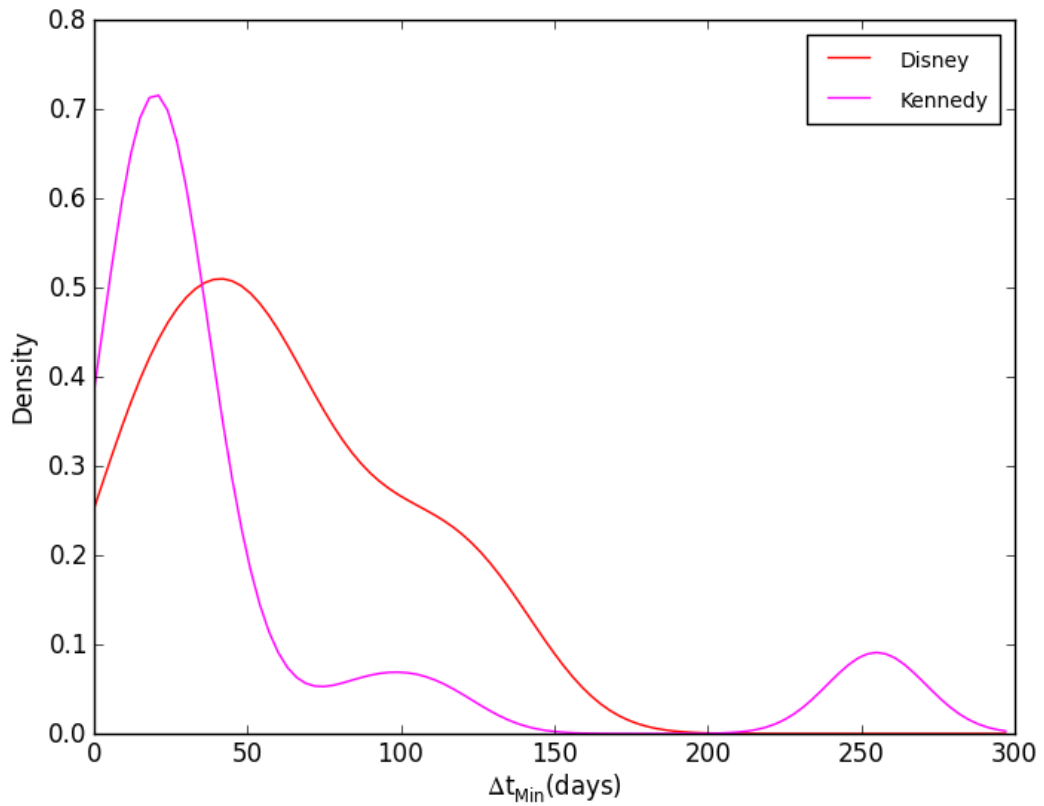
Figure 4.9.8: Frequency Distribution of *Δt*_min for Disney and Kennedy

Figures 4.9.9 and 4.9.10 show the *Bias* and *MAE* error between the actual and

Similar *ET* fused *ET* maps as a function of Δt_{min} for Disney and Kennedy. It would seem

that the error should increase as Δt_{min} increases. For Disney, there is some evidence for

this once Δt_{min} reaches around 100 days. This conclusion is not very robust though

because there are only about 3 scenes with Δt_{min} this large. It is interesting to see that *Bias*

and *MAE* are somewhat constant for Δt_{min} less than 100 days. For Kennedy, there is a

wide range of error even for scenes with a very small Δt_{min}. Once again there are not

many days with large Δt_{min} (only about 3 greater than 40 days), but all of them are on the

large end of the error range. It would be interesting to run simulation in which neighbors

were chosen so that Δt_{min} was greater than 100 for Disney and greater than 50 for

Kennedy. It would seem that larger Δt_{min} would result in larger errors on average but the

evidence for this did not robustly appear in the current analysis. In the end, the

acceptability of the error on a seasonal time scale for Disney and monthly time scale for

Kennedy is very encouraging.
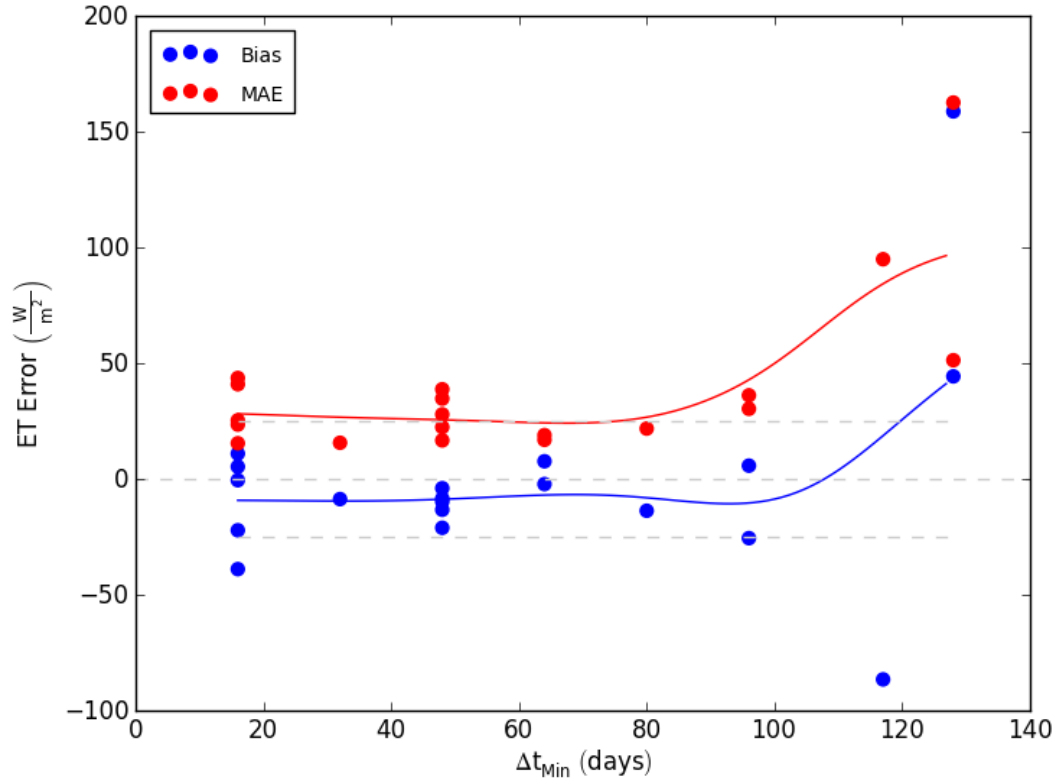
Figure 4.9.9: *ET* Error vs. *Δt*_{min} using Similar *ET* Fusion for Disney
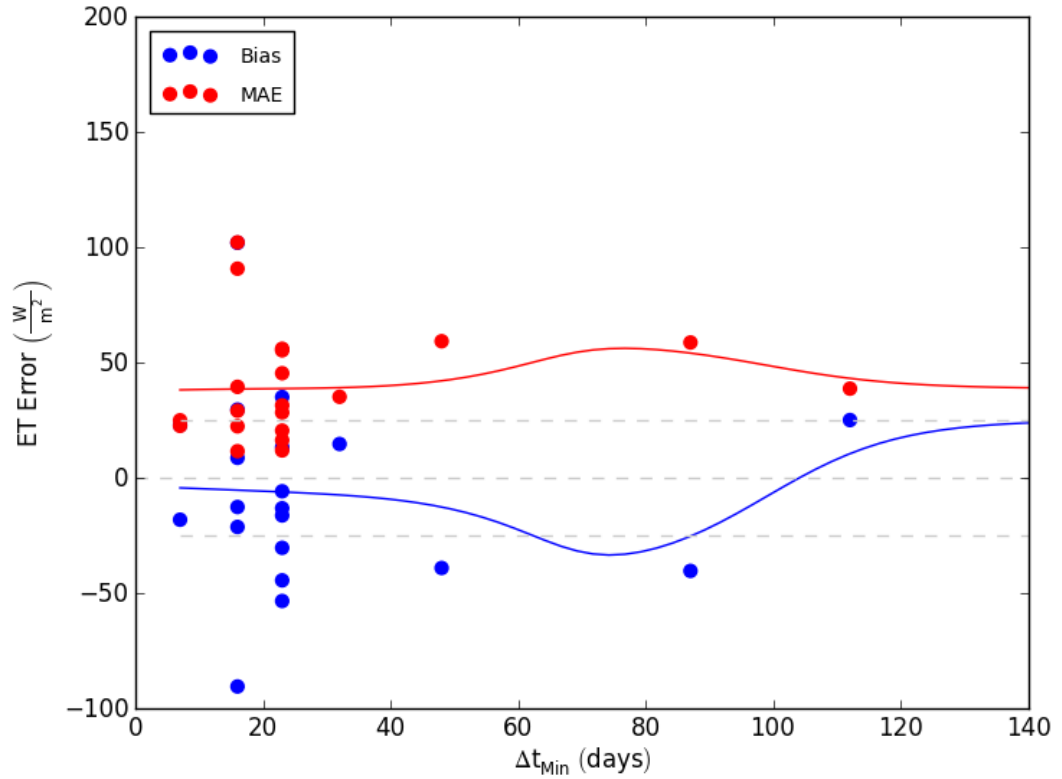
Figure 4.9.10: *ET* Error vs. *Δt*_{min} using Similar *ET* Fusion for Kennedy

4.9.3 Examination of Spatial Variability of Data Fusion Errors

It is useful to look at maps of *Bias* and *MAE* errors which shows the aggregation of error over time for individual pixels. This allows one to determine whether certain areas of the image are more susceptible to errors. It is interesting to compare the spatial distribution of errors using the Simple Interval method to the Similar *ET* method. Figures 4.9.11 and 4.9.12 show maps of the *ET Bias* error from the 1st run for Simple Interval Fusion and Similar *ET* Fusion respectively. The first thing to notice is that Simple Interval produces much more "blocky" pattern of errors than Similar *ET*. This is because the change for an entire block or coarse pixel is the same for Simple Interval, but Similar *ET* searches for the change among all blocks which most fits each individual pixel. For Similar *ET,* the errors seem to coincide with the features in the landscape more readily and the *Bias* is more balanced between over and under estimation compared to Simple Interval. For example, *ET* is understimated for the lake area but overestimated for the areas of vegetation. The dry areas to the west have no clear pattern of error. Figures 4.9.13 and 4.9.14 show the same maps of *ET Bias* excpet for Kennedy. For Kennedy the blocky pattern also appears for Simple Interveal but the error is a bit more balance between over and under estimation. For Similar *ET* the error pattern is once again smoother showing overestimation for dry areas and underestimation for the wet areas.

The effect of the blockiness of the Simple Interval fusion is shown in Figure 4.9.15 which shows the mean *ET* map for Disney over the 2nd run sequence. Most of the blockiness is located over the lake and it is intersting how smooth the results are elsewhere. This is because the range of the errors are much smaller than the range of the actual *ET* values so that the errors are not so evident in the final product. Figure 4.9.16

demonstrates the ability of Similar *ET* fusion to produce a smooth *ET* map, but for the

most part both methods produce similar looking results in terms of mean *ET* over the

time series. Figure 4.9.17 and 4.9.18 show the mean *ET* for the 2nd run in Disney for the

actual retrieved *ET* and Similar *ET* fusion respectively. Figure 4.9.18 and 4.9.16 are the

same except 4.9.18 is classified so that *ET* values can be more easily translated from the

map. A comparison of Figure 4.9.17 and 4.9.18 shows that Similar *ET* fusion does a good

job of determining the pattern of *ET* in the landscape. Figures 4.9.19-4.9.22 shows the

results of the same analysis explained above but for Kennedy. It is interesting that the

blocky pattern does not appear for Simple Interval fusion in Kennedy because the *Bias*

map was very blocky. The small range of errors once again blend into the larger

variability of mean *ET*. Also Figures 4.9.21 and 4.9.22 show that Similar *ET* fusion is

succesful at reporeducing the pattern of *ET* in the landscape.
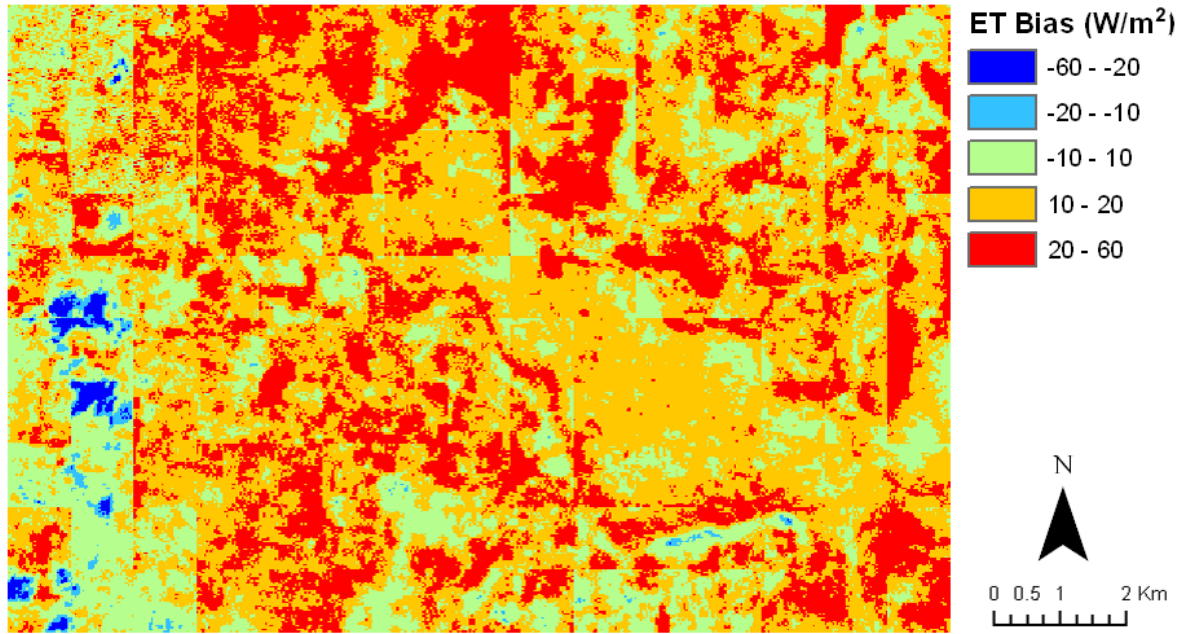
Figure 4.9.11: Map of *ET Bias* using Simple Interval Fusion for Disney 1st Run
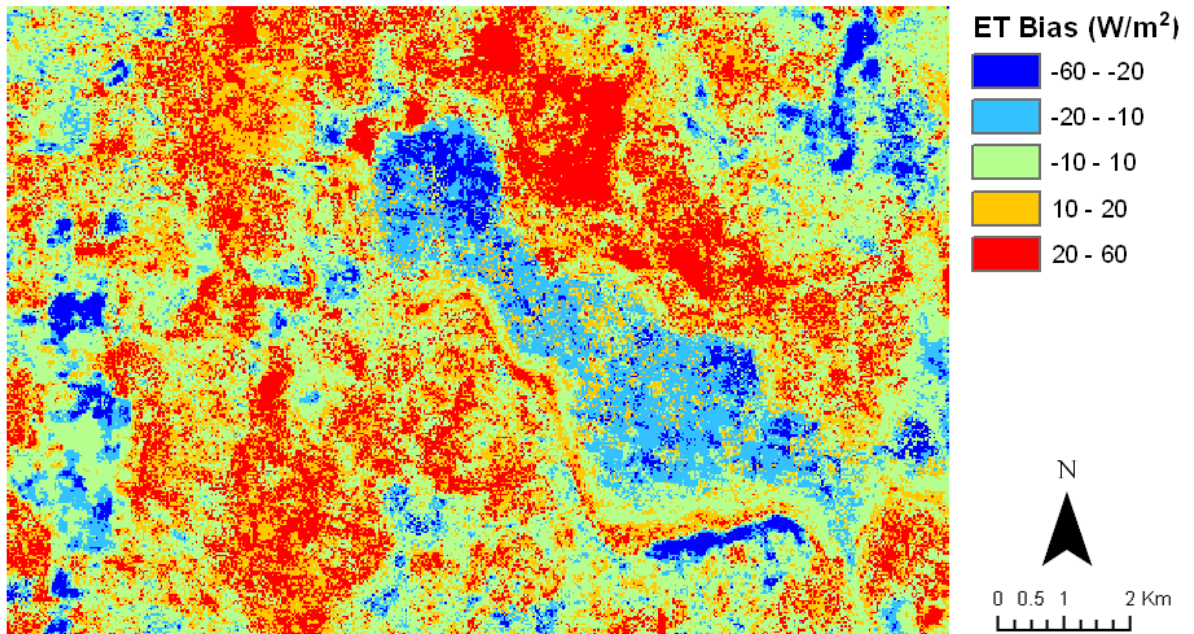
Figure 4.9.12: Map of *ET Bias* using Similar *ET* Fusion for Disney 1st Run
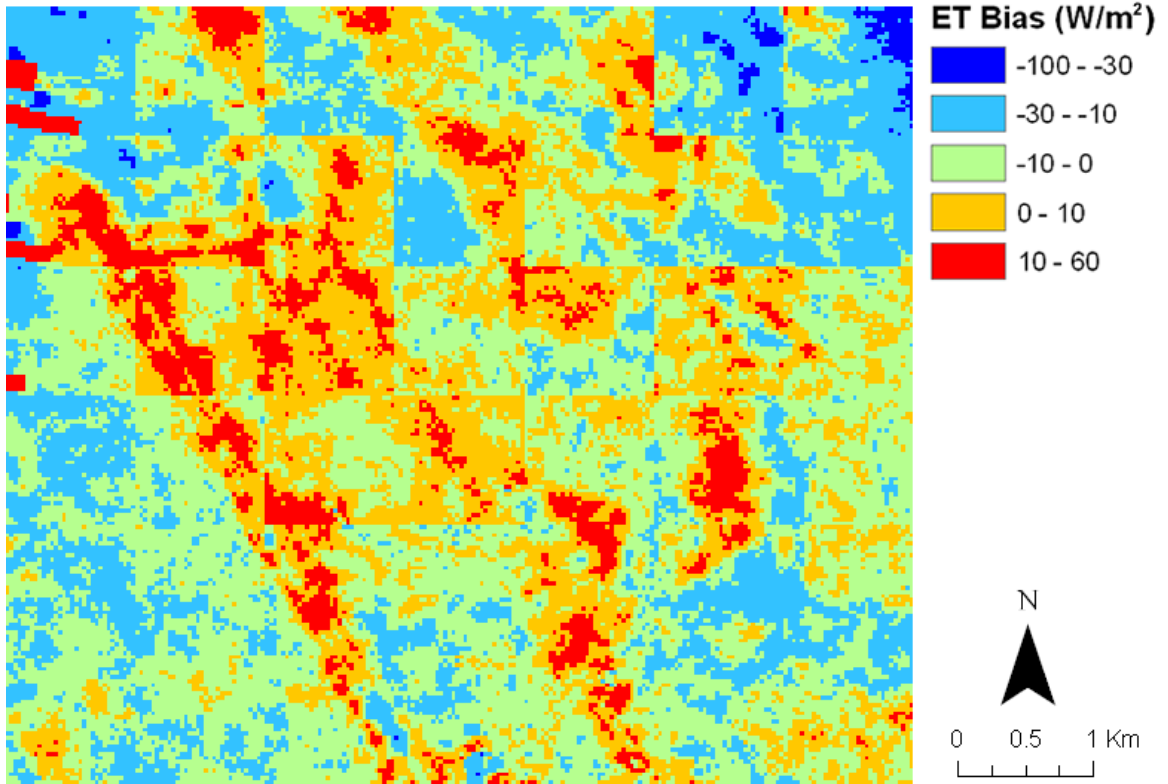
Figure 4.9.13: Map of *ET Bias* using Simple Interval Fusion for Kennedy 1st Run
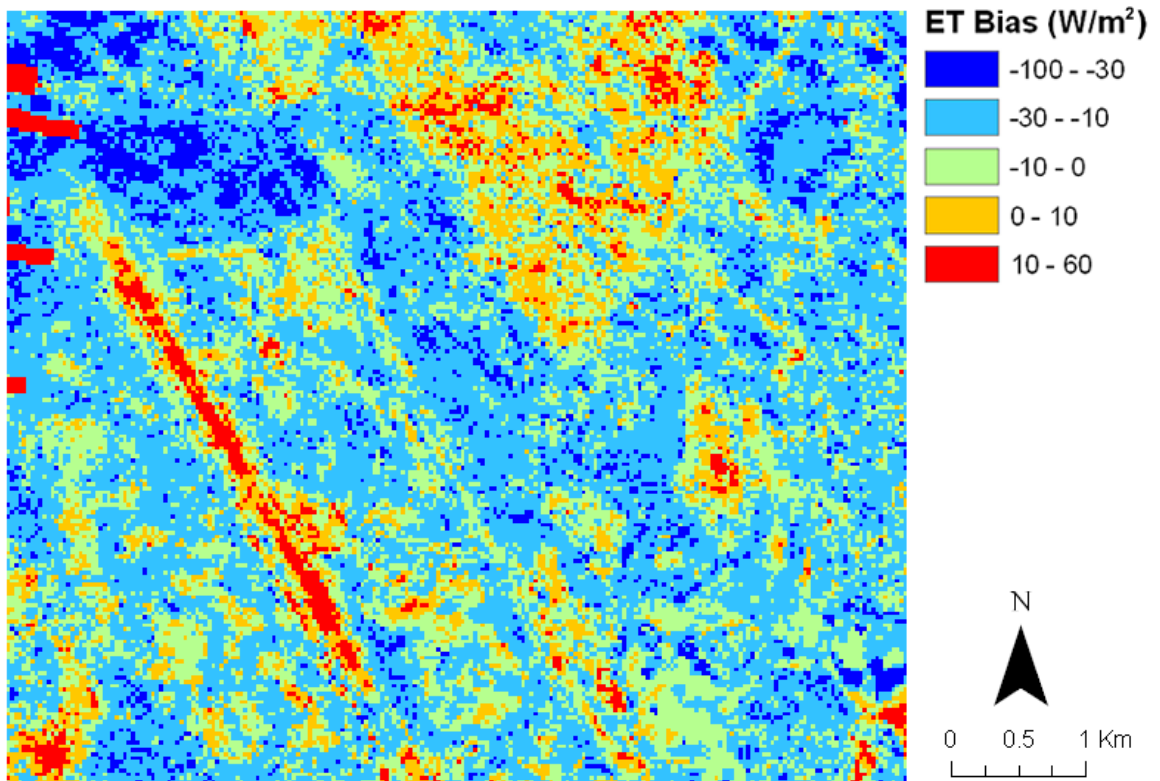
Figure 4.9.14: Map of *ET Bias* using Similar *ET* Fusion for Kennedy 1st Run
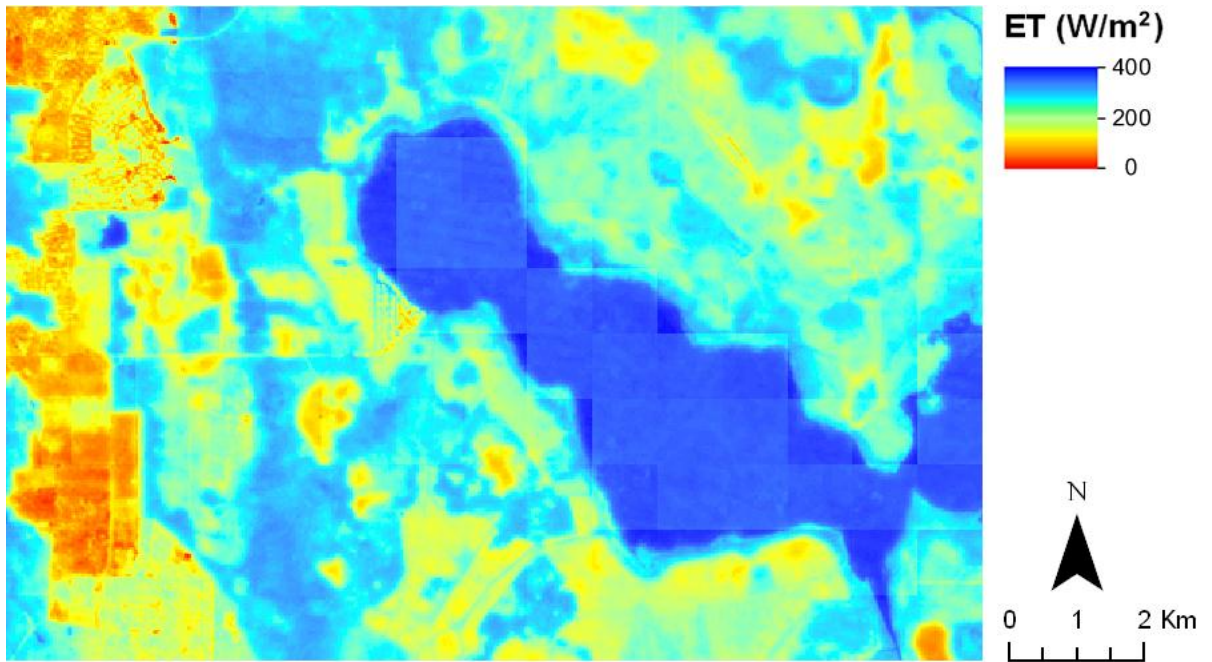
Figure 4.9.15: Continuous Mean *ET* Map using Simple Interval Fusion for Disney 2nd Run
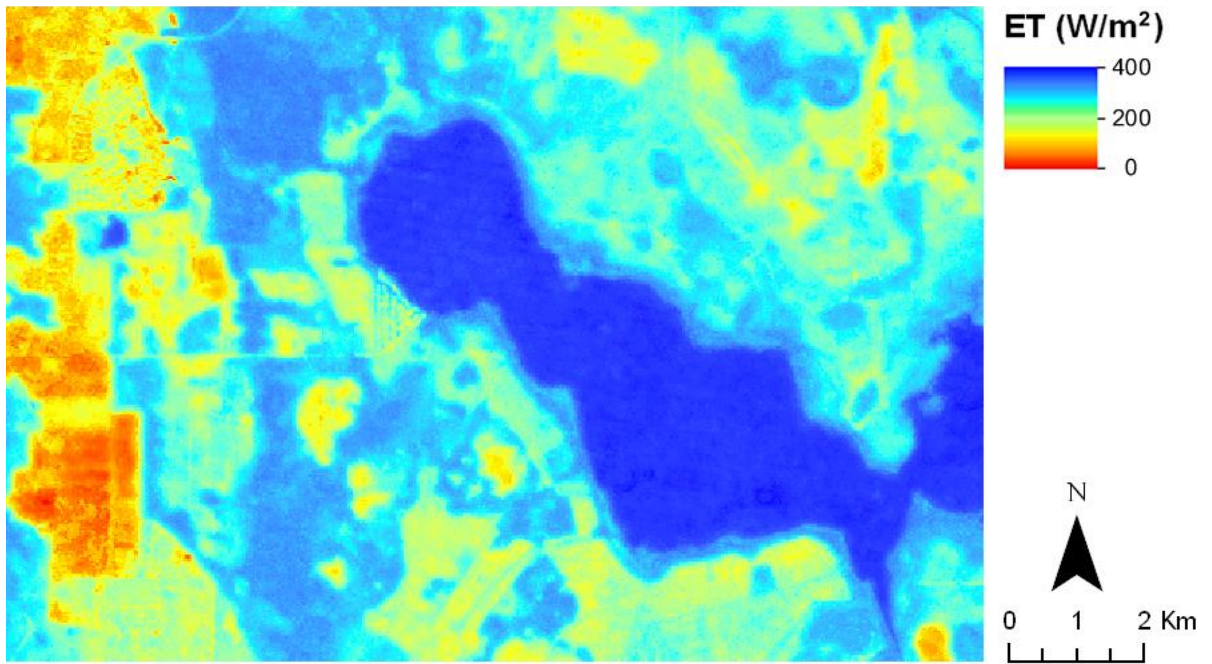
Figure 4.9.16: Continuous Mean *ET* Map using Similar *ET* Fusion for Disney 2nd Run
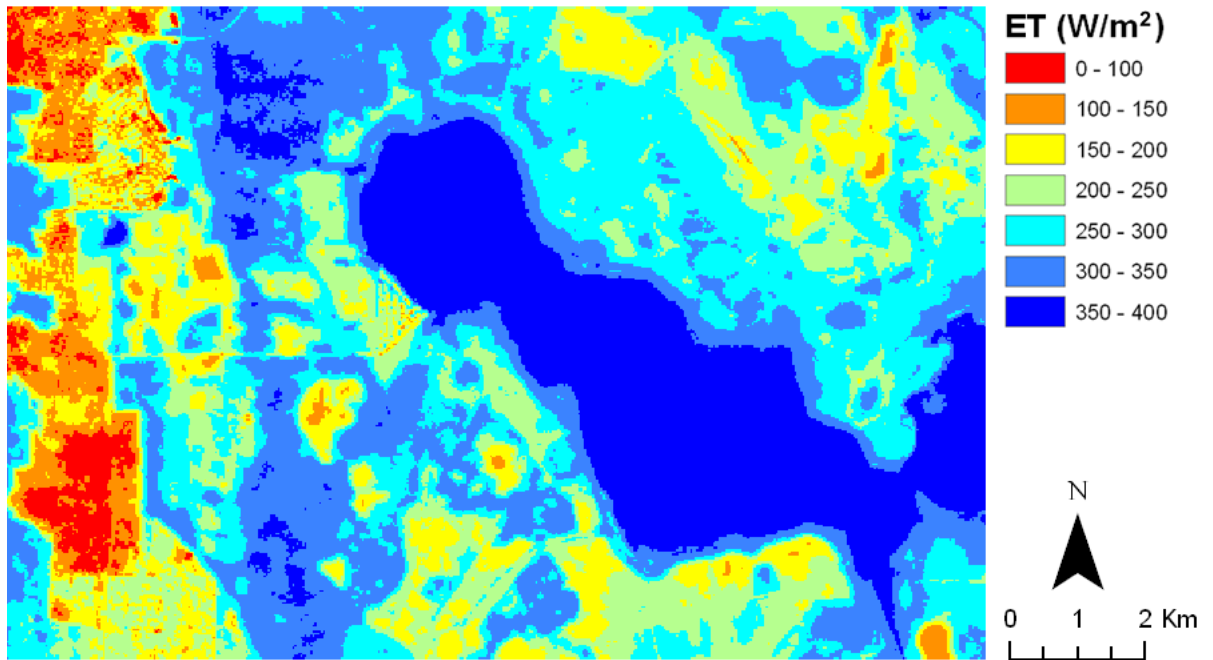
Figure 4.9.17: Classified Map of Original Mean *ET* for Disney 2nd Run
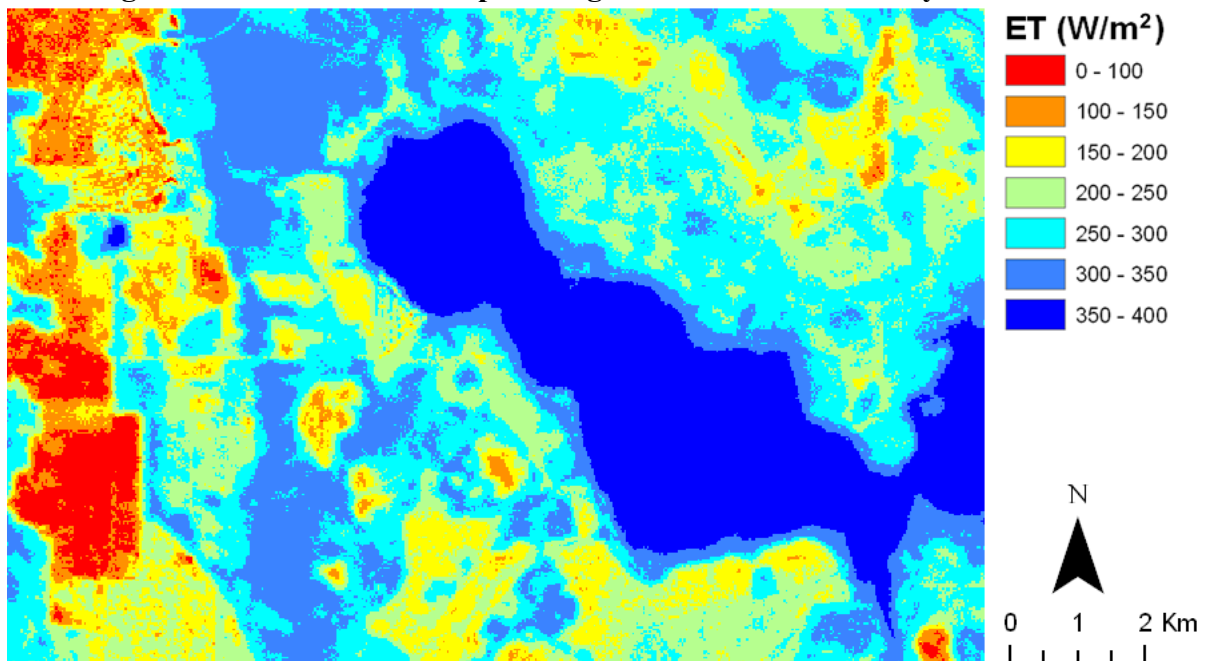
Figure 4.9.18: Classified Map of Mean *ET* using Similar *ET* Fusion for Disney 2nd Run
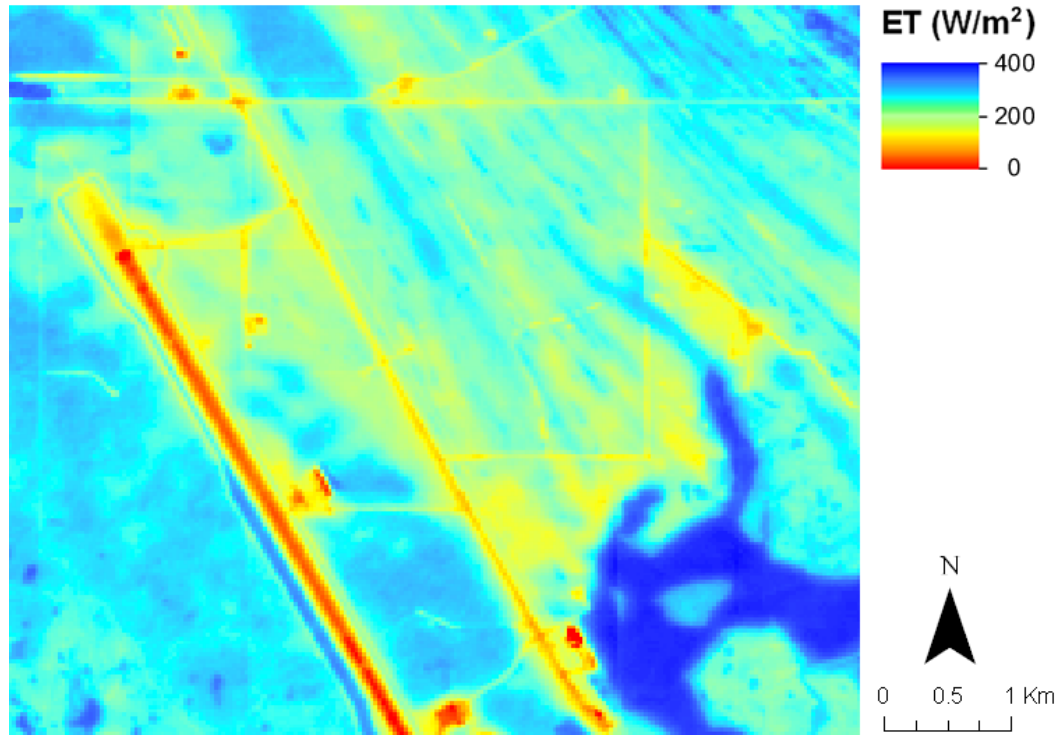
Figure 4.9.19: Continuous Map of Mean *ET* using Simple Interval Fusion for Kennedy 2nd Run
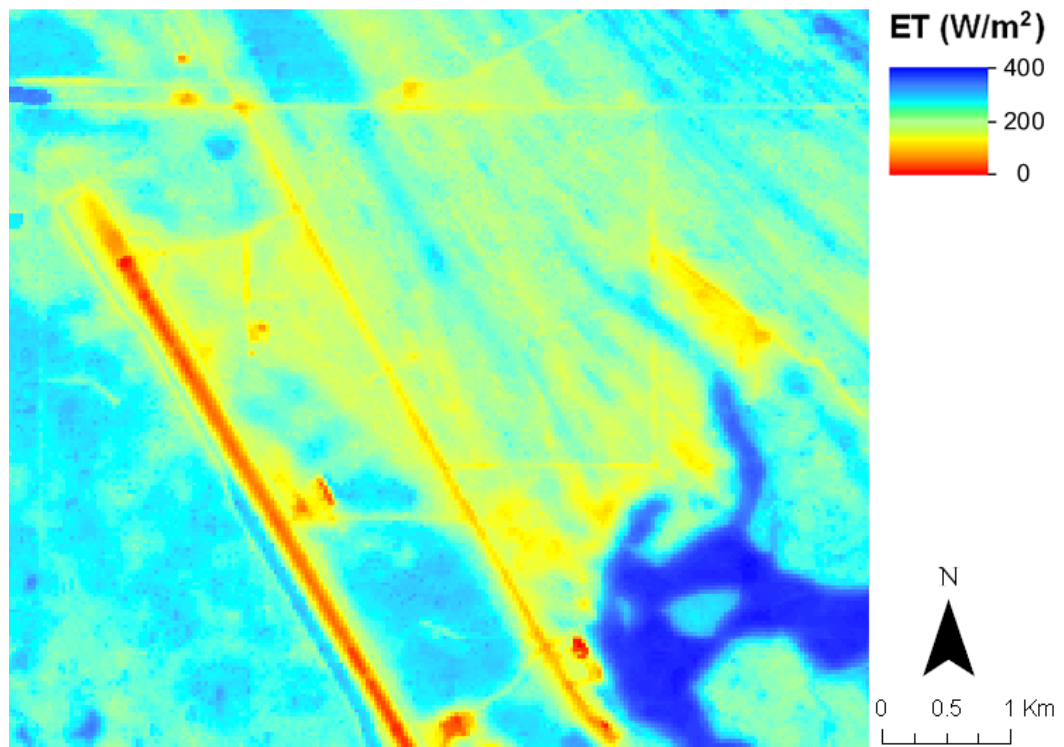
Figure 4.9.20: Continuous Map of Mean *ET* using Similar *ET* Fusion for Kennedy 2nd Run

215
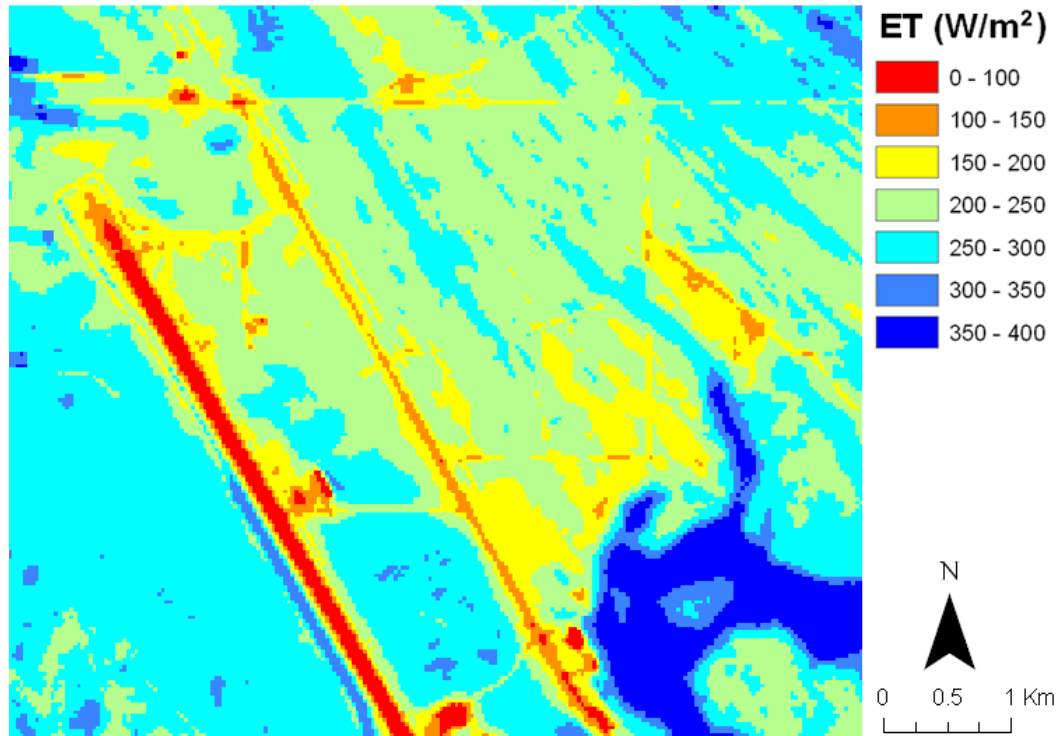
Figure 4.9.21: Classified Map of Original Mean *ET* for Kennedy 2nd Run
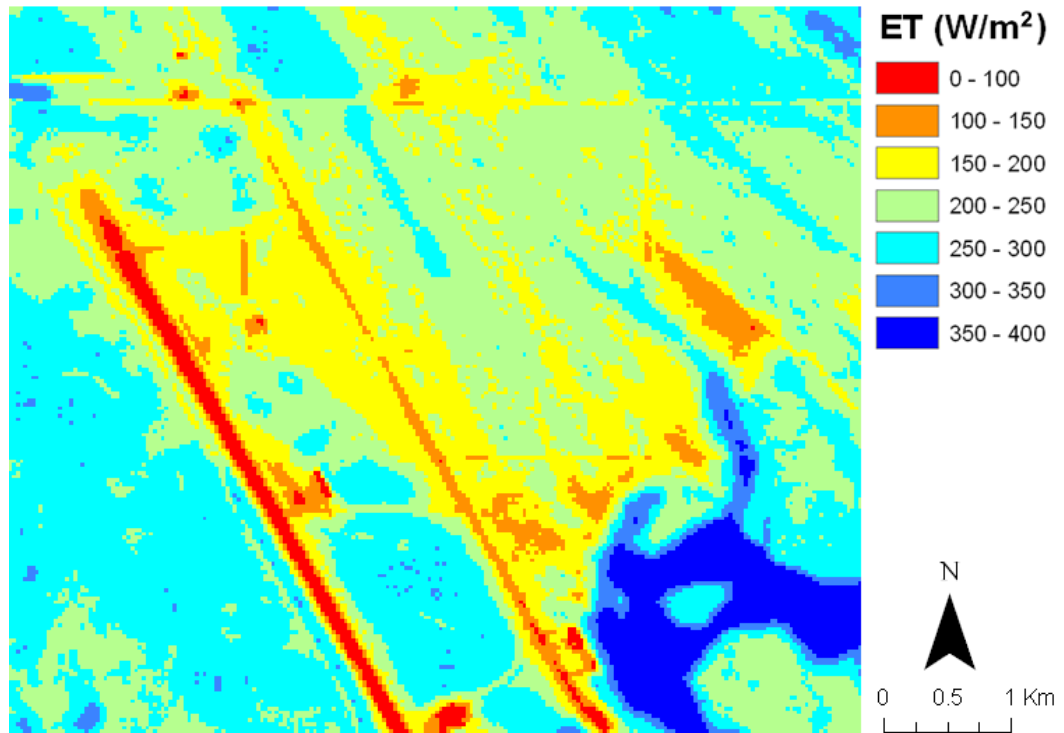
Figure 4.9.22: Classified Map of Mean *ET* using Similar *ET* Fusion for Kennedy 2nd Run

216

5. Conclusions and Future Work

With respect to measuring instantaneous *ET*, the automated calibration which included only dry pixels slightly outperformed the calibration which also included wet pixels for Big Cypress and Gainesville. For Disney, Everglades and Kennedy the calibration which included wet pixels was significantly better. In addition, the *ΔT* vs. *T* model was the best for the optimal Big Cypress and Gainesville cases, but *H* vs. *T* model was the best for the optimal Disney, Everglades and Kennedy cases. The reason for this could be because the vegetation heights for Big Cypress and Gainesville are taller than the other study areas. The algorithm developed here was very successful for the identification of dry pixels when they existed in the landscape. The development of an automated identification of wet pixels was not pursued as exhaustively as dry pixel identification. It turns out that wet pixels could be identified sufficiently using an absolute maximum *NDVI* threshold of 0. The difficulty in using wet pixels is estimating their sensible heat. This dissertation would suggest that these automatically detected wet and dry pixels were able to calibrate the *ET* retrieval algorithm with acceptable results. Although the *MAE* was large for some applications, the *Bias* was low. For Kennedy and Disney the *Bias* error was only about 2% of mean *ET*. The large *MAE* might indicate inaccurate estimates at the daily time scale, but the small *Bias* error would suggest that the algorithm has the potential to accurately describe *ET* at monthly or seasonal time scales. This offers the possibility for *ET* retrieval algorithms which rely on internal

calibration to become more operational. This would not only save time for the user, but it would also reduce the subjectivity inherent in manual calibration.

The dry pixel calibration developed here could be considered an extension of the S-SEBI concept (Roernik et al, 2000). An important modification is the use of available energy or ΔT in place of surface reflectance which allows for the ability to account for surface roughness. Often it is considered an advantage that surface roughness is not required in a model, but this is only true if the uncertainty in surface roughness increases error more than accounting for the surface roughness reduces error. The dry pixel calibration does not require a prediction of a "cold" line where $EF=1$ that is used in S-SEBI. This "cold" line is often difficult to find on the image because the EF does not reach one. During this study for Florida, the EF over the eddy covariance towers for the useable clear sky days never reached one. Possibly in a more arid environment over water the EF would reach one. In theory, it is not necessary to determine this cold line in the first place. This cold line should not vary with surface reflectance, but remain equal to the temperature of the atmosphere. This information is already available by extrapolating the dry pixels to a point where the available energy equals zero. In practice, it was found that the dry pixels are not always so reliable for determining the dependence of H or ΔT vs. temperature. However, the dry pixels do seem very useful for determining a dry end member which could be used in conjunction with a wet end member for finding an H or ΔT vs. temperature relationship.

The author is not aware of any studies for Florida using LANDSAT data that have analyzed as many ET maps as was done in this dissertation. A total of 81 scenes were processed and validated over 5 study areas during a period of over 10 years. The

location of these 5 study areas varied from North to South and from coastal to inland. Because some study areas consisted of more than one eddy covariance station, 138 in-situ measurements were compared to snapshots of retrieved *ET* maps. However, a major criticism of the imagery used is that it consisted mostly of scenes from the dry season. This problem is somewhat unavoidable with LANDSAT in Florida because of the high frequency of cloud cover. The study area that was able to produce the most data for all seasons was Gainesville, but the algorithm was found to have the most difficulty in this study area. However, the algorithm produced a low *Bias* error overall for Gainesville, except for the summer in which it tended to underestimate instantaneous *ET*.

Another criticism of this study might be the manner in which eddy covariance towers were used for validation. These towers only represent a very small area of the landscape being mapped. A low error with respect to the towers doesn't describe how well the algorithm performs in other areas of the image. A successful result might only mean the algorithm works well over the type of surface located at flux towers. Possibly the calibration data could come from a surface which is similar to the validation data. For example, a reference crop surface is used to calibrate the model, but the validation data also comes from a similar well watered agricultural surface. Under these circumstances the results will be a bit misleading. By using calibration data which consists of surfaces types which are not similar to the surfaces at the eddy covariance towers, a more conservative estimate is produced. Estimates from mass balance could be compared over long terms, but this study produced mainly snapshots of *ET*. Another possible source of validation could be transects measured by airborne missions, but these are very costly. Another technique which is increasing in popularity is scintillometry which works by

transmitting a laser beam to a receiver and measuring the changes in the received light. Since turbulent heat fluxes affect the passage of light through the atmosphere, micrometerological theory can be used to convert changes in received light to sensible heat. This technique has been used to validate remote sensing of sensible heat (Brunsell et al, 2011; Kleissl et al, 2009). The advantage of this approach is that it measures fluxes over a long transect instead of a relatively small footprint. The disadvantage is that it typically requires modeling the physics of the atmosphere. Currently the author is not aware of any airborne or scintollometer data available for Florida.

Sensitivity tests are a way to evaluate the algorithm over the entire landscape. Although it does not provide a means in which to validate the entire map, it does provide a way to determine the effect of the uncertainty in the inputs over the entire map assuming the model physics are acceptable. Of course uncertainties in available energy would directly affect the resulting *ET*, but it turns out that uncertainties in available energy do not affect evaporative fraction very strongly. If accurate estimates of available energy are available at the daily time scale, then the error would depend on *EF*. That is why it was important to test sensitivity of *EF* to instantaneous energy. For example, uncertainties in ground or water heat flux that would add error to estimates of instantaneous available energy would not have such a large effect on the snapshot *EF*. Therefore, daily available energy at 2 km resolution calculated using GOES could be combined with *EF* calculated from LANDSAT temperature and energy necessary for calibration. When using only dry pixels, the calibration is insensitive to temperature which is the point of the calibration. When wet pixels are included, sensitivity to temperature becomes important. This is due to the sensitivity of Priestly Taylor equation

220

to temperature. Since temperature retrievals are inherently poor using LANDSAT, this could be an issue. A possible solution to this problem could be the introduction of FAWN sites to be used for wet pixels. At these sites the vertical temperature gradient is often measured allowing the estimation of sensible heat. These estimates might not be consistent with calibration data produced using pure satellite data though. *EF* has the capability to be very sensitive to roughness length in a non-linear fashion. Once errors in roughness length reach around 0.1 m, errors in *EF* are noticeable. Using a first order approximation, this means that the height of the vegetation should be known within 1 m. This sensitivity to roughness length could possibly explain problems with large *MAE* for Gainesville *ET*. A very surprising result in regards to the sensitivity of the algorithm to wind speed was found. When a constant mean wind speed was used for all days, a decrease in both *MAE* and *Bias* error was produced. However, a visualization of the errors revealed this did not mean using constant mean wind speed was better, but possibly acceptable.

The results of the data fusion simulations performed determined that data fusion can be used to predict missing LANDSAT scenes. It was also found that simple linear interpolation of *EF* also predicted missing LANDSAT scenes fairly well in terms of *Bias* error. Relative to *MAE* errors, data fusion out performed interpolation to an even larger degree though. This would suggest that data fusion would predict time scales between very long and daily (such as monthly or seasonally) with more accuracy. Data fusion using Similar *ET* also performed the most consistently among various study areas and time series tested. The Similar and Homogenous *ET* method developed here could be a practical application of data fusion. Other more complex methods such as the STARFM

221

method (Gao, 2006) have been used successful, but it requires the estimation of many

parameters. In addition, it is more computationally intensive than the methods tested in

this dissertation. An advantage of the Similar and Homogeneous *ET* method is that it only

requires one parameter (homogeneity weight) while being computationally rather simple.

If only similarity is used then no parameters are required and the algorithm still produces

smooth patterns of change. If similarity is assumed to infer homogeneity, then Similar *ET*

can be performed without parameter estimation. Future work would involve the

comparison of STARFM to Similar and Homogenous *ET*. This work was outside the

scope of this dissertation because it would involve the optimization of the parameters

used in STARFM. In practice knowing these parameters in advance of theirapplication

would be difficult. Therefore the Similar *ET* algorithm developed here could be a good

practical alternative.

Based on the work conducted in this dissertation, it is foreseeable that the

automated calibration could be used to map evaporative fraction for the entire state of

Florida. *EF* maps could be combined with the 2 km USGS product for daily *PET*, *RET*

and solar insolation maps to produce daily actual *ET*. To produce an *EF* map for the

entire state of Florida would require merging many maps each calibrated over much

smaller extents. One of the major challenges for this effort would be to determine the

allowable spatial extent that could be used. This dissertation demonstrated the effects of

having an extent that is both too large and too small. Future work systematically testing

the effect that the size of the extent has on the calibration would be very beneficial to this

effort. Another problem would be to determine when surface roughness should be

accounted for or ignored. LIDAR data could be useful for producing a better estimate of

surface roughness, but it has limited availability. One option would be to produce a relationship between albedo and surface roughness which was calibrated for Florida in areas in which LIDAR was available. The development of methods for improving the estimate of wet pixel sensible heat is also warranted. The automatic detection of wet reference surfaces would allow the inclusion of *RET* measurements into the calibration. Another source of wet pixels could come from sensible heat measurements estimated from vertical temperature profiles at FAWN stations. This dissertation did not conclusively show that one model was universally better than the other. It would be beneficial to determine a method for estimating the error in applying just one model to the entire state (eg. Dry Pixels Only with ΔT vs. *T* or Include Wet Pixels with *H* vs. *T*). The development of a decision fusion model for determining the optimal variation for a specific area would also be very useful.

This dissertation produced mainly small contributions born from the common goal of producing maps of evaporative fraction for entire state of Florida which could be combined with current maps of available energy to produce maps of actual evapotranspiration. 1) The quantity of data that was analyzed in this dissertation was large in terms of number of scenes analyzed. 2) An automated calibration was developed which is necessary if a calibration method is to be used to produce a map for the entire state. 3) Sensitivity analysis showed that snapshots of available energy produced at LANDSAT resolution should not be too restrictive towards the production of *EF* maps. 4) Data fusion or even possibly linear interpolation could be a feasible alternative for producing estimates of *EF* on days in which clear sky LANDSAT imagery is not available. Even though the desired final product might not be LANDSAT resolution *ET*

maps, the automated calibration designed here requires the heterogeneity of LANDSAT imagery. This calibration could then be used to produce *ET* maps at a 2 km resolution. There are also plans to integrate the python scripts consisting of the *ET* mapping and calibration algorithm into ARC GIS toolboxes. These toolboxes can then be distributed to the *ET* mapping community for collaboration and comparison. An important step in the future of *ET* mapping is comparing available techniques against the same available data. There are many small variations within the standard techniques that can change results for specific instances. Therefore it is necessary for researchers to be able to reproduce each other's results. Many excellent results exist in the literature, but it is also necessary to determine where and when techniques do not work and why. In the future, a community effort allowing researchers to share exact methodologies (including computer code) and data sets would concentrate individual research into an entity more powerful than the individual parts.

Appendix A – Usable Clear Sky Scenes a7nd Flux Station Validation Data

Appendix A contains the data used in validation. Tables A.1-6 show the usable

clear sky scenes from LANDSAT and the corresponding number of stations where

evaporative fraction (N_{EF}) was available and the number of stations where wind speed at

blending height (N_{U200}) was available. In addition the tables show the mean wind speed at

blending height for the scene ($\overline{u}_{200}$) used in retrieval. Tables A.7-.13 show the flux

tower data for each station. These tables report the evaporative fraction (*EF*), Available

Energy (A) and the wind speed at blending height (u_{200}).

Table A.1: Usable Clear Sky Scenes for Big Cypress

Date	N_{EF}	$\overline{U}_{200}$ (m/s)	N_{U200}
4/23/2008	3	3.4	2
10/3/2009	4	1.33	2
10/19/2009	4	5.7	4
2/8/2010	3	3.67	3

Table A.2: Usable Clear Sky Scenes for Everglades

Date	N_{EF}	$\overline{U}_{200}$ (m/s)	N_{U200}
4/23/2008	1	1.68	2
10/3/2009	3	1.68	2
10/19/2009	3	5.16	2
2/8/2010	1	6.24	1
11/10/2011	1	4.71	2

Table A.3: Usable Clear Sky Scenes for Disney Preserve

Date	N_{EF}	$\overline{U}_{200}$ (m/s)	$N_{U_{200}}$
5/5/2004	1	4.5	1
11/29/2004	1	3.57	1
12/15/2004	1	11.92	1
4/22/2005	1	1.63	1
9/24/2005	1	4.87	1
1/19/2006	1	5.15	1
3/8/2006	1	5.41	1
4/25/2006	1	3.82	1
11/19/2006	1	7.17	1
2/7/2007	1	1.66	1
2/23/2007	1	7.96	1
3/11/2007	1	4.51	1
3/13/2008	1	6.5	1
4/30/2008	1	5.61	1
11/8/2008	1	2.31	1
1/11/2009	1	3.69	1
11/27/2009	1	7.17	1
4/4/2010	1	4.66	1
7/9/2010	1	2.68	1
11/14/2010	1	4.32	1
12/16/2010	1	3.01	1

Table A.4: Usable Clear Sky Scenes for Gainesville (Part 1)

Date	N_{EF}	$\bar{U}_{200}$ (m/s)	$N_{U_{200}}$
3/28/1999	1	3.57	2
1/26/2000	1	5.41	1
3/14/2000	2	4.29	1
1/28/2001	3	1.58	2
4/2/2001	3	4.73	2
4/18/2001	2	3.51	1
8/8/2001	3	1.86	2
8/24/2001	3	3.45	2
2/19/2003	3	2.15	1
12/20/2003	3	6.05	1
4/10/2004	2	1.41	2
12/22/2004	2	5.61	2
1/23/2005	3	8.64	3
3/12/2005	1	6.29	1
11/23/2005	2	6.12	2
1/26/2006	1	2.91	1
2/27/2006	1	2.03	1

Table A.5: Usable Clear Sky Scenes for Gainesville (Part 2)

Date	N_{EF}	$\overline{U}_{200}$ (m/s)	$N_{U_{200}}$
4/16/2006	2	4.78	2
5/2/2006	2	2.72	2
5/18/2006	1	5.2	1
9/23/2006	2	4.6	1
10/25/2006	3	2.27	3
12/28/2006	2	4	1
1/29/2007	2	3.33	2
2/17/2008	2	6.46	1
4/21/2008	2	4.27	1
6/8/2008	2	2.15	1
10/30/2008	1	4.91	1
3/7/2009	1	3.86	1
4/24/2009	2	2.08	2
10/4/2010	1	1.34	1
1/8/2011	1	6.71	1
3/13/2011	1	1.78	1
7/19/2011	1	2.94	1
10/23/2011	1	0.8	1

Table A.6: Usable Clear Sky Scenes for Kennedy Space Center

Date	N_{EF}	$\overline{U}_{200}$ (m/s)	$N_{U_{200}}$
5/26/2000	1	2.59	1
6/20/2000	1	3.54	1
9/15/2000	1	2.75	1
2/6/2001	1	1.9	1
2/22/2001	1	3.05	1
5/6/2001	1	7.67	1
5/13/2001	1	1.87	1
1/24/2002	1	7.46	1
11/24/2002	1	4.16	1
1/20/2003	2	6.1	1
2/12/2003	1	5.94	1
4/1/2003	1	9.89	1
11/20/2003	1	8.55	1
3/11/2004	1	7	1
4/3/2004	1	4.52	1
11/6/2004	1	6.67	1
11/29/2004	1	4.27	1
1/9/2005	1	1.24	1
1/25/2005	1	6.17	1
2/17/2005	1	7.53	1
3/5/2005	1	3.34	1
3/30/2005	1	2.67	1
4/22/2005	1	1.51	1
3/8/2006	1	4.88	1
11/19/2006	1	6.01	1

Table A.7: Flux Station Data for Big Cypress

Date	Station	EF	A (W/m^2)	U_{200} (m/s)
4/23/2008	CypressSwamp	0.701	492.1	3.14
4/23/2008	DwarfCypress	0.592	156.0	-
4/23/2008	PineUpland	0.54	537.3	3.66
10/3/2009	CypressSwamp	0.571	545.0	1.42
10/3/2009	DwarfCypress	0.587	567.0	1.24
10/3/2009	PineUpland	0.386	391.0	-
10/3/2009	WetPrairie	0.609	583.7	-
10/19/2009	CypressSwamp	0.342	432.0	6.94
10/19/2009	DwarfCypress	0.893	459.0	6.18
10/19/2009	PineUpland	0.342	348.0	4.58
10/19/2009	WetPrairie	0.578	492.0	5.11
2/8/2010	CypressSwamp	0.447	358.0	4.55
2/8/2010	PineUpland	0.189	429.0	3.0
2/8/2010	WetPrairie	0.506	421.7	3.46

Table A.8: Flux Station Data for Disney

Date	Station	EF	A (W/m^2)	U_{200} (m/s)
5/5/2004	Grassland	0.41	584.0	4.5
11/29/2004	Grassland	0.517	333.0	3.57
12/15/2004	Grassland	0.147	320.0	11.92
4/22/2005	Grassland	0.574	526.0	1.63
9/24/2005	Grassland	0.67	504.0	4.87
1/19/2006	Grassland	0.323	334.0	5.15
3/8/2006	Grassland	0.289	461.0	5.41
4/25/2006	Grassland	0.479	557.0	3.82
11/19/2006	Grassland	0.265	381.0	7.17
2/7/2007	Grassland	0.309	369.0	1.66
2/23/2007	Grassland	0.274	416.0	7.96
3/11/2007	Grassland	0.247	449.0	4.51
3/13/2008	Grassland	0.488	433.0	6.5
4/30/2008	Grassland	0.361	651.0	5.61
11/8/2008	Grassland	0.476	399.9	2.31
1/11/2009	Grassland	0.414	308.3	3.69
11/27/2009	Grassland	0.398	393.2	7.17
4/4/2010	Grassland	0.389	546.6	4.66
7/9/2010	Grassland	0.691	598.0	2.68
11/14/2010	Grassland	0.472	397.2	4.32
12/16/2010	Grassland	0.197	327.4	3.01

Table A.9: Flux Station Data for Everglades

Date	Station	EF	A (W/m^2)	U_{200} (m/s)
4/23/2008	Mangroves	0.711	451.9	1.41
4/23/2008	ShortMarsh	0.616	631.5	10.37
10/3/2009	LongMarsh	0.791	678.7	1.96
10/3/2009	LongMarsh	0.47	672.0	10.65
10/3/2009	Mangroves	0.474	380.3	7.98
10/19/2009	LongMarsh	0.388	421.4	4.82
10/19/2009	ShortMarsh	0.375	650.2	5.06
10/19/2009	ShortMarsh	0.464	377.7	5.5
2/8/2010	LongMarsh	0.51	513.0	6.24
11/10/2011	Mangroves	0.588	516.1	4.35

Table A.10: Flux Station Data for Gainesville (Part 1)

Date	Station	EF	A ($^W/_{m^2}$)	U_{200} (m/s)
3/28/1999	Donaldson	0.422	592.5	3.67
1/26/2000	Mize	0.462	350.4	5.41
3/14/2000	Donaldson	0.432	559.3	4.29
3/14/2000	Mize	0.481	441.7	-
1/28/2001	AustinCary	0.449	349.9	-
1/28/2001	Donaldson	0.016	277.0	1.5
1/28/2001	Mize	0.068	-	1.66
4/2/2001	AustinCary	0.432	601.2	-
4/2/2001	Donaldson	0.428	544.9	5.22
4/2/2001	Mize	0.543	399.0	4.25
4/18/2001	Donaldson	0.239	608.0	3.51
4/18/2001	Mize	0.519	496.9	-
8/8/2001	AustinCary	0.446	632.1	-
8/8/2001	Donaldson	0.751	611.7	1.88
8/8/2001	Mize	0.709	519.3	1.84
8/24/2001	AustinCary	0.486	595.5	-
8/24/2001	Donaldson	0.749	582.8	3.72
8/24/2001	Mize	0.758	521.4	3.18
2/19/2003	AustinCary	0.39	372.1	-
2/19/2003	Donaldson	0.477	325.6	2.15
2/19/2003	Mize	0.433	495.8	-

Table A.11: Flux Station Data for Gainesville (Part 2)

Date	Station	EF	A ($^W/_{m^2}$)	U_{200} (m/s)
12/20/2003	AustinCary	0.405	456.9	-
12/20/2003	Donaldson	0.45	411.8	6.05
12/20/2003	Mize	0.481	493.4	-
4/10/2004	AustinCary	0.357	586.0	1.23
4/10/2004	Donaldson	0.572	580.5	1.59
12/22/2004	Donaldson	0.284	296.3	4.63
12/22/2004	Mize	0.613	396.5	6.6
1/23/2005	AustinCary	0.028	334.1	8.69
1/23/2005	Donaldson	0.052	296.3	8.87
1/23/2005	Mize	0.29	315.1	8.36
3/12/2005	Donaldson	0.656	444.9	6.29
11/23/2005	AustinCary	0.023	330.9	7.85
11/23/2005	Donaldson	0.446	421.1	4.38
1/26/2006	Donaldson	0.315	195.2	2.91
2/27/2006	Donaldson	0.379	308.8	2.03
4/16/2006	Donaldson	0.407	490.1	5.2
4/16/2006	Mize	0.369	685.8	4.36
5/2/2006	Donaldson	0.47	634.9	2.87
5/2/2006	Mize	0.505	553.5	2.58
5/18/2006	Donaldson	0.48	653.1	5.2
9/23/2006	AustinCary	0.53	-	4.6
9/23/2006	Donaldson	0.453	563.5	-

Table A.12: Flux Station Data for Gainesville (Part 3)

Date	Station	EF	A ($^W/_{m^2}$)	U_{200} (m/s)
10/25/2006	AustinCary	0.542	436.8	2.29
10/25/2006	Donaldson	0.389	479.8	2.18
10/25/2006	Mize	0.437	504.6	2.34
12/28/2006	AustinCary	0.298	299.1	-
12/28/2006	Mize	0.317	298.2	4.0
1/29/2007	Donaldson	0.206	387.1	3.41
1/29/2007	Mize	0.33	373.2	3.26
8/9/2007	Donaldson	0.604	565.1	-
2/17/2008	Donaldson	0	443.9	-
2/17/2008	Mize	0.034	353.0	6.46
4/21/2008	Donaldson	0.419	720.4	-
4/21/2008	Mize	0.47	616.1	4.27
6/8/2008	AustinCary	0.48	-	2.15
6/8/2008	Donaldson	0.648	696.9	-
10/30/2008	AustinCary	0.413	457.7	4.91
3/7/2009	Donaldson	0.504	486.2	3.86
4/24/2009	AustinCary	0.231	595.8	2.34
4/24/2009	Donaldson	0.438	599.3	1.82
10/4/2010	Donaldson	0.348	533.9	1.34
1/8/2011	AustinCary	0.412	416.1	6.71
3/13/2011	AustinCary	0.359	606.1	1.78
7/19/2011	AustinCary	0.509	656.9	2.94
10/23/2011	AustinCary	0.497	466.2	0.8

Table A.13: Flux Station Data for Kennedy Space Center

Date	Station	EF	A (W/m^2)	U_{200} (m/s)
5/26/2000	ScrubOak	0.456	499.2	2.59
6/20/2000	ScrubOak	0.498	660.7	3.54
9/15/2000	ScrubOak	0.698	439.6	2.75
2/6/2001	ScrubOak	0.464	-	1.9
2/22/2001	ScrubOak	0.468	513.5	3.05
5/6/2001	ScrubOak	0.486	646.8	7.67
5/13/2001	ScrubOak	0.55	632.0	1.87
1/24/2002	ScrubOak	0.487	352.4	7.46
11/24/2002	SlashPine	0.627	425.7	4.16
1/20/2003	ScrubOak	0.265	344.0	-
1/20/2003	SlashPine	0.355	468.4	6.1
2/12/2003	ScrubOak	0.482	412.5	5.94
4/1/2003	ScrubOak	0.39	-	9.89
11/20/2003	ScrubOak	0.36	444.8	8.55
3/11/2004	ScrubOak	0.312	546.1	7.0
4/3/2004	ScrubOak	0.319	621.3	4.52
11/6/2004	ScrubOak	0.648	482.7	6.67
11/29/2004	ScrubOak	0.61	407.6	4.27
1/9/2005	ScrubOak	0.617	389.3	1.24
1/25/2005	ScrubOak	0.261	424.9	6.17
2/17/2005	ScrubOak	0.455	472.6	7.53
3/5/2005	ScrubOak	0.501	543.4	3.34
3/30/2005	ScrubOak	0.455	629.8	2.67
4/22/2005	ScrubOak	0.515	628.5	1.51
3/8/2006	ScrubOak	0.374	560.0	4.88
11/19/2006	ScrubOak	0.551	-	6.01

Appendix B – Bin Size Selection

Determining the bin sizes to be used was done mostly visually from plots of ΔT vs. T. The *RMS* error between points and predicted upper and lower boundary lines was also used as criteria. This criterion was not robust though because as the bin size increased, the number of points in boundary decreased which reduced the error. On visual inspection this lower error was misleading because the points did not successfully describe the boundary. An analysis was done using ΔT vs. T method for Gainesville study area on April 23, 2008. The variation of *RMS* with bins size is shown in Figures B.1a and B.1b. Once the bin size becomes greater than about ΔT=0.1 the *RMS* becomes erratic. Figure B.2 shows the actual boundary points chosen for the bin sizes varying from 0.01 to 1.0 K. The position of the lower boundary is fairly down to a bin size of about 0.1 K but after that the position of the lower boundary line begins to change. For practical purposes a very large number of points did not seem feasible. Therefore a bin size = 0.1 K for the ΔT vs. T method was chosen. A similar exercise was performed for the H vs. T method where a bin size = 10 W/m^2 was chosen. When using ΔT vs. T method assuming neutral conditions much larger ΔT values were produced. This resulted in bin size = 1 K being used.
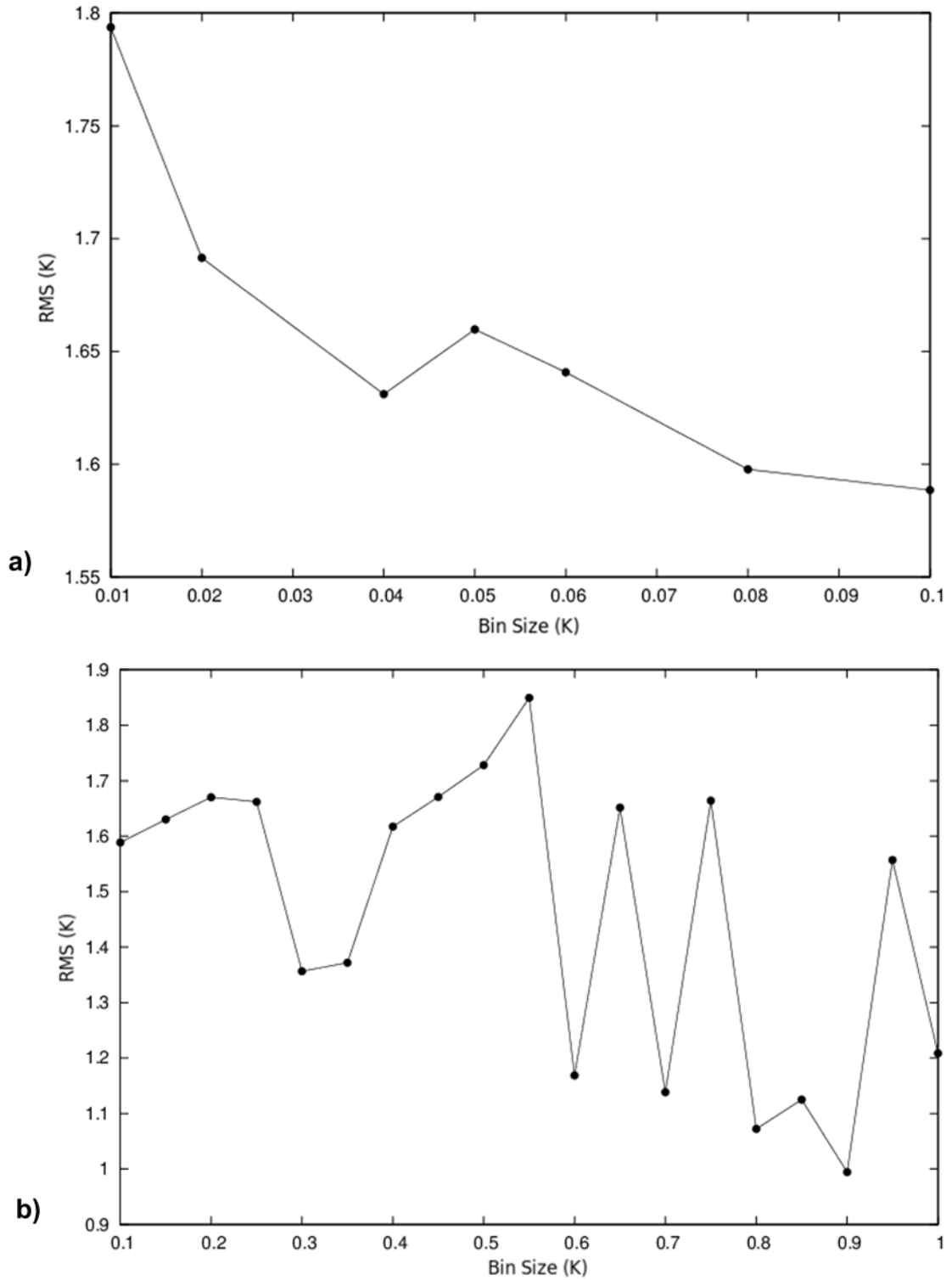
Figure B.1: Variation of RMS Error with Bin Size for *ΔT* vs. *T* Calibration

a) Bin Size = 0.01 K

b) Bin Size = 0.05 K

c) Bin Size = 0.1 K

d) Bin Size = 0.3 K

e) Bin Size = 0.5 K

f) Bin Size = 1.0 K
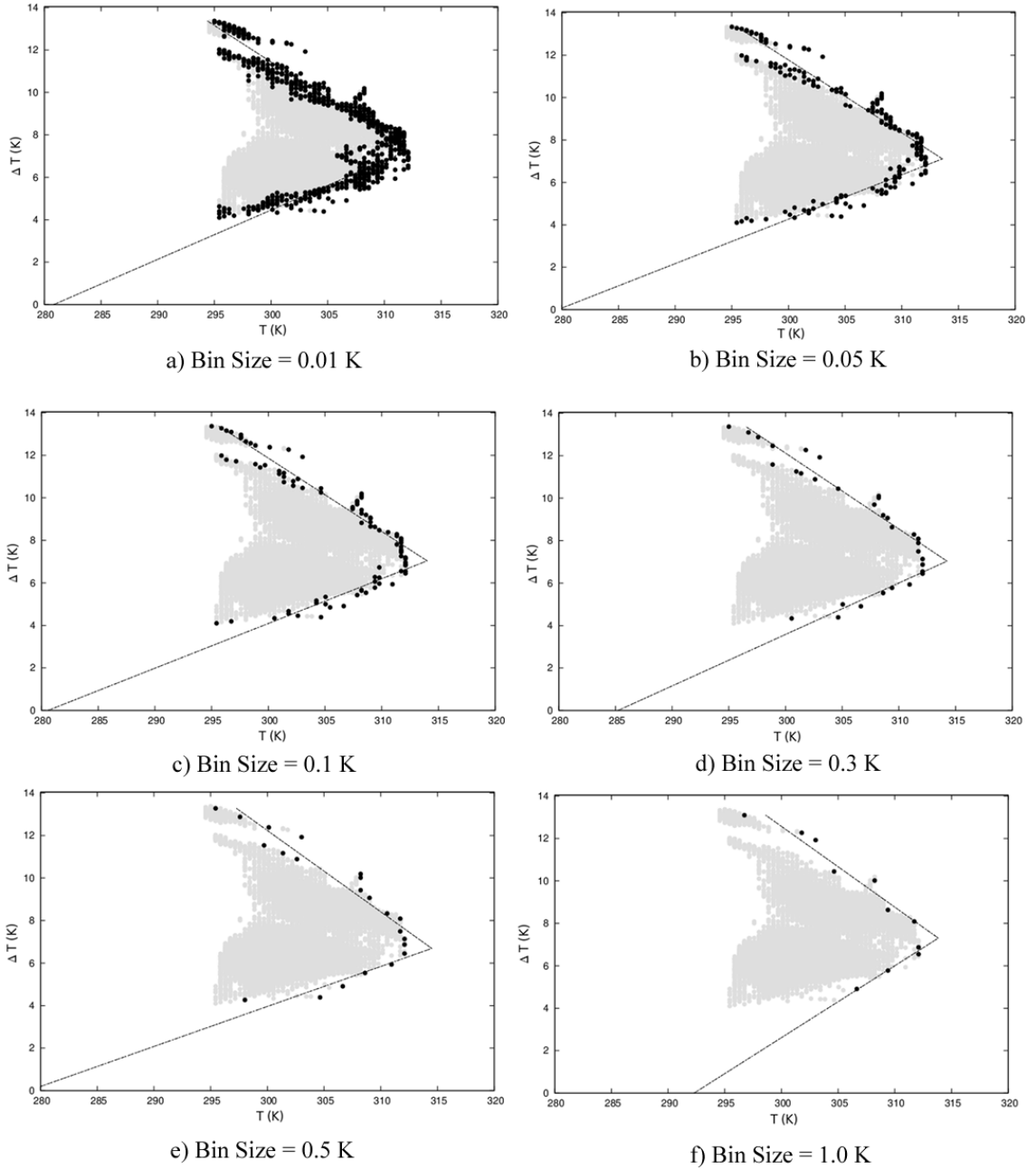
Figure B.2: *ΔT* vs. *T* Boundary for Various Bin Sizes

Appendix C – License Agreement for Figures

JOHN WILEY AND SONS LICENSE

TERMS AND CONDITIONS

Jun 06, 2014

This is a License Agreement between Aaron H Evans ("You") and John Wiley and Sons ("John Wiley and Sons") provided by Copyright Clearance Center ("CCC"). The license consists of your order details, the terms and conditions provided by John Wiley and Sons, and the payment terms and conditions.

All payments must be made in full to CCC. For payment instructions, please see information listed at the bottom of this form.

License Number: 3403270921712

License Date: Jun 06, 2014

Licensed Content Publisher: John Wiley and Sons

Licensed Content Publication: Water Resources Research

Licensed Content Title: Estimation of Surface Evaporation Map Over Southern Great Plains Using Remote Sensing Data

Licensed Copyright Line: Copyright 2001 by the American Geophysical Union.

Licensed Content Author: Le Jiang, Shafiqul Islam

Licensed Content Date: Jul 9, 2010

Start Page: 329

End Page: 340

Type of Use: Dissertation/Thesis

Requestor Type: University/Academic

Format: Print and Electronic

Portion: Figure/Table

Number of Figures/Tables: 1

Original Wiley Figure/Table Number(s): Figure 2

Will you be translating? No

Title of Your Thesis/Dissertation: REMOTE SENSING OF EVAPOTRANSPIRATION USING AUTOMATED CALIBRATION: DEVELOPMENT AND TESTING IN THE STATE OF FLORIDA

Expected Completion Date: Jul 2014

Expected Size (Number of Pages): 200

Total 0.00 USD

Terms and Conditions

TERMS AND CONDITIONS

6/6/2014 Rightslink Printable License

https://s100.copyright.com/AppDispatchServlet 2/7

This copyrighted material is owned by or exclusively licensed to John Wiley & Sons, Inc. or one of its group companies (each a"Wiley Company") or handled on behalf of a society with which a Wiley Company has exclusive publishing rights in relation to a particular work (collectively "WILEY"). By clicking accept in connection with completing this licensing transaction, you agree that the following terms and conditions apply to this transaction (along with the billing and payment terms and conditions established by the Copyright Clearance Center Inc., ("CCC's Billing and Payment terms and conditions"), at the time that you opened your Rightslink account (these are available at any time at http://myaccount.copyright.com).

Terms and Conditions

The materials you have requested permission to reproduce or reuse (the "Wiley Materials") are protected by copyright.

You are hereby granted a personal, non-exclusive, non-sub licensable (on a stand-alone basis), non-transferable, worldwide, limited license to reproduce the Wiley Materials for the purpose specified in the licensing process. This license is for a one-time use only and limited to any maximum distribution number specified in the license. The first instance of republication or reuse granted by this licence must be completed within two years of the date of the grant of this licence (although copies prepared before the end date may be distributed thereafter). The Wiley Materials shall not be used in any other manner or for any other purpose, beyond what is granted in the license. Permission is granted subject to an appropriate acknowledgement given to the author, title of the material/book/journal and the publisher. You shall also duplicate the copyright notice that appears in the Wiley

241

publication in your use of the Wiley Material. Permission is also granted on the understanding that nowhere in the text is a previously published source acknowledged for all or part of this Wiley Material. Any third party content is expressly excluded from this permission.

With respect to the Wiley Materials, all rights are reserved. Except as expressly granted by the terms of the license, no part of the Wiley Materials may be copied, modified, adapted (except for minor reformatting required by the new Publication), translated, reproduced, transferred or distributed, in any form or by any means, and no derivative works may be made based on the Wiley Materials without the prior permission of the respective copyright owner. You may not alter, remove or suppress in any manner any copyright, trademark or other notices displayed by the Wiley Materials. You may not license, rent, sell, loan, lease, pledge, offer as security, transfer or assign the Wiley Materials on a stand-alone basis, or any of the rights granted to you hereunder to any other person.

The Wiley Materials and all of the intellectual property rights therein shall at all times remain the exclusive property of John Wiley & Sons Inc, the Wiley Companies, or their respective licensors, and your interest therein is only that of having possession of and the right to reproduce the Wiley Materials pursuant to Section 2 herein during the continuance of this Agreement. You agree that you own no right, title or interest in or to the Wiley Materials or any of the intellectual property rights therein. You shall have no rights hereunder other than the license as provided for above in Section 2. No right, license or interest to any trademark, trade name, service mark or other branding ("Marks") of WILEY or its licensors is granted hereunder, and you agree that you shall not assert any such right, license or interest with respect thereto.

NEITHER WILEY NOR ITS LICENSORS MAKES ANY WARRANTY OR REPRESENTATION OF ANY KIND TO YOU OR ANY THIRD PARTY, EXPRESS, IMPLIED OR STATUTORY, WITH RESPECT TO THE MATERIALS OR THE ACCURACY OF ANY INFORMATION CONTAINED IN THE MATERIALS, INCLUDING, WITHOUT LIMITATION, ANY IMPLIED WARRANTY OF MERCHANTABILITY, ACCURACY, SATISFACTORY QUALITY, FITNESS FOR A PARTICULAR PURPOSE, USABILITY, INTEGRATION OR NONINFRINGEMENT AND ALL SUCH WARRANTIES ARE HEREBY EXCLUDED BY WILEY AND ITS LICENSORS AND WAIVED BY YOU WILEY shall have the right to terminate this Agreement immediately upon breach of this Agreement by you.

You shall indemnify, defend and hold harmless WILEY, its Licensors and their respective directors, officers, agents and employees, from and against any actual or threatened claims, demands, causes of action or proceedings arising from any breach of this Agreement by you. IN NO EVENT SHALL WILEY OR ITS LICENSORS BE

LIABLE TO YOU OR ANY OTHER PARTY OR ANY OTHER PERSON OR ENTITY FOR ANY SPECIAL, CONSEQUENTIAL, INCIDENTAL, INDIRECT, EXEMPLARY OR PUNITIVE DAMAGES, HOWEVER CAUSED, ARISING OUT OF OR IN CONNECTION WITH THE DOWNLOADING, PROVISIONING, VIEWING OR USE OF THE MATERIALS REGARDLESS OF THE FORM OF ACTION, WHETHER FOR BREACH OF CONTRACT, BREACH OF WARRANTY, TORT, NEGLIGENCE, INFRINGEMENT OR OTHERWISE (INCLUDING, WITHOUT LIMITATION, DAMAGES BASED ON LOSS OF PROFITS, DATA, FILES, USE, BUSINESS OPPORTUNITY OR CLAIMS OF THIRD PARTIES), AND WHETHER OR NOT THE PARTY HAS BEEN ADVISED OF THE POSSIBILITY OF SUCH DAMAGES. THIS LIMITATION SHALL APPLY NOTWITHSTANDING ANY FAILURE OF ESSENTIAL PURPOSE OF ANY LIMITED REMEDY PROVIDED HEREIN.

Should any provision of this Agreement be held by a court of competent jurisdiction to be

illegal, invalid, or unenforceable, that provision shall be deemed amended to achieve as nearly as possible the same economic effect as the original provision, and the legality, validity and enforceability of the remaining provisions of this Agreement shall not be affected or impaired thereby.

The failure of either party to enforce any term or condition of this Agreement shall not constitute a waiver of either party's right to enforce each and every term and condition of this Agreement. No breach under this agreement shall be deemed waived or excused by either party unless such waiver or consent is in writing signed by the party granting such waiver or consent. The waiver by or consent of a party to a breach of any provision of this Agreement shall not operate or be construed as a waiver of or consent to any other or subsequent breach by such other party.

This Agreement may not be assigned (including by operation of law or otherwise) by you without WILEY's prior written consent.

Any fee required for this permission shall be non-refundable after thirty (30) days from receipt by the CCC.

These terms and conditions together with CCC's Billing and Payment terms and conditions (which are incorporated herein) form the entire agreement between you and WILEY concerning this licensing transaction and (in the absence of fraud) supersedes all prior agreements and representations of the parties, oral or written. This Agreement may not be amended except in writing signed by both parties. This Agreement shall be binding upon and inure to the benefit of the parties' successors, legal representatives, and authorized assigns. In the event of any conflict between your obligations established by these terms and conditions and those established by CCC's Billing and Payment terms and conditions, these terms and conditions shall prevail.

WILEY expressly reserves all rights not specifically granted in the combination of (i) thelicense details provided by you and accepted in the course of this licensing transaction, (ii) these terms and conditions and (iii) CCC⬚s Billing and Payment terms and conditions. This Agreement will be void if the Type of Use, Format, Circulation, or Requestor Type was misrepresented during the licensing process.

This Agreement shall be governed by and construed in accordance with the laws of the State of New York, USA, without regards to such state⬚s conflict of law rules. Any legal action, suit or proceeding arising out of or relating to these Terms and Conditions or the breach thereof shall be instituted in a court of competent jurisdiction in New York County in the State of New York in the United States of America and each party hereby consents and submits to the personal jurisdiction of such court, waives any objection to venue in such court and consents to service of process by registered or certified mail, return receipt requested, at the last known address of such party.

WILEY OPEN ACCESS TERMS AND CONDITIONS

Wiley Publishes Open Access Articles in fully Open Access Journals and in Subscription journals offering Online Open. Although most of the fully Open Access journals publish open access articles under the terms of the Creative Commons Attribution (CC BY) License only, the subscription journals and a few of the Open Access Journals offer a choice of Creative Commons Licenses:: Creative Commons Attribution (CC-BY) license Creative Commons Attribution Non-Commercial (CC-BY-NC) license and Creative Commons Attribution Non-Commercial-NoDerivs (CC-BYNC-ND) License. The license type is clearly identified on the article.

Copyright in any research article in a journal published as Open Access under a Creative Commons License is retained by the author(s). Authors grant Wiley a license to publish the article and identify itself as the original publisher. Authors also grant any third party the right to use the article freely as long as its integrity is maintained and its original authors, citation details and publisher are identified as follows: [Title of Article/Author/Journal Title and Volume/Issue. Copyright © [year] [copyright owner as specified in the Journal]. Links to the final article on Wiley⬚s website are encouraged where applicable.

The Creative Commons Attribution License

The Creative Commons Attribution License (CC-BY) allows users to copy, distribute and transmit an article, adapt the article and make commercial use of the article. The CC-BY license permits commercial and non-commercial re-use of an open access article, as long as the author is properly attributed.

244

245

If article content is copied, downloaded or otherwise reused for non-commercial research and education purposes, a link to the appropriate bibliographic citation (authors, journal, article title, volume, issue, page numbers, DOI and the link to the definitive published version on Wiley Online Library) should be maintained. Copyright notices and disclaimers must not be deleted.

Any translations, for which a prior translation agreement with Wiley has not been agreed, must prominently display the statement: "This is an unofficial translation of an article that appeared in a Wiley publication. The publisher has not endorsed this translation."

Use by commercial "for-profit" organisations

Use of Wiley Open Access articles for commercial, promotional, or marketing purposes requires further explicit permission from Wiley and will be subject to a fee. Commercial purposes include:

Copying or downloading of articles, or linking to such articles for further redistribution, sale or licensing; Copying, downloading or posting by a site or service that incorporates advertising with such content;

The inclusion or incorporation of article content in other works or services (other than normal quotations with an appropriate citation) that is then available for sale or licensing, for a fee (for example, a compilation produced for marketing purposes, inclusion in a sales pack)

Use of article content (other than normal quotations with appropriate citation) by for-profit organisations for promotional purposes Linking to article content in e-mails redistributed for promotional, marketing or educational purposes;

Use for the purposes of monetary reward by means of sale, resale, licence, loan, transfer or other form of commercial exploitation such as marketing products

Print reprints of Wiley Open Access articles can be purchased from:

corporatesales@wiley.com

Further details can be found on Wiley Online Library

http://olabout.wiley.com/WileyCDA/Section/id-410895.html

Other Terms and Conditions: V1.9

246

ELSEVIER LICENSE

TERMS AND CONDITIONS

Jun 06, 2014

This is a License Agreement between Aaron H Evans ("You") and Elsevier ("Elsevier") provided by Copyright Clearance Center ("CCC"). The license consists of your order details, the terms and conditions provided by Elsevier, and the payment terms and conditions.

All payments must be made in full to CCC. For payment instructions, please see information listed at the bottom of this form.

Supplier:
Elsevier Limited
The Boulevard,Langford Lane
Kidlington,Oxford,OX5 1GB,UK

Registered Company Number: 1982084

Customer Name: Aaron H Evans

Customer Address:
PO Box 16141
West Palm Beach, Fl 33416

1st License Number: 3403250248225

1st License Date: Jun 06, 2014

1st Licensed Content Publisher: Elsevier

1st Licensed Content Publication: Physics and Chemistry of the Earth, Part B: Hydrology, Oceans and Atmosphere

1st Licensed Content Title: S-SEBI: A Simple Remote Sensing Algorithm to Estimate the Surface Energy Balance

1st Licensed Content Author: G.J Roerink, Z Su, M Menenti

1st Licensed Content Date: 2000

1st Licensed Content Volume Number: 25

1st Licensed Content Issue Number: 2

1st Number of Pages: 11

1st Start Page: 147

1st End Page: 157

1st Type of Use Reuse: In a Thesis/Dissertation

1st Intended Publisher of New Work: Other

1st Portion: Figures/Tables/Illustrations

1st Number of Figures/Tables/Illustration: 1

1st Format: Both Print and Electronic

1st Are You the Author of This Elsevier Article? No

1st Will You Be Translating? No

2nd License Number: 3403241482379

2nd License Date: Jun 06, 2014

2nd Licensed Content Publisher: Elsevier

2nd Licensed Content Publication: Agricultural and Forest Meteorology

2nd Licensed Content Title: S-SEBI: Spatial representativeness and the location bias of flux footprints over inhomogeneous areas

2nd Licensed Content Author: Hans Peter Schmid,Colin R. Lloyd

2nd Licensed Content Date: 12 March 1999

2nd Licensed Content Volume Number: 93

2nd Licensed Content Issue Number: 3

2nd Number of Pages: 15

2nd Start Page: 195

2nd End Page: 209

2nd Type of Use: Reuse in a Thesis/Dissertation

2nd Portion: Figures/Tables/Illustrations

2nd Number of Figures/Tables/Illustration: 1

2nd Format: Both Print and Electronic

2nd Are You the Author of This Elsevier Article? No

2nd Will You Be Translating? No

Title of Your Thesis/Dissertation: Remote Sensing Of Evapotranspiration Using Automated

Calibration: Development and Testing In The State Of Florida

Expected Completion Date: Jul 2014

Estimated Size (Number Of Pages): 200

Elsevier Vat Number: Gb 494 6272 12

Permissions price 0.00 USD

VAT/Local Sales Tax 0.00 USD / 0.00 GBP

Total 0.00 USD

Terms and Conditions

INTRODUCTION

1.The publisher for this copyrighted material is Elsevier. By clicking "accept" in connection with completing this licensing transaction, you agree that the following terms and conditions apply to this transaction (along with the Billing and Payment terms and conditions established by Copyright Clearance Center, Inc. ("CCC"), at the time that you opened your Rightslink account and that are available at any time at http://myaccount.copyright.com).

GENERAL TERMS

2. Elsevier hereby grants you permission to reproduce the aforementioned material subject to the terms and conditions indicated.

3. Acknowledgement: If any part of the material to be used (for example, figures) has appeared in our publication with credit or acknowledgement to another source, permission must also be sought from that source. If such permission is not obtained then that material may not be included in your publication/copies. Suitable acknowledgement to the source must be made, either as a footnote or in a reference list at the end of your publication, as follows:

"Reprinted from Publication title, Vol /edition number, Author(s), Title of article / title of chapter, Pages No., Copyright (Year), with permission from Elsevier [OR APPLICABLE SOCIETY COPYRIGHT OWNER]." Also Lancet special credit - "Reprinted from The Lancet, Vol. number, Author(s), Title of article, Pages No., Copyright (Year), with permission from Elsevier."

4. Reproduction of this material is confined to the purpose and/or media for which permission is hereby given.

5. Altering/Modifying Material: Not Permitted. However figures and illustrations may be altered/adapted minimally to serve your work. Any other abbreviations, additions, deletions and/or any other alterations shall be made only with prior written authorization of Elsevier Ltd. (Please contact Elsevier at permissions@elsevier.com)

6. If the permission fee for the requested use of our material is waived in this instance, please be advised that your future requests for Elsevier materials may attract a fee.

7. Reservation of Rights: Publisher reserves all rights not specifically granted in the combination of

(i) the license details provided by you and accepted in the course of this licensing transaction, (ii) these terms and conditions and (iii) CCC's Billing and Payment terms and conditions.

8. License Contingent Upon Payment: While you may exercise the rights licensed immediately upon issuance of the license at the end of the licensing process for the transaction, provided that you have disclosed complete and accurate details of your proposed use, no license is finally effective unless and until full payment is received from you (either by publisher or by CCC) as provided in CCC's Billing and Payment terms and conditions. If full payment is not received on a timely basis, then any license preliminarily granted shall be deemed automatically revoked and shall be void as if never granted. Further, in the event that you breach any of these terms and conditions or any of CCC's Billing and Payment terms and conditions, the license is automatically revoked and shall be void as if never granted. Use of materials as described in a revoked license, as well as any use of the materials beyond the scope of an unrevoked license, may constitute copyright infringement and publisher reserves the right to take any and all action to protect its copyright in the materials.

9. Warranties: Publisher makes no representations or warranties with respect to the licensed material.

10. Indemnity: You hereby indemnify and agree to hold harmless publisher and CCC, and their respective officers, directors, employees and agents, from and against any and all claims arising out of your use of the licensed material other than as specifically authorized pursuant to this license.

11. No Transfer of License: This license is personal to you and may not be sublicensed, assigned, or transferred by you to any other person without publisher's written permission.

12. No Amendment Except in Writing: This license may not be amended except in a writing signed by both parties (or, in the case of publisher, by CCC on publisher's behalf).

13. Objection to Contrary Terms: Publisher hereby objects to any terms contained in any purchase order, acknowledgment, check endorsement or other writing prepared by you, which terms are inconsistent with these terms and conditions or CCC's Billing and Payment terms and conditions. These terms and conditions, together with CCC's Billing and Payment terms and conditions (which are incorporated herein), comprise the entire agreement between you and publisher (and CCC) concerning this licensing transaction. In the event of any conflict between your obligations established by these terms and conditions and those established by CCC's Billing and Payment terms and conditions, these terms and conditions shall control.

14. Revocation: Elsevier or Copyright Clearance Center may deny the permissions described in this License at their sole discretion, for any reason or no reason, with a full refund payable to you. Notice of such denial will be made using the contact information provided by you. Failure to receive such notice will not alter or invalidate the denial. In no event will Elsevier or Copyright Clearance Center be responsible or liable for any costs, expenses or damage incurred by you as a result of a denial of your permission request, other than a refund of the amount(s) paid by you to Elsevier and/or Copyright Clearance Center for denied permissions.

LIMITED LICENSE

The following terms and conditions apply only to specific license types:

15. Translation: This permission is granted for non-exclusive world English rights only unless your license was granted for translation rights. If you licensed translation rights you may only translate this content into the languages you requested. A professional translator must perform all translations and reproduce the content word for word preserving the integrity of the article. If this license is to re-use 1 or 2 figures then permission is granted for non-exclusive world rights in all languages.

16. Posting licensed content on any Website: The following terms and conditions apply as follows: Licensing material from an Elsevier journal: All content posted to the web site must maintain the copyright information line on the bottom of each image; A hyper-text must be included to the Homepage of the journal from which you are licensing at http://www.sciencedirect.com/science/journal/xxxxx or the Elsevier homepage for books at http://www.elsevier.com; Central Storage: This license does not include permission for

a scanned version of the material to be stored in a central repository such as that provided by Heron/XanEdu.

Licensing material from an Elsevier book: A hyper-text link must be included to the Elsevier homepage at http://www.elsevier.com . All content posted to the web site must maintain the copyright information line on the bottom of each image.

Posting licensed content on Electronic reserve: In addition to the above the following clauses are applicable: The web site must be password-protected and made available only to bona fide students registered on a relevant course. This permission is granted for 1 year only. You may obtain a new license for future website posting.

For journal authors: the following clauses are applicable in addition to the above: Permission granted is limited to the author accepted manuscript version* of your paper.

*Accepted Author Manuscript (AAM) Definition: An accepted author manuscript (AAM) is the author's version of the manuscript of an article that has been accepted for publication and which may include any author-incorporated changes suggested through the processes of submission processing, peer review, and editor-author communications. AAMs do not include other publisher value-added contributions such as copy-editing, formatting, technical enhancements and (if relevant) pagination.

You are not allowed to download and post the published journal article (whether PDF or HTML, proof or final version), nor may you scan the printed edition to create an electronic version. A hyper-text must be included to the Homepage of the journal from which you are licensing at http://www.sciencedirect.com/science/journal/xxxxx. As part of our normal production process, you will receive an e-mail notice when your article appears on Elsevier's online service ScienceDirect (www.sciencedirect.com). That e-mail will include the article's Digital Object Identifier (DOI). This number provides the electronic link to the published article and should be included in the posting of your personal version. We ask that you wait until you receive this e-mail and have the DOI to do any posting.

Posting to a repository: Authors may post their AAM immediately to their employer's institutional repository for internal use only and may make their manuscript publically available after the journal-specific embargo period has ended.

Please also refer to Elsevier's Article Posting Policy for further information.

18. For book authors the following clauses are applicable in addition to the above: Authors are permitted to place a brief summary of their work online only.. You are not allowed to download and post the published electronic version of your chapter, nor may you scan the printed edition to create an electronic version. Posting to a repository: Authors are permitted to post a summary of their chapter only in their institution's repository.

20. Thesis/Dissertation: If your license is for use in a thesis/dissertation your thesis may be submitted to your institution in either print or electronic form. Should your thesis be published commercially, please reapply for permission. These requirements include permission for the Library and Archives of Canada to supply single copies, on demand, of the complete thesis and include permission for UMI to supply single copies, on demand, of the complete thesis. Should your thesis be published commercially, please reapply for permission.

Elsevier Open Access Terms and Conditions

Elsevier publishes Open Access articles in both its Open Access journals and via its Open Access articles option in subscription journals.

Authors publishing in an Open Access journal or who choose to make their article Open Access in an Elsevier subscription journal select one of the following Creative Commons user licenses, which define how a reader may reuse their work: Creative Commons Attribution License (CC BY), Creative Commons Attribution – Non Commercial - ShareAlike (CC BY NC SA) and Creative Commons Attribution – Non Commercial – No Derivatives (CC BY NC ND)

Terms & Conditions applicable to all Elsevier Open Access articles:

Any reuse of the article must not represent the author as endorsing the adaptation of the article nor should the article be modified in such a way as to damage the author's honour or reputation.

The author(s) must be appropriately credited.

If any part of the material to be used (for example, figures) has appeared in our publication with credit or acknowledgement to another source it is the responsibility of the user to ensure their reuse complies with the terms and conditions determined by the rights holder.

Additional Terms & Conditions applicable to each Creative Commons user license:

CC BY: You may distribute and copy the article, create extracts, abstracts, and other revised versions, adaptations or derivative works of or from an article (such as a translation), to include in a collective work (such as an anthology), to text or data mine the article, including for commercial purposes without permission from Elsevier

CC BY NC SA: For non-commercial purposes you may distribute and copy the article, create extracts, abstracts and other revised versions, adaptations or derivative works of or from an article (such as a translation), to include in a collective work (such as an anthology), to text and data mine the article and license new adaptations or creations under identical terms without permission from Elsevier

CC BY NC ND: For non-commercial purposes you may distribute and copy the article and include it in a collective work (such as an anthology), provided you do not alter or modify the article, without permission from Elsevier

Any commercial reuse of Open Access articles published with a CC BY NC SA or CC BY NC ND license requires permission from Elsevier and will be subject to a fee.

Commercial reuse includes:

· Promotional purposes (advertising or marketing)

· Commercial exploitation (e.g. a product for sale or loan)

· Systematic distribution (for a fee or free of charge)

Please refer to Elsevier's Open Access Policy for further information.

21. Other Conditions:

v1.7

References

Albertson, J. D., & Parlange, M. B. (1999). Natural integration of scalar fluxes from complex terrain. Advances in Water Resources, 23(3), 239-252.

Albertson, J. D., Kustas, W. P., & Scanlon, T. M. (2001). Large-eddy simulation over heterogeneous terrain with remotely sensed land surface conditions. *Water Resources Research*, *37*(7), 1939-1953.

Alduchov, O. A., & R. E. Eskridge, 1996: Improved Magnus form approximation of saturation vapor pressure. *J. Appl. Meteor.*, 35, 601–609

Allen, R., Irmak, A., Trezza, R. , Hendrickx, J.M.H. , Bastiaanssen, W. & Kjaersgaard, J. (2011). Satellite-based ET estimation in agriculture using SEBAL and METRIC. *Hydrological Processes*. 25:4011-4027.

Allen, R.G., L.S. Pereira, D. Raes, & M. Smith. (1998). Crop Evapotranspiration: Guidelines for computing crop water requirements. Irrigation and Drainage Paper 56, Food and Agriculture Organization of the United Nations, Rome, 300 pp.

Allen RG, Tasumi M, & Trezza R. (2007). Satellite-based energy balance for mapping evapotranspiration with internalized calibration (METRIC) –model. *Journal of Irrigation and Drainage Engineering*, ASCE 133: 380–394.

Anderson, M. C., Kustas, W. P., Norman, J. M., Hain, C.R., Mecikalski, J. R., Schultz, L., Gonz´alez-Dugo, M. P., Cammalleri, C. , d'Urso, G., Pimstein, A., & Gao, F. (2011). Mapping daily evapotranspiration at field to continental scales using

255

geostationary and polar orbiting satellite imagery. *Hydrology Earth Systems Science*. 15:223-239.

Allen, R., Irmak, A., Trezza, R. , Hendrickx, J.M.H. , Bastiaanssen, W. & Kjaersgaard, J. (2011). Satellite-based ET estimation in agriculture using SEBAL and METRIC. *Hydrological Processes*. 25:4011-4027.

Allen, R.G., L.S. Pereira, D. Raes, & M. Smith. (1998). Crop Evapotranspiration: Guidelines for computing crop water requirements. Irrigation and Drainage Paper 56, Food and Agriculture Organization of the United Nations, Rome, 300 pp.

Allen RG, Tasumi M, Trezza R. (2007). Satellite-based energy balance for mapping evapotranspiration with internalized calibration (METRIC) –model. *Journal of Irrigation and Drainage Engineering*, ASCE 133: 380–394.

Anderson, M. C., Kustas, W. P., Norman, J. M., Hain, C.R., Mecikalski, J. R., Schultz, L., Gonz´alez-Dugo, M. P., Cammalleri, C. , d'Urso, G., Pimstein, A., and Gao, F. (2011). Mapping daily evapotranspiration at field to continental scales using geostationary and polar orbiting satellite imagery. *Hydrology Earth Systems Science*. 15:223-239.

Anderson, M. C., Norman, J. M., Diak, G. R., Kustas, W. P., & Mecikalski, J. R. (1997). A Two-Source Time Integrated Model for Estimating Surface Fluxes Using Thermal Infrared Remote Sensing. *Remote Sensing of the Environment*, 60: 195-216.

Anderson, M. C., Norman, J. M., Mecikalski, J. R., Torn, R.D., Kustas, W. P., & Basara, J.B. (2004). A Multiscale Remote Sensing Model for Disaggregating Regional Fluxes to Micrometeorological Scales *Journal of Hydrometeorology*, 5: 343-363.

Avissar, R., Eloranta, E. W., Gürer, K., & Tripoli, G. J. (1998). An evaluation of the large-eddy simulation option of the regional atmospheric modeling system in simulating a convective boundary layer: a FIFE case study. *Journal of the atmospheric sciences*, *55*(7), 1109-1130.

Avissar, R., & Schmidt, T. (1998). An evaluation of the scale at which ground-surface heat flux patchiness affects the convective boundary layer using large-eddy simulations. *Journal of the Atmospheric Sciences*, *55*(16), 2666-2689.

Baldocchi, D. D., Hincks, B. B., & Meyers, T. P. (1988). Measuring biosphere-atmosphere exchanges of biologically related gases with micrometeorological methods. *Ecology*, 1331-1340.

Bastiaanssen, W. G. M., Menenti, M., Feddes, R. A., & Holtslag, A. A. M. (1998). A remote sensing surface energy balance algorithm for land (SEBAL). 1. Formulation. Journal of hydrology, 212, 198-212.

Bastiaanssen, W. G. M., Pelgrum, H., Wang, J., Ma, Y., Moreno, J. F., Roerink, G. J., & Van der Wal, T. (1998). A remote sensing surface energy balance algorithm for land (SEBAL).: Part 2: Validation. Journal of hydrology,212, 213-229.

F., Roerink, G. J., & Van der Wal, T. (1998). A remote sensing surface energy balance algorithm for land (SEBAL).: Part 2: Validation. Journal of hydrology,212, 213-229.

Bastiaanssen, W. G. M., Noordman, E. J. M., Pelgrum, H., Davids, G., Thoreson, B. P., & Allen, R. G. (2005). SEBAL model with remotely sensed data to improve water-resources management under actual field conditions.*Journal of irrigation and drainage engineering*, *131*(1), 85-93.

257

Bhattarai, N., Dougherty, M., Marzen, L. J., & Kalin, L. (2012). Validation of
evaporation estimates from a modified surface energy balance algorithm for land
(SEBAL) model in the south-eastern United States. Remote Sensing Letters,3(6),
511-519.

Bohrer, G., Katul, G. G., Walko, R. L., & Avissar, R. (2009). Exploring the effects of
microscale structural heterogeneity of forest canopies using large-eddy
simulations. *Boundary-layer meteorology*, *132*(3), 351-382.

Brunsell, N. A., Ham, J. M., & Arnold, K. A. (2011). Validating remotely sensed land
surface fluxes in heterogeneous terrain with large aperture
scintillometry.*International Journal of Remote Sensing*, *32*(21), 6295-6314.

Carlson, T. (2007). An Overview of the "Triangle Method" for Estimating Surface
Evapotranspiration and Soil Moisture from Satellite Imagery. *Sensors*, 7, 1612-
1629.

Carlson, T., Ripley, D. & Schmugge, T. (2004) . Rapid Soil drying and its implications
for remote sensing of soil moisture and the surface energy fluxes. In D.
Quattrochi & J. Luvall (Eds), *Thermal Remote Sensing in Land Surface
Processes* (pp. 185-204). Boca Raton:CRC Press.

Choi, M., Jacobs, J. M., & Kustas, W. P. (2008). Assessment of clear and cloudy sky
parameterizations for daily downwelling longwave radiation over different land
surfaces in Florida, USA. *Geophysical research letters*, *35*(20).

Cho, J., Miyazaki, S., Yeh, J., Kim, W., Kanae, S., & Oki, T. (2012). Testing the
hypothesis on the relationship between aerodynamic roughness length and albedo

258

using vegetation structure parameters. *International Journal of Biometeorology*. 56:411-418.

Courault, D., Seguin, B., & Olioso, A. (2005). Review on estimation of evapotranspiration from remote sensing data: From empirical to numerical modeling approaches. *Irrigation and Drainage systems*, *19*(3-4), 223-249.

Douglas, E. M., Jacobs, J. M., Sumner, D. M., & Ray, R. L. (2009). A Comparison Of Models for Estimating Potential Evapotranspiration for Florida Land Cover Types. *Journal of hydrology*, *373*(3), 366-376.

Evans, A. (2013a). Remote Sensing of Evaporative Fraction in Big Cypress National Preserve: A Comparison of Methods. *The Florida Geographer*, *44*.

Evans, A. (2013b). Remote Sensing of Evapotranspiration in Florida Using Dry Pixel Calibration. *Papers in Applied Geography*, 36:107-116.

Falkenmark, M. & Rockstrom, J. (2006). The New Blue and Green Water Paradigm: Breaking New Ground for Water Resources Planning and Management. *Journal of Water Resources and Management*, 132(3), 129-132

Fisher, J.B., Tu, K.P., & Baldocchi, D.D. (2008). Global estimates of the land–atmosphere water flux based on monthly AVHRR and ISLSCP-II data, validated at 16 FLUXNET sites. *Remote Sensing of Environment*, 112: 901-919.

Foken, T. (2008). *Micrometeorology*. Springer-Verlag Berlin Heidelberg.

Foken, T. (2008). The Energy Balance Closure Problem: An Overview. *Ecological Applications*, 18(6): 1351-1367.

Gao, F., Masek, J., Schwaller, M., & Hall, F. (2006). On the Blending of the Landsat and MODIS Surface Reflectance: Predicting Daily Landsat Surface Reflectance. *IEEE Transactions of Geoscience and Remote Sensing*, 44(8):2207-2218.

Gowda, P. H., Chávez, J. L., Howell, T. A., Marek, T. H., & New, L. L. (2008). Surface energy balance based evapotranspiration mapping in the Texas high plains. *Sensors*, *8*(8), 5186-5201.

Gowda, P. H., Chavez, J. L., Colaizzi, P. D., Evett, S. R., Howell, T. A., & Tolk, J. A. (2008). ET mapping for agricultural water management: present status and challenges. *Irrigation Science*, *26*(3), 223-237.

Guzinski, R., Anderson, M. C., Kustas, W. P., Nieto, H., & Sandholt, I. (2013). Using a thermal-based two source energy balance model with time-differencing to estimate surface energy fluxes with day-night MODIS observations.*Hydrology and Earth System Sciences Discussions*, *10*(2), 1897-1941.

Held, IM & Soden, BJ. (2000). Water Vapor and Global Warming. *Annual Review of Energy and the Environment*, 25, 441-475.

Jiang, L., & S. Islam (2001). Estimation of surface evaporation map over Southern Great Plains using remote sensing data, *Water Resources Research*, 37(2), 329–340

Jiang L., Islam, S., Guo, W., Jutla, A.S., Senarath, S.U.S., Ramsay, B.H., & Eltahir, E. (2009). A satellite-based Daily Actual Evapotranspiration estimation algorithm over South Florida. *Global and Planetary Change*, 67:62–77.

Ju, Junchang & Roy, David P. (2008). The availability of cloud-free Landsat ETM+ data over the conterminous United States and globally. *Remote Sensing of Environment*, 112, 1196–1211.

Kiehl, J. T. & Trenberth, K. E. (1997) Earth's Annual Global Mean Energy Budget. *Bull. Amer. Meteor. Soc*., 78, 197-208.

Kleissl, J., Hong, S. H., & Hendrickx, J. M. (2009). New Mexico scintillometer network: supporting remote sensing and hydrologic and meteorological models.*Bulletin of the American Meteorological Society*, *90*(2), 207-218.

Kormann, R., & Meixner, F.X. (2001) An analytical footprint model for non-neutral stratification. *Boundary-Layer Meteorology* 99:207–224

Kosa, P. (2011). The Effect of Temperature on Actual Evapotranspiration based on Landsat 5 TM Satellite Imagery (SEBAL). In L. Labedzki (Eds.), *Evapotranspiration* (pp. 209-228). Rijeka, Croatia :InTech.

Layman, C.A., & Quattrochi, D.A. (2004). Estimating spatially distributed surface fluxes in a semi-arid Great Basin desert using Landsat TM thermal data. In D. Quattrochi & J. Luvall (Eds), *Thermal Remote Sensing in Land Surface Processes* (pp. 133-158). Boca Raton:CRC Press.

Li, F., & Lyons, T. J. (1999). Estimation of regional evapotranspiration through remote sensing. *Journal of applied meteorology*, *38*(11), 1644-1654.

Li, Z. L., Tang, B. H., Wu, H., Ren, H., Yan, G., Wan, Z., Trigo, I.F. & Sobrino, J. A. (2013). Satellite-derived land surface temperature: Current status and perspectives. *Remote Sensing of Environment*, 131, 14-37.

Lloyd, C.R. (1995). The effect of heterogeneous terrain on micrometeorological flux measurements: a case study from HAPEX-SAHEL. *Agricultural and Forest Meteorology*, 73:209-216.

Loheide II, S. & Gorelick, S. (2005). A local-scale, high-resolution evapotranspiration mapping algorithm (ETMA) with hydroecological applications at riparian meadow restoration sites. *Remote Sensing of the Environment*, 98, 182-200.

Long, D., & Singh, V. P. (2012). A two-source trapezoid model for evapotranspiration (TTME) from satellite imagery. *Remote Sensing of Environment*, *121*, 370-388.

Long, D., & Singh, V. P. (2013). Assessing the impact of end-member selection on the accuracy of satellite-based spatial variability models for actual evapotranspiration estimation. *Water Resources Research*, *49*(5), 2601-2618.

Mallick, K., Jarvis, A., Fisher, J. B., Tu, K. P., Boegh, E., & Niyogi, D. (2013). Latent Heat Flux and Canopy Conductance Based on Penman-Monteith, Priestley-Taylor Equation, and Bouchet's Complementary Hypothesis. *Journal of Hydrometeorology*, 14(2).

Mecikalski, J.R., Sumner, D.M., Jacobs, J.M., Pathak, C.S., Paech, S.J., & Douglas, E.M. (2011) . Use of Visible Geostationary Operational Meteorological Satellite Imagery in Mapping Reference and Potential Evapotranspiration over Florida. In L. Labedzki (Eds.), *Evapotranspiration* (pp. 241-254). Rijeka, Croatia :InTech.

Mu, Q., Zhao,M., & Running,S.W. (2011). Improvements to a MODIS global terrestrialevapotranspiration algorithm. *Remote Sensing of Environment* 115:1781–1800.

Monteith, J. L., (1965). Evaporation and environment. *The State and Movement of Water in Living Organisms*, G. E. Fogg, Ed., Symposia of the Society for Experimental Biology, Vol. 19, Academic Press, 205–234.

Moran, M. S., Clarke, T. R., Inoue, Y., & Vidal, A. (1994). Estimating crop water deficit using the relation between surface-air temperature and spectral vegetation index. *Remote sensing of environment*, *49*(3), 246-263.

Norman J.M., Anderson M.C., & Kustas W.P. (2006) Are single-source, remote-sensing surface-flux models too simple? *AIP Conference Proceedings*. 852 , pp. 170-177.

Owen, T. W., Carlson, T. N. & Gillies, R. R. (1998) An assessment of satellite remotely-sensed land cover parameters in quantitatively describing the climatic effect of urbanization. *Int. J. Remote Sensing*, 19(9), 1663-1681.

Paech, S. J., Mecikalski, J. R., Sumner, D. M., Pathak, C. S., Wu, Q., Islam, S., & Sangoyomi, T. (2009). A Calibrated, High-Resolution GOES Satellite Solar Insolation Product for a Climatology of Florida Evapotranspiration1.*JAWRA Journal of the American Water Resources Association*, *45*(6), 1328-1342.

Penman, H. L., 1948: Natural evaporation from open water, bare soil, and grass. *Proc. Roy. Soc. London*, A193, 120–146.

Priestley, C. H. B., & R. J. Taylor, (1972) On the assessment of surface heat flux and evaporation using large-scale parameters. *Mon. Wea. Rev.*, 100, 81–92.

Rodriguez-Iturbe, I. & Porporato, A. .(2004) . *Ecohydrology of water-controlled ecosystem:soil moisture and plant dynamics*. Cambridge University Press, Cambridge

Roerink, G., Su, Z., & Menenti, M. (2000). S-SEBI: A Simple Remote Sensing Algorithm to Estimate the Surface Energy Balance. *Physics and Chemistry of the Earth, Oceans and Atmosphere*. 25(2):147-157.

Sanford, W. E., & Selnick, D. L. (2013). Estimation of Evapotranspiration Across the
Conterminous United States Using a Regression With Climate and Land-Cover
Data1. *JAWRA Journal of the American Water Resources Association*, *49*(1), 217-
230.

Schedlbauer, J. L., Munyon, J. W., Oberbauer, S. F., Gaiser, E. E., & Starr, G. (2012).
Controls on ecosystem carbon dioxide exchange in short-and long-hydroperiod
Florida Everglades freshwater marshes. *Wetlands*, 32(5), 801-812.

Schaudt, K.J., & Dickinson, R.E. (2000). An approach to deriving roughness length and
zero-plane displacement height from satellite data, prototyped with BOREAS
data. *Agricultural and Forest Meteorology* 104:143–155

Schmid, H.P., & Lloyd, C.R. (1999). Spatial representativeness and the location bias of
flux footprints over inhomogeneous areas. *Agricultural and Forest Meteorology*
93:195-209

Schmugge, T., Hook, S. J., & Coll, C. (1998). Recovering surface temperature and
emissivity from thermal infrared multispectral data. *Remote Sensing of
Environment*, 65(2), 121-131.

Schuepp, P. H., Leclerc, M. Y., MacPherson, J. I., & Desjardins, R. L. (1990). Footprint
prediction of scalar fluxes from analytical solutions of the diffusion
equation. *Boundary-Layer Meteorology*, 50(1-4), 355-373.

Shoemaker, W.B., Lopez, C.D., & Duever, Michael, (2011). Evapotranspiration over
spatially extensive plant communities in the Big Cypress National Preserve,
southern Florida, 2007–2010: U.S. Geological Survey Scientific Investigations
Report 2011–5212, 46 p.

Sinclair, T. R., Tanner, C. B., & Bennett, J. M. (1984). Water-use efficiency in crop
production. *BioScience*, *34*(1), 36-40.

Spellman, Frank R. (2009). *The science of air: concepts & applications*. CRC Press,
Boca Raton.

Stull, R. B. (1988). *An Introduction to Boundary Layer Meteorology* (Vol. 13). Springer.

Su, Z. (2002). The Surface Energy Balance System (SEBS) for estimation of turbulent
heat fluxes. *Hydrology and Earth System Sciences*, 6(1), 85-99.

Tasumi M. (2003). Progress in operational estimation of regional evapotranspiration
using satellite imagery. PhD Dissertation, University of Idaho, Moscow, ID; 357

Tasumi M, Allen RG, Trezza R. (2008). At-surface albedo from Landsat and MODIS
satellites for use in energy balance studies of evapotranspiration. *Journal of
Hydrologic Engineering* 13: 51–63.

Timmermans, W. J., Bertoldi, G., Albertson, J. D., Olioso, A., Su, Z., & Gieske, A. S. M.
(2008). Accounting for atmospheric boundary layer variability on flux estimation
from RS observations. *International Journal of Remote Sensing*,*29*(17-18), 5275-
5290.

Woolf, H. M. (1968). *On the computation of solar elevation angles and the determination
of sunrise and sunset times*. National Aeronautics and Space Administration.

Yang, F., White, M., Michaelis, A., Ichii, K., Hashimoto, H., Votava, P., Zhu, A. &
Nemani, R. (2006). Prediction of Continental-Scale Evapotranspiration by
Combining MODIS and AmeriFlux Data Through Support Vector Machine. *IEEE
Transactions on Geoscience and Remote Sensing*, 44(11), 3452-3461.

265

Yebra, M., Van Dijk, A., Leuning, R., Huete, A., & Guerschman, J. P. (2013). Evaluation of optical remote sensing to estimate actual evapotranspiration and canopy conductance. *Remote Sensing of Environment*, *129*, 250-261.

Zhengming, W., & Dozier, J. (1989). Land-surface temperature measurement from space: Physical principles and inverse modeling. *Geoscience and Remote Sensing, IEEE Transactions on*, *27*(3), 268-278.

VITA

Aaron Henry Evans was born in Walnut Creek, California in 1972. After graduating from

Pagosa Springs High School in 1990, Aaron attended Fort Lewis College in Durango, CO

and University of Colorado in Boulder. He received a Bachelor of Science in Civil and

Environmental Engineering in 1995 and a Master of Science in Atmospheric and Oceanic

Sciences in 1998. For the next two years Aaron worked as a research associate studying

the remote sensing of cirrus clouds. Over the next decade he pursued a career as a web-

based database application developer. In 2010 Aaron returned to graduate school at

Florida Atlantic University in Boca Raton, FL and pursued interests in Ecohydrology,

Remote Sensing and Micrometeorology. He earned his PhD in Geosciences from FAU in

2014.